Concerns about microplastic pollutants in the sea *p. 144*

Big data peering into your checkbook *p. 212*

A step toward precision cancer treatment *p. 215*

Science

$10
11 JULY 2014
sciencemag.org

AAAS

SPECIAL ISSUE

Staying a step ahead of HIV/AIDS

A success story in Australia holds lessons for its neighbors *p. 152*

CONTENTS

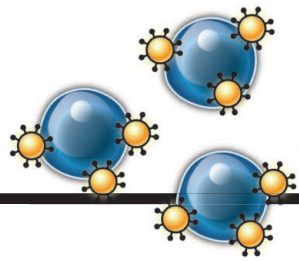

136 & 178
Viral fitness affects HIV transmission

11 JULY 2014 • VOLUME 345 • ISSUE 6193

NEWS

IN BRIEF

122 Roundup of the week's news

IN DEPTH

125 **UNCONTACTED TRIBE EMERGES**
Anthropologists worry about the threat from infections and resource conflicts *By H. Pringle*

126 **MEDICAL ISOTOPES CONFOUND NUCLEAR TEST MONITORING**
Medical isotope plants vow to cut xenon emissions *By C. Wald*

127 **CONFLICT OVER BRAIN PROJECT**
Hundreds of scientists threaten to boycott the Human Brain Project
By M. Enserink and K. Kupferschmidt

128 **INDIA PLANS GRAND CANALS**
Nationwide water network could aid farms but harm environment *By P. Bagla*

129 **RIP FOR A KEY HOMO SPECIES?**
Questioning a claimed common ancestor of Neandertals and modern humans *By M. Balter*

FEATURE

130 **MONKEY FEVER UNBOUND**
The spread of an emerging virus sounds alarm bells in India *By R. Stone*

INSIGHTS

PERSPECTIVES

134 **TAKING THE PULSE OF OCEAN MICROBES**
Gene expression patterns of open-ocean microbes are tightly coupled
By E. V. Armbrust
▸ REPORT P. 207

136 **A FITNESS BOTTLENECK IN HIV-1 TRANSMISSION**
Infection is linked to how close a viral genome is to an ideal sequence
By S. B. Joseph and R. Swanstrom
▸ SPECIAL SECTION P. 152; RESEARCH ARTICLE P. 178

SPECIAL SECTION

Strategies against HIV/AIDS

INTRODUCTION

152 Australia shows its neighbors how to stem an epidemic

NEWS

Stories by J. Cohen

156 First, do harm reduction

157 The limits of success

158 In PNG, the epidemic that wasn't

160 Prevention, Papua New Guinea style

161 The circumcision conundrum

162 A consummate insider pushes ideas from outside Indonesia

164 Malaysia tries to follow Australia's path

OPINION

166 End of AIDS—Hype versus hope
By W. M. El-Sadr et al.

PERSPECTIVE

167 A critical question for HIV vaccine development: Which antibodies to induce? *By S. Zolla-Pazner*

REVIEW

169 Immunologic strategies for HIV-1 remission and eradication
By D. H. Barouch and S. G. Deeks

SEE ALSO

- ▸ PERSPECTIVES PP. 136, 141, & 143
- ▸ RESEARCH ARTICLES PP. 178 & 179
- ▸ *SCIENCE* EXPRESS REPORT
- ▸ VIDEOS
- ▸ www.sciencemag.org/special/hiv2014

ON THE COVER

Transgender sex workers in Jakarta. This "key affected population" has high HIV prevalence but is largely ignored by government efforts. Australia, in contrast, has aggressively targeted its prevention interventions to high-risk groups. See page 152. *Photo: Romeo Gacad/Agence France-Presse/Getty Images*

137 **LOW-ENERGY ELECTRON DIFFRACTION AT ULTRAFAST SPEEDS**
Structural changes in a thin polymer film can be quickly resolved
By E. T. J. Nibbering
▸ REPORT P. 200

138 **AN OPTICAL TWIST FOR TRIPLET SUPERCONDUCTORS**
Optical measurements may reveal the secrets of exotic superconductivity
By D. van der Marel and G. A. Sawatzky
▸ REPORT P. 190

139 **A FLIPPING CELL WALL FERRY**
How bacteria "flip" carbohydrate precursors across the cytoplasmic membrane *By K. D. Young*
▸ REPORT P. 220

141 **HEPATITIS C CAN BE CURED GLOBALLY, BUT AT WHAT COST?**
New drugs to cure hepatitis C should be made available at low costs in developing countries *By A. Hill and G. Cooke*
▸ SPECIAL SECTION P. 152

142 **FISHING FOR PEROXIDASE PROTONS**
Where are the protons in heme protein catalysis? *By J. T. Groves and N. C. Boaz*
▸ REPORT P. 193

143 **PERSISTENCE BY PROLIFERATION?**
Latently HIV-infected cells may challenge eradication strategies
By D. Margolis and F. Bushman
▸ SPECIAL SECTION P. 152; RESEARCH ARTICLE P. 179

Published by AAAS

CONTENTS

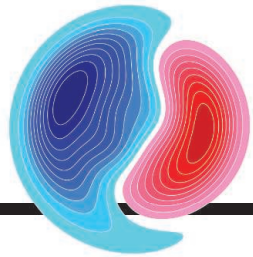

184
Interplay of Earth's magnetosphere and ionosphere

11 JULY 2014 • VOLUME 345 • ISSUE 6193

144 MICROPLASTICS IN THE SEAS
Contamination of the marine environment by microplastics causes concern *By K. L. Law and R. C. Thompson*
▸ PODCAST

BOOKS *ET AL.*

146 THE AGE OF RADIANCE
By C. Nelson, reviewed by D. L. Sanchez

147 CONSCIOUSNESS AND THE SOCIAL BRAIN
By M. S. A. Graziano, reviewd by A. Schurger

LETTERS

148 TWITTER: BIG DATA OPPORTUNITIES
By D. A. Broniatowski et al.

148 RESPONSE
By D. Lazer et al.

149 LEADERSHIP VOID FOR "DESIGNER BABY" ETHICS
By I. H. Carmen

149 TECHNICAL COMMENT ABSTRACTS

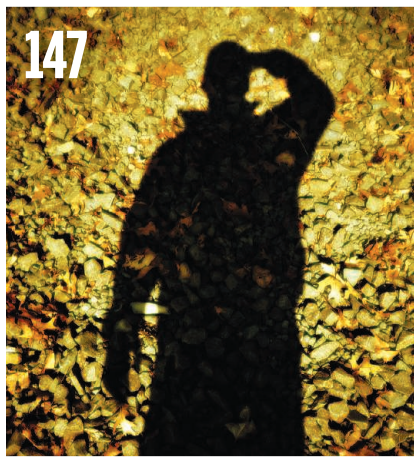

REPORTS

184 SPACE WEATHER
Ionospheric control of magnetotail reconnection *W. Lotko* et al.

187 SUPERCONDUCTIVITY
Fermi arcs in a doped pseudospin-1/2 Heisenberg antiferromagnet *Y. K. Kim* et al.

190 SUPERCONDUCTIVITY
Observation of broken time-reversal symmetry in the heavy-fermion superconductor UPt_3 *E. R. Schemm* et al.
▸ PERSPECTIVE P. 138

193 HEME ENZYMES
Neutron cryo-crystallography captures the protonation state of ferryl heme in a peroxidase *C. M. Casadei* et al.
▸ PERSPECTIVE P. 142

197 CATALYSIS
Assessing the reliability of calculated catalytic ammonia synthesis rates *A. J. Medford* et al.

200 IMAGING TECHNIQUES
Ultrafast low-energy electron diffraction in transmission resolves polymer/graphene superstructure dynamics *M. Gulde* et al.
▸ PERSPECTIVE P. 137

204 EARTHQUAKE DYNAMICS
Supershear rupture in a M_w 6.7 aftershock of the 2013 Sea of Okhotsk earthquake *Z. Zhan* et al.

207 OCEAN MICROBES
Multispecies diel transcriptional oscillations in open ocean heterotrophic bacterial assemblages *E. A. Ottesen* et al.
▸ PERSPECTIVE P. 134

212 MICROECONOMICS
Harnessing naturally occurring data to measure the response of spending to income *M. Gelman* et al.

216 CANCER THERAPY
Ex vivo culture of circulating breast tumor cells for individualized testing of drug susceptibility *M. Yu* et al.

220 BACTERIAL CELL WALL
MurJ is the flippase of lipid-linked precursors for peptidoglycan biogenesis *L.-T. Sham* et al.
▸ PERSPECTIVE P. 139

222 GENETIC OSCILLATIONS
A Doppler effect in embryonic pattern formation *D. Soroldoni* et al.

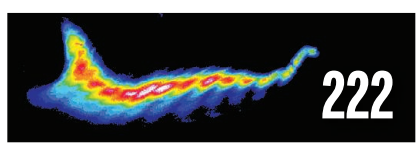

RESEARCH

IN BRIEF

175 From *Science* and other journals

RESEARCH ARTICLES

178 HIV TRANSMISSION
Selection bias at the heterosexual HIV-1 transmission bottleneck *J. M. Carlson* et al.
RESEARCH ARTICLE SUMMARY; FOR FULL TEXT: HTTP://DX.DOI.ORG/10.1126/SCIENCE.1254031
▸ PERSPECTIVE P. 136; SPECIAL SECTION P. 152

179 HIV LATENCY
Specific HIV integration sites are linked to clonal expansion and persistence of infected cells *F. Maldarelli* et al.
▸ PERSPECTIVE P. 143; SPECIAL SECTION P. 152; *SCIENCE* EXPRESS REPORT

DEPARTMENTS

121 EDITORIAL
A focus on child development
By Karlee L. Silver and Peter A. Singer

234 WORKING LIFE
In praise of early independence
By Elisabeth Pain

Science Staff 120
New Products 226
Science Careers 227

SCIENCE (ISSN 0036-8075) is published weekly on Friday, except the last week in December, by the American Association for the Advancement of Science, 1200 New York Avenue, NW, Washington, DC 20005. Periodicals mail postage (publication No. 484460) paid at Washington, DC, and additional mailing offices. Copyright © 2014 by the American Association for the Advancement of Science. The title SCIENCE is a registered trademark of the AAAS. Domestic individual membership and subscription (51 issues): $153 ($74 allocated to subscription). Domestic institutional subscription (51 issues): $1282; Foreign postage extra: Mexico, Caribbean (surface mail) $55; other countries (air assist delivery) $85. First class, airmail, student, and emeritus rates on request. Canadian rates with GST available upon request, GST #1254 88122. Publications Mail Agreement Number 1069624. **Printed in the U.S.A.**
Change of address: Allow 4 weeks, giving old and new addresses and 8-digit account number. **Postmaster:** Send change of address to AAAS, P.O. Box 96178, Washington, DC 20090–6178. **Single-copy sales:** $10.00 current issue, $15.00 back issue prepaid includes surface postage; bulk rates on request. **Authorization to photocopy** material for internal or personal use under circumstances not falling within the fair use provisions of the Copyright Act is granted by AAAS to libraries and other users registered with the Copyright Clearance Center (CCC) Transactional Reporting Service, provided that $30.00 per article is paid directly to CCC, 222 Rosewood Drive, Danvers, MA 01923. The identification code for *Science* is 0036-8075. *Science* is indexed in the *Reader's Guide to Periodical Literature* and in several specialized indexes.

PHOTO: (RIGHT) DANIELE SOROLDONI, ANDREW OATES

Published by AAAS

EDITORIAL

A focus on child development

By September 2014, the United Nations (UN) Open Working Group will present its final report on the Sustainable Development Goals to the UN Secretary General and President of the General Assembly, who will finalize these goals by September 2015. Because these goals (the successors to the Millennium Development Goals) will guide global action through 2030, it is unfortunate that early child development is not yet effectively addressed in this framework. Investing in child development is the foundation for improved health, economic, and social outcomes. Not getting the early years "right" is linked to violent behavior, depression, higher rates of noncommunicable disease, and lower wages, and it negatively affects a nation's gross domestic product. Unless early child development is addressed effectively in the UN Sustainable Development Goals, countries will be locked into poverty, and sustainable development will not be achieved.

Emphasis on child development is needed

"Unless early child development is addressed effectively ... countries will be locked into poverty..."

Child development is reflected in the post-2015 goals but in an implicit and fragmented way. Relevant targets appear under various goals: under health as ending preventable newborn and child mortality; under hunger and nutrition as ending child stunting and wasting; under education as providing access to quality early childhood care and pre-primary education; under sanitation as achieving adequate sanitation for all; and under peaceful and inclusive societies as ending abuse, exploitation, and violence against children. However, these actions would be executed more effectively and efficiently if they were considered together, under a single goal. This would put the focus where it belongs: on the end beneficiary, the child, and her or his potential for development. It would also provide an integrated approach and suggest a common means of implementation: Eliminating one risk will not allow children to thrive if they face multiple adversities, which is often the case for children growing up in poverty. This reframing would also highlight the fundamental importance of early child development to overall sustainable development, a message that is currently lost in the UN Sustainable Development Goals.

These targets could be combined with those on ending preventable maternal, newborn, and child deaths under a single integrated goal that focuses on women and children. Such a goal would build on the progress on maternal and child survival (the focus of two of the original Millennium Development Goals) and extend it to ensuring that children who survive reach their full potential. Recent advances in neuroscience indicate the importance of healthy brain development in the early years to human capital formation. Many of the same interventions (nutrition, vaccines, sanitation, and newborn resuscitation) that save children's lives also save children's brains. A society only reaps the full benefits of a child's survival if that child becomes a productive individual as an adult. Moreover, such a goal would respond to recent calls, such as that by Canadian Prime Minister Stephen Harper,* to place maternal, newborn, and child health at the heart of the post-2015 agenda.

Given the advanced state of the draft UN Sustainable Development Goals, an alternative is to better link early child development to ending poverty and inequality, the *leitmotif* of the post-2015 agenda, with an explicit target of reducing by 50% the number of children who fail to reach their full economic and social potential later in life. But either way, progress on healthy brain development in the early years could be directly tracked by a composite indicator of age-appropriate development that includes self-regulation, language, and responsive parenting (for infants) or social interaction (for children 3 to 5 years old). An increase in thriving children over the next 15 years would lay a stronger foundation for healthy, prosperous, and peaceful societies. It is difficult to see how the world could end poverty and inequality without addressing early child development.

A key challenge for the UN is finding focus and coherence in the Sustainable Development Goals. A more effective emphasis on early child development could also generate an overarching aspirational narrative for the Sustainable Development Goals: fulfilling human potential.

– Karlee L. Silver and Peter A. Singer

Karlee L. Silver is vice president of Targeted Challenges, Grand Challenges Canada, Toronto, Ontario, Canada. E-mail: karlee.silver@grandchallenges.ca

Peter A. Singer is chief executive officer of Grand Challenges Canada, Toronto, Ontario, Canada. E-mail: peter.singer@grandchallenges.ca

*http://scim.ag/pmCanada

10.1126/science.1257424

PHOTOS: (TOP RIGHT) GRAND CHALLENGES CANADA; (BOTTOM RIGHT) MICHAEL PEAKE; (INSET) HAN LANS/GETTY IMAGES

Downloaded from www.sciencemag.org on July 11, 2014

Published by AAAS

99.6% Failure rate for Alzheimer's disease (AD) drug development from 2002 to 2012, according to the first-ever analysis of AD clinical trials, by researchers at the Cleveland Clinic.

IN BRIEF

Scuffle over sage grouse

Development threatens the greater sage grouse's habitat in Wyoming.

Conservation biologists aren't happy with U.S. government plans to largely adopt the state of Wyoming's strategy for protecting the greater sage grouse (*Centrocercus urophasianus*)—a declining grassland bird at the center of a national controversy. The strategy fails to preclude intrusive development in key habitat and preserve the bird's wintering range, the scientists say in a report issued this week by Defenders of Wildlife. The critique comes in response to last month's decision by the federal Bureau of Land Management to start implementing elements of the state plan on some 800,000 hectares of federal land in Wyoming. Grouse numbers have declined by half in recent decades and the state, which holds an estimated one-third of the remaining population, developed its strategy in 2011 in a bid to prevent the bird from being added to the federal endangered species list. Such an endangered species listing worries officials in the 11 states where the grouse lives because it could trigger extensive regulation of oil and gas drilling and other land uses.

AROUND THE WORLD

Carbon observatory in orbit

LOMPOC, CALIFORNIA | The Orbiting Carbon Observatory-2 (OCO-2), a NASA mission to measure atmospheric carbon dioxide, reached orbit on 2 July after launching from Vandenberg Air Force Base. The $468 million spacecraft is a replacement for OCO, which failed soon after launch in 2009 when the nose cone on a Taurus XL rocket didn't open. By measuring carbon dioxide in a column of air a couple of kilometers across, OCO-2 should enable a precise accounting of regional carbon budgets—in particular the net exchange above carbon sinks such as the Amazon rainforest (*Science*, 13 June, p. 1211). Furthermore, the spacecraft will detect the faint fluorescent glow that accompanies photosynthesis, allowing for an estimate of carbon uptake. Researchers on the mission hope to remove uncertainties from global carbon budgets and also see how different regions will respond to the pressures of climate change.

Research funding needs overhaul

PARIS | France's research system is too "rigid" and "complex," according to a report by the Organisation for Economic Co-operation and Development (OECD). The study, released in late June, urges the government to continue reforms set in motion over the past decade but criticizes France's tax credit system for R&D as ineffective and too generous. "French research … seems to be among the most inert in the world in terms of specialisation," the report says. Most public science in France is centered around large national organizations, which plan, fund, and carry out research. According to the review, which was requested by the French government, some 10% of France's public research funds are awarded to specific projects on a competitive basis—the lowest figure among OECD's 34 member countries. The report recommends raising the percentage to stimulate competition and adjust research priorities more quickly.
http://scim.ag/Frenchfunding

Downloaded from www.sciencemag.org on July 11, 2014

PHOTO: ACK MILCHANOWSKI/AGE FOTOSTOCK SPAIN S.L./CORBIS

Published by AAAS

Seismic cruise spurs lawsuit

TRENTON | The state of New Jersey is suing the National Science Foundation and the National Oceanic and Atmospheric Administration in a bid to block a planned summer research cruise that would use blasts of sound to map ocean sediments. In a 3 July court filing, state officials argue that the agencies didn't properly finish environmental studies before approving plans by New Jersey's Rutgers University and the University of Texas to conduct acoustic imaging off the state's coast. The study is aimed at better understanding sea-level rise that occurred tens of millions of years ago. If nothing else, state officials and environmentalists would like the cruise moved to another, less busy season. The researchers say they have already taken protective measures, such as enlisting wildlife monitors who can halt the research.
http://scim.ag/NJseismic

Senate budgetmakers nix ITER

WASHINGTON, D.C. | Budgetmakers in the U.S. Senate moved to pull the United States out of ITER, the international fusion experiment under construction in Cadarache, France. The Senate's version of the budget bill for fiscal year 2015 would provide $75 million for the U.S. ITER effort, half of what the White House requested and enough to wind it down, Senator Lamar Alexander (R–TN) said in a 17 June Senate appropriations subcommittee meeting. However, on 18 June, appropriators in the House of Representatives approved a bill that would continue the U.S. ITER effort and give it $225 million. And as *Science* went to press, the Senate budget bill remains stuck in committee, snagged by wrangling over the Obama administration's plan to limit carbon emissions from power plants.
http://scim.ag/SenateITER

ITER under construction in April.

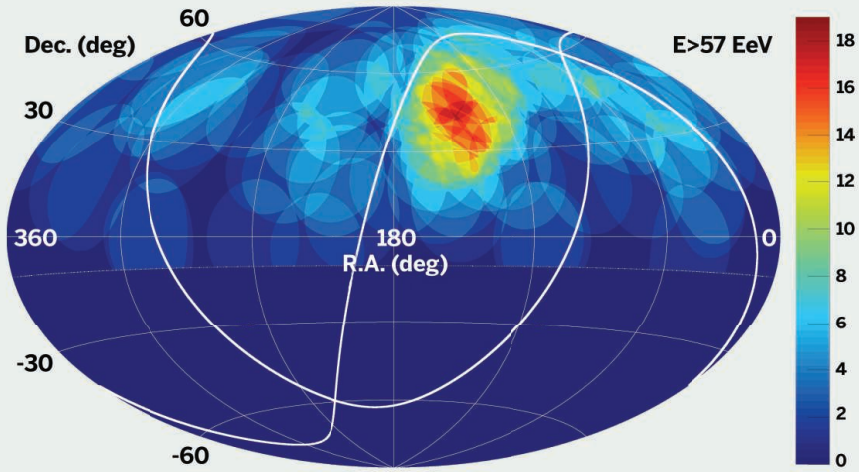

A font of cosmic rays

Physicists have long sought the sources of ultra–high-energy cosmic rays, which can strike the atmosphere with as much energy as a well-thrown baseball. Now, researchers with the Telescope Array, a collection of 507 particle detectors covering 700 square kilometers of desert in Utah, have observed a broad "hotspot" in the sky in which such cosmic rays seem to originate. In 2007, researchers with the Pierre Auger Observatory, an even bigger array in Argentina, reported that ultra–high-energy cosmic rays appeared to spring from certain galaxies, but that correlation weakened with more data. The Telescope Array team took a simpler approach, looking only for evidence that the cosmic rays do not arrive in equal numbers in all directions. From 2008 to 2013, they spotted 72 ultra–high-energy rays, 19 of which clustered in a hotspot (in red) in the sky about 20° in radius, as the team reports in a paper in press at *The Astrophysical Journal Letters*. http://scim.ag/rayhotspot

Probing more medical mysteries

BETHESDA, MARYLAND | The National Institutes of Health (NIH) announced last week that it plans to add six new clinical sites to its Undiagnosed Diseases Program, an effort launched in 2008 to diagnose intractable medical cases and collect data for the scientists studying rare diseases. The new sites—Baylor College of Medicine; the Harvard teaching hospitals; Duke University; Stanford University; the University of California, Los Angeles; and Vanderbilt University Medical Center—will each receive a 4-year grant of roughly $7.2 million to host patients for weeklong examinations. About 150 patients now participate annually, but NIH plans to accommodate 50 patients per year at each site by 2017. Harvard Medical School, tapped in December to act as "coordinating center," will make data widely available through public repositories. http://scim.ag/_UDP

The case of the stolen seeds

DES MOINES | Expanding an existing case, U.S. prosecutors have accused a Chinese agricultural scientist of conspiring to smuggle patented corn seed to China. The 1 July indictment of Mo Yun, a research head at Beijing-based Dabeinong Technology Group, increases the number of defendants in the trade secrets case to seven. Prosecutors allege that Mo Yun helped her brother, Mo Hailong, coordinate a group that roamed rural Illinois, Indiana, and Iowa in rented cars, digging up seedlings, stealing ears of corn, and illegally obtaining packages of seed. The investigation began in 2011, after an employee of corn breeding giant DuPont Pioneer spotted one defendant on his knees in a field, digging. According to court documents, the alleged thieves also attempted to smuggle patented seeds to China in microwave popcorn boxes.
http://scim.ag/seedtheft

CREDITS: (TOP TO BOTTOM) TELESCOPE ARRAY COLLABORATION; ITER ORGANIZATION

Published by AAAS

Smallpox found in federal lab

BETHESDA, MARYLAND | Federal researchers discovered six forgotten vials of smallpox virus in a storage room at the National Institutes of Health (NIH). The vials, apparently dating to the 1950s, were found in a Food and Drug Administration lab at NIH, according to the Centers for Disease Control and Prevention (CDC). On 7 July, CDC transferred the vials to its high-containment lab in Atlanta, where testing confirmed they contained variola virus DNA. CDC says the vials will be destroyed per a 1979 World Health Organization agreement that allows smallpox stocks to be retained only at CDC and at Russia's VECTOR laboratory in Novosibirsk. Most Americans born since 1972 are not vaccinated against smallpox, which killed hundreds of millions before it was declared eradicated in 1980.

Gunung Padang's andesite columnar rocks.

PHOTO: IKHLASUL AMAL/FLICKR

Ancient 'pyramid'—or volcano?

A controversial research project in West Java, Indonesia, claims that piles of columnar andesite rock littering the site of Gunung Padang represent remnants of "the world's oldest civilization." But Indonesia's scientific community disputes the claim, saying that the rocks are likely just remnants of a volcano. Lead scientist Danny Hilman Natawidjaja, who received a Ph.D. in geology from the California Institute of Technology and is now at the Indonesian Institute of Sciences, says that beneath the jumbled rock columns lies an underground pyramid constructed more than 10,000 years ago. A tomographic analysis of the site reveals a low-velocity zone that he says is likely humanmade—like a large room. But geologists dispute this; for example, Awang Satyana, a senior geologist at Indonesia's Ministry of Energy and Mineral Resources, told Kompas.com in October 2013 that the low-velocity zone could be due to the presence of partial melt or even a natural cave—consistent with a volcanic origin. Natawidjaja, however, says he is undaunted by the skepticism. "We're not stupid to put our reputation at risk," he says. The project has drawn some support from Indonesia's president, Susilo Bambang Yudhoyono, who issued a presidential regulation to protect it from vandals after local villagers attacked the site last year for fear that drilling could generate landslides.

Published by AAAS

IN DEPTH

An uncontacted Amazon tribe watches a plane in a 2010 photograph.

PHOTO: © GLEISON MIRANDA/FUNAI/SURVIVAL

INDIGENOUS PEOPLES

Uncontacted tribe in Brazil emerges from isolation

Anthropologists worry about the threat from novel infections and conflicts with other tribes

By **Heather Pringle**

In a terse, one-page announcement last week, Brazil's Indian affairs department (FUNAI) let it be known that an isolated tribe in the Amazon region had just taken a momentous and potentially tragic step. Emerging from dense rainforest along the Upper Envira River in the state of Acre, Brazil, the group willingly approached a team of Brazilian government scientists on 29 June and made peaceful contact with the outside world.

The event—Brazil's first official contact with an isolated tribe since 1996—was not entirely unexpected. Since early June, fearful villagers in the region had radioed Brazilian authorities at least twice about a group of some 35 tribal strangers who were raiding their crops and trying to make off with machetes and other tools. Recognizing the potential for trouble, FUNAI dispatched a team of specialists, including medical personnel and Brazilian anthropologist José Carlos Meirelles, an adviser on indigenous matters to the government of Acre.

FUNAI's swift response is commendable, says anthropologist Kim Hill of Arizona State University, Tempe, who has conducted extensive fieldwork among Amazon rainforest tribes. Since 1987, the agency has maintained a no-contact policy, except in cases where a tribe's survival was deemed to be in peril. That was probably the case here, Hill notes. "There was a serious threat of violence between two native populations, and the intervention should eliminate that," he says. But Hill and others remain deeply concerned about the future of the newly contacted tribe as it encounters novel diseases and resource-hungry outsiders. As much as 60% of a newly contacted Nahua population in the Peruvian Amazon died between 1983 and 1985 from influenza, whooping cough, and other diseases caught from loggers, noted Beatriz Huertas Castillo, a private Peruvian scholar, in a 2004 report.

The massive Amazon rainforest holds the world's largest concentration of isolated tribes—at least 70 in the Brazilian Amazon alone, according to FUNAI. Many, if not most, have had at least fleeting contact with the outside world, particularly during Brazil's rubber boom in the late 19th and early 20th centuries, when rubber tappers made a practice of rounding up and enslaving indigenous tribespeople. After that, many populations fled to remote Amazon headwaters and cut off all contact with outsiders.

It is not yet clear what prompted the tribe along the Upper Envira River to end its long seclusion. The FUNAI field team has yet to identify the tribe's language, much less ask for its story, and has now requested the assistance of linguists.

But officials think the tribe most likely migrated from a large area in Peru that includes Murunahua Territorial Reserve and Alto Purús National Park, some 300 kilometers away (see map, p. 126). Although the land is protected on paper, illegal loggers there have built roads and set up base camps to cut down valuable mahogany. The logging is selective, but the heavy machinery may be frightening off wild game, an important source of food for isolated people.

The cocaine trade is also encroaching on the protected area, according to an online report in *GeoJournal* in 2011 by geographer David Salisbury of the University of Richmond and Chris Fagan, executive director of the Upper Amazon Conservancy in Jackson, Wyoming. Processors have set up camps to make cocaine paste, and heavily armed traffickers now use the tribes' traditional migratory trails to reach river tributaries in order to transport the product into Brazil. "On the Purús River, the number of conflicts between uncontacted tribes and both coca workers and loggers has increased in recent years resulting in deaths on both sides," Salisbury and Fagan wrote.

The newly contacted tribespeople may have been fleeing such conflicts, but Hill says that they may also have scouted out desirable resources such as game in the Upper Envira River area in Brazil. Or, he adds, "they might have discovered that they can raid weaker neighbors and get goodies."

> ***"There was a serious threat of violence between two native populations, and the intervention should eliminate that."***
>
> **Kim Hill,** Arizona State University, Tempe

Either way, the tribe's decision to move and make contact with the outside world

Downloaded from www.sciencemag.org on July 11, 2014

Corrected 9 July, 2014; see full text.

A homeland under pressure

Brazilian officials think the uncontacted tribe fled from illegal loggers and drug traffickers in two parks in Peru

leaves them vulnerable. The top priority now, says anthropologist Robert Walker of the University of Missouri, Columbia, is to prevent disease transmission by quarantining the area, giving access only to individuals screened by medical personnel, and providing food and medical care to the elderly and young, who are at the highest risk of infection. "Vaccinations are a possibility at some point," Walker says. But he adds that immunizations may frighten tribespeople, causing them to flee and carry "pathogens to currently uncontacted people."

In the end, Hill says, the fate of the newly contacted people may depend on whether FUNAI is willing to provide long-term medical monitoring and assistance, as well as a parcel of land that they can call their own. "So often in the past, people have been abandoned," says Fiona Watson, research director of Survival International, a nongovernmental organization based in London. "And that first year of contact is extremely important, because that's when you see these astronomically high figures of people dying."

More details about the tribe are likely to emerge soon, but there is little doubt, Hill says, that these people "would like interaction with more humans on the planet." Interviews with small populations generally show that they "remain isolated out of fear, not from some deep desire to avoid all other human societies." ■

NUCLEAR WEAPONS

Medical isotopes confound nuclear test monitoring

Gases from medical isotope plants can mimic the signature of a bomb, but makers say they will cut emissions

By **Chelsea Wald**, *in Vienna*

If a rogue nation tries to hide a nuclear test, a faint whiff of radioactive xenon leaking from the test site can unmask it. But a peaceful nuclear technology—the manufacture of medical isotopes—can produce almost identical emissions, confounding detection. Now, medical isotope–makers are pledging to help tame the problem; this month, the list of cooperating companies reached six.

At stake is a worldwide network of hundreds of detectors—including 80 for radionuclides—that the Vienna-based Comprehensive Nuclear-Test-Ban Treaty Organization (CTBTO) is setting up to sense any violations of the treaty, which 183 countries have signed and 162 have ratified (*Science*, 24 July 2009, p. 382). If plants' emissions mask the signal of an actual bomb, it will be much harder to verify an apparent violation and hold a country to account.

The problem came to light in the early 2000s, when scientists in Freiburg, Germany, were testing noble gas detectors for CTBTO. The detectors kept getting unexpected hits of radioxenon, says Ted Bowyer, a nuclear explosion monitoring expert at Pacific Northwest National Laboratory in Richland, Washington, and chair of the CTBT radionuclide expert group. It took 5 years of sleuthing using atmospheric modeling to trace the gas to plants making radioisotopes for imaging and therapy.

Medical isotope facilities fire neutrons from a nuclear reactor at a uranium plate, which is then dissolved to remove the isotopes. The process also creates short-lived radioactive xenon isotopes, which are vented as waste. The levels of radioactivity from the vented xenon are too low to cause health problems but high enough to trip CTBTO's alarms. When a sensor in northern Canada picked up xenon following North Korea's first nuclear test in 2006, the proximity of a large Canadian medical isotope plant reduced scientists' confidence in their conclusion.

CTBTO has little leverage over the isotope makers. What's more, producers are already under intense pressure to switch their reactor fuel from highly enriched to low-enriched uranium to reduce the risk of nuclear proliferation, says W. Randy Bell, director of CTBTO's International Data Centre in Vienna. Nonetheless, some have started to cooperate with CTBTO. So far, six have signed a pledge to keep emissions low, as well as to share their emissions data. Data sharing is helpful but "not a panacea," Bowyer says.

One solution is an extra-large activated-charcoal trap to hold the xenon until it decays away, says Johan Camps of the Belgian Nuclear Research Centre in Mol. "You will really have to build a new building," with shielding to protect people from the trapped radioxenon. Camps's team is also developing a new compact trap using a novel silver-exchanged zeolite material, which their tests have shown has 15 times the efficiency of activated charcoal.

A rash of new plant construction prompted by isotope shortages following production problems at older plants (*Science*, 21 January 2011, p. 277) may also offer an opportunity. Bell estimates that 20 new producers, many in the developing world, could come online by the end of the decade. Mitigation could be designed into the new plants from the start.

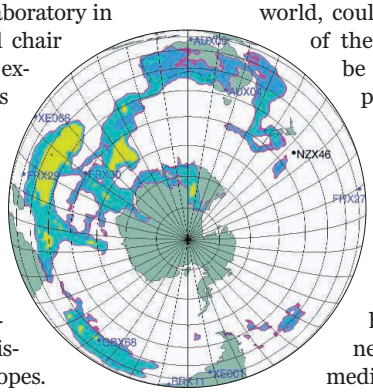

Test-ban monitors can trace xenon using atmospheric models.

With mitigation technologies yet to mature, however, scientists are nervous about a planned medical isotope plant in South Korea. It is among the plants that have agreed to limit emissions, but the stakes are high. After North Korea's last nuclear test on 12 February 2013, noble gas detectors in Japan were the first to identify a radioxenon signal. With tension high in the region, the last thing CTBTO's scientists want to contend with is a lot of false hits. ■

Chelsea Wald is a writer based in Vienna.

CREDIT: (GLOBE) CTBTO

Published by AAAS

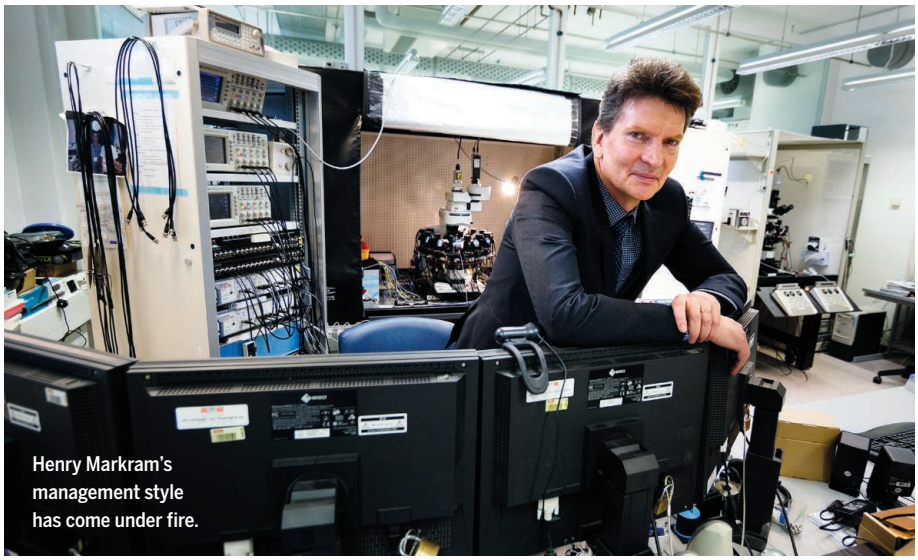

Henry Markram's management style has come under fire.

PHOTO: VALENTIN FLAURAUD/REUTERS/LANDOV

EUROPE

Conflict erupts over landmark E.U. neuroscience plan

Scientists threaten to boycott the Human Brain Project

By **Martin Enserink** *and* **Kai Kupferschmidt**

Henry Markram wanted to be a uniter, not a divider. When the European Commission announced last year that Markram's controversial brainchild, the Human Brain Project (HBP), would be showered with up to €1 billion in research funding, the neuroscientist at the Swiss Federal Institute of Technology in Lausanne called on skeptical colleagues to join him in his ambitious plan to revolutionize understanding of the brain through information technology. "At the moment, everyone is digging in his little corner," Markram said last year. "We are asking the whole world of neuroscience to come together."

The opposite happened. In an open letter to the commission published at neurofuture.eu on 7 July, more than 300 neuroscientists, largely from Europe, lash out at the massive research effort, which they say is likely to fail because it's too narrowly focused and poorly managed. The group asks the commission to tighten a planned review of the project and make corrections, threatening to boycott HBP if that does not happen. "Let's try to fix this, and if we cannot fix this, let's do something else," says Zachary Mainen of the Champalimaud Centre for the Unknown in Lisbon, one of the driving forces behind the letter.

The list of signatories "reads like a *Who's Who* of European neuroscience," says Anthony Movshon, a neuroscientist at New York University in New York City. "It's a chorus of voices that cannot be ignored."

HBP is one of two so-called Flagship projects that won out in the European Union's Future and Emerging Technologies initiative, aimed at boosting innovation and economic development (*Science*, 1 February 2013, p. 497). (The other focuses on graphene.) The commission has pledged to provide up to €500 million for each project over 10 years; member states are supposed to contribute an equal amount. HBP aims to bring together the vast amounts of data from neuroscience in computer models of how the human brain works. But some see the attempt as premature and fear it could sap funding for actual lab science. "The notion that we know enough about the brain to know what we should simulate is crazy, quite frankly," says Peter Dayan, a computational neuroscientist at University College London who has signed the open letter.

The trigger for the open letter was the decision of HBP's Governing Board, led by Markram, to cut one of 13 subprojects from a proposal it needed to file with the commission in June for the next batch of funding. Called Cognitive Architectures and led by French neuroscientist Stanislas Dehaene, it aimed to map the connections between various brain regions during tasks such as reading, talking, or face recognition—a long-standing goal in neuroscience. The open letter says nixing the subproject further narrowed the HBP's scope and eliminated 18 labs from the project.

But Markram says the cognitive neuroscientists involved "just want to do the same thing they have been doing," with HBP money, without embracing the broader concept. HBP is "a methodological paradigm shift, and it's a very exciting one, but not for everybody who does this sort of traditional individual research in the lab," he says.

Katrin Amunts, a German researcher who leads another subproject, says the letter writers don't understand that HBP is an information technology project. "It's not a matter of neuroscience money going somewhere else; it's vice versa," she says. "It's a great chance for neuroscience."

Without mentioning Markram directly, the letter also criticizes his management style as closed and inflexible. HBP "is not a democracy, it's Henry's game, and you can either be convinced by his arguments or else you can leave," Mainen says. Markram concedes "a project like this does need some pressure to synchronize all our efforts at the beginning and then transition to a broader governance. We acknowledge that we should have communicated better."

The letter lists demands for the commission's planned review of the program, such as a diverse, independent panel and full transparency about the procedures. If those conditions can't be met, the authors say the commission should end its funding and support neuroscience in other ways, for instance through the European Research Council. They also threaten not to apply for the HBP-related funding from E.U. member states and to urge colleagues to do the same.

In a statement sent to *Science*, a representative for the commission didn't address the critics' concerns but says the first annual review is planned in January. It's "too early to draw conclusions on the success or failure of the project," the statement said.

A similarly ambitious U.S. effort called BRAIN (Brain Research through Advancing Innovative Neurotechnologies) has sparked debate as well (*Science*, 1 March 2013, p. 1022), but it has "a much better approach," Dayan says. For BRAIN, "they decided what we need to develop are the technologies" for research, rather than trying to focus on computer simulations, Dayan says. In contrast, Mainen says, the European Union's massive bet on a focused project was ill-timed. "You need to find a moment in scientific history when this works," he says, "like sorting out the human genome." ■

With reporting by Emily Underwood.

Downloaded from www.sciencemag.org on July 11, 2014

Published by AAAS

Under the river-linking project, surplus water from the Brahmaputra River would be diverted to parched regions in northern India.

PHOTO: P. BAGLA

WATER

India plans the grandest of canal networks

Nationwide water transfer scheme could aid farming, but critics fear ecological havoc

By **Pallava Bagla**, *in New Delhi*

In one of the most ambitious engineering projects ever conceived, the Indian government is preparing to forge ahead on a plan to build a 15,000-kilometer-long network of canals and tunnels that would move 174 billion cubic meters of water each year—almost a third of the amount the United States withdraws from aquifers each year—from areas with surplus water to parched regions of India.

The prime rationale for the $168 billion National River Linking Project (NRLP) is simple: To feed its growing population, the Indian government has determined that it must drastically expand its arable land. Now, about 100 million hectares in India are irrigated; NRLP, if fully implemented, would increase that amount to about 135 million hectares, while also curtailing flood damage during the summer monsoon season and adding another 34 gigawatts of hydropower capacity. The current plan, honed by India's National Water Development Agency, envisions 16 links between Himalayan-fed rivers and rivers in drought-afflicted western India, and another 14 links in the southern half of the peninsula (see map). Newly elected Indian Prime Minister Narendra Modi has hailed the "river interlinking project" as a national "dream."

Thanks to Modi's patronage, that dream is moving closer to reality. "All possibilities will be explored for early implementation of the river interlinking project," Uma Bharti, India's new water minister, told *Science* at a meeting here on 7 July on cleaning up the Ganges River. But NRLP, which could take upward of a quarter-century to complete, faces political hurdles and scientific dissent. Critics contend that the water transfer would spread invasive species and waterborne diseases and interfere with fish migration. Water-rich states may also balk at sharing. "There will undoubtedly be winners and losers," says Donald Alford, a hydrologist who has studied the Himalayas with the firm Mountain Hydrologic Systems in Billings, Montana. "Who, and where they are, will help to define feasibility."

The Indian government first proposed a "national water grid" in 1972, but the idea, featuring a 2640-kilometer-long canal between the Ganges and Cauvery rivers, was shelved due to cost. Over the years, as the project's aspirations grew, political support "waxed and waned," says Upali Amarasinghe, a statistician with the International Water Management Institute in Hyderabad. Several links were built, including one between the Narmada and Sabarmati rivers in Gujarat state, which Modi governed before becoming prime minister.

India's previous government, led by Manmohan Singh, was never enamored with NRLP and did not push for broad implementation. "River interlinking is against the forces of nature," says chemist T. Ramasami, the former secretary of the Department of Science and Technology who chaired a Supreme Court–mandated expert committee on water issues. "Intense scientific scrutiny," he says, is necessary "before such a big project is undertaken."

NRLP critics say that Singh was right to keep the project on ice. "The equation that flooding means surplus water and drought means deficit is misleading and wrong," argues Himanshu Thakkar, an engineer with the South Asia Network on Dams, Rivers and People, an advocacy group based here. He points out that areas with heavy monsoon rainfalls can face water scarcity during the dry season. Moreover, NRLP's viability depends on states sharing water resources—an unreasonable assumption, Thakkar says, because "all of them are equally facing increasing scarcity of water. From this point of view alone, the links are unviable."

That's not how Bharti sees it. She contends that Singh's government "slept" on the project, even after the Supreme Court in February 2012 held that NRLP "is a matter of national benefit." In a sign that the new government will push ahead, last month it granted permission to Gujarat to raise the height of the Sardar Sarovar Dam by 17 meters, taking it to 138 meters. Completed in 2006, the hydropower project transfers water across basins to irrigate 1.8 million hectares; raising the height would irrigate another 68,000 hectares.

Modi's government is still thrashing out just how fast it will move on NRLP. Its near-term ambitions will become apparent when it releases its first budget, for 2014 to 2015, later this month. Whatever shape NRLP takes, Bharti assures *Science* that "no environmental laws will be broken." ■

No more going with the flow

India's plan calls for 15,000 kilometers of canals and tunnels (not all are shown)

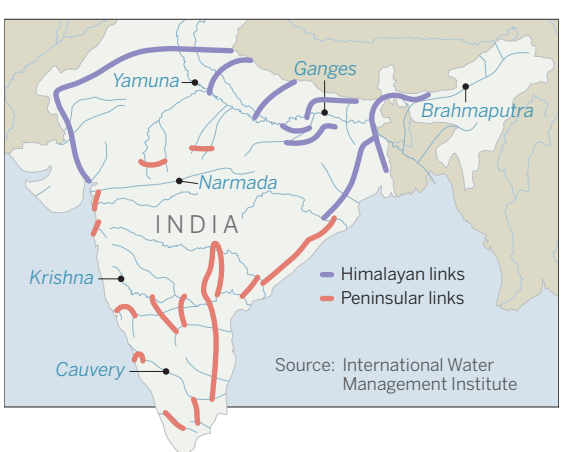

Downloaded from www.sciencemag.org on July 11, 2014

Published by AAAS

PALEOANTHROPOLOGY

RIP for a key Homo *species?*

Researchers consider killing off a claimed common ancestor of Neandertals and modern humans

By **Michael Balter**, *in Tautavel, France*

"If someone kills one person they go to jail," anthropologist Zeresenay Alemseged of the California Academy of Sciences in San Francisco noted last month at a meeting here in France's deep south. "But what happens if you kill off a whole species?" The answer soon became apparent: anguished debate. In the balance was *Homo heidelbergensis,* a big-brained human ancestor generally seen as a pivotal figure during a murky period of evolution. At the invitation-only meeting, researchers debated whether this species really was a major player—or no more than a paleoanthropologists' construct.

The big-brained *H. heidelbergensis* has claimed an important perch in the human evolutionary tree: It's regarded by many as the common ancestor of modern humans and our extinct closest cousins, the Neandertals. Dating to roughly half a million years ago, it is thought to link those species and the earlier *H. erectus,* which had spread across Africa, Asia, and Europe beginning 1.8 million years ago. But based on a new look at the incomplete fossil evidence, some scientists argue that the picture was much more complicated, and that the transition between small-brained *H. erectus* and larger brained hominins occurred multiple times. If so, the concept of a single, multicontinental, intermediary species could dissolve into a plethora of hominin specimens with no single name to unite them.

At the meeting, held near the cliffside Arago Cave where French prehistorians Henry and Marie-Antoinette de Lumley found one of the key fossils in 1971, this debate went further, as researchers sparred over whether this supposedly pivotal species existed. One researcher began her talk with a call for "a moment of silence for the death of *H. heidelbergensis*." But to others, such as anthropologist Philip Rightmire of Harvard University, the announcement of the species' death was definitely premature. "*Homo heidelbergensis* is likely to stay with us for a little while longer," Rightmire said. He argued that this species fits up to 20 specimens from Europe, Africa, and Asia dated to between 800,000 and 200,000 years ago, just before *H. sapiens* appears in Africa.

H. heidelbergensis has a history of controversy. The species is based on a single lower jaw found in 1907 at Mauer, near Heidelberg, in Germany. Estimated at about 600,000 years old, the jaw has an unusually thick ramus—the vertical projection that hinges to the skull—and nothing quite like it has been found since. For decades, the name failed to catch on, until anthropologists including Rightmire and Chris Stringer of the Natural History Museum in London noted distinctive thick brow ridges and large faces in skulls of roughly similar age from sites including Arago; Petralona in Greece; Broken Hill in Zambia; Yunxian in China; and Bodo in Ethiopia. All of these skulls also housed much larger brains than *H. erectus*, about 1200 cubic centimeters, within range of modern human brains, which average about 1400 cc. (Neandertal brains may be slightly larger.)

In the 1970s, Stringer and others postulated a single species spanning Europe, Africa, and Asia, and resurrected the *H. heidelbergensis* name to describe it. The species' larger brain was reflected in the complex tools attributed to it, such as wooden spears at Schöningen in Germany (*Science*, 6 June, p. 1080).

Some researchers were skeptical, arguing that the African fossils were a separate species called *H. rhodesiensis,* which led to our ancestors. *H. heidelbergensis* got a big boost when researchers working at the site of Sima de los Huesos in Spain attached the name to the remains of 28 hominins found there. But in a paper last month in *Science* (20 June, p. 1358), the Sima team, led by Juan Luis Arsuaga of the Complutense University of Madrid, argued that these 430,000-year-old hominins were more closely related to Neandertals and don't belong in *H. heidelbergensis.*

At the meeting, Arsuaga went a big step further and proposed eliminating *H. heidelbergensis* altogether. He argued that the Mauer jaw, the type specimen on which the species is based, cannot be closely matched with any other fossil, in part because few other jaws are preserved. To keep the species alive, researchers need to find and designate a new type specimen that has both a jaw and skull, but such a specimen would surely spark new debates, Arsuaga said. The better course "would be to let the species die."

This new reconstruction ties France's Arago skull to *Homo heidelbergensis*.

Anthropologist Yoel Rak of Tel Aviv University in Israel supported this argument by comparing the Mauer jaw with the few jaws claimed to be *H. heidelbergensis* fossils, including three partial jaws from Arago. "The Mauer specimen is one of a kind," Rak concluded in his talk.

But others fought vigorously to save both the species and the simpler, more straightforward view of human evolution that it represents. Rightmire analyzed 34 *H. erectus* and 11 potential *H. heidelbergensis* skulls, and found that their similarities—including massive brow ridges, large faces, and flattened frontal bones—stemmed from true relatedness, rather than convergent evolution. "Calling them *H. heidelbergensis* is the correct position," he said.

And paleoanthropologist Ian Tattersall of the American Museum of Natural History in New York City argued that the Mauer jaw isn't so singular after all: He found close affinities between it and the Arago jaws, especially in the teeth. Specimens from Arago preserve both the face and jaws, Tattersall notes, and the face resembles those of other claimed members of *H. heidelbergensis*, thus completing the link between the type specimen and skulls from several continents.

New fossils from this mysterious time period would help. At the meeting, paleontologist Berhane Asfaw of the Rift Valley Research Service in Addis Ababa offered a rare glimpse of new finds from Ethiopia's Middle Awash region. His team has found partial skulls and jaws from 32 hominin individuals, roughly dated by animal bones to 300,000 years ago. These as-yet-unpublished fossils may link the Bodo skull from Ethiopia, which resembles Arago, and modern human skulls from the Middle Awash site of Herto. Expect fresh debate when these key fossils make it into print. ■

PHOTO: GASPARD GUIPERT *ET AL.*, 2014

Downloaded from www.sciencemag.org on July 11, 2014

Published by AAAS

Monkey fever unbound

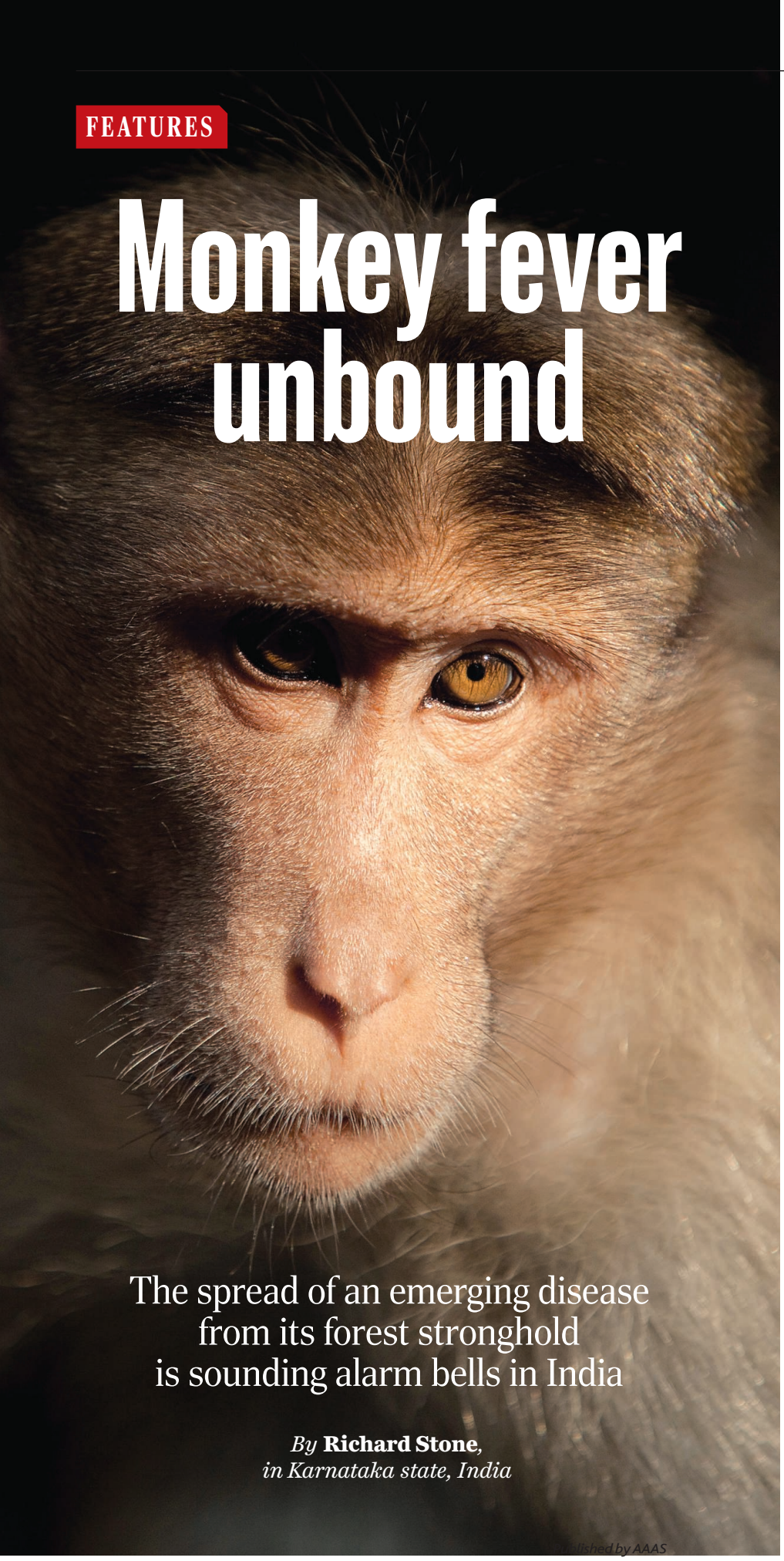

The spread of an emerging disease from its forest stronghold is sounding alarm bells in India

By **Richard Stone**,
in Karnataka state, India

On a sweltering April day, Hoovanna Gowda shuffles from his porch to a backyard apiary shaded by coconut palms. The 76-year-old beekeeper in the village of Kannangi is grateful to be moving at all. In February, running a raging fever, he collapsed on his porch. Today, Gowda is still suffering from joint pain and fatigue as he pulls honeycomb from his hives and extracts the honey in a hand-cranked centrifuge.

"Many people in the village were falling ill," he says. "We knew what it was." A month earlier, villagers had come across dead bonnet macaques in the nearby forest, and from experience they understood that this presaged an outbreak of Kyasanur forest disease (KFD), a hemorrhagic fever known in India as monkey fever. Within a few weeks, the disease hit the village hard; unusually, no one died.

Here in the forested Shimoga district of southwestern India's Karnataka state, KFD has been a regular visitor since 1956, when the virus, transmitted through tick bites, first emerged. A group of top-gun virologists once included it on a roster of hemorrhagic fever viruses that pose a high risk of being turned into bioweapons, alongside Ebola and Marburg. But that was a rare moment of notoriety. For the most part, KFD did not seem to pose more than a local threat. Year after year, Shimoga saw, on average, about 400 cases and a couple of dozen deaths.

That has changed, and as Gowda talks about his village's lucky escape, virologist Govindakarnavar Arunkumar of Manipal University in south Karnataka frowns. In the winter of 2012 to 2013, the virus made a geographic break. Four hundred kilometers away in the Bandipur Tiger Reserve, a popular ecotourism destination straddling Karnataka, Kerala, and Tamil Nadu states, forest workers who had incinerated infected monkey corpses became ill with KFD. "It's a mystery how the virus appeared 400 kilometers away from the original epicenter, without any sign of disease in between," says Arunkumar, who fears that KFD is poised to become "a major public health threat."

KFD's wider emergence drew new attention to this poor, remote, and verdant corner of the subcontinent. Southwestern India's high biodiversity and heavy human-animal interactions make it a flashpoint for viral emergence, says Stuart Nichol, chief of the Viral Special Pathogens Branch at the U.S. Centers for Disease Control and Prevention's (CDC's) National Center for Emerging and Zoonotic Infectious Diseases in Atlanta. Factor in a booming population, he adds, and "you have the potential for a perfect storm." Health officials here are already coping with

Downloaded from www.sciencemag.org on July 11, 2014

PHOTO: © PHILIP LEE HARVEY/CORBIS

...lished by AAAS

the recent arrival of another nasty tick-borne disease—Crimean-Congo hemorrhagic fever—as well as outbreaks of Nipah virus, which is spread by bats, and Chandipura virus, an emerging pathogen transmitted by sandflies that causes an often fatal brain inflammation. They are wondering what other, still nameless, animal viruses have begun sickening people and are poised for wider spread. "Every one of these people is a petri dish," Nichol says.

The Bandipur outbreak alerted Indian scientists to disconcerting gaps in knowledge about KFD, and it reinforced a sense that the nation is acutely ill-prepared to combat emerging viruses. After an initial flurry of research in the late 1950s and early 1960s, most scientists ignored KFD. It's unclear how the virus circulates in the wild, for instance, how far it and its close kin have roamed in Asia, and how many of India's tens of thousands of unexplained fever deaths a year are caused by the KFD virus or other viruses.

To fill these gaps and gird itself against other emerging pathogens, the Indian government in 2013 launched a 5-year, $107 million effort to open 160 virology research laboratories nationwide. "We are very alert to the wider threat," says Vishwa Mohan Katoch, secretary of India's Department of Health Research and the initiative's chief architect. "As people penetrate into the forests," he says, "we run the risk of catching new viruses."

"Spreading out capability is a great idea," says Roger Hewson, a specialist on hemorrhagic fevers at Public Health England's special pathogens center near Salisbury in the United Kingdom. Already, 15 labs are up and running and another 19 are slated to open by the end of the year; the initiative's first state-level outfit is the Manipal Centre for Virus Research (MCVR), which Arunkumar directs. This spring, MCVR launched an epidemiological survey of acute febrile illnesses in southwestern India with a $1.2 million grant from CDC. But at the top of its agenda is finding a way to reinvigorate the fight against KFD. "We need to reassess our approach," Arunkumar says, "instead of blindly following what was done 50 years ago."

Fanning out

Recent sightings of KFD virus and the related Alkhurma virus

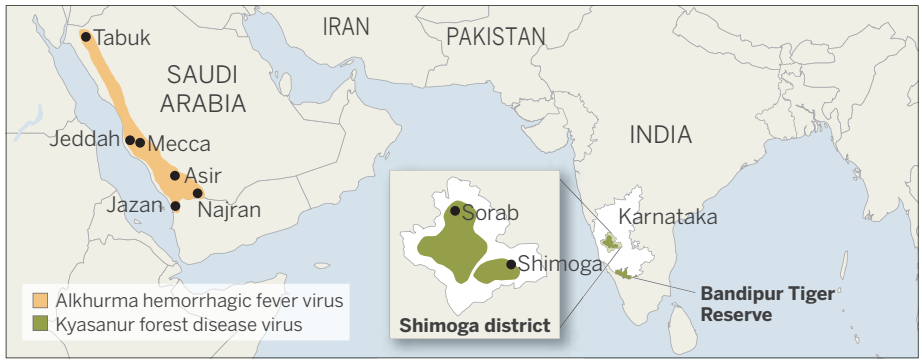

Source: Adapted from M. R. Holbrook, *Antiviral Research* **96,** PubMed Dec. 2012

IN A SCRUBBY FOREST scorching under the midday sun, epidemiologist Jazeel Abdul Majeed, a study manager at MCVR, sweeps a 2-meter-long bamboo pole over dead leaves and ground-hugging vegetation. Villagers in Karnataka regularly venture into forest fringes like this to collect firewood and leaves, which they mix with cow dung to spread as fertilizer or burn in stoves. Bonnet macaques are a common sight. They often steal onto farm fields to feast on Malabar mangoes and chiku fruit and on cash crops such as cashews and areca nuts, which the locals wrap in betel leaves and eat as a mild stimulant. Troops of another monkey, the black-faced langur, also prowl the forest, as do leopards. A third primate—Naxalite guerrillas—had strongholds in these woods as well until they made peace with the Indian government a few years ago.

Abdul Majeed wields the pole like a metal detector, hoping to snare the forest's stealth bloodsuckers: ticks. A swatch of white muslin flutters from the end of the pole. Ticks latch on and get entangled in the coarse cloth.

KFD first emerged here, following another plague—bubonic plague itself. In the 1930s, that bacterial disease, spread by rodents carrying infected fleas, devastated Shimoga, and villagers emigrated en masse. But by the 1950s, settlers were flocking back, clearing land for crops and livestock grazing and harvesting timber more intensely than before.

In the spring of 1956, bonnet macaques and black-faced langurs died in droves in the forest. Then came the fevers, and people began dying as well. Scientists descended on the village.

PHOTO: R. STONE/*SCIENCE*

Like many in his village, Hoovanna Gowda fell ill with KFD last February.

Hunched on a stool in his shaded kitchen in the village of Kyasanur, Shivaram Bhat remembers the "Rockefeller doctors" who rolled into the village in a Jeep during the spring of 1957. If anyone had a fever, the scientists would draw blood and take it back to Pune for analysis at the Virus Research Centre (VRC), which had been set up a few years earlier by the Indian Council of Medical Research and the Rockefeller Foundation, one of seven overseas virology laboratories that the New York–based nonprofit helped establish in a pioneering program in the early 1950s. Bhat, whose family is from the privileged Brahman caste, was in school and could chat in English with the scientists. He still resents them naming the disease after his village. "Nobody wanted to marry people from Kyasanur," Bhat says. "It was a stigma, and it still is."

The resettlement of the district after the bubonic plague dissipated may have lit the fuse for the outbreak. "When the forest was intact, monkeys rarely came down from the trees," which means they rarely picked up virus-ridden ticks from the forest floor, Arunkumar says. Meanwhile, the expanding plantations and paddies drew monkeys and their tick passengers closer to people. "Human-animal conflict is driving this disease," says K. P. Achyut, the district health officer of Sagar, a KFD hotspot in Shimoga.

At first, VRC Director Telford Work and his team thought they were dealing with yellow fever, a mosquito-borne disease endemic to Africa and South America that had never been seen in India. But when infections tapered with the onset of the monsoon—at a time when mosquito-borne infections surge—they realized they were facing a new foe. In a fast bit of disease sleuthing, Work and his colleagues in a few months isolated a new pathogen whose

Published by AAAS

Ticks like *H. spinigera* are collected in the forest, then ground up and tested for KFD virus.

closest kin was a complex of viruses responsible for encephalitis outbreaks in Russia.

At the request of the Indian government, the Walter Reed Army Institute of Research ginned up a vaccine against the virus complex, figuring it would also work against KFD. Tested in the Shimoga district in 1958 and 1959, it failed miserably. Within a few years, however, scientists had concocted a moderately effective vaccine derived from killed KFD virus. Whenever dead monkeys infected with the virus were found near a village, health workers would swoop in to immunize residents. But the protective effect is fleeting. "This is not a refined vaccine," Arunkumar says. A second dose is needed after just 1 month, followed by annual booster doses—a strain on India's frail health system.

Still, that strategy kept the virus hemmed in for more than half a century. KFD would flare after the monsoon rains ended in early winter, peak in spring, then recede with the monsoon's onset in summer. Working primarily from a field station in Sagar, VRC researchers isolated KFD virus from 16 tick species, but only one, *Haemaphysalis spinigera*, is considered the main disease vector. The studies are risky: More than 100 researchers have been infected with KFD virus over the years, mostly while out in the field and mostly during the concentrated initial investigations in the 1950s.

Although only primates seem to contract KFD, the virus turned up in rats, bats, and cattle, and antibodies to it were found in goats, shrews, birds, and other species. Cows shed live virus in their urine, dispersing it in the environment, and can harbor masses of adult ticks. But no animal host stands out as the reservoir that would sustain the virus from year to year, except perhaps ticks themselves: The virus passes through eggs from adults to larvae.

The biggest threat may be young ticks, or nymphs, which are most active during the dry season. They are nimbler and more energetic than their elders, and when they jump onto an animal, they can hunker down and feed for days, Arunkumar says. "Nymphs are very hungry. They need a lot of blood during molting," he says.

Outside Karnataka state, KFD registered as only a faint blip on the public health radar. Complacency set in. "Everybody's interest dropped. The problem was solved," Arunkumar says. Then came "a big wake-up call for India," he says: the 2003 outbreak of SARS, a novel coronavirus from southern China that spread from person to person, killing about 10% of those infected. India was spared, but health officials had learned an important lesson from the country's struggles to brace for SARS. "It was obvious that India had very little preparedness to handle emerging infections," Arunkumar says.

IN THE INFECTIOUS DISEASE WARD of Kasturba Hospital in Manipal, a woman in a patterned burgundy sari lies on her side in bed, facing the wall. Annapoorna is a 45-year-old farmer from Shimoga who has tested positive for KFD. As in Kannangi, people in her village began to fall ill in February, after dead macaques were seen in paddies and areca plantations. Suffering from a high fever, nausea, and severe headaches, Annapoorna and a relative made their way by a 7-hour bus ride to Kasturba, a teaching hospital affiliated with Manipal University.

When Arunkumar and two team members approach and greet her, she turns toward them languidly, insisting she feels better and is ready to go home. But she's not in the clear. Most people with KFD recover in a week. But in some the virus takes refuge in organs such as the liver or lungs and busily replicates. After another week or so, the harried immune system sets off a second bout of fever. In severe cases, patients die from internal bleeding or septic shock. Annapoorna won't be discharged until it is certain she has avoided or pulled through this second phase.

In the meantime, at the other end of the Manipal campus, MCVR has just received a plastic vial full of ticks collected by an epidemiologist in the Bandipur Tiger Reserve, where KFD sickened people in 2012 and 2013. Arunkumar is thrilled: These are the first ticks collected in Kerala for KFD surveillance. A technician carefully opens the tube in a biosafety cabinet and uses tweezers to nudge the ticks into a petri dish for identification, before transferring them to a glass test tube. "This is a tedious process, but hurrying can be dangerous," Arunkumar says. The technician grinds the ticks with a stirring rod and adds a pinkish solution that rips open the virus's lipid envelope. The team will use real-time PCR to probe for virus. Although Kerala did not report any KFD cases this spring, searching for the virus far from Shimoga is part of the heightened vigilance that Arunkumar is agitating for. "We are looking for an early warning."

It may be necessary to post sentinels outside India. In 1995, a close relative of KFD virus, the Alkhurma hemorrhagic fever virus, emerged near Jeddah, Saudi Arabia, primarily infecting people who butcher sheep and camels. Genetic data indicate that the new virus was a descendant of KFD virus, which arrived in the Middle East in the late 1970s or early 1980s, possibly via infected ticks on migratory birds. There, it mutated into Alkhurma virus, which had spread to Egypt by 2010.

In its home territory, meanwhile, the KFD virus, whose genes are composed of RNA, could change to become more deadly, infectious, or more easily transmitted. "RNA viruses adapt quickly to new circumstances," says Public Health England's Hewson—a point exquisitely driven home by the SARS outbreak.

Arunkumar believes India is moving away from its "knee-jerk response" to KFD outbreaks. In Pune, the National Institute of Virology—which opened the country's first biosafety level 4 laboratory in late 2012 for handling the most perilous viruses, including the one responsible for KFD—is working on a new antibody-based test for the disease. India's nationwide virology lab network should be fully operational by 2018. And one day, the perennial scourge of monkey fever may be driven back deep into the forest, where it belongs. ■

PHOTOS: R. STONE/*SCIENCE* (3)

Published by AAAS

INSIGHTS

Ultrafast surface electron diffraction *p. 137*

Proliferation of latently HIV-infected cells *p. 143*

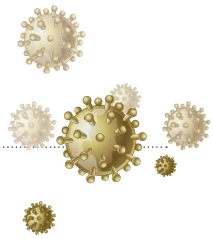

PERSPECTIVES

This scanning electron micrograph shows marine microbial picoplankton concentrated by tangential flow filtration from oligotrophic central ocean surface waters. Morphologically distinct individual cells have been colorized for contrast.

PHOTO: ED DELONG, DAVID KARL, BROOKS BAYS/UNIVERSITY OF HAWAII

MICROBIOLOGY

Taking the pulse of ocean microbes

Gene expression patterns of open-ocean microbes are tightly coupled

By **E. Virginia Armbrust**

Far from land, relatively few types of very small microbes thrive in the warm, nutrient-poor surface waters of the subtropical gyres. Here, the cyanobacterium *Prochlorococcus* dominates photosynthesis and generates a sizable fraction of the organic matter that fuels the growth of abundant bacteria, including *Pelagibacter* and a number of uncultured strains (*1*, *2*). On page 207 of this issue, Ottesen *et al.* (*3*) use high-resolution sampling to document an exquisitely tight coupling between light-driven gene expression patterns of *Prochlorococcus* and gene expression patterns of other members of the bacterial community in surface waters at Station Aloha in the North Pacific Subtropical Gyre (see the photo and figure). The study illustrates the power of combining at-sea observation technology with DNA sequencing to understand marine microbial processes.

To obtain microbial samples at sea, oceanographers commonly follow "drifters" that track currents, collecting samples from as close to the drifter as possible with the goal of repeatedly sampling the same parcel of water. The robotic environmental sample processor used by Ottesen *et al.* represents a crucial advance in sampling technology: It both tracks a given parcel of water and automatically filters and preserves microbial communities for community gene transcription (transcriptome) analysis. Such innovations in autonomous sampling are essential for understanding how marine organisms respond to the rapid chemical and physical changes in today's oceans.

One motivation for sampling microbial communities at sea is the premise that the

Published by AAAS

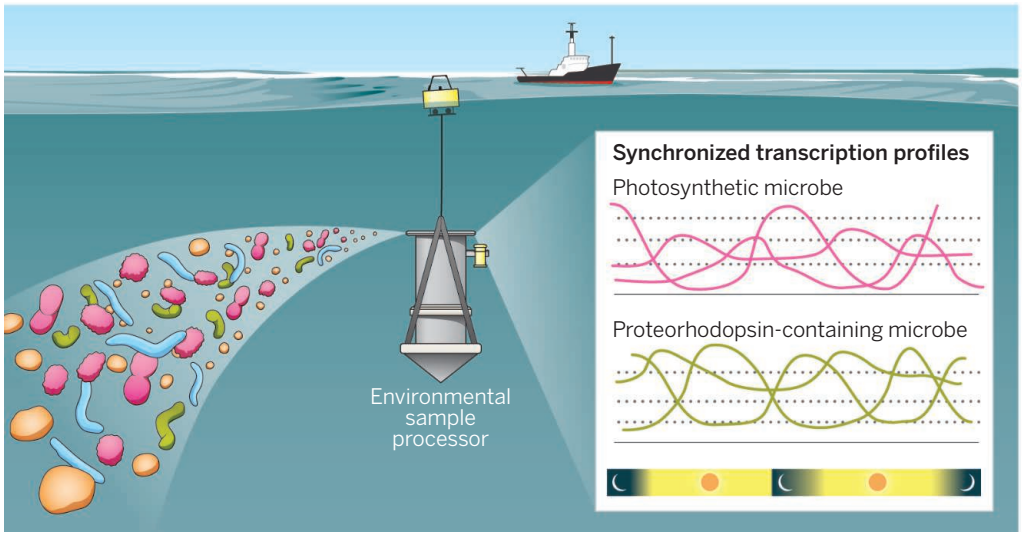

Exquisite synchrony. Surface waters of subtropical gyres contain relatively few types of abundant microbes, as indicated by the different colors. Photosynthesis in these regions is dominated by the cyanobacterium *Prochlorococcus*. Ottesen *et al*. have used autonomous sampling technology to obtain in situ transcription profiles of microbial communities over the day/night cycle. Profiles for a subset of genes from two idealized microbes are shown—one photosynthetic, such as *Prochlorococcus*, and the other containing the light-driven proton pump proteorhodopsin. The bar at the bottom indicates night (dark bar) and day (yellow bar). The observed periodicity in transcription profiles may translate into a periodicity of metabolic processes in these open-ocean communities.

ocean environment is far too complex to be adequately mimicked in the laboratory. Yet Ottesen *et al*. show that the transcriptional patterns of wild *Prochlorococcus* are remarkably similar to those of a cultured *Prochlorococcus* strain kept under controlled laboratory conditions. How can growth in an artificial setting be so similar to that in the natural environment? One possible explanation is that the very small genome of *Prochlorococcus* has eliminated nuance, resulting in a limited range of regulatory responses to a given environmental condition (*4*). Alternatively, the input of light energy and the resulting synchronization of cell division of wild *Prochlorococcus* cells may dominate their regulatory network. The observed similarities illustrate the importance of developing model marine microbes in parallel with field studies.

Ottesen *et al*. also uncover differences between the field and the laboratory. A small subset of genes that display diel cycling in the field is missing from the laboratory strain, reiterating the potential importance of the genetic diversity in natural *Prochlorococcus* populations (*5*). A larger subset of genes shows different periodicities in the field and the laboratory, with a large fraction of these genes encoding proteins of unknown function. Identifying their roles may help to explain how these organisms adapt to their environment.

A second motivation for at-sea experiments is that most marine bacteria cannot yet be cultured in the lab; knowledge of them comes from environmental DNA sequence information or from transcriptome studies of natural microbial communities. In the sunlit surface waters at Station Aloha, most bacteria that require organic carbon also possess proteorhodopsin, a light-driven proton pump that presumably supplements different metabolic activities, especially when organic carbon is scarce (*6*). Transcription of the proteorhodopsin gene is tightly synchronized to the day/night cycle, which Ottesen *et al*. attribute to optimized light energy capture by these organisms. But is proteorhodopsin enough to create the observed transcriptional synchrony across multiple genes and organisms? Earlier work by the same group (*7*) in Monterey Bay suggests not. Despite the use of similar approaches, a synchronized response to the light/dark cycle was missing at the coastal station. What could so tightly synchronize the bacteria to the day/night cycle at Station Aloha?

Each day, photosynthetic organisms like *Prochlorococcus* harvest light energy to drive carbon fixation. *Prochlorococcus* commonly releases up to 25% of its fixed organic carbon into the seawater (*8*). Previous studies (*9*, *10*) suggest that bacterial communities that require organic carbon for growth could synchronize their growth with the light/dark cycle because of the light-driven release of organic matter by photosynthetic organisms. This synchrony may be particularly important and is more easily observed in the open ocean, far from the influence of land-derived organic matter. But the exquisite coupling of waves of gene expression across different types of bacteria seen by Ottesen *et al*. still comes as a surprise.

The observed synchrony of gene expression may rely on at least two factors: The pulse of organic carbon from *Prochlorococcus* may harmonize the overall transcriptional responses of the bacteria, and proteorhodopsin may further synchronize the transcriptional patterns of particular suites of genes to the light/dark cycle. These microbial interactions could be particularly important in nutrient-poor open-ocean environments, in which genomic streamlining (*1*) may leave organisms dependent on one another for lost metabolic functions (the black queen hypothesis) (*11*). Additional tiers of microbial interactions could also be at play if specific organic molecules serve as signals that manipulate the behavior of microorganisms in manners similar to that seen in terrestrial ecosystems (*12*). The enormous data set generated by Ottesen *et al*. provides a fantastic resource with which to address these questions.

The ability to simultaneously monitor transcriptional profiles of multiple organisms in situ over time provides the opportunity to answer questions about how microorganisms interact with their environment and with each other, and how these interactions influence ecosystem stability. The large proportion of genes with unknown functions will continue to present challenges. The greatest challenge will be to understand how far-reaching the genetic choreography observed at Station Aloha is over time and space, and how these interactions expand across the entire microbial community. ■

School of Oceanography, University of Washington, Seattle, WA 98195, USA. E-mail: armbrust@uw.edu

ILLUSTRATION: P. HUEY/*SCIENCE*

REFERENCES

1. B. K. Swan *et al*., *Proc. Natl. Acad. Sci. U.S.A.* **110**, 11463 (2013).
2. S. J. Giovannoni, T. B. Britschgi, C. L. Moyer, K. G. Field, *Nature* **345**, 60 (1990).
3. E. A. Ottesen *et al*., *Science* **345**, 207 (2014).
4. E. R. Zinser *et al*., *PLOS ONE* **4**, e5135 (2009).
5. N. Kashtan *et al*., *Science* **344**, 416 (2014).
6. E. F. DeLong, O. Béjà, *PLOS Biol.* **8**, e1000359 (2010).
7. E. A. Ottesen *et al*., *Proc. Natl. Acad. Sci. U.S.A.* **110**, E488 (2013).
8. S. Bertilsson, O. Berglund, M. J. Pullin, S. W. Chisholm, *Vie Milieu* **55**, 225 (2005).
9. J. A. Fuhrman, R. W. Eppley, Å. Hagström, F. Azam, *Mar. Ecol. Prog. Ser.* **27**, 9 (1985).
10. J. M. Gasol *et al*., *Mar. Ecol. Prog. Ser.* **164**, 107 (1998).
11. J. J. Morris, R. E. Lenski, E. R. Zinser, *MBio* **3**, e00036-12 (2012).
12. K. M. Jones, H. Kobayashi, B. W. Davies, M. E. Taga, G. C. Walker, *Nat. Rev. Microbiol.* **5**, 619 (2007).

10.1126/science.1256578

Published by AAAS

HIV/AIDS

A fitness bottleneck in HIV-1 transmission

A successful infection is determined in part by how close a viral genome is to an ideal sequence

By **Sarah B. Joseph**[1] *and* **Ronald Swanstrom**[1,2,3]

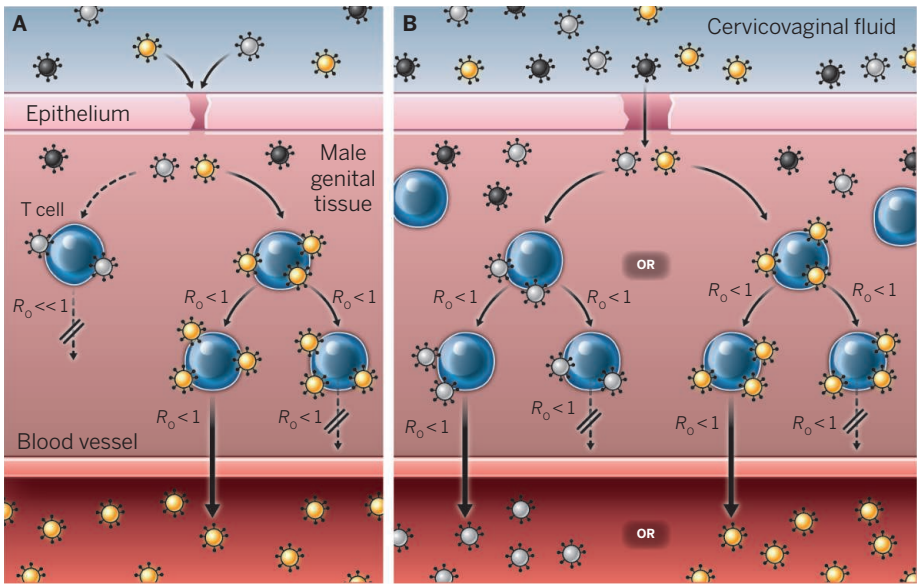

Bias at the bottleneck. Sexual intercourse may expose a recipient to HIV-1 virions with low (black), intermediate (gray), and/or high (yellow) fitness. (**A**) Female-to-male transmission favors high-fitness variants. The average infected cell has a low R_0 (shown) and does not contribute to systemic infection (not shown). (**B**) The bias toward transmission of high-fitness variants is reduced when the female donor has a higher viral load or when the male recipient has a recent genital ulcer or inflammation, which could increase the number of target T cells and/or increase T cell exposure to virions. These conditions make it more likely that intermediate- or low-fitness variants will be transmitted ($R_0 << 1$ increases to $R_0 < 1$).

Identifying factors that determine the successful transmission of HIV-1 may help enable the development of better prevention measures. This is what makes the findings of Carlson *et al.* (*1*) so relevant. On page 178 of this issue, the authors provide evidence for a bottleneck in HIV-1 transmission that selects for high-fitness viruses. Fitness in this analysis would be reflected either in the infectiousness of each viral particle or in the number of particles produced by an infected cell (burst size). Thus, this fitness bottleneck would act during infection of the first cell or during the first few rounds of local viral replication at the site of transmission where the infection could be extinguished.

An important feature of this study is the use of a large cohort of couples who were discordant for their HIV-1 infection (one was infected and the other was not). The authors analyzed 137 transmission events identified in the cohort over 10 years despite a two-thirds reduction in infections (the result of counseling and condom use). Comparison of the viral sequences in the chronically infected donors and their newly infected recipient partners forms the basis of the study.

HIV-1 is genetically diverse both across the epidemic and within an infected person. Yet, although its evolution on a global scale hovers around a consensus sequence that is optimal for viral gene functions, the virus never attains this idealized genome sequence. In the study of Carlson *et al.*, differences from the consensus sequence of the cohort ("polymorphisms") are assumed to reduce viral fitness. Each viral genome contains multiple polymorphisms across the genome, and within an individual a polymorphism at one site can coexist as a mixed population with the corresponding consensus at that site. Despite the complexity of the viral population in a donor, heterosexual transmission typically results in the outgrowth of a single transmitted/founder virus (*2*, *3*). Thus, transmission reduces the genetic diversity seen in the donor to a single viral genome that is identical to the consensus sequence at some positions but carries polymorphisms at other positions.

Carlson *et al.* compared the predominant amino acid sequence in the proteins encoded by the HIV-1 genes *gag*, *pol*, and *nef* of the paired donors and recipients. The surprising outcome is that a donor genome that more closely matched the consensus was more likely to be transmitted than were donor genomes that on average encoded more amino acid polymorphisms. This outcome is most easily explained if there is a period at or immediately after transmission when the virus is replicating in the recipient under adverse conditions and the probability of spread is influenced by viral fitness.

There is a conceptual framework for describing the probability of virus spread, which is captured in the reproductive number (R_0). R_0 is the average number of cells infected from a single host cell (*4*). When R_0 is greater than 1, the infection will spread to other cells, and when R_0 is less than 1, the infection will die out. During the first rounds of HIV-1 viral replication, R_0 is low but rapidly increases after the initial seeding of a systemic infection. Thus, a viral genome sequence that slightly increases R_0 increases the probability that the virus will spread to the point where exponential growth takes over and a systemic infection is assured.

After detecting mutations that alter fitness and affect replication during this early period of selection, Carlson *et al.* made further comparisons within subsets of the cohort. The reduction in population complexity during transmission clearly includes a stochastic bottleneck that limits transmission of all viruses (e.g., the mucosal barrier) but also includes a fitness bottleneck that selects for transmission of high-fitness variants. The fitness bottleneck was more severe in female-to-male transmission compared to male-to-female transmission, with infection of females allowing the transmission of genomes encoding more polymorphisms. Moreover, exposure to higher donor viral load or recent genital ulcer or inflammation (GUI) in a male recipient could attenuate the fitness bottleneck in female-to-male transmission but not the reverse. Whereas Carlson *et al.* examined polymorphisms in virion proteins (Gag and Pol) and a viral protein expressed in the host cell (Nef),

[1]*Lineberger Comprehensive Cancer Center, University of North Carolina, Chapel Hill, NC 27599, USA.* [2]*Department of Biochemistry and Biophysics, University of North Carolina, Chapel Hill, NC 27599, USA.* [3]*UNC Center for AIDS Research, University of North Carolina, Chapel Hill, NC 27599, USA.*
E-mail: sbjoseph@email.unc.edu; ron_swanstrom@med.unc.edu

ILLUSTRATION: C. BICKEL/*SCIENCE*

Published by AAAS

an earlier study indicated that a bottleneck selecting for reduced glycosylation of the virion surface Env protein is also stronger in female-to-male transmission (*5*).

That the fitness bottleneck observed in female-to-male transmission is more severe, but can be reduced by viral load and/or GUI, suggests that barriers to infection of the first cell may reduce transmission in males compared to females. The exposed surface area of epithelium and/or the density of target cells in or just beneath the epithelium in the male versus the female genital tract may be sufficient to explain this difference, but the ability to spread after infection of the initial cell may also be selected (see the figure). The transmitted virus is well adapted to entering cells with a high density of its receptor CD4 (*5*–*7*), making $CD4^+$ T cells the most likely target, although the virus can infect macrophages less efficiently (*6*, *8*, *9*). Examination of vaginal tissue in macaques after exposure to the related virus SIV showed that resting $CD4^+$ T cells are the predominant infected cells, but infected activated $CD4^+$ T cells are also observed (*10*). A paucity of $CD4^+$ T cells in genital tract tissue could be sufficient to define the low probability of the first infected cell both being infected and then passing virus on to the next cell. It has been suggested that a local innate immune response generates type 1 interferon, a cytokine that can limit viral replication (*11*, *12*). Whether the selection for fitness is due to low target cell density, a local innate immune response, or both is not known.

This new view of HIV-1 transmission suggests that there may be more initial infectious events than infections that become systemic ($R_0 << 1$). There are exposures of target cells to virus that fail to initiate an infection, and there is spread of virus from the initially infected cell(s) that fails to become a systemic infection, collectively adding a bias to the distribution of polymorphisms in the transmitted/founder virus population. Thus, there is a period during transmission of a low R_0 that HIV-1 must navigate in the new host to initiate a successful infection. ■

REFERENCES

1. J. M. Carlson *et al.*, *Science* **345**, 1254031 (2014).
2. B. F. Keele *et al.*, *Proc. Natl. Acad. Sci. U.S.A.* **105**, 7552 (2008).
3. M. R. Abrahams *et al. J. Virol.* **83**, 3556 (2009).
4. R. M. Ribeiro *et al.*, *J. Virol.* **84**, 6096 (2010).
5. L. H. Ping *et al.*, *J. Virol.* **87**, 7218 (2013).
6. S. B. Joseph *et al.*, *J. Virol.* **88**, 1858 (2014).
7. N. F. Parrish *et al.*, *PLOS Pathog.* **8**, e1002686 (2012).
8. J. Isaacman-Beck *et al.*, *J. Virol.* **83**, 8208 (2009).
9. C. Ochsenbauer *et al.*, *J. Virol.* **86**, 2715 (2012).
10. A. T. Haase, *Nature* **464**, 217 (2010).
11. A. E. Fenton-May *et al.*, *Retrovirology* **10**, 146 (2013).
12. N. F. Parrish *et al.*, *Proc. Natl. Acad. Sci. U.S.A.* **110**, 6626 (2013).

10.1126/science.1257425

ILLUSTRATION: P. HUEY/*SCIENCE*

IMAGING TECHNIQUES

Low-energy electron diffraction at ultrafast speeds

Thermally induced structural changes in a thin polymer film could be resolved with picosecond time resolution

By **Erik T. J. Nibbering**

Low-energy electron diffraction (LEED) has been used to determine the surface structure of crystalline materials because the diffracted electrons only probe the top atomic layers. First reported by Davisson and Germer in 1927 (*1*), the LEED technique became widely used when ultrahigh vacuum techniques introduced in the 1960s allowed surfaces to remain relatively free from adsorbed background gases during a typical experiment. However, the information LEED provides about the relative ordering of atoms on a surface, whether at atomic resolution or on a larger mesoscopic scale, can only be understood in a time-averaged, quasi-stationary manner. Dynamical aspects, such as changes with temperature, have been only grasped indirectly with well-developed theoretical models to describe the averaged measured quantities. Time-resolved monitoring of LEED patterns would enable direct visualization of lattice motions or light-induced ultrafast phase transitions.

Max Born Institut für Nichtlineare Optik und Kurzzeitspektroskopie, Max Born Strasse 2A, 12489 Berlin, Germany. E-mail: nibberin@mbi-berlin.de

On page 200 of this issue, Gulde *et al.* (*2*) report an ultrafast implementation of LEED and have resolved the ultrafast melting of a poly(methylmethacrylate) (PMMA) layer adsorbed to a graphene substrate.

In LEED, electrons are generated at a cathode, accelerated, and focused by electrodes into an electron beam pointing to the sample of interest. The diffracted electrons are then usually detected in reflection using phosphorescent screens (see the figure, panel A.).

Gulde *et al.* achieved time resolution in the picosecond regime with a pump-probe configuration in their transmission ultrafast LEED (T-ULEED) experiment. An ultrashort laser pump pulse heats up the PMMA layer, and the structural changes resulting from the melting process are monitored as a function of time delay by probing its diffraction patterns (distinct from those of graphene) with electron pulses lasting a few picoseconds (see the figure, panel B). The electron pulses are generated from a sharp tungsten tip (50-nm radius of curvature) by illumination with a second-harmonic pulse originating from the same laser output as the laser pump pulse. This method ensures accurate timing (time delay *t*) between the two pulses.

The PMMA layer on graphene consists of three domains of two-dimensional folded

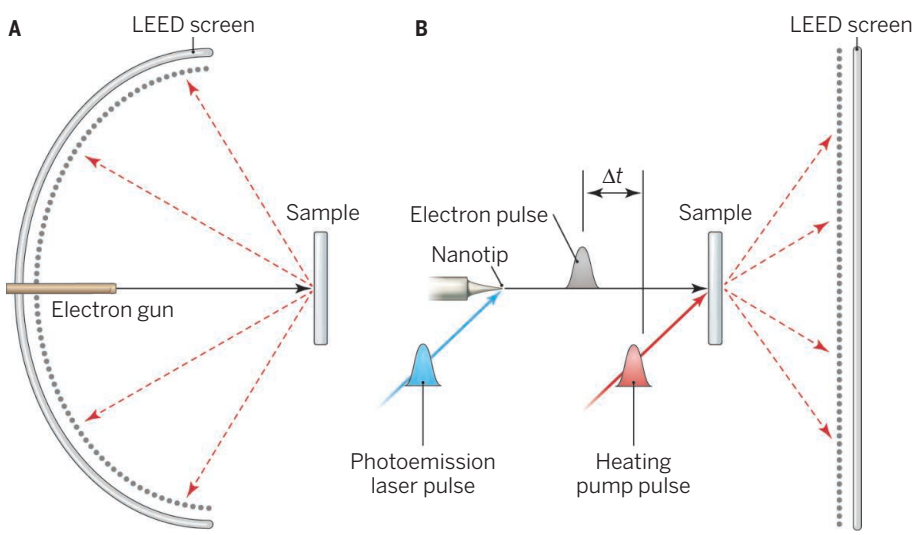

Forward with LEED. (**A**) Conventional LEED works by reflecting electrons back to a phosphor screen. (**B**) Time-resolved LEED described by Gulde *et al.* uses forward scattering in transmission of electron pulses generated by photoemission.

Published by AAAS

chain crystallites. The T-ULEED experiment revealed that ultrafast melting of the PMMA follows a hierarchy of events. The graphene substrate absorbing the laser pump energy increased its temperature to 540 K within the pump-pulse duration of 80 fs. Energy transfer to the PMMA bilayer led to an elevated temperature equilibration with a characteristic time of 43 ps. When the magnitude of transferred energy (heat) was sufficient, a loss of PMMA crystallinity, a change in PMMA chain spacing, and structural relaxation to the amorphous phase occurred on characteristic times of hundreds of picoseconds.

The innovative part of the T-ULEED experiment is the short-pulse illumination of a tungsten nanotip to produce the electron pulses. In recent years, it has been shown that few-cycle laser pulses focused to the apex of metal tips can induce field-driven photoemission of ultrashort electron pulses (*3*, *4*). This phenomenon has now been explored in cases ranging from multiphoton ionization to above threshold ionization and strong-field tunneling emission, including carrier-envelope phase effects (*5*).

Exploiting strong-field emission from a metal nanotip opens up the new frontier of ultrafast LEED techniques by substantially miniaturizing the electron diffraction apparatus compared with the high-energy diffraction methods that have recently come to fruition (*6*–*8*). Ultrafast electron or x-ray diffraction (*9*) techniques have provided insight into the structural dynamical events underlying processes as diverse as photoinduced chemical reactions in the gas phase, charge transfer in bulk systems, and melting of metal or semiconductor superstructures.

The T-ULEED method of Gulde *et al.* widens the field of ultrafast structural dynamics to surface science. Previous ultrafast electron diffraction methods relied on sophisticated experimental set-ups to produce the intense, short electron pulses needed to probe irreversible structural changes or to achieve femtosecond time resolution. Achieving similar time resolution with the T-ULEED experiment will be the next challenge. ■

REFERENCES

1. M. Gulde *et al.*, *Science* **345**, 200 (2014).
2. C. Davisson, L. H. Germer, *Phys. Rev.* **30**, 705 (1927).
3. P. Hommelhoff, C. Kealhofer, M. A. Kasevich, *Phys. Rev. Lett.* **97**, 247402 (2006).
4. C. Ropers, D. R. Solli, C. P. Schulz, C. Lienau, T. Elsaesser, *Phys. Rev. Lett.* **98**, 043907 (2007).
5. B. Piglosiewicz *et al.*, *Nat. Photonics* **8**, 37 (2014).
6. A. H. Zewail, *Science* **328**, 187 (2010).
7. R. J. D. Miller, *Annu. Rev. Phys. Chem.* **65**, 583 (2014).
8. F. O. Kirchner, A. Gliserin, F. Krausz, P. Baum, *Nat. Photonics* **8**, 52 (2014).
9. T. Elsaesser, M. Woerner, *J. Chem. Phys.* **140**, 020901 (2014).

10.1126/science.1256199

PHYSICS

An optical twist for triplet superconductors

Optical measurements may help reveal the secrets of exotic superconductivity and manipulate the pair condensate

By **Dirk van der Marel**[1] *and* **George Albert Sawatzky**[2]

The discovery of superconductivity in UPt_3 (*1*, *2*) immediately led to ideas and speculations about how the electrons pair up and condense into a superconducting state. Specifically, questions have surrounded the symmetry of the order parameter in these materials (a measure of the density of the condensed electron pairs, and of their phase). From the outset, it was suspected that these so-called heavy-fermion systems were "odd-parity" or "p-wave" superconductors (*3*); that is, instead of the electrons pairing up into spin-singlet states with opposite spins as in conventional superconductors, they would form spin-triplet states where the spins of the paired electrons point in the same direction. To date, consensus concerning the microscopic pairing mechanism applicable to these heavy-fermion systems has been lacking. On page 190 of this issue, Schemm *et al.* (*4*) report results of magneto-optical experiments that define the nature of the superconducting pairing in these compounds. The Kerr-rotation experiments provide compelling evidence in favor of the odd-parity mechanism, and show that UPt_3 belongs to the same universality class as superfluid ^{3}He and the ruthenates.

Various mechanisms favoring odd-parity superconductivity have been presented, either mediated by ferromagnetic spin-fluctuations (*5*) or by Hund's rule coupling (*6*–*9*). Other models have favored singlet superconductivity (*10*). Historically, the observation of strong mass renormalization in UPt_3 and other heavy-fermion metals suggested a close analogy with ^{3}He, which is also a Fermi liquid characterized by strong mass renormalization. Taken together with the high-spin susceptibility, the possibility was explored that the pairing symmetry in UPt_3 would also have similarities with ^{3}He, which is of the triplet variety.

Before the unique playground offered by these unconventional superconductors can be exploited, several questions must be answered. One concerns the interactions responsible for selecting the p-wave (triplet) pairing with a pair spin, $S = 1$, rather than the more conventional s-wave (singlet) pairing in which the pairs have zero spin. It could be that p-wave pairing occurs much more often than was generally assumed, but has gone unnoticed because the experiments were unable to detect the p-wave pairing aspects. In this regard, one of the first indicators of unconventional pairing was the extreme sensitivity to impurities. So what other tests, if any, of p-wave superconductivity are possible beyond the existing ones, including the extremely high-sensitivity magneto-optical measurements that Schemm *et al.* report?

> ***"... finding the correct balance between these interaction channels may be sufficient to form an exotic superconductor with a desired set of properties."***

It is also desirable to distinguish between the various proposed mechanisms for the pairing. Recently, Hund's rule coupling has become popular in the description of correlated electron systems such as the iron-based pnictide superconductors as so-called Hund's rule metals. In Hund's metals, the mass of the electrons is enhanced because of the Hund's rule interaction, J, that tends to align the spin of electrons when they occupy the same uranium atom.

Another question is whether the $S = 1$ character of the paired electrons can be exploited in potential spintronics applications that would use the flow of a supercurrent carried by condensed pairs and carrying with it a magnetic moment.

Most superconducting materials are of the conventional $S = 0$ variety in which

[1]*Département de Physique de la Matière Condensée, Ecole de Physique, Université de Genève, Quai Ernest-Ansermet 24, Genève, Genève CH-1211, Switzerland.* [2]*Department of Physics and Astronomy, University of British Columbia, 6224 Agricultural Road, Vancouver, British Columbia V6T 1Z1, Canada. E-mail: dirk.vandermarel@unige.ch; sawatzky@physics.ubc.ca*

Published by AAAS

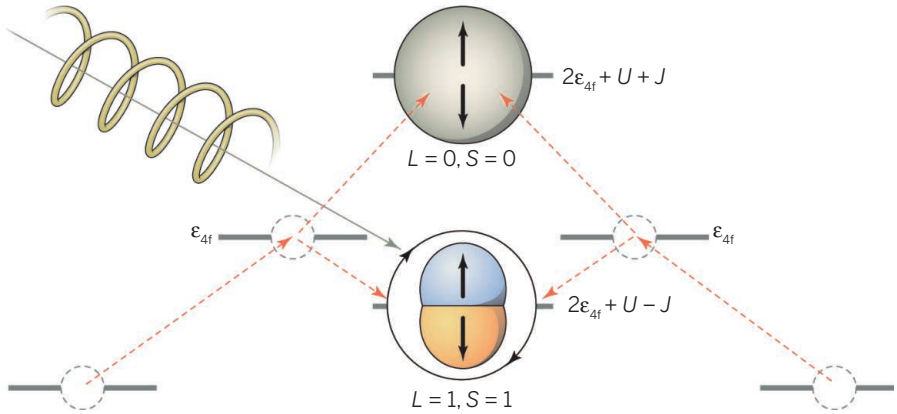

Upon reflection. Image showing how circularly polarized light interacts with superconducting Cooper pairs bound by Hund's rule coupling. Two electrons that move into the 5f shell of the same uranium atom have an interaction energy $U + J$ if they form a singlet spin = 0 state, and $U - J$ if they form a triplet spin = 1 state. Here, U represents the average Coulomb interaction between two electrons occupying the same 5f shell, and J is the Hund's rule exchange interaction. U is much more strongly screened than J. For $U < J$, an attractive interaction results between two conduction electrons hybridizing with the same uranium atom, but only if their spins are parallel. The antiparallel spin state would result in a repulsive interaction with this mechanism. Because of the angular momentum of the pair, left-handed and right-handed photons do not have the same absorption coefficient, and, because linear polarized light is a superposition of left- and right-handed light, the handedness of the absorption causes a finite rotation of the polarization angle.

magnetism was thought to be incompatible with the superconducting state. This view, however, has changed with the advent of the high-temperature superconducting cuprates and, more recently, by the iron pnictides and chalcogenides, both of which are fundamentally magnetic. The possibility of mixed singlet-triplet character has been proposed, because the low symmetry of the underlying crystal lattice allows for such a mixture to exist. If the interactions present that give rise to this type of pairing can be identified, finding the correct balance between these interaction channels may be sufficient to form an exotic superconductor with a desired set of properties.

Recently, superconducting two-dimensional electron gases have been generated by molecular beam epitaxy methods to physically grow dissimilar materials in layered structures, creating entirely new properties at the interfaces. Controlling the nature of the pairing interaction for triplet superconductors could lead to ways of creating new triplet superconductors based on the interface properties. The road of materials engineering combining ferromagnetism and superconductivity in a single material has been paved by the discovery of magnetic field–induced superconductivity in the pseudoternary europium-tin-molybdenum chalcogenides (*11*), and the demonstration of spin triplet supercurrent through the half-metallic ferromagnet CrO_2 (*12*). Because of the nature of the pairing type, p-wave superconductors are more compatible with ferromagnetism than conventional s-wave superconductors. Further improvement of these materials may be possible if they can be based on triplet (instead of singlet) superconductivity.

In the experiments reported by Schemm *et al.*, the sensitivity to time-reversal symmetry breaking relies on the chiral nature of the photon. Left-handed and right-handed photons will have different absorption coefficients if the state of matter of the material to which they couple has itself a certain handedness (see the figure). However, as the energy of the two states is independent of the handedness, textures (in ^{3}He, for example, textures are observed in the form of lines, planes, and points) involving these two degenerate states can in principle exist. And because each circularly polarized photon transfers a quantum of angular momentum, one may speculate on future spintronic devices in which the spin state of the pair-condensate is manipulated by the transfer of photon angular momentum. ■

ILLUSTRATION: P. HUEY/*SCIENCE*

REFERENCES

1. G. R. Stewart, Z. Fisk, J. O. Willis, J. L. Smith, *Phys. Rev. Lett.* **52**, 679 (1984).
2. A. de Visser, J. J. M. Franse, A. Menovsky, T. T. M. Palstra, *Physica* **127**, 442 (1984).
3. C. M. Varma, *Comm. Solid State Phys.* **11**, 221 (1985).
4. E. R. Schemm *et al.*, *Science* **345**, 190 (2014).
5. P. W. Anderson, *Phys. Rev. B* **30**, 1549 (1984).
6. D. van der Marel, G. Sawatzky, *Solid State Commun.* **55**, 937 (1985).
7. M. R. Norman, *Phys. Rev. Lett.* **72**, 2077 (1994).
8. A. Kleinberg, J. Spalek, *J. Phys. Condens. Matter* **11**, 6553 (1999).
9. J. E. Han, *Phys. Rev. B* **70**, 054513 (2004).
10. J. E. Hirsch, *Phys. Rev. Lett.* **54**, 1317 (1985).
11. H. W. Meul *et al.*, *Phys. Rev. Lett.* **53**, 497 (1984).
12. R. S. Keizer *et al.*, *Nature* **439**, 825 (2006).

10.1126/science.1255925

MICROBIOLOGY

A flipping cell wall ferry

How bacteria "flip" carbohydrate precursors across the cytoplasmic membrane

By **Kevin D. Young**

Most bacteria surround themselves with a tough, highly interconnected polymer called peptidoglycan. To create this wall, bacteria synthesize precursors in the cytoplasm, attach them to a lipid carrier (lipid II), transport ("flip") this compound across the cytoplasmic membrane, and then polymerize and cross-link the monomers to the existing cell wall (*1*). The enzymes responsible for the cytoplasmic and extracytoplasmic steps are well known. However, hydrophilic precursors must cross the hydrophobic membrane, and the protein that conducts this critical transfer has stubbornly resisted identification. On page 220 of this issue, Sham *et al.* (*2*) present evidence that the MurJ protein of *Escherichia coli* performs this "flippase" function in vivo, thus solving a major puzzle in the basic pathway that synthesizes the bacterial cell wall. The new data are somewhat disconcerting, though, because in vitro experiments identified another candidate, FtsW, as the relevant flippase, with MurJ being inactive (*3*). We are left with the tantalizing question of how these results are to be reconciled and which protein fills this fundamental biochemical role.

At issue is how hydrophilic compounds traverse a highly hydrophobic and nearly impenetrable lipid bilayer. Numerous receptors, transporters, pores, pumps, and transducers help transform lipid bilayers into the semipermeable membranes required for cellular life, but it is unclear how several important carbohydrates cross bacterial and eukaryotic membranes (*1*, *4*). There are a limited number of ways to export polysaccharides, so studying the mechanisms used by *E. coli* has the potential to shed light on other transport systems (*5*). The issue has practical import, as well, since the cell wall allows bacteria to exist in the osmotically inhospitable environments that cover most of Earth and oceans, and removing the wall or inhibiting its synthesis is one of the most frequently used means of controlling bacterial infection.

Published by AAAS

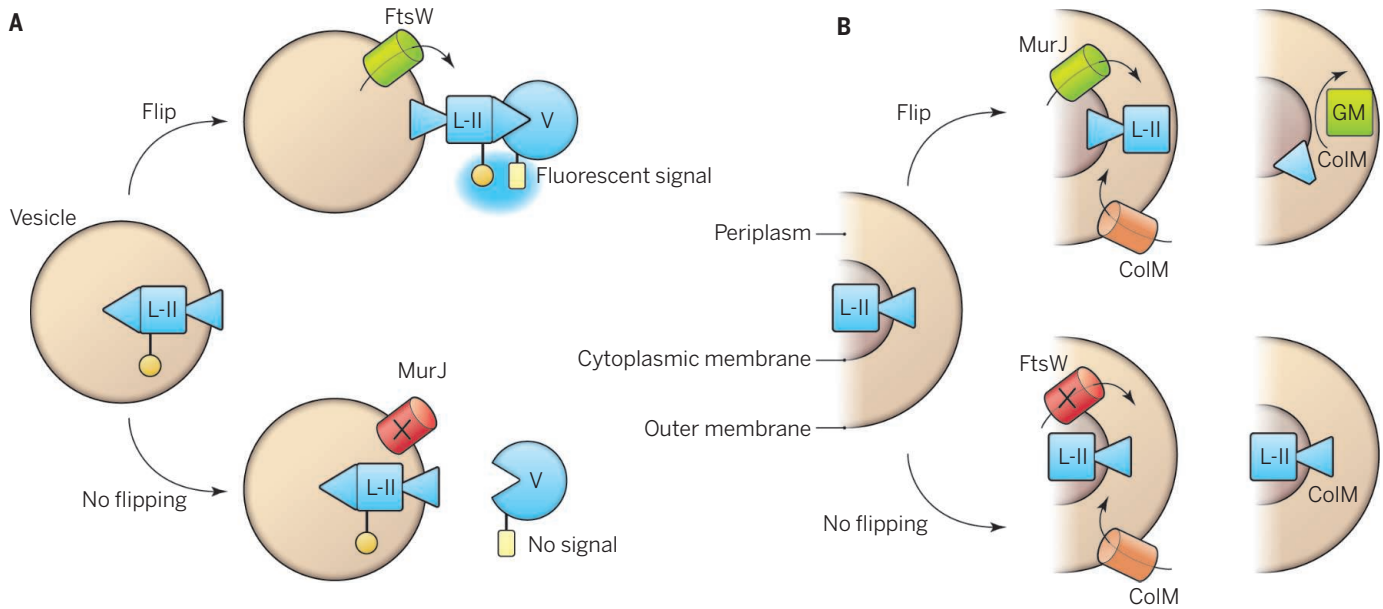

Dueling flippase assays. (**A**) The in vitro assay (*3*) traps donor-labeled lipid II (L-II, with orange circle) in membrane vesicles. If lipid II is flipped across the membrane (top), then an acceptor-labeled vancomycin derivative (V, with yellow square) binds to it and a fluorescence signal is created. If no flipping occurs (bottom), no signal develops. (**B**) The in vivo assay (*2*) monitors living *E. coli*. If flipping occurs (top), ColM cleaves lipid II in the periplasm and produces a soluble disaccharide-pentapeptide (GM). If no flipping occurs (bottom), lipid II remains in the cytoplasm, attached to the cytoplasmic membrane.

The *E. coli* peptidoglycan flippase has long been theorized to be either FtsW or RodA (*6*). Both are integral membrane proteins; each is a member of a protein family involved in cell shape, elongation, division, and sporulation; and the genes for each are located in operons related to peptidoglycan synthesis. These associations were deemed strong indirect evidence that FtsW and RodA might be the flippases that supplied precursors to the cell division and elongation machineries, respectively.

MurJ is also an integral membrane protein, of the MOP (multidrug, oligosaccharidyl-lipid, polysaccharide) family, which places it among the few confirmed flippases (*7*, *8*), and a bioinformatics screen identified MurJ as a leading flippase candidate (*9*). Also, when MurJ is depleted, *E. coli* and *Burkholderia cenocepacia* accumulate lipid-linked precursors in the cytoplasm, consistent with the pathway being stalled at the flippase step (*10*, *11*), whereas cells depleted of FtsW accumulate downstream products (*10*). Yet, the *murJ* gene is located far from other cell wall–related genes, and four MurJ homologs are not essential in *Bacillus subtilis* (*12*).

A definitive answer about the identity of the flippase enzyme turns on dueling assays, both of which detect products that become accessible to a modifying reagent only if the substrate has been flipped. Previously, Mohammadi *et al.* created an in vitro fluorescence-transfer procedure that detects the status of lipid II in *E. coli* membrane vesicles (*3*) (see the figure, panel A). Membranes from cells overproducing FtsW can flip lipid II, but those from cells with increased MurJ cannot (*3*). Specific FtsW residues mediate this reaction, lending credence to the idea that flipping is inherent to FtsW (*13*). In contrast, Sham *et al.* devised an in vivo flippase assay (*2*) (see the figure, panel B) using the ColM toxin to cleave lipid II located on the outer face of the cytoplasmic membrane (i.e., lipid II that has been flipped), which releases a soluble product and leaves an isoprenoid fragment in the membrane. In this assay, MurJ is active but FtsW is not.

Sham *et al.* strengthened the case for MurJ by testing 39 variants in which amino acid residues throughout the protein were replaced with cysteine. Tellingly, four of these variants flip lipid II unless they are inactivated with a cysteine-reactive compound, confirming that flipping requires active MurJ.

The in vivo assay is a simple one-step procedure that targets flipped lipid II in intact living cells. In contrast, the in vitro assay suffers some interpretive difficulties, including the use of a derivatized lipid II, the freeze-thaw introduction of substrate into vesicles, the need to overproduce the tested proteins before a signal can be detected, conducting the assay at 14°C, and testing a purified His-tagged version of MurJ. Any of these might affect the activity of MurJ and account for its lack of flipping in vitro. On the other hand, because FtsW functions transiently during cell division, its overall activity may be too low to be detected by the in vivo assay. Also, this procedure would not report FtsW activity if ColM were unable to reach the pool of lipid II being flipped during cell division. Despite these uncertainties, there is at least one appealing explanation that could reconcile these results. Because the membranes tested in vitro contain wild-type MurJ, increasing amounts of FtsW might enhance MurJ activity [though the mutated residues in inactive FtsW variants seem to suggest a more direct role (*13*)].

The study by Sham *et al.* is an important milestone in the search for the peptidoglycan flippase, even if it seems that, for at least a bit longer, some uncertainty will cloud the relationships among these "flipping" contenders. ■

Department of Microbiology and Immunology, University of Arkansas for Medical Sciences, 4301 West Markham Street, Little Rock, AR 72205, USA. E-mail: kdyoung@uams.edu

REFERENCES

1. A. L. Lovering, S. S. Safadi, N. C. Strynadka, *Annu. Rev. Biochem.* **81**, 451 (2012).
2. L.-T. Sham *et al.*, *Science* **345**, 220 (2014).
3. T. Mohammadi *et al.*, *EMBO J.* **30**, 1425 (2011).
4. S. Sanyal, A. K. Menon, *ACS Chem. Biol.* **4**, 895 (2009).
5. C. Whitfield, *Annu. Rev. Biochem.* **75**, 39 (2006).
6. K. Ehlert, J. V. Höltje, *J. Bacteriol.* **178**, 6766 (1996).
7. Y. Hong, P. R. Reeves, *J. Bacteriol.* **196**, 1713 (2014).
8. S. T. Islam, J. S. Lam, *Environ. Microbiol.* **15**, 1001 (2013).
9. N. Ruiz, *Proc. Natl. Acad. Sci. U.S.A.* **105**, 15553 (2008).
10. B. Lara, D. Mengin-Lecreulx, J. A. Ayala, J. van Heijenoort, *FEMS Microbiol. Lett.* **250**, 195 (2005).
11. Y. F. Mohamed, M. A. Valvano, *Glycobiol.* **24**, 564 (2014).
12. A. Fay, J. Dworkin, *J. Bacteriol.* **191**, 6020 (2009).
13. T. Mohammadi *et al.*, *J. Biol. Chem.* **289**, 14707 (2014).

10.1126/science.1256585

ILLUSTRATION: P. HUEY/*SCIENCE*

Published by AAAS

MEDICINE

Hepatitis C can be cured globally, but at what cost?

New drugs to cure hepatitis C should be made available at low costs in developing countries

By **Andrew Hill**[1] *and* **Graham Cooke**[2]

Worldwide, an estimated 185 million people have been infected with the hepatitis C virus (HCV). Untreated, the infection can lead to cirrhosis, liver failure, and liver cancer, causing up to 500,000 related deaths per year (*1*, *2*), and killing more people than tuberculosis or malaria (*3*, *4*). New treatments are available that can cure over 90% of people with HCV within 12 weeks (*5*). So what is the problem?

The "new generation" of drugs for HCV that are now available in the United States cost $84,000 (sofosbuvir) and $66,000 (simeprevir) per person, for a 12-week course of treatment (*6*) (see the figure). Even newer drugs are undergoing regulatory review (daclatasvir and "3D"). However, these treatments could be manufactured for as little as $78 to $166 per person for a 12-week course of two drugs, according to our recent analysis (*5*). Efforts have begun by the manufacturer to make sofosbuvir affordable in some low-income countries like Egypt ($1000), but no country is yet able to access this drug at a cost that is close to the predicted minimum production price. No other pharmaceutical company has announced similar access prices for their treatments outside the United States and Europe.

There is no vaccine against HCV, and existing "old generation" treatments are challenging. Therapies based on the cytokine interferon and the drug ribavirin (which blocks RNA synthesis by some viruses including HCV) require a course of 24 to 48 weeks, have high rates of side effects (rash, anemia, and flu-like symptoms), and fail to cure many patients (*7*). Moreover, different viral genotypes require different choice and durations of therapy. Despite these challenges, there is good news. The more recent drugs can cure the majority of people with HCV, with much improved side-effect profiles and simple oral dosing (*5*). Data are expected to show greatly improved "pan-genotypic" activity of the newer drugs. But the cost and affordability of treatment remain the biggest barrier to scaling up treatment.

As long as U.S. patents for new hepatitis C drugs are enforced, high prices will continue to restrict access to treatment. The patents on simeprevir, daclatasvir, and sofosbuvir expire in 2026, 2027, and 2029, respectively (*8*–*10*). Companies can only start production of generic versions 12 to 15 years from now, when an estimated 6 to 7.5 million more people will have died from hepatitis C if untreated, given current death rates and given that the epidemic would continue to grow.

Over the past 15 years, licensing to manufacturers of generics, economies of scale, and improvements in manufacturing processes have driven the cost of antiretroviral (ARV) treatment for HIV infection down by more than 99%, with standard HIV treatment now costing as little as $60 per patient per year, using the same standard of care that patients receive in the richest nations (*11*). This price could not have been imagined when effective HIV treatment was introduced at over $10,000 per patient per year in the late 1990s (*12*). Universal access to treatment for HIV/AIDS in developing countries was initially considered too complex and expensive to be feasible. With the invention of a simple and effective therapy (ARVs), a competitive market was created for companies to mass produce generics, which, in turn, lowered costs and made treatment affordable. Along with associated international funding, treatment scale-up became possible (*12*). There are now more than 10 million people receiving treatment for HIV in poor countries, at a very low price.

Similar innovation and progress is possible for hepatitis C treatment. There is no reason to predict that the new generation of HCV drugs should be particularly expensive to manufacture. For example, one of the most promising early combination treatments for hepatitis C—sofosbuvir and daclatasvir—cured over 90% of patients after 12 weeks (*13*). A 12-week course of these drugs could be manufactured for between $78 and $166 per person if the same methods of mass-producing generic drugs for HIV/AIDS are applied (*5*). But who will pay for the treatments (even at reduced prices) and the related costs of screening, diagnosis, and care? The current high prices of new hepatitis C treatments will place a strain on all healthcare systems. In the United States, Congress is investigating the pricing of sofosbuvir, including the methods used to establish the cost. In the United Kingdom, national reimbursement authorities may not recommend payment for sofosbuvir.

Of the 20 countries with the largest HCV epidemics, 12 are classified as low or lower-middle income (*5*). In many of the poorest countries, there are few or no programs to treat HCV, so new funding streams are needed to support the scale-up of treatment as part of comprehensive control and prevention programs. Such funding needs to be matched with commitments from pharmaceutical companies in wealthy nations so that new-generation drugs can be made at minimal cost. Thus, pharmaceutical companies should allow generic companies to

Costs of new drugs for hepatitis C per person, 12-week course

New generation drugs for HCV

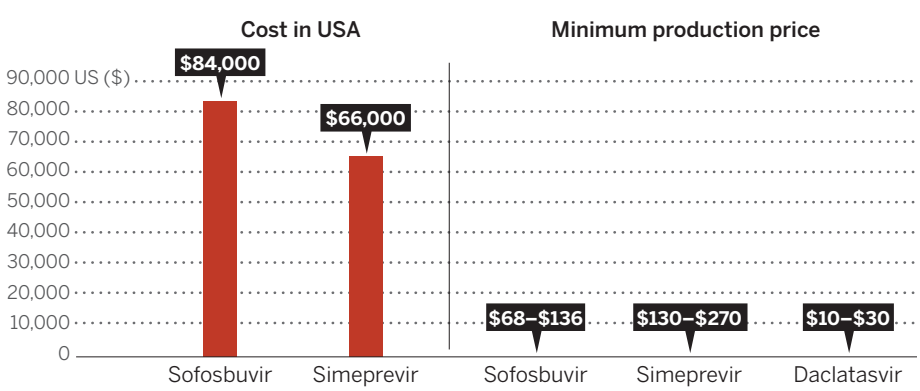

[1]Department of Pharmacology and Therapeutics, University of Liverpool, Liverpool L69 3BX, UK. [2]Imperial College London, London SW7 2AZ, UK. E-mail: microhaart@aol.com

Published by AAAS

mass produce these treatments for use in low-income countries at a cost close to the cost of production, with a small royalty paid back to the pharmaceutical companies. This is the same mechanism used to sell vaccines in low-income countries. In some countries, reductions in the price of HIV-1 treatments were only achieved after long legal battles with pharmaceutical companies. In some cases, countries overruled company patents on drugs and started importing generic drugs at lower costs—so-called compulsory licensing—which is permitted in cases of national medical emergencies.

Creating a new funding mechanism for poor nations is difficult in the current economic climate, but HIV has left a legacy of structures ready to adapt to hepatitis C to complement government and private-sector efforts. UNITAID, the United Nations agency created in 2006 to overcome market barriers for treatments of HIV, tuberculosis, and malaria, recently announced its first funding for hepatitis C, with an aim of reducing treatment costs to $500 to $1000 per patient (*14*). It plans to scale up treatment through a multinational group of HIV programs run by Médicins Sans Frontières, the international medical humanitarian organization. The Global Fund, which addresses HIV/AIDS, tuberculosis, and malaria, has funded treatment programs with old-generation HCV drugs in several developing countries for the past 3 years.

If we can learn from the lessons of HIV/AIDS, mass production of generics can save millions of lives. This has been an inspiring medical success story which need not stand alone but can be repeated, even more rapidly, for hepatitis C. ■

REFERENCES AND NOTES

1. K. Mohd Hanafiah, J. Groeger, A. D. Flaxman, S. T. Wiersma, *Hepatology* **57**, 1333 (2013).
2. R. Lozano *et al.*, *Lancet* **380**, 2095 (2012).
3. K. N. Ly *et al.*, *Ann. Intern. Med.* **156**, 271 (2012).
4. G. S. Cooke *et al.*, *J. Viral Hepat.* **20**, 600 (2013).
5. A. Hill, S. Khoo, J. Fortunak, B. Simmons, N. Ford, *Clin. Infect. Dis.* **58**, 928 (2014).
6. Fair Pricing Coalition, Activists condemn Gilead for exorbitant price of its new hepatitis C drug; www.thebody.com/content/73462/activists-condemn-gilead-for-exorbitant-price-of-t.html (2013).
7. N. Ford *et al.*, *Clin. Infect. Dis.* **54**, 1465 (2012).
8. Medivir, 2012 Annual Report, Stockholm (2012), p. 26.
9. Bristol-Myers Squibb Company, Form 10-K: Annual report pursuant to section 13 or 15(d) of the securities exchange act of 1934. Fiscal year ending Dec 31, 2011, p. 9.
10. Pharmasset, Inc. Form 10-K: Annual report pursuant to section 13 or 15(d) of the securities exchange act of 1934. Fiscal year ending Sep 30, 2011, p. 26.
11. MSF Drug Access Team, Untangling the web of antiretroviral price reductions: 16th edition (Geneva, 2012); www.msfaccess.org/reports.
12. B. Schwartländer, I. Grubb, J. Perriëns, *Lancet* **368**, 541 (2006).
13. M. S. Sulkowski *et al.*, *N. Engl. J. Med.* **370**, 211 (2014).
14. www.unitaid.org/en/resources/press-centre/releases/1352-unitaid-approves-grants-of-160-million

10.1126/science.1257737

BIOCHEMISTRY

Fishing for peroxidase protons

Where are the protons in heme protein catalysis?

By **John T. Groves** *and* **Nicholas C. Boaz**

Cytochrome c peroxidase (CcP) consumes hydrogen peroxide in mitochondria, using electrons derived from reduced cytochrome c. This and a related enzyme, horseradish peroxidase (HRP), have played key roles in the development of structural and mechanistic biochemistry and are used in biocatalysis and chemiluminescent bioassays (*1*). On page 193 of this issue, Casadei *et al.* (*2*) use neutron diffraction to reveal the role and origin of protons in heme oxidation by hydrogen peroxide, a key step in this essential enzymatic reaction.

CcP and HRP were the first heme enzymes for which oxidized intermediates were observed (*1*). In the textbook mechanism for heme oxidation, protonated histidine N-H assists O-O bond heterolysis in an Fe(III)-OOH intermediate (CcP-0), producing CcP compound I (CcP-I) and water. The overall course of this reaction was established long ago. But where are the protons? Casadei *et al.* use neutron diffraction to reveal the positions of protons in resting CcP and CcP-I. They show that the iron(IV) of CcP-I is an unprotonated ferryl, Fe(IV)=O. The results bring new clarity to heme oxidation by hydrogen peroxide (see the figure).

Neutron diffraction has distinct advantages over x-ray diffraction techniques for the structural characterization of enzymes that contain redox-active metals. Non-ionizing neutron beams avoid the photoreduction that often plagues structural analysis with x-rays and that also occurs in the laser beams used for resonance Raman spectroscopy. Laser and x-radiation lead to ambiguities in the oxidation states of redox-active metals such as iron or manganese. By contrast, neutrons interact only with atomic nuclei and scatter much more effectively from hydrogen and, especially, deuterium atoms. Catalytic proton networks and even deuterated hydronium ions (D_3O^+) have been observed in proteins by means of neutron diffraction (*3*, *4*).

Efforts to understand the atomic and electronic structure of the oxidized intermediates in the CcP catalytic cycle have been hampered by the fact that Fe(III)/Fe(IV) redox potentials in heme proteins lie in the same range as those of the porphyrin ring and those of tryptophan and tyrosine. This "redox non-innocence" greatly increases the complexity of these systems because it increases the number of plausible sites of oxidation. In HRP-I and in model porphyrin complexes, ferryl states, Fe(IV)=O, with very short Fe-O bond lengths have been reported (*5*, *6*). The distinction between Fe(IV)=O species and their hydroxylated equivalents, Fe(IV)-OH, has taken on considerable importance with recent evidence that cytochrome P450 compound II is protonated and that the basicity of ferryl oxygen strongly affects heme protein reactivity (*7*).

To identify the positions of active-site protons in CcP and CcP-I, Casadei *et al.*

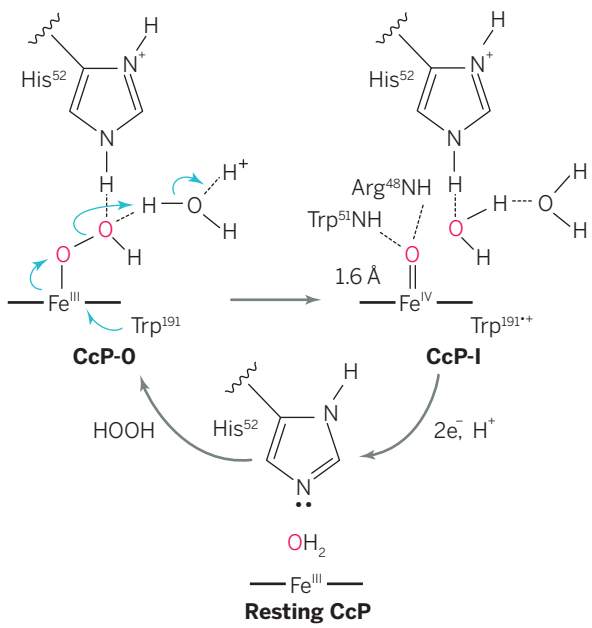

Proton-mediated mechanism. Reaction of ferric CcP with H_2O_2 first gives CcP-0, followed by O-O bond scission driven by external protonation to afford CcP-I. Casadei *et al.* now report neutron diffraction data that pinpoint the locations of the protons and elucidate the catalytic mechanism.

Department of Chemistry, Princeton University, Princeton, NJ 08544, USA. E-mail: jtgroves@princeton.edu

Published by AAAS

have compared neutron and x-ray diffraction data from both species. The authors first replaced exchangeable protons with deuterons in large (1 mm) crystals of CcP, and then treated a CcP crystal with hydrogen peroxide to produce CcP-I. The results show that the catalytic imidazole of His^{52} is not protonated in resting CcP, as expected (see the figure). In CcP-I, both nitrogen atoms in His^{52} are protonated (deuterated), which was unexpected according to the generally accepted mechanism. This means that the protons required for O-O bond cleavage in CcP-0 (see the figure) must have come from another source, such as an adjacent water molecule. In this snapshot of the catalytic cycle, the ferryl oxygen, Fe(IV)=O, of CcP-I is not protonated, and the short iron-oxygen distance expected for the ferryl is confirmed.

Visualizing the mechanistically pertinent protons has important implications for the mechanism of O-O bond scission mediated by CcP and other heme proteins. A "wet" version of the peroxidase mechanism has been proposed, in which a water molecule adjacent to His^{52} mediates O-O bond cleavage (*1*, *8*, *9*). Retention of the His^{52} proton adjacent to the ferryl heme after O-O bond heterolysis, as revealed by Casadei *et al.*, suggests that another proton, likely traveling through an aqueduct of water molecules leading to the active-site cavity, is also necessary (see the figure).

CcP-catalyzed peroxide bond heterolysis thus seems to occur via a proton relay mechanism similar to that of cytochrome P450 (*10*), with electrons arriving through Trp^{191} (see the figure). In this scenario, deprotonation of His^{52} would occur during subsequent reduction of CcP-I by another enzyme, ferrocytochrome c. This realization points to a water-mediated, acid-catalyzed process for O-O bond heterolysis, which is mechanistically satisfying because of its analogies to other proton relay mechanisms, such as that of cytochrome P450. Further, the need for a water channel and an external proton in peroxidase catalysis are highly informative for the design and construction of new heme-iron biocatalysts. ■

REFERENCES

1. T. L. Poulos, *Chem. Rev.* **114**, 3919 (2014).
2. C. M. Casadei *et al.*, *Science* **345**, 193 (2014).
3. M. G. Cuypers *et al.*, *Angew. Chem. Int. Ed.* **52**, 1022 (2013).
4. S. J. Tomanicek *et al.*, *J. Biol. Chem.* **288**, 4715 (2013).
5. J. T. Groves, *J. Inorg. Biochem.* **100**, 434 (2006).
6. J. E. Penner-Hahn *et al.*, *J. Am. Chem. Soc.* **108**, 7819 (1986).
7. T. H. Yosca *et al.*, *Science* **342**, 825 (2013).
8. P. Vidossich *et al.*, *J. Phys. Chem. B* **114**, 5161 (2010).
9. K. Sen, W. Thiel, *J. Phys. Chem. B* **118**, 2810 (2014).
10. X. Wang, S. Peter, M. Kinne, M. Hofrichter, J. T. Groves, *J. Am. Chem. Soc.* **134**, 12897 (2012).

10.1126/science.1256754

ILLUSTRATION: V. ALTOUNIAN/*SCIENCE*

HIV/AIDS

Persistence by proliferation?

Latently HIV-infected cells driven to proliferate may raise a further challenge for eradication strategies

By **David Margolis**[1] *and* **Frederic Bushman**[2]

The persistence of HIV-1 infected cells in individuals on antiretroviral therapy (ART) presents an obstacle for cure of infection. ART is the best available remedy for millions of infected people, but treatment must be life-long because HIV establishes latent infection that is unaffected by antiretrovirals and is invisible to immune surveillance. Because decades of treatment may be unsustainable, there is intense interest in reversing latency. If quiescent HIV in $CD4^+$ T cells can be identified and activated without enhancing new infection, HIV-targeted immune response might be able to control or even clear infection. On page 179 in this issue and in this week's *Science* Express, Maldarelli *et al.* (*1*) and Wagner *et al.* (*2*), respectively, raise a new challenge for these efforts suggesting that proliferation of latently infected cells may be a key factor in sustaining this durable viral reservoir.

Latent HIV proviruses (viral genome integrated into the host cell DNA) are found most often in resting $CD4^+$ T cells within the central memory arm of the immune system (*3*–*5*), although other T cell subpopulations have been implicated (*6*, *7*). The latent pool shows minimal or absent decay (*8*), which is not fully understood. One possible explanation is that ongoing low-level HIV replication during ART replenishes the pool. However, viral genetic diversity does not increase over time in individuals during ART (*9*), at odds with this view.

Other evidence suggests that virus emerges from the pool of latently infected cells periodically. Even patients whose viral load is well suppressed show intermittent bursts of viremia ("blips"), and in many patients viremia is detectable in specialized assays (*10*, *11*). Given that the pool of latently infected cells must be primarily established before ART, it is difficult to understand why such periodic induction of the pool does not lead to it running dry.

Homeostatic proliferation of infected transitional memory T cells (*6*) has been proposed as a source that could maintain the pool, but this does not explain persistence in the dominant central memory reservoir. Latently infected stem cell–like memory T cells could proliferate (*7*), and it will be of great interest to compare integration patterns seen in these cells and in more differentiated cell populations.

Maldarelli *et al.* and Wagner *et al.* harvested DNA from the blood cells of HIV-infected individuals after a decade of successful ART, and analyzed the distribution of sites of proviral integration in the human genome. Typically, HIV favors integration in regions of the genome that are transcriptionally active (*12*), but a unique pattern was seen in rare proviruses from well-suppressed patients. Both groups found expanded proviral clones that were enriched for proviruses in or near a limited set of cellular genes, some of which

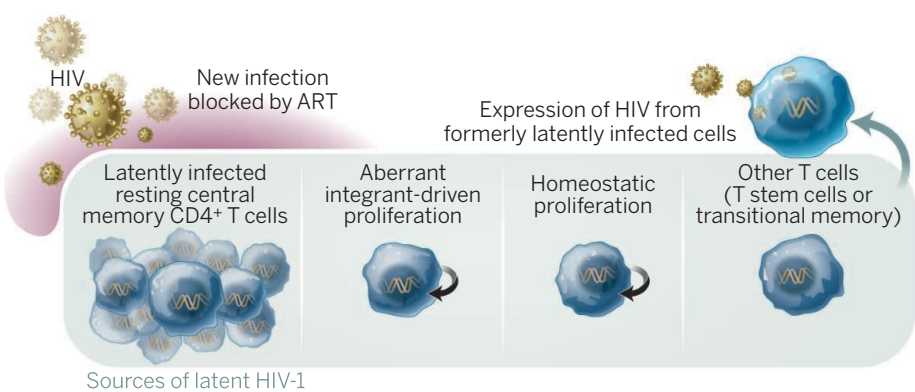

The persistent pool of HIV-1. Antiretroviral therapy can prevent the creation of new latently infected cells, but it does not affect cells in which latency was initially established. Intermittent bursts of viremia originate in part from this latent reservoir. Forcing these cells to exit the latent state without enhancing new infection could make the virus vulnerable to clearance by an HIV-targeted immune response. Blocking the proliferation of these latently infected T cells could deplete the pool if its stability is driven by such multiplication.

Published by AAAS

encode products involved in controlling the cell division cycle or cancer progression. This supports the hypothesis that disruption of these genes by proviral insertion promotes growth or persistence of the host cell (*13*). Maldarelli *et al.* and Wagner *et al.* identify the host gene encoding the basic leucine zipper transcription factor 2 (BACH2) as a frequent site of HIV integration. BACH2 is a transcriptional regulator that controls $CD4^+$ T cell senescence and cytokine homeostasis (*14*). Thus, the new findings suggest a link between the persistence of latently infected cells and proviral integration in genes related to cell proliferation and cancer.

"...findings suggest a link between the persistence of latently infected cells and proviral integration in genes related to cell proliferation ..."

Further experiments should strengthen these ideas. There is as yet no molecular evidence that such integrations of HIV-1 lead directly to the proliferation of latently infected cells, but it should be possible to engineer viral integration into specific sites of the host cell genome and demonstrate cell proliferation. In addition, there is as yet no proof that the proviruses encode for replication-competent HIV genomes. Maldarelli *et al.* did carry out the Herculean task of single-genome amplification and sequencing tiny amounts of HIV RNA recovered from the plasma of some patients studied. This verified a close similarity of circulating viral envelope sequences to those found in integrated proviral genomes in expanded clones. However, like prior studies (*11*), such sequencing is limited to a small portion of the HIV genome, and cannot eliminate the possibility of inactivating mutations in other parts of the proviral genome, making the virus incompetent to replicate. Given that the cells harboring quiescent HIV-1 are only a tiny minority of the total $CD4^+$ T cell population examined by Maldarelli *et al.* or Wagner *et al.,* and that years of ART have allowed for years of selection, alternative interpretations of the data are possible. For example, it is not yet ruled out that the expanded T cell clones detected could be expanding for other reasons (e.g., in response to stimulation by a specific antigen). There may be other reasons for preferential viral integration into the genes described as well. There may also be "survivor bias" in the detection of replication-incompetent genomes. Indeed, given the model, it is puzzling that no increase in the total number of HIV DNA-positive cells was observed.

The findings of Maldarelli *et al.* and Wagner *et al.* raise additional issues. Lentiviral vectors are used extensively in therapeutic gene transfer, so monitoring for related events of proliferation-promoting integration with these vectors during gene therapy is important. Indeed, clonal expansion was observed in the case of a lentiviral-based gene correction of the blood disorder beta-thalassemia in which integration at the site of a proto-oncogene increased cell proliferation (*15*). In this case, the host gene encoding high-mobility group AT-hook 2 (HMGA2) produced a truncated mRNA due to vector insertion within the gene. HMGA2 is a transcription regulatory protein. The truncated mRNA removed a binding site for a microRNA that negatively controls HMGA2 expression. The result was increased accumulation of HMG2A mRNA and protein. HMGA2 was not an integration target in the cells studied by Maldarelli *et al.* or Wagner *et al.*, raising questions about the differences between latent HIV infections and beta-thalassemia gene therapy.

Both studies also mention the concern that HIV integration could contribute to the development of cancers by insertional mutagenesis. However most HIV-related malignancies are not T cell cancers, and even most HIV-related lymphomas are of B cell origin. HIV cancers are not thought to harbor integrated HIV DNA, although this could be reinvestigated.

If blocking proliferation of latently infected cells proves to be necessary, it will complicate efforts to clear the latent reservoir. But clearance of this reservoir is crucial to achieve a cure of HIV infection. ■

REFERENCES

1. F. Maldarelli *et al.*, *Science* **345**, 179 (2014).
2. T. Wagner *et al.*, *Science*; 10.1126/science.1256304 (2014).
3. D. Finzi *et al.*, *Science* **278**, 1295 (1997).
4. T.-W. Chun *et al.*, *Proc. Natl. Acad. Sci. U.S.A.* **94**, 13193 (1997).
5. J. K. Wong *et al.*, *Science* **278**, 1291 (1997).
6. N. Chomont *et al.*, *Nat. Med.* **15**, 893 (2009).
7. M. J. Buzon *et al.*, *Nat. Med.* **20**, 139 (2014).
8. J. D. Siliciano *et al.*, *Nat. Med.* **9**, 727 (2003).
9. M. F. Kearney *et al.*, *PLOS Pathog.* **10**, e1004010 (2014).
10. J. R. Bailey *et al.*, *J. Virol.* **80**, 6441 (2006).
11. J. A. Anderson *et al.*, *J. Virol.* **85**, 5220 (2011).
12. A. R. Schröder *et al.*, *Cell* **110**, 521 (2002).
13. T. Ikeda *et al.*, *J. Infect. Dis.* **195**, 716 (2007).
14. M. Kuwahara *et al.*, *Nat. Commun.* **5**, 3555 (2014).
15. M. Cavazzana-Calvo *et al.*, *Nature* **467**, 318 (2010).

[1]*Departments of Medicine, Microbiology and Immunology, and Epidemiology, University of North Carolina at Chapel Hill, 120 Mason Farm Road, Chapel Hill, NC 27599–7042, USA.* [2]*Perelman School of Medicine, 3610 Hamilton Walk, Philadelphia, PA 19104, USA. E-mail: dmargo@med.unc.edu; bushman@mail.med.upenn.edu*

10.1126/science.1257426

OCEANS

Microplastics in the seas

Concern is rising about widespread contamination of the marine environment by microplastics

By **Kara Lavender Law**[1] *and* **Richard C. Thompson**[2]

Plastic debris in the marine environment is more than just an unsightly problem. Images of beach litter and large floating debris may first come to mind, but much recent concern about plastic pollution has focused on microplastic particles too small to be easily detected by eye (see the figure). Microplastics are likely the most numerically abundant items of plastic debris in the ocean today, and quantities will inevitably increase, in part because large, single plastic items ultimately degrade into millions of microplastic pieces. Microplastics are of environmental concern because their size (millimeters or smaller) renders them accessible to a wide range of organisms at least as small as zooplankton, with potential for physical and toxicological harm.

Since its introduction in the published literature in 2004 (*1*), the term microplastic has been widely used to describe plastic fragments in the marine environment. Typically considered to be smaller than 5 mm in diameter, microplastics are ill defined by size, with ranges that vary between studies. In most open-water studies, microplastics are measured with plankton nets, and particles smaller than the net mesh (typically ~0.33 mm) can evade capture. In marine sediment, bulk sampling can retain particles of all sizes; however, efficient identification is a serious challenge in quantifying microplastic loads, especially with decreasing size. Spectroscopic analysis has identified individual fragments of common plastics as small as 20 μm in diameter.

The sources of microplastic include fragmentation of larger items entering by rivers, runoff, tides, winds, and catastrophic events, together with at-sea sources, including lost cargo and fishing and aquaculture gear. There are also direct inputs of microplastics as micrometer-sized particles, such as cosmetic beads and clothing fibers

Published by AAAS

that pass through wastewater treatment into the environment. Although the sources are well known, knowledge of their relative contribution and geographic distribution is limited.

Once in the ocean, floating microplastics are transported passively by complex two- and three-dimensional physical flows, resulting in very large variability in surface concentrations that makes detection of long-term trends difficult even in the heavily sampled western North Atlantic (*2*) and eastern North Pacific Oceans (*3*). Oceanographic models [including (*4*)] and environmental observations find very high concentrations (up to 10^6 pieces km^{-2}) of floating microplastic in subtropical ocean gyres, far from land-based sources. In these gyres, converging surface currents trap and retain floating debris. Similarly high concentrations have been observed in enclosed basins such as the Mediterranean Sea (*5*).

Microplastics everywhere. Microplastics collected from seawater, shorelines, or marine sediments are typically defined as particles with a diameter of 5 mm or less. Sources include larger deteriorating plastic items, as well as microbeads used in the cosmetics industry. The microplastics in the photo were collected in the North Pacific subtropical gyre with a surface plankton net.

In coastal sediments around the world, microplastics also appear to be ubiquitous, with quantities typically ranging from 2 to 30 particles per 250 ml of sediment (*6*). Arctic sea ice is the most recently identified reservoir of microplastics (*7*). With the exception of localized spills, the relationship between microplastic concentration and its sources is poorly understood because of complex transport mechanisms and unknown fragmentation rates.

Because of their size, microplastics may have different effects from larger items of debris. For example, floating microplastics in open ocean gyres provide habitats for diverse communities of microorganisms, with assemblages that differ from those in surrounding seawater and that vary with polymer type (*8*). Furthermore, microplastics may be ingested by many diverse organisms, and some animals such as mussels can retain particles after ingestion (*9*); ingestion of small quantities of microplastics can disrupt physiological processes in marine worms, compromising their ability to store energy (*10*).

Plastic debris readily accumulates harmful chemicals such as dichlorodiphenyltrichloroethane (DDT), polychlorinated biphenyls (PCBs), and polybrominated diphenyl ethers (PBDEs) from seawater worldwide (*11*), increasing their concentration by orders of magnitude. This process is reversible, with microplastics releasing contaminants upon ingestion (*12*) and laboratory evidence of uptake in marine worms (*13*) and fish (*14*). Transfer depends on the polymer, contaminant, and conditions in the organism, particularly pH and temperature. These interactions are specific but not yet fully predictable (*15*). There is also concern that plastic debris might release monomers and potentially toxic additives such as plasticizers, flame retardants, and antimicrobial agents that are incorporated into plastics during manufacture.

This emerging evidence of harm comes primarily from laboratory studies. It is unclear whether microplastics in the environment transport chemicals to biota in concentrations high enough to cause substantial damage. The potential for harm from microplastics could increase with decreasing particle size, but size distributions and generation and degradation rates are essentially unknown, and the resulting effects on natural populations are difficult to ascertain. Nevertheless, ingestion of microplastics by mammals, fish, birds, and invertebrates is now well documented. Although quantities can be low, the widespread incidence in some natural populations together with evidence of potentially harmful effects is cause for concern.

Major questions remain about the risks from microplastics to marine organisms and ecosystems, as well as to food safety and public health. Research is urgently needed on the behavior of different polymers in the environment, including fragmentation, chemical release, degradation, transport, and accumulation; the rate at which organisms encounter microplastics, based on particle size and degradation time; and the physical, chemical, and interactive risks to organisms from these encounters, including possible magnification with increasing trophic level (biomagnification).

Given the concerns over microplastics, the temptation may be to "clean up the mess," but substantial removal of microplastic debris from the environment is not feasible. Identification and elimination of some of the major inputs of plastic waste is a more promising route, as is reduced consumption and the recognition of plastic waste as a resource. With the rapidly increasing human population, the need for greater resource efficiency could have a secondary benefit in reducing the quantities of debris entering the environment. ■

[1]*Department of Oceanography, Sea Education Association, Woods Hole, MA 02543, USA.* [2]*School of Marine Science and Engineering, Plymouth University, Plymouth PL4 8AA, UK. E-mail: klavender@sea.edu*

PHOTO: JESSICA DONOHUE/SEA EDUCATION ASSOCIATION

REFERENCES

1. R. C. Thompson *et al.*, *Science* **304**, 838 (2004).
2. K. L. Law *et al.*, *Science* **329**, 1185 (2010).
3. K. L. Law *et al.*, *Environ. Sci. Technol.* **48**, 4732 (2014).
4. N. Maximenko, J. Hafner, P. Niiler, *Mar. Pollut. Bull.* **65**, 51 (2012).
5. A. Collignon *et al.*, *Mar. Pollut. Bull.* **64**, 861 (2012).
6. M. A. Browne *et al.*, *Environ. Sci. Technol.* **45**, 9175 (2011).
7. R. W. Obbard *et al.*, *Earth's Future*, (2014); http://onlinelibrary.wiley.com/doi/10.1002/2014EF000240/abstract.10.1002/2014EF000240.
8. E. R. Zettler, T. J. Mincer, L. A. Amaral-Zettler, *Environ. Sci. Technol.* **47**, 7137 (2013).
9. M. A. Browne, A. Dissanayake, T. S. Galloway, D. M. Lowe, R. C. Thompson, *Environ. Sci. Technol.* **42**, 5026 (2008).
10. S. L. Wright, D. Rowe, R. C. Thompson, T. S. Galloway, *Curr. Biol.* **23**, R1031 (2013).
11. Y. Ogata *et al.*, *Mar. Pollut. Bull.* **58**, 1437 (2009).
12. E. L. Teuten *et al.*, *Phil. Trans. R. Soc. B* **364**, 2027 (2009).
13. M. A. Browne, S. J. Niven, T. S. Galloway, S. J. Rowland, R. C. Thompson, *Curr. Biol.* **23**, 2388 (2013).
14. C. M. Rochman *et al.*, *Nat. Sci. Rep.* **3**, 3263 (2013).
15. A. Bakir, S. J. Rowland, R. C. Thompson, *Environ. Pollut.* **185**, 16 (2014).

10.1126/science.1254065

Published by AAAS

BOOKS *et al.*

NUCLEAR PHYSICS

Blessing, with menace?

By **Daniel L. Sanchez**

There are few topics as controversial as nuclear power and nuclear weapons. High-profile tragedies, opaque risks, and the enigmatic science at nuclear's core have produced entrenched opinions and heated disputes among scientists and laypeople alike. Craig Nelson is keenly aware of this history, and *The Age of Radiance: The Epic Rise and Dramatic Fall of the Atomic Era* provides a comprehensive—if still subjective—treatment of the often-fraught relationships among nuclear science, public perception, political systems, and industry.

Nelson's narrative is at once a history of science, of culture, and of politics. It spans over a century, beginning with Wilhelm Röntgen's 1895 discovery of x-rays and concluding with Japan's 2011 Fukushima Daiichi disaster. Throughout, Nelson skillfully demonstrates the centrality of the atomic age to 20th-century and contemporary history. In addition to amusing references to popular conceptions of radiation and nuclear weapons—radium creams, the bikini, and comic books—the book also documents the interactions between political and scientific institutions. Important parallel political events affecting nuclear science include the Nazi-era treatment of Jewish scientists, scientific espionage by the Soviet Union, and the rise of government-sponsored science research.

Although historians have explored and documented many of these topics, portions of the book are novel and exemplary. Nelson's narration of the aftermath of Fukushima has not yet been attempted by other historians; his discussion of regulatory capture and cultures of secrecy in the Japanese and American nuclear industries is both timely and important. In a book teeming with information, Nelson relies on repetitive phrases to emphasize his main themes. Among them, "blessing, with menace" refers to the early uses and misuses of radioactive materials, while "bounce, bounce, bounce" refers to the accumulation of weapons capacities during the Cold War that, if deployed, could destroy ("bounce") civilization several times over.

It is clear that Nelson reveres science and scientists but laments the role of politics and public opinion in nuclear history. Marie Curie, Enrico Fermi, Lise Meitner, and Niels Bohr, for example, receive flattering portraits as part of a "great heroic generation." In contrast, Nelson casts harsh judgments on some political figures of the nuclear era, including Lewis Strauss, Edward Teller, Curtis LeMay, and Ronald Reagan (for his prioritization of the Strategic Defense Initiative, or Star Wars, over disarmament.) Interestingly, Nelson is far less sympathetic to J. Robert Oppenheimer than most previous accounts have been, accusing him of "'arrogance and occasional cruelty'" and suggesting, "If he could not be a genius, then at least he could be a handmaid to genius." In general, Nelson laments the bluster and nihilism of the Cold War, calling it "a dispiriting tragedy."

To teach children. The first issue (September 1953) of *Picture Parade* featured a story extolling the benefits of nuclear medicine, energy, and bombs.

Authors of histories reveal their biases through what they do or do not include about their subject. Despite his comprehensiveness, there are a few aspects of our atomic legacy that Nelson does not cover well, including the concept of nuclear winter, the effects of uranium mining (particularly on Native American communities in the American Southwest), and several "near misses" with weapons and reactors. His discussion is U.S.-centric and leaves out recent academic advances in nuclear science. Others have highlighted some scientific and historical inaccuracies in the book (*1*). While such omissions and errors subtract from a claim of completeness, they are not fatal flaws. They do, however, raise questions about the author's biases.

Nelson makes a puzzling attempt to downplay both the strategic importance and destructive capacity of nuclear weapons, claiming, "the great myth of nuclear arms is that they are different from conventional weapons in some magical way beyond their radioactive poisons." Indeed, his own description of the subsequent development of thermonuclear weapons and the expansive arms race between the United States and the Soviet Union contradicts his claim that conventional weapons possess destructive force and security implications similar to those of nuclear weapons. I suspect this aspect of the book reflects a desire to downplay the threats of nuclear energy and, more broadly, radiation.

The principal contribution of *The Age of Radiance* stems from its focus on the cultural and geopolitical impacts of the atomic era. Nelson's conclusions about the safety of nuclear power, common among nuclear scientists [e.g., (*2*)], resemble those of many of his predecessors. He claims that public distrust of the entire nuclear enterprise results from a "collection of myths" about radiation. Rather than blame the public for this distrust, Nelson sees it as a failure of imperfect institutions. He faults the atomic utility industry and governments for doing "such a poor job of both educating the general public and managing their crises that [nuclear power] will be driven out of business." Nelson's pessimistic take on the costs and viability of nuclear energy in the future contrasts with that of those predicting a renaissance for nuclear power plants. Regardless of whether one agrees with Nelson's conclusions, the book stands out in its accessible and nuanced documentation of the atomic age. ■

The reviewer is at the Energy and Resources Group, 310 Barrows Hall, University of California, Berkeley, CA 94720–3050, USA. E-mail: sanchezd@berkeley.edu

The Age of Radiance
The Epic Rise and Dramatic Fall of the Atomic Era
Craig Nelson
Scribner, 2014. 456 pp.

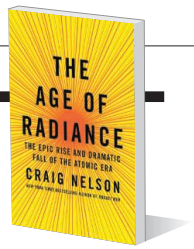

CREDIT: COURTESY CRAIG NELSON

REFERENCES

1. G. Segre, *Wall Street Journal*, 12 April 2014, p. C7.
2. J. Mahaffey, *Atomic Awakening: A New Look at the History and Future of Nuclear Power* (Pegasus, New York, 2009).

10.1126/science.1256191

Downloaded from www.sciencemag.org on July 11, 2014

Published by AAAS

NEUROSCIENCE

Consciousness perceived

By **Aaron Schurger**

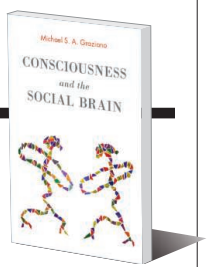

Consciousness and the Social Brain
Michael S. A. Graziano
Oxford University Press, 2013. 280 pp.

Perception is a description of reality constructed by the brain. We know it is a construct partly because of the myriad ways that it can deviate from reality. Ventriloquism provides a powerful example: the ventriloquist moves the puppet's mouth and utters the words, and yet it seems as if the puppet is doing the talking. We know the puppet is not really talking, but if the trick the ventriloquist plays on our brain works, then what we know to be true deviates from what we perceive to be true.

In *Consciousness and the Social Brain*, Michael Graziano argues that consciousness is a perceptual construct—the brain attributes it to other people in much the same way that the brain attributes speech to the ventriloquist's puppet. To clarify, imagine being greeted by a very lifelike android version of your best friend with a prerecorded behavioral program that had you genuinely fooled for a few minutes. From your perspective, for those minutes, the android was endowed with consciousness. Thus there need be no truth or falsity to the statement "My friend standing before me is conscious." Your brain decides that the android–best friend standing in front of you is conscious, and that is what you perceive to be true.

According to Graziano's "attention schema" theory, our own consciousness is also a perceptual construct—a unique one that emerges when the brain applies the same perceptual attribution recursively to itself. We attribute consciousness to others as part of our perceptual model of what they are paying attention to (an inference particularly useful for predicting their behavior). This model describes the process of attention as a mysterious something extra in the brains of beings that are selectively processing information that guides their behavior. When the brain applies the model to itself, "I" become endowed with this extra something as well—although, as with the android, it was never there in the first place.

According to the theory, consciousness is to attention what the body schema is to the body: it is the brain's perceptual description of its own process of attention. The two phenomena are thus locked "in a positive feedback loop," which explains the tight connection between attention and consciousness. In essence, consciousness is a descriptive story about a real physical phenomenon (attention). The ink in which the story is written (neural activity) is real, and the physical phenomenon that the story is "about" (attention) is real. But, like the talking puppet, the story itself need not be real. We say that we have consciousness, and that it seems irreducible to physical phenomena, because that is how the brain describes the process of attention (in ourselves and in others): as something ineffable.

PHOTO: © PETER CASOLINO/ALAMY

The reviewer is at the Brain-Mind Institute, Department of Life Sciences, École Polytechnique Fédérale de Lausanne, Station 19, AI 2101, 1015 Lausanne, Switzerland. E-mail: aaron.schurger@epfl.ch

The neural implementation of the attention schema remains a bit tentative even if well grounded in prior research. Graziano leans heavily on the temporoparietal junction, a relatively large area of cortex that has been implicated in a number of different phenomena (including spatial neglect, theory of mind, and even out-of-body experiences). However, gaps in the implementation do not require magic in order to be filled. The theory is clear on what computation(s) have to be performed, and further research will elaborate what regions might be involved (or simply refute the theory). Importantly, the idea of an attention schema could still be right, even if the proposed implementation proves wrong.

The attention schema theory is remarkable for the breadth of observable facts, extant data, and open questions it can account for. How does the theory solve the "hard problem" of consciousness (the problem of subjective experience)? That's simple, even if unsatisfying: there are no unobservable "further" facts to explain. The only thing that bears explaining is why we arrive so adamantly at the conclusion that there are. For some readers, this may sound familiar—the philosopher Daniel Dennett made a very similar argument (*1*). What Graziano adds is a plausible, neurally based, and testable mechanism that connects, like the missing piece of a puzzle, with Dennett's argument.

The author offers an engaging and accessible explanation of his theory. Rather than merely touting its merits, he aims to show how it is compatible with other popular theories. Avoiding technical details, he uses anecdotes, drawings, and metaphors to convey an understanding of the important concepts.

Well known for his work on the motor cortex, Graziano is a newcomer to the field of consciousness research. His ideas and approach here are outliers in the theoretical arena, but that makes *Consciousness and the Social Brain* all the more intriguing. It turns the field's contemporary wisdom on its head, and from its new vantage point one has the sense that an answer to the problem of consciousness might be in sight. Graziano's attention schema theory marks a milestone by offering a plausible, mechanistic answer to the hard problem, although some may not find that answer satisfactory. The author himself notes, "This approach is deeply unsatisfying—which does not argue against it. A theory does not need to be satisfying to be true." ■

REFERENCES

1. D. Dennett, *Consciousness Explained* (Little, Brown, Boston, 1991).

10.1126/science.1256012

Downloaded from www.sciencemag.org on July 11, 2014

Published by AAAS

LETTERS

Edited by **Jennifer Sills**

Twitter: Big data opportunities

IN THEIR POLICY FORUM "The parable of Google Flu: Traps in big data analysis" (14 March, p. 1203), D. Lazer *et al.* remark upon recent failures of Google Flu Trends (GFT) and cast these as limitations of big data analysis in general. However, many of these limitations have been overcome by other big data systems. Specifically,

analyses that use Twitter for influenza surveillance account for the concerns of replicability, overfitting, construct validity, granularity, and temporal confounds that Lazer *et al.* have identified.

For example, the results of GFT cannot be replicated because they are based on proprietary data, whereas Twitter data are open. A community of researchers has replicated analyses based on these data [e.g., (*1*)]. Changes to the social media platform itself, such as reengineering the underlying algorithms, need not adversely impact replicability as long as these data remain open.

Previous articles have correctly remarked that GFT and keyword-based systems overestimate influenza prevalence by conflating signals of influenza awareness (such as media attention) with signals of actual infection (*2*, *3*). These signals are separable on Twitter. Our work (*4*) has recently shown that the rate of tweets indicative of actual influenza infection is strongly correlated with the U.S. Center for Disease Control's Influenza-Like Illness rates, even though these rates were not used for system development and despite focused media attention. Furthermore, our Twitter evaluations do not suffer from peak overestimation as does GFT. Finally, our analysis explicitly controls for seasonality and temporal autocorrelation, meaning that our results directly capture flu trends and not simply seasonal variations.

Finally, New York City's Department of Health and Hygiene successfully conducted a blind evaluation of our method using municipal data, also resulting in a strong correlation. Our system successfully demonstrates the ability to understand the prevalence of flu at local levels. Concerns that are specific to GFT should not be overly generalized to other big data analyses.

David Andre Broniatowski,[1]*
Michael J. Paul,[2] Mark Dredze[2]

[1]Department of Engineering Management and Systems Engineering, George Washington University, Washington, DC 20052, USA. [2]Department of Computer Science, Johns Hopkins University, Baltimore, MD 21218, USA.

*Corresponding author. E-mail: broniatowski@gwu.edu

REFERENCES

1. S. Tuarob, C. S. Tucker, M. Salathe, N. Ram, *J. Biomed. Inform.* **49**, 255 (2014).
2. P. Copeland *et al.*, *Proc. Int. Soc. Negl. Trop. Dis.* 3 (2013).
3. D. Butler, *Nature* **494**, 155 (2013).
4. D. Broniatowski, M. J. Paul, M. Dredze, *PLOS ONE* **8**, e83672 (2014).

Response

WE THANK BRONIATOWSKI, Paul, and Dredze for giving us the opportunity to reemphasize the potential of big data and make the more obvious point that not all big data projects have the problems currently plaguing Google Flu Trends (GFT), nor are these problems inherent to the field in general.

Our Policy Forum is meant to provide a constructive critique by highlighting possible pitfalls of big data analysis. These pitfalls are not the same for all big data sets, but are certainly not unique to GFT. We do agree that Twitter has substantial scientific potential and is distinctive in the public availability of its data. Indeed, one of us (A.V.) is using Twitter data for influenza surveillance in the context of the recent Center for Disease Control (CDC) "Predict the Flu Challenge" (*1*).

Twitter data provide an excellent representation of those who choose to express an opinion publicly, which can be of tremendous value for many research purposes. However, these data may be manipulated by both the service provider (such as Google) and the user (such as companies marketing a product), as we explain in our Policy Forum. In light of these trends, whether these data can be used to represent the entire United States population remains an open question.

Who uses Twitter and how they use it have changed markedly over the past several years. The algorithmic underpinning of Twitter (which identifies "what's trending") is subject to constant and invisible tinkering. The system is under constant attack, with armies of bots ready to produce content for the highest bidder (*2*, *3*). The norms of expression on Twitter are heterogeneous and still rapidly evolving—who feels the need to publicly express that they have flu symptoms on Twitter, and are these predispositions evenly distributed throughout the population (*4*)? Bodnar and Salathé's cautionary tale (*5*) on Twitter-based influenza surveillance clearly shows that seemingly irrelevant tweets (such as those about zombies) are moderately indicative of influenza prevalence, and that the choice of validation methods has a large effect on reported success.

It is possible that one day we will have reliable prediction of flu prevalence from social media. Certainly, this would require a careful evaluation and recalibration of methodologies, public and independent replication of results, and the explicit evaluation of error processes. Clearly, all big data projects do not have the same syndromes as GFT presently does, but by building strong collaborations and adhering to rigorous standards, we should be able to extract considerably more information from these highly informative new data sources.

David Lazer,[1,2]* Ryan Kennedy,[1,3,4]
Gary King,[3] Alessandro Vespignani[5,6,3]

[1]Lazer Laboratory, Northeastern University, Boston, MA 02115, USA. [2]Harvard Kennedy School, Harvard University, Cambridge, MA 02138, USA. [3]Institute for Quantitative Social Science, Harvard University, Cambridge, MA 02138, USA. [4]University of Houston, Houston, TX 77204, USA. [5]Laboratory for the Modeling of Biological and Sociotechnical Systems, Northeastern University, Boston, MA 02115, USA. [6]Institute for Scientific Interchange Foundation, Turin, Italy.

*Corresponding author. E-mail: d.lazer@neu.edu

REFERENCES

1. CDC, CDC Competition Encourages Use of Social Media to Predict Flu (www.cdc.gov/flu/news/predict-flu-challenge.htm).
2. J. Zhang, R. Zhang, Y. Zhang, G. Yan, "On the impact of social botnets for spam distribution and digital-influence manipulation" [2013 IEEE Conference on Communications and Network Security (CNS), 2013].
3. N. Bilton, "Friends, and influence, for sale online" (20 April

Downloaded from www.sciencemag.org on July 11, 2014

PHOTO: MARK OLEKSIY/THINKSTOCK

Published by AAAS

2014); http://bits.blogs.nytimes.com/2014/04/20/friends-and-influence-for-sale-online/.
4. Y. Liu, C. Kliman-Silver, A. Mislove, in Proceedings of the 8th International AAAI Conference on Weblogs and Social Media (ICWSM'14) (Ann Arbor, MI, 2014).
5. T. J. Bodnar, M. Salathé, "Validating models for disease detection using Twitter," 1st International Workshop on Public Health in the Digital Age: Social Media, Crowdsourcing and Participatory Systems, WWW2013 (2013).

Leadership void for "designer baby" ethics

IN HIS PERSPECTIVE "Stirring the simmering 'designer baby' pot" (14 March, p. 1208), T. H. Murray discusses the ethical quandaries posed by looming genetic selection mechanisms designed to improve the health—and perhaps even the "quality"—of progeny. An underlying dilemma, in his view, is the lack of general agreement on an ethical framework to guide professional associations and public policy decision-makers in addressing the propriety of "designer" protocols. A critical step, he argues, is to agree on an appropriate forum for fleshing out various ethical claims and then selecting one among many sets of assumptions on which to base specific recommendations.

Murray suggests the President's Commission on Bioethics as a candidate for this forum, and he urges the Commission to intercede. However, the President's Commission is an advisory council, lacking the ability to coerce anyone to do anything, but rather advising the President of the United States on bioethical policy questions. If the committee issues a report the President does not like, it will gather dust. Even if President Obama did like the recommendations in a report, in the case of "designer babies," he would not have the constitutional power to impose his will in this area of human affairs. Many presidents have relied on such reports as tactics for galvanizing congressional action. But Congress, even when not in partisan gridlock, has been unable to enter the "reproductive liberty" environment with any degree of success.

Another candidate for this role could be the Food and Drug Administration (FDA), which has claimed [(*1*), p. 105] that human cloning falls within its purview. But is a reproductive strategy a food or a drug? More fundamentally, the key questions surrounding human cloning are matters of ethics and social accountability, and yet the FDA has no expertise in evaluating ethical, legal, and social issues (ELSI). In my view, even putative FDA jurisdiction over mitochondrial manipulation methodologies

PHOTO: HENRIK JONSSON GRAPHIC DESIGN/ISTOCKPHOTO

has focused on how to do it without any pretense of considering ELSI strategies. Furthermore, the FDA does not conduct open meetings at which the citizenry can petition for a redress of concerns, which makes it poorly suited to address first-order "designer baby" issues.

Another, less likely, candidate is the U.S. Patent Office. With much bravado, the Patent Office announced that a cloned human being could not be patented [(*1*), p. 94], even though other synthetically produced life forms could be. In explanation, the Patent Office argued that no person—cloned or otherwise—satisfies the "utility" standard (i.e., a person cannot be considered a functional artifact serving some ulterior purpose). Moreover, to give somebody a patent—a 20-year monopoly—on a flesh-and-blood human makes that person a sort-of slave, and slavery is outlawed by the Thirteenth Amendment. It is not clear whether processes for converting unfertilized human eggs into preembryos without using male gametes are patentable material. Nor is it clear what ELSI authority or capacity the Patent Office possesses to promulgate policy in this area.

Given that the President's Commission, the FDA, and the Patent Office all leave much to be desired in terms of steering public policy on this issue, the leadership void described by Murray remains. It is an anxious business when the political system fails to engage significant policy agendas. Perhaps we have gone about it in the wrong way. We have assumed that "designer babies" are a matter for national action. Instead, state legislatures could serve as laboratory systems, thrashing through each and every "designer baby" ELSI question and passing appropriate legislation. The federal system could then serve as a marketplace for state opinion, where some sort of consensus will inevitably emerge.

Ira H. Carmen

Cortlandt Manor, NY, 10567, USA. E-mail: irahcarmen@gmail.com

REFERENCE

1. I. H. Carmen, *Politics in the Laboratory* (Univ. of Wisconsin Press, Madison, WI, 2004).

TECHNICAL COMMENT ABSTRACTS

Comment on "Quantifying long-term scientific impact"

Jian Wang, Yajun Mei, Diana Hicks

■ Wang *et al.* (Reports, 4 October 2013, p. 127) claimed high prediction power for their model of citation dynamics. We replicate their analysis but find discouraging results: 14.75% papers are estimated with unreasonably large μ (>5) and λ (>10) and correspondingly enormous prediction errors. The prediction power is even worse than simply using short-term citations to approximate long-term citations.

Full text at http://dx.doi.org/10.1126/science.1248770

Response to Comment on "Quantifying long-term scientific impact"

Dashun Wang, Chaoming Song, Hua-Wei Shen, Albert-László Barabási

■ Wang, Mei, and Hicks claim that they observed large mean prediction errors when using our model. We find that their claims are a simple consequence of overfitting, which can be avoided by standard regularization methods. Here, we show that our model provides an effective means to identify papers that may be subject to overfitting, and the model, with or without prior treatment, outperforms the proposed naïve approach.

Full text at http://dx.doi.org/10.1126/science.1248961

Published by AAAS

southern strategies against HIV/AIDS

Published by AAAS

The Bali NGO Gaya Dewata distributes condoms outside gay bars in Seminyak.

PHOTO: MALCOLM LINTON

Australia shows its neighbors how to stem an epidemic

By **Jon Cohen**, *in Australia, Papua New Guinea, Indonesia, and Malaysia*

If Alistair Coia lived in any of Australia's poorer neighboring countries, he likely would not have seen his 50th birthday. But he celebrated it on 17 March this year, in a spacious hospital room, decorated with large balloons that his friends brought to mark the big five-zero. He is staying at a wing of the Alfred, Melbourne's venerable public hospital, specifically designed for AIDS patients. Called Fairfield House, it has 15 private rooms, each opening to a courtyard with a manicured garden; a kitchen where family and friends can cook meals with patients; and—most important—world-class, multidisciplinary care.

Coia needed it.

He checked in 1 month earlier with late-stage AIDS. His CD4 count, a measure of how much HIV had damaged his immune system, showed just 49 of these critical lymphocytes per microliter of blood. (Normal is 600 to 1200.) He had a life-threatening case of *Pneumocystis* pneumonia and severe exhaustion that kept him in bed 20 hours a day. "I got myself into a bit of a rut," says Coia, a former keyboardist for Kids in the Kitchen, a rock 'n' roll band that rode the new wave craze in the 1980s. "I feel brilliant now: 2014 will be the year I recover."

But now, this state-of-the-art AIDS ward may be closing—not because of lack of funding or political opposition, but because AIDS simply isn't a big problem in Melbourne anymore: Only six of Fairfield House's 15 beds are typically in use. Australia has had one of the most effective responses to HIV in the world. Since 1983, when

INSIDE

NEWS
First, do harm reduction *p. 156*
The limits of success *p. 157*
In PNG, the epidemic that wasn't *p. 158*
Prevention, Papua New Guinea style *p. 160*
The circumcision conundrum *p. 161*
A consummate insider pushes ideas from outside Indonesia *p. 162*
Malaysia tries to follow Australia's path *p. 164*

OPINION
End of AIDS—Hype versus hope *p. 166*

PERSPECTIVE
A critical question for HIV vaccine development: Which antibodies to induce? *p. 167*

REVIEW
Immunologic strategies for HIV-1 remission and eradication *p. 169*

SEE ALSO

▸ PERSPECTIVES pp. 136, 141, & 143
▸ RESEARCH ARTICLE SUMMARY p. 178
▸ RESEARCH ARTICLE p. 179
▸ *SCIENCE* EXPRESS REPORT
▸ VIDEOS
▸ www.sciencemag.org/special/hiv2014

Published by AAAS

the country had its first AIDS case, there have been fewer than 35,000 documented infections with HIV and fewer than 8000 deaths. The United States, in contrast, has 50,000 new infections and some 15,000 deaths each year. Yes, Australia has only 23 million people. But the country still has nearly fourfold fewer infections and sixfold fewer deaths per capita.

One reason is the country's universal health care, which provides access to the latest antiretroviral drugs. Another is the response that began soon after HIV arrived in Australia. Affected communities teamed up with clinicians and academics to pressure the government to promote prevention campaigns that targeted the most vulnerable populations. A harm reduction movement that became a model for the region (see p. 156) offers clean needles and syringes to people who inject drugs, as well as opiate substitutes like methadone that do not require needles. Provocative, blunt advertising campaigns spoke directly to gay men about the importance of using condoms, which were widely distributed for free. Several states legalized sex work. HIV/AIDS researchers joined international studies of experimental treatments and helped determine how best to use them. Basic researchers provided key insights into the interaction between the virus and the immune system, and today, they are a driving force behind efforts to find a cure for HIV/AIDS. "We've had really good public health policies that are upheld and valued," says virologist Sharon Lewin, a leading HIV cure researcher who heads the infectious disease department at the Alfred and who is co-chair of the 20th International AIDS Conference, which will take place in Melbourne 20 to 25 July.

Given its success on the homefront, Australia has become a major exporter of HIV/AIDS research advances, as well as strategies to curb the epidemic. This spring, *Science* visited Australia and three of its neighbors who have benefited: Papua New Guinea, Indonesia, and Malaysia.

Adeeba Kamarulzaman, arguably the most productive and influential HIV/AIDS researcher in Malaysia, completed both her undergraduate and medical degrees in Melbourne (see p. 164). The minister of health in Indonesia, Nafsiah Mboi, brought in Australian experts to persuade her country's top officials to support harm reduction efforts (see p. 162). Public health workers in Papua New Guinea work closely with scientists at the Kirby Institute for Infection and Immunity in Society, a branch of the University of New South Wales based in Sydney, on prevention efforts as well as basic research and surveillance to clarify how HIV is spreading through the island's remotely connected communities (see pp. 158, 160, and 161). "Australians have been boxing above their weight in the regional response," says epidemiologist Chris Beyrer of the Johns Hopkins Bloomberg School of Public Health in Baltimore, Maryland.

Cultures, geographies, economies, and governments shape AIDS epidemics, and each country faces unique challenges in trying to slow viral spread and help the infected. Indonesia has more infected people than any other country in Asia and the Pacific, except India and China. Papua New Guinea has an unusually large heterosexual epidemic for the region, while Malaysia is grappling with a startling rise in prevalence in men who have sex with men. Even Australia has seen a modest, but steady, rise in new infections (see p. 157).

In all four countries, turning knowledge into action is easier said than done. But the stakes could not be higher now that research has led to increasingly effective tools capable of blunting epidemics and, if forcefully applied, even bringing them to a halt.

As editorial content in this issue further explains, critical questions remain about how to develop even more effective responses against HIV. Debates over the best vaccine strategies continue (see Zolla-Pazner, p. 167), while preclinical studies explore prospects for eradicating the latent viral reservoir and curing the disease (see Barouch and Deeks, p. 169). Finally, researchers are grappling with how to describe the genuine progress against HIV without overselling it (see El-Sadr *et al.*, p. 166).

AIDS inpatients like Insio Henson (*left*) are still common in Papua New Guinea, but cases like Alistair Coia (*far right*), with HIV researcher Sharon Lewin, are a rarity in Australia.

PHOTOS: MALCOLM LINTON (2)

The Open Society Foundations provided a travel grant to correspondent Jon Cohen and photographer Malcolm Linton. All News stories written by Jon Cohen. This special issue has been edited by Leslie Roberts and Kristen Mueller.

Published by AAAS

HIV/AIDS in Australia and its neighbors

Diverse demographics and widely different responses shape unique epidemics in each country

HIV prevalence per 100,000 people, by country

Australia

22.5 million
Total population

31,000
HIV+

All HIV+
Treatment eligibility (CD4s)

19,000
On antiretrovirals

$421 million
Annual HIV/AIDS spending

27.4%
Intercourse before 15 years old

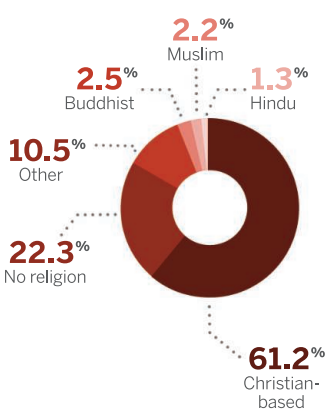

Papua New Guinea

6.5 million
Total population

31,945
HIV+

350
Treatment eligibility (CD4s)

13,905
On antiretrovirals

$44.8 million
Annual HIV/AIDS spending

11.1%
Intercourse before 15 years old

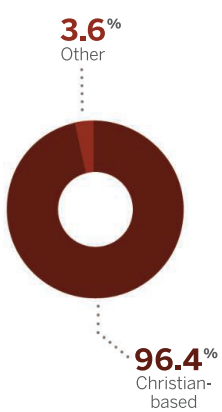

Indonesia

253 million
Total population

610,000
HIV+

350
Treatment eligibility (CD4s)

39,418
On antiretrovirals

$87 million
Annual HIV/AIDS spending

0.28%
Intercourse before 15 years old

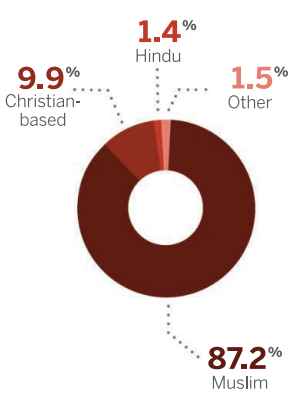

Malaysia

30.1 million
Total population

86,324
HIV+

<350
Treatment eligibility (CD4s)

17,369
On antiretrovirals

$56.5 million
Annual HIV/AIDS spending

1%
Intercourse before 15 years old

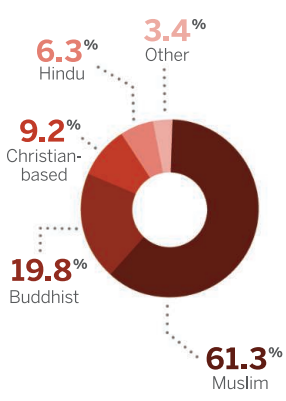

Source: UNAIDS, *HIV in Asia and the Pacific* (2013)/UNAIDS, *Global AIDS Response Progress Reporting* (2012 and 2014)/Indonesia Ministry of Health, *National AIDS Spending Assessment*/Papua New Guinea, CIA World Factbook

Published by AAAS

PHOTO: MICHAEL CLAYTON-JONES/*THE AGE*

AUSTRALIA

First, do harm reduction

Australia's aggressive efforts to stop HIV's spread via injecting drugs averted a catastrophe

Shortly after a test for HIV came to market in 1985, researchers at St. Vincent's Hospital in Sydney looked for the virus in 200 people receiving treatment for addiction to heroin and other injection drugs. At that point, the small but frightening AIDS epidemic was concentrated in gay men, and only one drug user tested positive. But a closer examination of this man's sexual and needle-sharing contacts, who were not in the initial study, told a more unsettling story: Four of six people tested had the virus. "That study was a real call to action," says Alex Wodak, director emeritus of the hospital's alcohol and drug service. "We knew that we had to do something quickly and what we did had to work."

Wodak convened a meeting of people who injected drugs and professionals who worked with them. "Everybody in the room had exactly the same focus and obsession," Wodak says. "We all wanted to stop the epidemic. And we were all prepared to do whatever it took." They collectively agreed on what was then a radical plan: They would launch needle and syringe exchange programs as widely as they could to provide clean equipment to users. This was in violation of the country's drug laws, but they so fervently believed in what today is called harm reduction that they decided to take the risk.

The program began in November 1986, and the police vice squad soon called in Wodak, the public face of the effort, for a grilling. "I spoke without pausing for breath and explained to them that this was a serious issue," Wodak recalls. He barraged the police with statistics about how quickly HIV can spread among people who inject drugs, infecting 50% of a needle-sharing population within 6 months and dramatically accelerating sexual spread. Contaminated needles and syringes, not drugs, transmit viruses, he stressed. A senior policeman then pulled Wodak aside and told him that they wouldn't be pressing charges. "I knew then that we had won," Wodak says.

Had they ever.

When it comes to HIV infections in people who inject drugs, "we have the most boring graph in the world," says epidemiologist John Kaldor of the Kirby Institute for Infection and Immunity in Society, a branch of the University of New South Wales in Sydney. In many of Australia's neighboring countries, including Indonesia and Malaysia, people who inject drugs account for a high percentage of infections. But in Australia, only 17 out of 3490 injecting drug users who received yearly HIV tests between 1995 and 2012 became infected, Kaldor and his colleagues reported in the 14 January issue of *AIDS*. The Kirby Institute's latest annual HIV surveillance report

> ***"We all wanted to stop the epidemic. And we were all prepared to do whatever it took."***
>
> **Alex Wodak,** St. Vincent's Hospital

Published by AAAS

Downloaded from www.sciencemag.org on July 11, 2014

Widespread distribution of needles and syringes worked.

IMAGE: AUSTRALIAN FEDERATION OF AIDS ORGANISATIONS/THE NATIONAL ASSOCIATION OF PEOPLE LIVING WITH HIV/AIDS

found that between 2008 and 2012, injecting drug use accounted for just 2% of new HIV diagnoses in Australia. Men having sex with men accounted for most new diagnoses (67%), followed by heterosexual sex (25%).

By 1987, the state of New South Wales endorsed needle and syringe programs, and in 1989, the first national HIV/AIDS strategy plan said this would be a key component of the country's response. Overall, needle and syringe programs had averted more than 57,000 HIV infections by 2009, according to Australia's Department of Health and Ageing. Between 2000 and 2009, the country's investment of just over US$200 million had saved US$1.2 billion in health care costs.

Today, Australia has more than 3000 sites that distribute some 30 million needles and syringes to drug users each year. The U.S. government, in contrast, bans funding of similar programs, although about 200 sites operate legally in various states. According to the U.S. Centers for Disease Control and Prevention, 16% of the people living with HIV in the country were infected by sharing needles and syringes.

Australia's early embrace of HIV harm reduction strategies was sparked in no small part by a "national psychodrama" that was playing out at the time, Wodak says: When the AIDS epidemic emerged in Australia, the prime minister's daughter was battling heroin addiction. Other factors entered in

The limits of success

Only 1253 people received an HIV diagnosis in Australia in 2012, a testament to nearly 3 decades of aggressive prevention efforts. But there's a troubling caveat: The number of new diagnoses jumped 10% from the preceding year, and cases have steadily risen since 1999. And 70% of the new infections occurred in men who have sex with men (MSM).

Every country in the world has struggled to slow the spread in MSM. But the growing problem in Australia has spotlighted the limitations of one of the most promising new prevention tools. A landmark 2011 study proved that if infected people faithfully took their antiretroviral (ARV) drugs and had undetectable viral levels on standard tests, the risk of transmission via heterosexual sex was nearly eliminated, falling by 96% (*Science*, 23 December 2011, p. 1628). Hopes soared that adding treatment as prevention to the arsenal of proven interventions could bring AIDS epidemics in communities to a halt.

Australia has universal health care and access to the latest ARVs, and most people who learn they are infected promptly start treatment. In a study published in the July 2012 issue of *PLOS Medicine*, epidemiologist David Wilson of the Kirby Institute for Infection and Immunity in Society in Sydney noted that as many as 75% of MSM in Australia reported taking an HIV test annually, and 70% of infected people received ARVs. In 90% of those, viral levels were fully suppressed. But that has not stopped the rise in new cases among MSM. "Why's there a disconnect with 'test and treat?' " asks David Cooper, who heads the Kirby Institute.

One possible answer is that treatment as prevention simply doesn't work as well with MSM. Anal intercourse has an 18-fold higher probability of transmitting HIV than vaginal intercourse, according to a 2010 study. MSM also tend to have more partners, increasing the odds that the virus will spread.

Wilson, a mathematical modeler and head of the Kirby's surveillance division, also notes that more treatment means more HIV-infected people

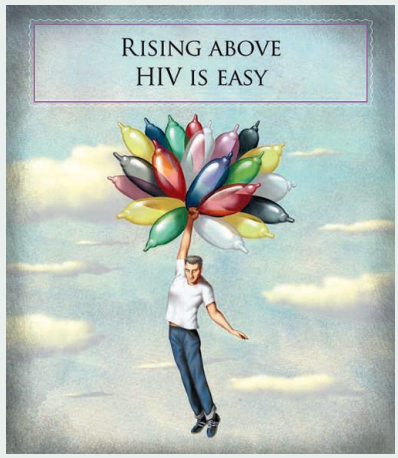

MSM-targeted Fear Less Live More poster.

survive who can potentially spread the infection, as some undoubtedly will remain infectious. Treated people may also engage in riskier behavior that, in a population sense, overwhelms the benefits of the drugs. And the virus is often transmitted by recently infected people who have yet to develop high enough antibody levels to be detected on standard tests.

Clearly, if every infected person took ARVs every day and had undetectable viral levels, transmission would likely plummet in MSM communities. But that's unrealistic. So Wilson and his team published a modeling exercise online on 7 February in *Sexual Health* that explored what it would take to lower new HIV infection rates in Australia's MSM population. The researchers looked at the impact of earlier detection of infection and initiation of treatment. But the factor that stood out most was the effect treatment has on transmission.

If ARVs indeed lower the risk of transmission in MSM by 96%—as much as it does in heterosexuals—then treating 90% of people would cut new infections by 55% in 5 years. On the other hand, if ARVs offer a mere 26% protection in MSM, the same scenario would avert a measly 9% of infections. "The jury is still out with regard to how much treatment decreases infectivity with male-to-male sex," Wilson says.

Even if it does work as well in MSM, which the Kirby Institute is now studying, the country still must substantially increase the number of people on ARVs—and it's notoriously difficult to improve on success. ■

Published by AAAS

as well. Neal Blewett, the minister of health, rallied bipartisan support for a strong HIV/AIDS response and included representatives from the drug-using community in the discussions. And Wodak believes that Australia's history as a British penal colony helped, too. "Convicts are practical people—they're not ideologues," he says.

The Australian government soon went beyond its support of needle and syringe programs, allowing a center to open in 2001, under the auspices of a church group, where users could inject drugs with clean equipment under medical supervision—without fear of prosecution. Located near a busy subway stop, the Sydney Medically Supervised Injecting Centre (MSIC) was the first facility of its kind outside of a few European countries, and the feedback from clients has been overwhelmingly positive, says the center's medical director, Marianne Jauncey. "The single starkest, most commonly repeated phrase is, 'Thank you for treating me like a human being,' " Jauncey says.

Marianne Jauncey, a physician, oversees an injection center where people can fix in a safe environment.

A series of independent reviews has found that MSIC has delivered on its promise. The latest, published by the accounting firm KPMG in 2010, found that the center had supervised more than 600,000 injections, referring about one-third of its clients to drug treatment. It managed nearly 3500 overdoses without a single death and saved the health system some US$600,000 per year. Since the site's opening, HIV infection rates have dropped in the nearby neighborhoods, although the review did not have enough data to link MSIC to the decline.

Australia's harm reduction effort has had its limits, which the hepatitis C virus (HCV) spotlights. HCV is transmitted by needle and syringe sharing much more easily than HIV is, and it was already widespread when harm reduction efforts began for HIV. According to Department of Health and Ageing estimates, this liver-damaging virus had infected more than 80,000 people by 1986. That number grew to 200,000 by 2000, despite needle and syringe programs. Yet, without those programs, the country would have faced a much larger HCV epidemic: The health department estimates that they prevented more than 100,000 new HCV infections.

Harm reduction programs for both HIV and HCV also overlooked some marginalized populations for a time. A study published in the October 2006 issue of *Addiction* found few services were available for "ethnic minorities"—a group that included indigenous Australians and immigrants from Vietnam and other Southeast Asian countries—who injected drugs in Sydney and in less urban sites around New South Wales. "It was a harm reduction nightmare," says Lisa Maher, an epidemiologist at the Kirby Institute who led the study. Over 3 years, 31% of the ethnic minorities in the 368-person study became infected with HCV, a rate three times higher than seen in the non–ethnic minority group. Needle and syringe programs and the accompanying health services for people who inject drugs have since expanded to these communities.

VIDEO

Harm reduction in Australia, http://scim.ag/hiv2014.

Wodak stresses that harm reduction can only do what its name implies. "We're happy to make a bad problem less bad," Wodak says. "We don't have to eradicate the problem in order to feel that we've succeeded." ■

PAPUA NEW GUINEA

In PNG, the epidemic that wasn't

Data vacuum despite improved surveillance

A decade ago, the forecast for the island of New Guinea was dire. A heterosexual epidemic was set to explode, a team of leading international epidemiologists predicted in a report called *AIDS in Asia: Face the Facts*. They warned that "there is every indication that the island is facing an epidemic which resembles those seen in parts of sub-Saharan Africa." Papua New Guinea (PNG), which shares the island with Indonesia, structured its response to its epidemic based on those early predictions. But the bomb never went off.

To this day, PNG struggles to describe not only why those early predictions were so wide off the mark, but also the exact contours of the smaller, but still serious, epidemic the country is experiencing today. That confusion has come at a steep price, particularly when it comes to decisions about where to target prevention efforts. "It gives rise to a very unfocused program," says Stuart Watson, country coordinator in PNG for the Joint United Nations Programme on HIV/AIDS (UNAIDS). "We don't know exactly what we're responding to, and, as a result, we respond to everything."

Epidemiologists have long had good reason to fear a serious heterosexual epidemic in PNG. Reported condom use is low. Medically supervised circumcision, which protects heterosexual men from HIV, is rare. Sexual violence, in contrast, is rampant; a survey published in the October 2013 issue of *The Lancet Global Health* found that 40% of PNG men interviewed reported having raped a female "non-partner." One recent study in a highlands community and Port Moresby, the capital, found that more than 20% of the 154 people tested at sexual health clinics were infected with chlamydia or gonorrhea.

Early predictions suggested that by 2014, 10% of the adults in PNG would be infected with HIV. According to the PNG National Department of Health, the estimate of the adult prevalence today is 0.65%. Watson thinks that understates the true prevalence. "Ask most people cold-face if they believe those

PHOTO: MALCOLM LINTON

Published by AAAS

Angela Kelly-Hanku (*left*) with Jolyn Gane in an AIDS ward at Goroka General Hospital.

PHOTO: MALCOLM LINTON

figures: no," he says. But he believes the actual figure is well short of 10%.

"The epidemic in PNG doesn't make a lot of sense in some ways," says epidemiologist Andrew Vallely, who lives in Milne Bay province and works with both the PNG Institute of Medical Research (IMR) and the University of New South Wales (UNSW) in Sydney. "Why has HIV not taken off?"

In trying to gauge HIV prevalence in PNG, epidemiologists have had far more assumptions than hard data. Joanne Robinson, a strategic information adviser at UNAIDS in PNG, notes that from 1993 to 2001, the only official HIV prevalence data came from one antenatal clinic at the general hospital in Port Moresby. "They did have very high prevalence rates, but it wasn't representative of the rest of the country," Robinson says. Today, data come from 380 sites, and as surveillance has expanded to ever more remote, rural areas, the overall prevalence has dropped.

But the data still give an incomplete—if not outright misleading—picture. "Our estimates are based on extremely limited samples of the population to this day," Watson says. He notes that only 60% of pregnant women attend antenatal clinics and a mere 40% receive HIV tests. The government has not done systematic, large-scale studies of several "key populations" that often have high HIV prevalence: men who have sex with men (MSM), transgenders, and sex workers. A small study done in Port Moresby by IMR in 2010 did show extremely high HIV prevalence in people who sold sex, whether they were females (19%), males (8.8%), or transgender women (23.7%).

> ***"We don't know exactly what we're responding to, and, as a result, we respond to everything."***
>
> **Stuart Watson,** UNAIDS

Moreover, the epidemic is geographically patchy, with high heterosexual prevalence in some regions. As the PNG health department noted that year, just five of the country's 22 provinces, all in the highlands, accounted for 60% of reported HIV cases even though they have just 40% of the population. "PNG is now experiencing an epidemic concentrated in particular geographical locations and population groups," states an HIV/AIDS response progress report it filed in March with UNAIDS.

Such patchiness complicates surveillance. For one, it is hard to access many isolated communities on this island of steep volcanic mountains. To reach the highland town of Goroka from Port Moresby,

Published by AAAS

for example, requires either an expensive flight or a torturous 7-day hike. And the 800 different languages spoken on the island reflect cultural variation, including sexual practices that can affect transmission, such as polygamy and the age of initiation. "What you say about one place is not what you say about another place," says social anthropologist Angela Kelly-Hanku, who lives in Goroka and works on Vallely's team.

One surprising cultural factor that may have had a role in curbing the epidemic is traditional penile cutting. Several large-scale studies in Africa have shown that medical circumcision—which removes the entire foreskin under sterile conditions—reduces the risk of sexual transmission of HIV from women to men by about 60%. While medical circumcision is uncommon in Papua New Guinea, up to 70% of men in some communities report having had a traditional penile cut as a boy, a procedure that involves cutting different types of slits into the foreskin but not removing it.

VIDEOS

Circumcision practices in PNG, understanding HIV's scope in PNG, and HIV in a PNG picture house, http://scim.ag/hiv2014.

Following a recommendation from UNAIDS and the World Health Organization in 2007 that prevention programs in high-prevalence countries should incorporate male circumcision, PNG health officials became interested in launching a national program. With funding from the Australian government, Vallely's group collaborated on a 4-year study to gauge the procedure's acceptability and potential impact. What they found surprised them.

When the researchers assessed penile cutting around the country, the places that practiced it the most had the lowest HIV prevalence. "It may help explain why the epidemic looks as it does in PNG," Vallely says. "To be honest, we never imagined when we heard of these practices that this would be the result."

PHOTO: MALCOLM LINTON

Prevention, Papua New Guinea style

Early on a Friday evening in March in Kids Kona, one of the many villages tucked into the hills that surround the town of Goroka, some 75 people cram into a mud-floored hut with a corrugated tin roof and excitedly wait for the show to begin. This village cinema, or *haus piksa* in the local pidgin, has a generator that provides electricity—a rarity here in the country's Eastern Highlands province—and, of course, a screen, which in this case is an old TV set. The standing-room-only audience is so swept up by tonight's video that no one leaves when the generator cuts out, candles are lit, and someone has to make a trip to town for more fuel.

This is not *Rambo* or a rugby match, both of which are wildly popular in this country known by the shorthand PNG. The slick video, a University of Goroka production titled *One More Chance*, is part of an innovative campaign to prevent HIV's spread, which has hit some PNG communities hard (see main story, p. 158). It tells the story of Siparo Bangkoma, a local man whose complicated family life was turned upside down by HIV. Siparo became deathly ill from the virus, but he hid his infection from his two wives until the second wife became weak herself and confronted him. When he confessed, the ailing wife told the other. Both women discovered they, too, had become infected. Rage eventually gave way to acceptance, and the two mothers decided they would raise their children together, but agreed that Siparo would no longer have a physical relationship with the second wife.

Siparo is at the screening and speaks to the crowd when the video ends. "You can get HIV and you can live with it," he announces. "I'm happy because I can stand in front of you and talk out. In my country, many people feel ashamed. I'm not ashamed. God gave me one more chance. Make sure your children are educated. This is a true story. It's my life story. You have to change your attitude and thinking," he says.

"This is a way to do HIV prevention that's really true to PNG," says Angela Kelly-Hanku, an Australian social anthropologist who studies HIV/AIDS with the PNG Institute of Medical Research in Goroka, where she lives, and the University of New South Wales in Sydney. After the screening, Kelly-Hanku shows off a bottle of antiretroviral (ARV) drugs. "When you take the ARVs, it's like putting a gate around your garden," Kelly-Hanku says. "Now, the pigs can't go inside."

The student filmmakers who produced *One More Chance* have made four other HIV/AIDS videos as part of a project called Komuniti Tok Piksa. They target rural communities, which are missed by mass media campaigns and often have low levels of literacy, teaching people how HIV is spread, the importance of testing, and that lifesaving treatments exist. The stories are told in pidgin.

Verena Thomas, who leads the project, says the 110 screenings so far have all been well attended. Says Thomas: "People on the screen are the heroes, whether they're Rambos or Siparos." ■

Published by AAAS

In collaboration with colleagues in PNG, Vallely and co-workers are now conducting epidemiologic studies to see if the link holds up. At UNSW's Kirby Institute for Infection and Immunity in Society, another group is doing lab studies with foreskins from PNG to explore fundamental mechanistic questions: How does medical circumcision thwart HIV, and does traditional cutting have any impact (see sidebar, right)? Vallely says if traditional penile cutting does prove capable of lowering the risk of HIV infection, it may ultimately alter public health campaigns. "We don't want to stop something that prevents HIV from taking off in PNG," he says.

Watson maintains that confusion about the epidemic's contours and its drivers wastes precious resources. In 2012, most government spending went toward managing the response, not delivering services like prevention, treatment, and care. "We have a very top-heavy national response that gobbles up nearly 80% of the funding," he says, noting that the National AIDS Council employs more than 100 people.

The painful Catch-22 is that PNG is left with little money to improve surveillance and figure out how best to curtail its epidemic. "We don't have the resources for that because we're still responding to an epidemic we don't have," Watson says. ■

A crowd filled the *haus piksa* to watch an HIV/AIDS video.

PHOTO: THOMAS HOPE, NORTHWESTERN UNIVERSITY'S FEINBERG SCHOOL OF MEDICINE

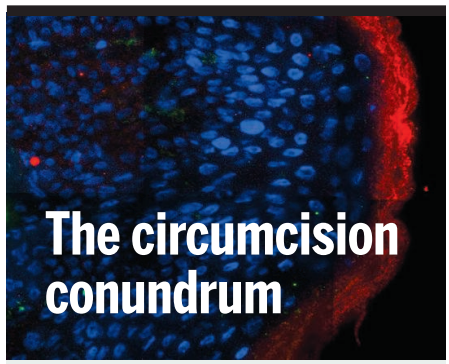

The circumcision conundrum

Stuart Turville had a surprising item to declare last September when he arrived here from Papua New Guinea (PNG) on a Friday evening flight: a cooler that contained five freshly harvested foreskins packed on ice. "Coming in with samples like this is always somewhat amusing to customs officials in Australia," says Turville, a virologist at the Kirby Institute for Infection and Immunity in Society in Sydney.

Turville's team regularly imports this precious cargo from its neighbor to answer a fundamental but underexplored question: How does male circumcision protect against HIV?

Studies have clearly shown that medical circumcision works, but confusion remains about the mechanism. Foreskins surgically removed from men in PNG who opt to go through medical circumcision offer an intriguing opportunity to address the question. Whereas some had fully intact foreskins, many had various traditional penile cuts as boys (see main story, p. 158).

Turville is leading lab studies that incubate these different foreskins with fluorescently labeled HIV (pictured). That allows researchers to assess how the transmission process is affected by factors that vary among the foreskins, including the degree of keratinization (in red) and the presence of immune target cells.

Surprisingly few groups have published studies about the protective mechanism of circumcision, says virologist Thomas Hope of Northwestern University's Feinberg School of Medicine in Chicago, Illinois, a veteran researcher of foreskins and HIV who has begun collaborating with the Kirby Institute group. "And a lot of it is wrong." ■

Published by AAAS

Islamic concerns complicate HIV/AIDS prevention efforts.

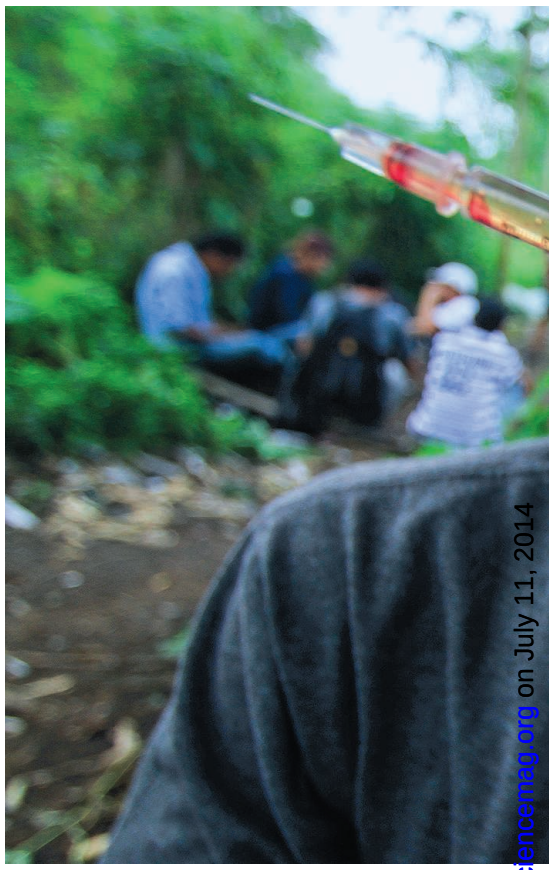

Downloaded from www.sciencemag.org on July 11, 2014

INDONESIA

A consummate insider pushes ideas from outside Indonesia

Sex and drugs rock Health Minister Mboi's reign

On 14 June 2012, Nafsiah Mboi's first day on the job as this country's minister of health, she announced a new campaign to distribute condoms to people at high risk of HIV infection. A loud uproar followed, leading Mboi—more commonly known by the honorific Ibu Naf—to post a YouTube video to explain that she was not advocating distributing condoms in high schools, as rumors had it.

Indonesia's HIV/AIDS politics are fiery—and Ibu Naf seems to like the heat. A pediatrician by training, Ibu Naf has had a prominent political life, first as the wife of the governor of East Nusa Tenggara province and then as a member of parliament for 5 years in the 1990s. She went on to do a stint in Geneva, Switzerland, at the World Health Organization as the director of gender and women's health, and in 2006, she was appointed secretary of Indonesia's National AIDS Commission. She held the job for 6 years before being tapped to serve as minister of health. In June 2013, the Global Fund to Fight AIDS, Tuberculosis and Malaria appointed her chair of its board.

VIDEO

Interview with Nafsiah Mboi, http://scim.ag/hiv2014.

Indonesia has a serious epidemic: New infections jumped 2.6-fold between 2001 and 2012, according to the Joint United Nations Programme on HIV/AIDS. The epidemic began mainly in injecting drug users, but today the highest spread occurs in men who have sex with men (MSM), sex workers and their clients, and transgenders. One exception is the two Indonesian provinces on New Guinea, which have a largely heterosexual epidemic that mirrors the one on the other side of the island in Papua New Guinea (see p. 158).

Ibu Naf has successfully lobbied for expanded access to antiretroviral drugs for HIV-infected people. She pushed through legislation that decriminalized drug use and allows government-run clinics to provide methadone and clean needles and syringes. Tuti Parwati Merati, a clinician who heads a nongovernmental organization (NGO) devoted to HIV/AIDS in Bali and also works at Udayana University in Denpasar there, says Ibu Naf "can pick the most difficult and make it happen."

Yet Ibu Naf acknowledges that serious problems remain. Police harassment of drug users continues, and the epidemic in MSM is largely ignored. *Science* spoke with Ibu Naf at her office in Jakarta about the country's response to HIV/AIDS and the challenges it faces. This interview has been edited for clarity and brevity.

Q: Reports long warned that HIV/AIDS would become a huge problem if you didn't ramp up harm reduction for people who inject drugs. Did this take too long?

A: For my taste, yes, but indeed the fight was not easy. When I became the secretary of the National AIDS Commission in 2006, we already knew that we had prevalence rates of more than 60% in several areas because of people who inject drugs. The first thing I did was invite everybody: the legal beagles, as well as people from the health sector, several ministries, the police, the narcotics boards, welfare, and said, "OK,

PHOTOS: (LEFT TO RIGHT) MALCOLM LINTON; SUTANTA ADITYA/AFP/GETTY IMAGES

Published by AAAS

Nafsiah Mboi pushed through harm reduction efforts.

what do we do? It is estimated that we have 330,000 kids injecting. Do we want to kill them or save them? If we don't do anything, if we keep fighting, they will die. They will die of AIDS. They will die of overdose. They will die of hepatitis. They will die in prison because they'll beat them in there. If we want to save them, we have to work together." There was silence. Total silence. But then I was very happy because it was the police who said, "Ibu, you're right. We have to save our kids. Actually, my son is a drug user and I don't know what to do."

Q: What happened?
A: First of all, I said, "The law says they're criminals and we should decriminalize them." We put a new regulation together, but it was very hard to convince the different ministers. So I invited our colleagues from Australia to do a cost analysis and presented that in front of all the ministers and said, "This is what it will cost us if they all get HIV infected and hepatitis." That was the thing that changed it.

Q: Did you have needle and syringe exchange right away or was that a battle also?
A: I knew that the NGOs had started it, but they were hiding under cover. It was illegal and if they were caught, they went to prison. But I'm very proud to say we have very courageous NGOs. These NGOs got together with the networks of people who inject drugs. And then the Global Fund provided the resources.

Q: The government accepted it?
A: Not always very happy, but we did it.

Q: When you became minister, you had to very quickly fight over condoms.
A: We've been fighting about condoms since the minute I came back from Geneva when I was secretary of the National AIDS Commission. As the minister it was different, you see. Here was an amoral minister of health who is promiscuous who wanted to distribute condoms to schoolchildren. So they demonstrated. I said, "OK, come in." So we talked and I gave them the data of sexual transmission, of housewives being infected and babies born. I said, "Look, what else can we do? You're religious leaders, and you have been telling them that they are not allowed to go to brothels or whatever, but I cannot do that. I'm just the minister of health. All I can do is prevent the transmission of the disease and I can only do that with condoms." Then they said, "Yeah but it's wrong if the government does it." And they said, "You have to beat them in public. Beat them to death. It's the Islamic Shariah." And I said, "But it's not in our law." So I said, "Let's agree to disagree. You do your work so that no man will ever go to brothels and no young person will ever have sex before marriage. I will do my work with those who engage in risky sex and tell them to wear condoms."

Q: You came from a Muslim background and converted to Catholicism. How do you view the Islamic community that challenges prevention interventions because they violate their moral tenets?
A: It has changed a lot actually. From the beginning, there was only a small group who were really aggressively looking at [HIV/AIDS] from the moral point of view. A lot of people actually knew that yes, what we were doing was the right thing to do. All they needed was somebody to be the—how do you call that?—the one to get the stones thrown at.

Q: They're still throwing stones at you. Muslim leaders attacked National Condom Week in December 2013, and the Health Ministry halted the annual event.
A: Yes, yes. But not as fiercely as before.

Q: One criticism is that the government hasn't spent enough on the MSM community. What do you think?
A: Yeah. It is because we believe that MSM can only be reached by their peers. It's not that I don't want to spend money. Unfortunately, there are still a lot of districts or provinces where this cannot be done by our local government. Once I had to basically fire the secretary of the local AIDS commission because he said, "Ibu, I will do anything you say, but don't ask me to work with men who have sex with men. It's against my conscience." And I said, "Then you cannot be the secretary of the local AIDS commission." MSM is still much hated in many areas in Indonesia, I'm sorry to say.

Q: Your supporters are worried about you getting kicked out of office with the elections coming up.
A: Most probably so, yes.

Q: Are you worried about whether there will be continuity?
A: I am, but the only thing I can do is strengthen my colleagues who will still be here, empowering them, as well as the NGO community. We have a strong NGO community, and they need a stronger voice in the government. And I can still do things from outside, I think. I may not be as powerful as the minister, but I can always say what I want. ■

Published by AAAS

Adeeba Kamarulzaman (*left*) talks the talk and walks the walk.

MALAYSIA

Malaysia tries to follow Australia's path

A top researcher and advocate pushes for change

In 1997, a year after Adeeba Kamarulzaman returned here with a medical degree from Australia and a specialty in infectious diseases, she spoke with the head of the Malaysian AIDS Council (MAC), Marina Mahathir, who was the daughter of the country's prime minister at the time. "I asked her, 'Do you have needle and syringe programs here?' " Kamarulzaman recalls. It was a pertinent question given that Malaysia had a budding epidemic in people who inject drugs—and Australia had all but derailed HIV with its harm reduction efforts (see p. 156). "She said, 'Are you kidding? We can barely say the word 'AIDS.' "

Kamarulzaman set out to change the HIV/AIDS response in Malaysia, a multiethnic country with a Muslim majority that has ultraconservative views on many social issues. "It was clear to me that this was crazy," Kamarulzaman says. "Patient after patient became infected by drug use and we weren't doing anything about it."

That's no longer true, thanks in part to her efforts, but Kamarulzaman, dean of the faculty of medicine here at the University of Malaya, still has serious misgivings about her country's approach to its HIV/AIDS epidemic. "We have done all right in terms of getting harm reduction programs off the ground, but even so, I think the coverage is still far from where we should be," she says. "And the real problems are now with prevention for MSM [men who have sex with men], transgenders, and sex workers. There's almost no kind of nationwide program to make any dent in the epidemic amongst these populations."

Kamarulzaman, who also attended high school in Australia and speaks English with a slight Aussie accent, is related to Malaysian royalty and can speak her mind with little fear of serious consequences. She continues to do so. "She makes a lot of enemies, particularly in government offices," says Hisham Hussein, who serves with her on the executive committee of MAC. "I can't see anyone in the country who can speak up like she can without fear or favor. No one. *No one*."

Kamarulzaman has published more than 100 studies of HIV/AIDS in Malaysia that look at everything from harm reduction efforts to the molecular epidemiology of viral spread to the efficacy of new treatments. She also has won passionate supporters in affected communities. "She's my idol," says Elisha Kor, an HIV-infected transgender woman who runs a program for sex workers at the PT Foundation, a nongovernmental organization (NGO) here that also helps MSM. "She brings a lot of opportunities to Malaysia, and opens the eyes of my government with HIV/AIDS issues."

Stopping the spread of HIV among injecting drug users was Kamarulzaman's first campaign. In 2003, she received a grant from the U.S. National Institutes of Health that set out to influence drug policy, which then heavily focused on punishment, by gathering comprehensive data about HIV and users who injected—and accounted for 76% of the infections. She also created a harm reduction working group with help from Australian experts. But their data did little to sway the National Anti-Drugs Agency and the police. "It became clear that we were not going to get anywhere until we got the attention of the politicians," Kamarulzaman says.

In January 2005, she secured a meeting with the Cabinet Committee

PHOTO: MALCOLM LINTON

Downloaded from www.sciencemag.org on July 11, 2014

Published by AAAS

on Drugs, which later approved a pilot project to convert injecting drug users to methadone. That June, the government, to Kamarulzaman's astonishment, announced it would also allow small-scale needle and syringe exchange. As these efforts grew, the government slowly moved away from a strictly punitive attitude toward drug users to a more compassionate view that they had health issues. Prisons began offering methadone maintenance programs. And in 2010, voluntary "cure and care" centers began to replace compulsory drug rehabilitation centers.

Harm reduction in Malaysia still faces many challenges, including excessively harsh drug laws. (Hanging remains a sentencing option even for marijuana.) The country relies mainly on NGOs to supply needles and syringes. But as Kamarulzaman wrote in a commentary in the 15 June 2013 issue of *The Lancet* titled "Fighting the HIV epidemic in the Islamic world," harm reduction advocacy in both Malaysia and Indonesia has succeeded in part because it has emphasized "Islamic values about the preservation of life."

Those same arguments, however, have not persuaded the government to confront sexual transmission. "It's a little bit more difficult to argue for sex work and MSM along those veins," she says. Indeed, Shariah law in some states can imprison Malay Muslims for simply cross-dressing.

To Pang Khee Teik, one of the country's few openly gay HIV/AIDS activists, the government's inaction toward the lesbian, gay, bisexual, and transgender (LGBT) community has strong political overtones. In two infamous trials known as Sodomy 1 and Sodomy 2, the government beginning in 1998 prosecuted a former deputy prime minister who was hoping to lead the country, Anwar Ibrahim, for allegedly having sex with men. "They see LGBT as a political force and this has to do with the targeting of Anwar Ibrahim," Teik says.

The Ministry of Health recognizes the problem; its recent report to the United Nations noted that in relatively small surveys of MSM, HIV prevalence had a "whopping increase from 3.9% to 12.6%" between 2009 and 2012. "New HIV infections via sexual transmission have outnumbered drug injection for the past 3 years," says MAC's Hussein. "And until today, the government has not done anything new, and they are fully aware of what is happening."

Kamarulzaman says the government "urgently" needs to address its shortcomings, but she takes the long view, saying, "Given where we were, I guess we have made a good start." ■

Kajang Prison offers methadone and specialized HIV care.

PHOTO: MALCOLM LINTON

Published by AAAS

OPINION

End of AIDS—Hype versus hope

Wafaa M. El-Sadr is the director of ICAP at Columbia University and a professor at the Mailman School of Public Health, Columbia University, New York, NY. E-mail: wme1@columbia.edu

Katherine Harripersaud is a staff member of ICAP at Columbia University, New York, NY.

Ronald Bayer is a professor at the Mailman School of Public Health, Columbia University, New York, NY.

Since 2001, HIV incidence has declined by 33% worldwide, and more than 9.7 million people with HIV have gained access to treatment.* The Joint United Nations Programme on HIV/AIDS launched the Getting to Zero strategy (2011–2015) that includes zero new infections, zero deaths from HIV, and zero discrimination. Aspirational statements such as "the end of AIDS" have also prevailed. However, do such pronouncements help or hurt? Do they motivate action, or do they risk incredulity, leading to inaction? Do such aspirations epitomize hype or hope?

The history of public health is replete with aspirational campaigns, with varying success. In 1971, the United States launched a "war on cancer," increasing funding for cancer research. Although great progress has been made in our understanding, diagnosis, and management of cancer, this war has not yet been won. With a few exceptions, cures are rare, disparities in cancer outcomes remain, and investments in research are in question. On the other hand, despite skepticism about eradicating smallpox, the World Health Organization began a campaign in 1958 that focused on vaccination, surveillance, and containment. Twenty years later, smallpox was successfully eradicated.

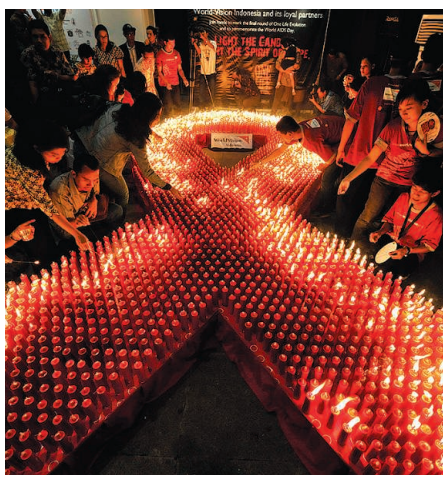

"a world without epidemic AIDS...Let this be the rallying call."

As for HIV, there are certainly reasons to be optimistic. Many countries with high HIV prevalence have scaled up programs for preventing mother-to-child transmission, and new pediatric infections are rare in several countries. Changes in therapy include earlier initiation of antiretroviral therapy (ART) and the treatment of pregnant HIV-infected women for life. These approaches have the potential to provide individual benefit to those living with HIV and prevent further HIV transmission. Additionally, new investments in health systems offer a foundation on which prevention and treatment services can be expanded further. However, implying imminent success may be perceived as minimizing the challenges that remain, resulting in the withdrawal of resources and a consequent resurgence of the presumed "controlled" disease. This risk is particularly relevant, because HIV expenditures are currently well short of the annual global target of U.S. $22 billion to $24 billion. Donor complacency would have catastrophic consequences.

Historically, some earlier optimistic predictions related to HIV have not met with success. These include the announcement in 1984 that an AIDS vaccine was forthcoming and early hope that ART would eradicate HIV infection. The potential of ART to control the HIV epidemic through a "test and treat" approach faces stark realities. Only 33.6% of women and 17.2% of men in low- and middle-income countries, and 34% of those eligible for treatment, have access to it,† and gaps in the HIV care continuum limit the potential of such an approach. Additionally, although overall incidence has declined, new infection rates among people who inject drugs, men who have sex with men, and young women in southern Africa are alarming. Several high-burden countries lag behind in expanding programs for preventing mother-to-child transmission, and the uptake of other prevention methods remains limited. Disappointingly, progress toward an efficacious vaccine—a critically needed intervention—has faltered, and although there is intense interest in finding a cure, scalable interventions are far from reality.

Why then have some scientists and advocates trumpeted the goal of an "end of AIDS"? We perceive that they are haunted by the fear of donor fatigue and a loss of momentum in the face of recognized challenges. However, despite these concerns, we believe that with concerted efforts and sustained commitments, we can make substantial advances toward the hope of a world in which AIDS is no longer an epidemic threat. The campaign against smallpox offers important lessons learned on how it is possible to maintain efforts despite many naysayers. Envisioning a world without epidemic AIDS is a deeply profound concept. Let this be the rallying call.

– Wafaa M. El-Sadr, Katherine Harripersaud, Ronald Bayer

*UNAIDS, *Global Report: UNAIDS Report on the Global AIDS Epidemic 2013* (UNAIDS, Geneva, Switzerland, 2013).
†WHO, UNICEF, UNAIDS, *Towards Universal Access: Scaling Up Priority HIV/AIDS Interventions in the Health Sector. Progress Report 2010* (WHO, UNICEF, and UNAIDS, Geneva, Switzerland, 2010).

10.1126/science.1255795

PHOTO: AFP/GETTY IMAGES/ADEK BERRY

Downloaded from www.sciencemag.org on July 11, 2014

Published by AAAS

PERSPECTIVE

A critical question for HIV vaccine development: Which antibodies to induce?

Susan Zolla-Pazner[1,2]

A vaccine against HIV-1 must prevent infection against genetically diverse virus strains. Two approaches are currently being pursued to elicit antibody-mediated protection: vaccines that induce potent and broadly reactive neutralizing antibodies (bnAbs) or vaccines that induce "conventional antibodies," which are less potent and broadly neutralizing in comparison. Although bnAbs may provide the greatest level of protection, their structural and genetic characteristics make their elicitation through vaccination a major challenge. In contrast, conventional HIV-1 antibodies have been induced by vaccination and correlated with reduced HIV-1 infection in a phase III vaccine trial. Here, I present evidence that both approaches should be pursued with equal vigor.

A major goal of HIV vaccine design is to elicit a protective immune response mediated primarily by antibodies (Abs). This is particularly challenging in the case of HIV because the virus mutates rapidly, leading to many viral subgroups. A successful vaccine would therefore need to elicit Abs that are able to recognize a range of genetically diverse strains.

[1]New York Veterans Affairs Harbor Healthcare System, New York, NY 10010, USA. [2]New York University School of Medicine, New York, NY 10016, USA.
E-mail: zollas01@med.nyu.edu

Although HIV infection induces a vigorous Ab response in nearly all infected individuals, only ~1% produce Abs that can neutralize a wide range of HIV subtype Abs (*1*) , and only ~10 to 25% of HIV-infected subjects produce cross-neutralizing Ab responses with moderate breadth and potency. The majority of infected individuals make "conventional Abs" that have limited breadth and potency in standard neutralization assays (*2*, *3*). Many vaccine candidates tested to date produce these conventional Abs, but none have yet induced broadly reactive neutralizing antibodies (bnAbs). A comparison of some of the characteristics of conventional and bnAbs is shown in Table 1. A great deal of effort and funding currently supports the design of vaccine regimens that will elicit these exceptional bnAbs, because it is thought that such a vaccine would induce high levels of protection. However, extensive data suggest that vaccine-induced conventional Abs may provide a level of protection that could have a considerable impact on the epidemic.

Many factors contribute to the rarity of bnAbs in patients and the difficulty of inducing them by vaccination: (i) the epitopes they target are poorly immunogenic; (ii) bnAbs are characterized by extensive somatic hypermutation (*4*, *5*); (iii) bnAbs are often polyreactive and/or autoreactive (*6*, *7*); (iv) bnAbs display unusual structural characteristics in their antigen binding region (*8*–*10*); and (v) bnAbs take months to years to evolve in response to virus evolution within the host (*11*–*13*). Since their discovery, a critical question for HIV vaccine development has been whether to design vaccines that stimulate these exceptional bnAbs. This approach would represent a departure from previous vaccine strategies that elicit conventional Abs—i.e., Abs that are normally induced by infection or vaccines that are not highly mutated from germline immunoglobulin genes and do not display unusual structural or genetic characteristics (*14*, *15*). Therefore, the induction of exceptional bnAbs through vaccination is a new and major challenge. Although this approach has not been attempted previously, there is a general consensus that a set of immunogens will be needed to "guide" the immune system through the complex process of affinity maturation (*16*). This lineage-based approach to vaccine design is based on the hypothesis that it will be necessary to initiate immunization with

Table 1. Comparison of conventional and exceptional broadly neutralizing antibodies.

Characteristics	Conventional antibodies	Exceptional broadly neutralizing antibodies
Neutralizing potency in vitro		
Tier 1 pseudoviruses	<0.02 to >50 ug/ml (*57*) <0.04 to 26 ug/ml (*58*)	<<1 ug/ml
Tier 2 pseudoviruses	0.6 to >50 ug/ml (*57*) 15 to >50 ug/ml (*58*)	0.02 to 27 ug/ml (*62*–*64*)
Percentage VH chain somatic hypermutation from germline	1 to 12% (*59*, *60*)	17 to 48% (*16*, *62*, *65*)
Breadth of neutralization		
Tier 1 pseudoviruses	29 to 42% (*57*); 50 to 90% (*26*); 7 to 50% (*58*)	100%
Tier 2 pseudoviruses	1 to 4% (*57*) 0 to 9% (*58*)	72 to 100% (*62*, *65*–*67*)
Vaccine strategy required	Prime (ALVAC) + Boost (gp120) (*43*) Prime (DNA or pox vector) + Boost (gp120 protein) or recombinant protein alone (*61*) Prime (DNA) + Boost (epitope-scaffold protein immunogen) (*20*)	Starting with a bnAb, infer the full antibody lineage, including the unmutated ancestor and early intermediates and use their sequences as templates for the design of HIV-1 immunogens with high-affinity binding to design sequential immunogens to guide the Ab response to produce bnAbs.
Prevalence in infection	Present in virtually all infected individuals	1 to 25% (*1*–*3*)
Time needed to evolve	Weeks to months (*41*, *42*)	Months to years (*11*, *12*)

an antigen that stimulates an appropriate germline immunoglobulin gene and then boost with a series of immunogens recapitulating the evolution of the virus as it escapes from Ab-mediated immune pressure, thus steering B cell differentiation through mutational steps that are required in vivo for the production of bnAbs. Targeting of more than one epitope will likely be needed, given the mutation rate of HIV. Notably, there are currently no data demonstrating that this approach is feasible.

Simultaneously, there is a growing literature describing rationally designed vaccines that induce protective conventional Abs. This approach depends on identification of the epitopes recognized by protective conventional monoclonal Abs (mAbs) and the subsequent use of structural, bioinformatics, and molecular methods to design immunogens that will induce polyclonal Abs similar to the originally identified protective mAbs. This approach has led to the design of vaccine candidates against several pathogens (*17*, *18*), and epitope-scaffold immunogens have already been shown to successfully induce conventional cross-clade neutralizing Abs against HIV (*19*–*21*). Initially, conventional Abs were shown to be protective against HIV by demonstrating that chimpanzees could be protected by infusing the challenged animals with immunoglobulin G (IgG) from an HIV-infected chimpanzee (*22*). Subsequently, human mAbs, representing conventional Abs made by most chronically infected individuals, were shown to neutralize multiple lab-adapted and/or primary isolates in vitro (*23*–*29*), and two of these mAbs, specific for the third variable region (V3) of the HIV gp120 envelope glycoprotein, provided protection against heterologous HIV strains in relevant animal models (*30*, *31*). More than 90% of chronically infected HIV+ subjects make similar V3 Abs (*32*).

Unlike in many viral infections, HIV-infected individuals can become "superinfected" with a second HIV strain. This might suggest that Abs that develop in HIV patients are not protective. However, several studies suggest that Abs made in HIV-infected individuals do affect the rate of superinfection. For instance, superinfected individuals had lower levels of cross-protective and autologous neutralizing Abs than the nonsuperinfected case-controls (*33*, *34*). Although some studies are contradictory to these (*35*, *36*), and other data suggest that cytotoxic T lymphocytes are capable of imposing selective pressure on HIV (*37*), results from a recent adequately powered study demonstrated that a first HIV infection reduces the risk of a subsequent infection by ~50% in high-risk Kenyan women (*38*). Additional evidence for the protective role of Abs comes from studies of maternal-fetal transmission. Although not replicated universally, several studies showed lower transmission rates from infected pregnant women with high Ab titers or with high-affinity/avidity Abs to portions of the HIV-1 envelope glycoproteins (*39*).

These studies complement those showing that Abs commonly exert strong and rapid immune pressure on viruses in vivo. For instance, when serial plasma samples from patients with primary HIV infection were examined for neutralizing activity against autologous viruses, the plasma virus continually and rapidly evolved to escape neutralization (*40*, *41*). Moreover, as early as 2 weeks after seroconversion, very low titers of neutralizing Abs select for escape viruses in acutely infected patients (*42*). These studies indicate that Abs produced in the majority of patients can eliminate viruses bearing cognate antigenic determinants. If a vaccine were to produce a similar conventional polyclonal Ab response in uninfected individuals, it may be possible that most or all of an incoming virus inoculum could be eliminated by these Abs.

Additional support for the role of Abs in protection comes from the RV144 clinical vaccine trial in which subjects received four doses of a recombinant HIV–avian pox virus and two doses of gp120 proteins from two different HIV subtypes. An estimated vaccine efficacy of 31% was noted at 3 years of follow-up (*43*) and 60% at 1 year after immunization (*44*). Higher levels of IgG Abs specific for epitopes in the second variable loop (V2) and V3 region of gp120—Abs commonly found in HIV-infected individuals (*32*, *45*, *46*)—were significantly associated with the reduced rate of infection (*47*–*49*). Several independent studies have confirmed that Abs to V2 and V3 correlated with the reduced rate of infection noted in RV144 vaccine recipients (*48*, *50*–*52*).

There are, therefore, many lines of evidence that indicate that despite their reduced potency and breadth as compared to bnAbs, conventional Abs made by the majority of HIV-infected individuals may be able to prevent infection. Moreover, conventional Abs display additive and synergistic activity (*53*–*56*) that may explain the ability of polyclonal conventional Ab responses to reduce the risk of HIV-1 infection.

At this point, there are no definitive data demonstrating that either vaccine-induced conventional or exceptional Abs will result in protection from HIV infection in humans. The clearest indication comes from the data emanating from the RV144 vaccine trial (*47*, *48*, *50*–*52*), but, strong as these data are, there is as yet no absolute proof of the hypothesis that conventional Abs are protective in humans. Nor do such data exist for bnAbs. In addition, it is possible that vaccine-induced conventional Abs will need to be induced at higher titers than bnAbs and may not protect against as many strains. The data do suggest that conventional Abs may be more feasible to induce, whereas bnAbs may ultimately be more effective. Therefore, both approaches have their strengths and weaknesses, and both must be pursued with equal vigor.

REFERENCES AND NOTES

1. M. D. Simek *et al.*, *J. Virol.* **83**, 7337–7348 (2009).
2. D. N. Sather *et al.*, *J. Virol.* **83**, 757–769 (2009).
3. Y. Li *et al.*, *J. Virol.* **83**, 1045–1059 (2009).
4. D. Sok *et al.*, *PLOS Pathog.* **9**, e1003754 (2013).
5. F. Klein *et al.*, *Cell* **153**, 126–138 (2013).
6. B. F. Haynes *et al.*, *Science* **308**, 1906–1908 (2005).
7. H. Mouquet *et al.*, *Nature* **467**, 591–595 (2010).
8. R. Pejchal *et al.*, *Proc. Natl. Acad. Sci. U.S.A.* **107**, 11483–11488 (2010).
9. A. P. West Jr. *et al.*, *Cell* **156**, 633–648 (2014).
10. B. F. Haynes, L. Verkoczy, *Science* **344**, 588–589 (2014).
11. M. Bonsignori *et al.*, *J. Virol.* **85**, 9998–10009 (2011).
12. P. L. Moore *et al.*, *J. Virol.* **87**, 4882–4894 (2013).
13. H. X. Liao *et al.*NISC Comparative Sequencing Program, *Nature* **496**, 469–476 (2013).
14. J. B. Robbins, R. Schneerson, S. C. Szu, *J. Infect. Dis.* **171**, 1387–1398 (1995).
15. S. A. Plotkin, *Clin. Infect. Dis.* **47**, 401–409 (2008).
16. J. R. Mascola, B. F. Haynes, *Immunol. Rev.* **254**, 225–244 (2013).
17. B. E. Correia *et al.*, *Nature* **507**, 201–206 (2014).
18. I. Delany, R. Rappuoli, K. L. Seib, *Cold Spring Harb Perspect Med* **3**, a012476 (2013).
19. M. Totrov *et al.*, *Virology* **405**, 513–523 (2010).
20. S. Zolla-Pazner *et al.*, *J. Virol.* **85**, 9887–9898 (2011).
21. S. Bhattacharyya *et al.*, *J. Biol. Chem.* **288**, 9815–9825 (2013).
22. E. A. Emini *et al.*, *J. Virol.* **64**, 3674–3678 (1990).
23. A. J. Conley *et al.*, *J. Virol.* **68**, 6994–7000 (1994).
24. M. K. Gorny *et al.*, *J. Virol.* **66**, 7538–7542 (1992).
25. M. K. Gorny *et al.*, *J. Virol.* **76**, 9035–9045 (2002).
26. C. E. Hioe *et al.*, *PLOS ONE* **5**, e10254 (2010).
27. D. Corti *et al.*, *PLOS ONE* **5**, e8805 (2010).
28. F. Klein *et al.*, *J. Exp. Med.* **209**, 1469–1479 (2012).
29. H. Mouquet *et al.*, *PLOS ONE* **6**, e24078 (2011).
30. J. D. Watkins *et al.*, *PLOS ONE* **6**, e18207 (2011).
31. L. Andrus *et al.*, *J. Infect. Dis.* **177**, 889–897 (1998).
32. S. Zolla-Pazner, *Hum. Antibodies* **14**, 69–72 (2005).
33. D. M. Smith *et al.*, *Virology* **355**, 1–5 (2006).
34. D. Basu *et al.*, *Retrovirology* **9**, 76 (2012).
35. C. A. Blish *et al.*, *J. Virol.* **82**, 12094–12103 (2008).
36. D. N. Forthal *et al.*, *J. Acquir. Immune Defic. Syndr.* **63**, 31–33 (2013).
37. J. F. Salazar-Gonzalez *et al.*, *J. Exp. Med.* **206**, 1273–1289 (2009).
38. K. Ronen *et al.*, *PLOS Pathog.* **9**, e1003593 (2013).
39. J. S. Lambert *et al.*, *J. Infect. Dis.* **175**, 283–291 (1997).
40. D. D. Richman, T. Wrin, S. J. Little, C. J. Petropoulos, *Proc. Natl. Acad. Sci. U.S.A.* **100**, 4144–4149 (2003).
41. X. Wei *et al.*, *Nature* **422**, 307–312 (2003).
42. K. J. Bar *et al.*, *PLOS Pathog.* **8**, e1002721 (2012).
43. S. Rerks-Ngarm *et al.*, *N. Engl. J. Med.* **361**, 2209–2220 (2009).
44. M. L. Robb *et al.*, *Lancet Infect. Dis.* **12**, 531–537 (2012).
45. Z. R. Israel, M. K. Gorny, C. Palmer, J. A. McKeating, S. Zolla-Pazner, *AIDS* **11**, 128–130 (1997).
46. M. K. Gorny *et al.*, *Virology* **427**, 198–207 (2012).
47. B. F. Haynes *et al.*, *N. Engl. J. Med.* **366**, 1275–1286 (2012).
48. S. Zolla-Pazner *et al.*, *PLOS ONE* **8**, e53629 (2013).
49. R. Gottardo *et al.*, *PLOS ONE* **8**, e75665 (2013).
50. M. Rolland *et al.*, *Nature* **490**, 417–420 (2012).
51. N. L. Yates *et al.*, *Sci. Transl. Med.* **6**, 228ra39 (2014).
52. S. Zolla-Pazner *et al.*, *PLOS ONE* **9**, e87572 (2014).
53. F. Verrier, A. Nádas, M. K. Gorny, S. Zolla-Pazner, *J. Virol.* **75**, 9177–9186 (2001).
54. S. Vijh-Warrier, A. Pinter, W. J. Honnen, S. A. Tilley, *J. Virol.* **70**, 4466–4473 (1996).
55. J. R. Mascola *et al.*, *J. Virol.* **73**, 4009–4018 (1999).
56. J. Pollara *et al.*, *J. Virol.* **88**, 7715–7726 (2014).
57. M. S. Seaman *et al.*, *J. Virol.* **84**, 1439–1452 (2010).
58. L. Li *et al.*, *PLOS ONE* **7**, e39534 (2012).
59. M. A. Moody *et al.*, *PLOS ONE* **6**, e25797 (2011).
60. T. Tiller *et al.*, *Immunity* **26**, 205–213 (2007).
61. M. Vaine *et al.*, *PLOS ONE* **5**, e13916 (2010).
62. L. M. Walker *et al.*, *Science* **326**, 285–289 (2009).
63. I. S. Georgiev *et al.*, *J. Immunol.* **192**, 1100–1106 (2014).
64. J. F. Scheid *et al.*, *Science* **333**, 1633–1637 (2011).
65. T. Zhou *et al.*, *Science* **329**, 811–817 (2010).
66. M. Shingai *et al.*, *Nature* **503**, 277–280 (2013).
67. P. D. Kwong, J. R. Mascola, *Immunity* **37**, 412–425 (2012).

ACKNOWLEDGMENTS

This work was sponsored by funds from the Department of Veterans Affairs, Veterans Health Administration, Office of Research and Development, and grants from the National Institutes of Health (P01 AI 100151 and R01 HL59725).

27 May 2014; accepted 18 June 2014
10.1126/science.1256526

REVIEW

Immunologic strategies for HIV-1 remission and eradication

Dan H. Barouch[1,2] and Steven G. Deeks[3]

Antiretroviral therapy (ART) is able to suppress HIV-1 replication indefinitely in individuals who have access to these medications, are able to tolerate these drugs, and are motivated to take them daily for life. However, ART is not curative. HIV-1 persists indefinitely during ART as quiescent integrated DNA within memory CD4$^+$ T cells and perhaps other long-lived cellular reservoirs. In this Review, we discuss the role of the immune system in the establishment and maintenance of the latent HIV-1 reservoir. A detailed understanding of how the host immune system shapes the size and distribution of the viral reservoir should lead to the development of a new generation of immune-based therapeutics, which may eventually contribute to a curative intervention.

HIV-1 is a retrovirus that integrates into the host genome, primarily in memory CD4$^+$ T cells that can harbor latent, replication-competent HIV-1 DNA for many years (*1*–*3*). This latent HIV-1 reservoir is thought to be established during acute infection (*4*–*6*), although precisely when, where, and how the reservoir is seeded remains to be determined. The reservoir has a remarkably long half-life and is resistant to antiretroviral therapy (ART), resulting in lifelong infection and viral rebound in the vast majority of HIV-1–infected individuals when ART is discontinued (*6*, *7*). Major research efforts are currently under way to understand the biology of the viral reservoir, the mechanism of viral latency, and the potential of various therapeutic approaches to target the reservoir (Fig. 1). Recent data indicate that the size of the viral reservoir may in fact be substantially larger than previously anticipated, suggesting the profound scope of this challenge (*8*).

Role of the immune system in shaping and maintaining the viral reservoir

HIV-1 infection causes profound and often irreversible changes to the adaptive and innate immune system. In the absence of ART, CD4$^+$ T cells are progressively depleted, CD8$^+$ T cells are often expanded, and much of the immune system is chronically activated. Some of these abnormalities improve during long-term ART, but the immune system rarely returns to normal, and chronic inflammation persists despite ART. This state of heightened inflammation is driven by multiple factors, including HIV-1 production, irreversible loss of the mucosal integrity, exposure to gut microbes, and an excess burden of other pathogens such as cytomegalovirus (CMV). The implications of this chronic inflammatory state for overall health and the HIV-1 reservoir are the focus of intense investigation (*9*).

HIV-1 preferentially infects activated memory CD4$^+$ T cells that express the chemokine receptor CCR5, although resting CD4+ T cells, naïve CD4$^+$ T cells, and macrophages can also be infected. The majority of infected and activated CD4$^+$ T cells die quickly (*10*), but a small fraction revert to a resting state and persist indefinitely as the latent reservoir. Because ART blocks all or nearly all new infection events, the reservoir that exists at the time ART is initiated becomes the reservoir that persists for the life of the individual. This viral reservoir is maintained during ART by the long half-life of infected memory T cells, homeostatic proliferation of these cells (*11*, *12*), and perhaps low levels of cell-to-cell virus transfer (cryptic replication) (*13*). Recent studies suggest that the HIV-1 genome is often found integrated in host genes associated with cell growth (*14*), indicating that HIV-1 may promote its own persistence in part by promoting the continual expansion of latently infected cells (*15*, *16*).

The viral reservoir in peripheral blood exists predominantly in memory CD4$^+$ T cells endowed with regenerative potential, including memory stem cells and central memory cells (*11*, *17*). The reservoir also persists in potentially shorter-lived CD4$^+$ T effector cell populations, but whether these cells represent a stable reservoir or one that is constantly being regenerated via proliferation and differentiation is unknown. The distribution of the viral reservoir differs in tissues compared with blood, with the frequency of infection generally higher on a per-cell basis in lymphocyte-rich tissues such as peripheral lymph nodes, the ileum, and perhaps the spleen (*18*, *19*). The higher frequency of target cell infection in these tissues may reflect cell-to-cell virus spread (*20*) and/or the presence of other immune cells that contribute to the maintenance of latency (*21*).

In the absence of therapy, the frequency of activated T cells is associated with the level of viremia. During long-term suppressive ART, a similar albeit less consistent association

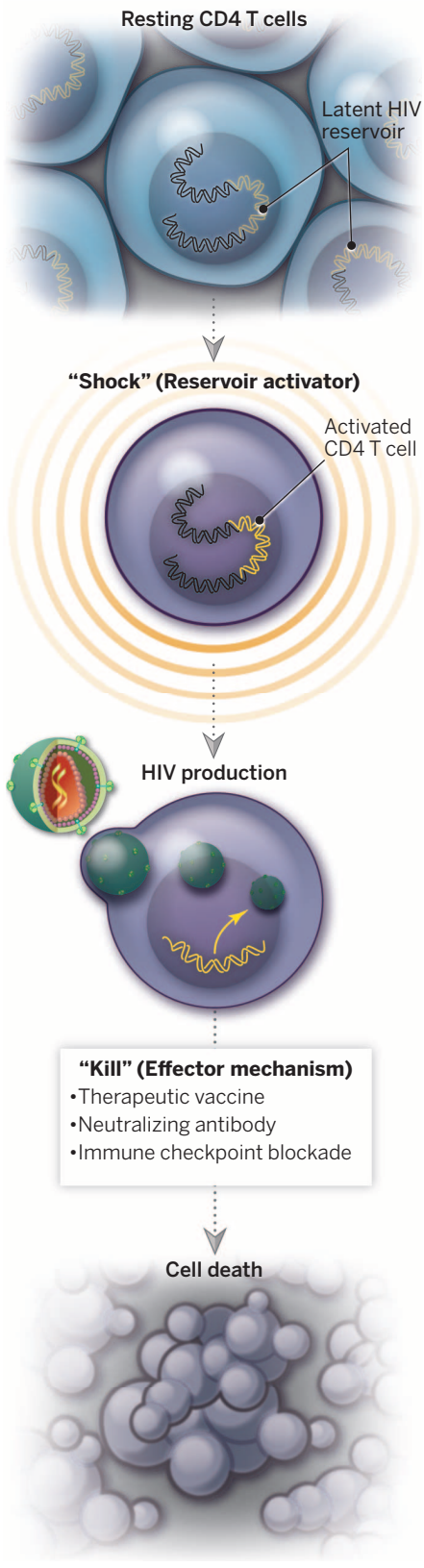

Fig. 1. "Shock and kill" strategies. Latent HIV-1 reservoirs in resting CD4$^+$ T cells can be activated ("shocked"), which might make them more susceptible to be eliminated ("killed") by immunologic effector mechanisms.

[1]Center for Virology and Vaccine Research, Beth Israel Deaconess Medical Center, Harvard Medical School, Boston, MA 02215, USA. [2]Ragon Institute of Massachusetts General Hospital (MGH), Massachusetts Institute of Technology, and Harvard University, Cambridge, MA 02139, USA. [3]University of California, San Francisco, San Francisco, CA 94110, USA. **E-mail: dbarouch@bidmc.harvard.edu (D.H.B.); sdeeks@php.ucsf.edu (S.G.D.)**

exists, with the frequency of activated $CD4^+$ T cells expressing human leukocyte antigen–DR (HLA-DR), CCR5, and programmed cell death protein-1 (PD-1) correlated with the frequency of cells containing HIV-1 RNA or DNA (*22*, *23*). The mechanism for this association is unknown but likely is bidirectional and multifactorial. Low levels of virus replication and/or production may lead to T cell activation. When stable ART is intensified with the addition of a potent HIV-1 integrase inhibitor, markers of low-level HIV-1 replication and inflammation decline at least in some individuals, indicating that replication persists during ART and triggers an inflammatory response (*13*, *24*).

Alternatively, an inflammatory immune environment may contribute to the persistence of the viral reservoir by a number of mechanisms (*25*). T cell activation promotes cell-to-cell virus transfer because activated cells are more likely to produce virus and to become infected. T cell receptor engagement by cognate antigen or cytokines [e.g., interleukin (IL)–7] stimulates $CD4^+$ T cell proliferation and the expansion of the infected cell population (*12*). $CD4^+$ T cell proliferation may in fact be the most important mechanism leading to the stability of the reservoir (Fig. 2) (*11*). A chronic inflammatory environment would also be expected to prevent the generation of optimal HIV-1–specific immune responses. Chronic inflammation stimulates potent and sustained immunoregulatory responses, including expansion of T regulatory cells and up-regulation of PD-1 and other negative regulators on effector cells (*11*, *26*). HIV-1–associated inflammation also stimulates the deposition of collagen in secondary lymphoid organs, which in turn leads to tissue fibrosis, persistent immunodeficiency, and poor host clearance mechanisms (*27*).

Understanding the complex virus-host interactions that lead to the establishment and maintenance of the latent HIV-1 reservoir will require advances in our fundamental understanding of T cell biology. How are memory $CD4^+$ T cells generated and maintained? What are the life spans of the various $CD4^+$ T cell subsets? How are the properties of T cells in the blood different from those in lymphoid tissues? How do the fates of $CD4^+$ T cells activated via cognate antigen differ from those stimulated to proliferate by homeostatic mechanisms? How do myeloid cells, including dendritic cells, contribute to the generation and maintenance of T cell memory and latency? How will inhibitors of the pathways that regulate T cell survival and function change the life span of individual cell types?

There are also a number of critical unanswered questions related to the immunology of HIV-1 persistence. Because the size, distribution, and stability of the viral reservoir during ART are determined in part by the host immune system, factors that influence immune function—including gender, ethnicity, chronic inflammatory diseases, chronic infectious diseases, obesity, and substance abuse—are all likely to have important but unknown effects on the viral reservoir. The age at which the virus is acquired and ART is initiated is also likely to be important. ART administered at 30 hours of age in a perinatally infected infant resulted in sustained remission and a possible cure (*28*), and the administration of ART in the first 3 months of life was associated with a sustained decay in the reservoir (*29*). Given that the development of memory $CD4^+$ T cell responses generally occurs after birth, perhaps limited by immunoregulatory responses (*30*), it is possible that seeding the viral reservoir may be less efficient in infants (*31*). This hypothesis remains a largely unexplored area of HIV-1 cure research.

The Berlin and Boston patients

Much of the enthusiasm for HIV-1 cure research is derived from the case of the "Berlin patient" (*32*). In 2007, an HIV-1–infected adult living in Berlin developed acute myelogenous leukemia and received an allogeneic hematopoietic stem cell transplant from a donor who carried a homozygous deletion of *CCR5*, which renders cells highly resistant to HIV-1 infection. The procedure worked, and the patient has appeared to be free of both cancer and HIV-1 for over 5 years (*33*). Despite intense efforts, this outcome has not yet been repeated. Finding suitable HLA-matched donors homozygous for the *CCR5* deletion is challenging, and the few transplants that have been performed have failed because of recurrence of the underlying cancer or emergence of CXCR4-tropic viruses. Nevertheless, this case has galvanized gene therapy efforts to modify $CD4^+$ T cells (*34*) and potentially also stem cells (*35*, *36*) to render them resistant to HIV-1 infection.

A related approach is to use ART to protect transplanted donor cells until full chimerism occurs. This strategy is illustrated by two cases of HIV-1–infected adults in Boston who received hematopoietic stem cell transplants for treatment of refractory lymphoma (*37*). Under the coverage of ART, full donor chimerism was apparently achieved, with the donor immune cells eventually replacing the original immune cells over a period of years. As that occurred, HIV-1 DNA gradually declined to undetectable levels. Therapy was then interrupted in both individuals. Virus failed to rebound within the first few weeks, leading to initial optimism that these individuals may have been cured. Unfortunately, virus then dramatically rebounded at weeks 12 and 32 after treatment interruption, indicating that the transplant caused a profound but incomplete elimination of the viral reservoir. This failure highlights the need either to eradicate all replication-competent virus or to enhance the capacity of the host immune system to contain the limited residual virus that may persist after a curative intervention. These observations also illustrate the limitation of our current biomarkers for HIV-1 persistence. The development and validation of a highly sensitive biomarker that can reliably detect and quantify the total body burden of replication-competent HIV-1 during ART is one of the highest current priorities of the field.

Comparing the outcomes of the Berlin and Boston cases is informative. Graft versus host disease (GVHD) occurred in all three cases and likely contributed to reductions of the viral reservoirs. As has been observed with beneficial graft-versus-tumor effects, alloreactive donor cells targeting hematopoietic cells likely reduced the number of recipient $CD4^+$ T cells harboring latent HIV-1. These cases have also led to increased interest in modifying host responses with immune-based therapeutics as part of a curative strategy (*38*). Assuming that the Berlin patient achieved a complete sterilizing cure and that ART was fully effective in the Boston cases, why was the virus eradicated only in the former case? One key difference in the transplant protocols was the extent of pretransplant myeloablation, which would be expected to reduce the size of the reservoir. The Berlin patient received an aggressive regimen of chemotherapy and total body irradiation, whereas a milder approach was used in the Boston cases. The Berlin patient also received more aggressive immunosuppressive therapies for GVHD, and, as outlined below, suppressing T cell activation and proliferation might result in further control of the reservoir.

"Shock and kill"

Hematopoietic stem cell transplantation is too risky and too complex for the majority of HIV-1–infected individuals worldwide. Other approaches that have generated considerable enthusiasm include pharmacologic strategies to induce latently infected cells to produce virus ("shock") together with interventions that would enhance the ability of the host to clear these virus-producing cells ("kill") (Fig. 1). Histone deacetylase (HDAC) inhibitors have been shown to increase production of HIV-1 RNA and, to a lesser degree, virus particles from the viral reservoir in vivo (*39*). However, the magnitude of the effect of HDAC inhibitors has to date been modest, and this class of drugs has not yet demonstrated a consistent effect on the frequency of cells that harbor replication-competent HIV-1 (*40*–*42*). Other classes of antilatency drugs and immunomodulators are therefore being explored for their capacity to stimulate the viral reservoir (*40*, *42*, *43*).

To augment the capacity of the host to eliminate reservoir cells after activation, several immunologic strategies are being explored. These strategies include therapeutic vaccines, monoclonal antibodies, and immune checkpoint inhibitors (Fig. 2).

Therapeutic vaccines

It is likely that a latency-reversing agent will need to be coupled with an immunologic strategy to clear virus-producing cells. One approach is to expand HIV-1–specific CD8+ T lymphocyte responses (*44*). As has been well-established in natural control of HIV-1 (i.e., "elite" control), potent $CD8^+$ T lymphocytes can control HIV-1 by selectively killing virus-producing cells (*45*). This concept has led to a renewed interest in therapeutic vaccines, namely the administration of candidate HIV-1 vaccines to HIV-1–infected individuals typically on suppressive ART, with the goal of augmenting virus-specific immune responses and either

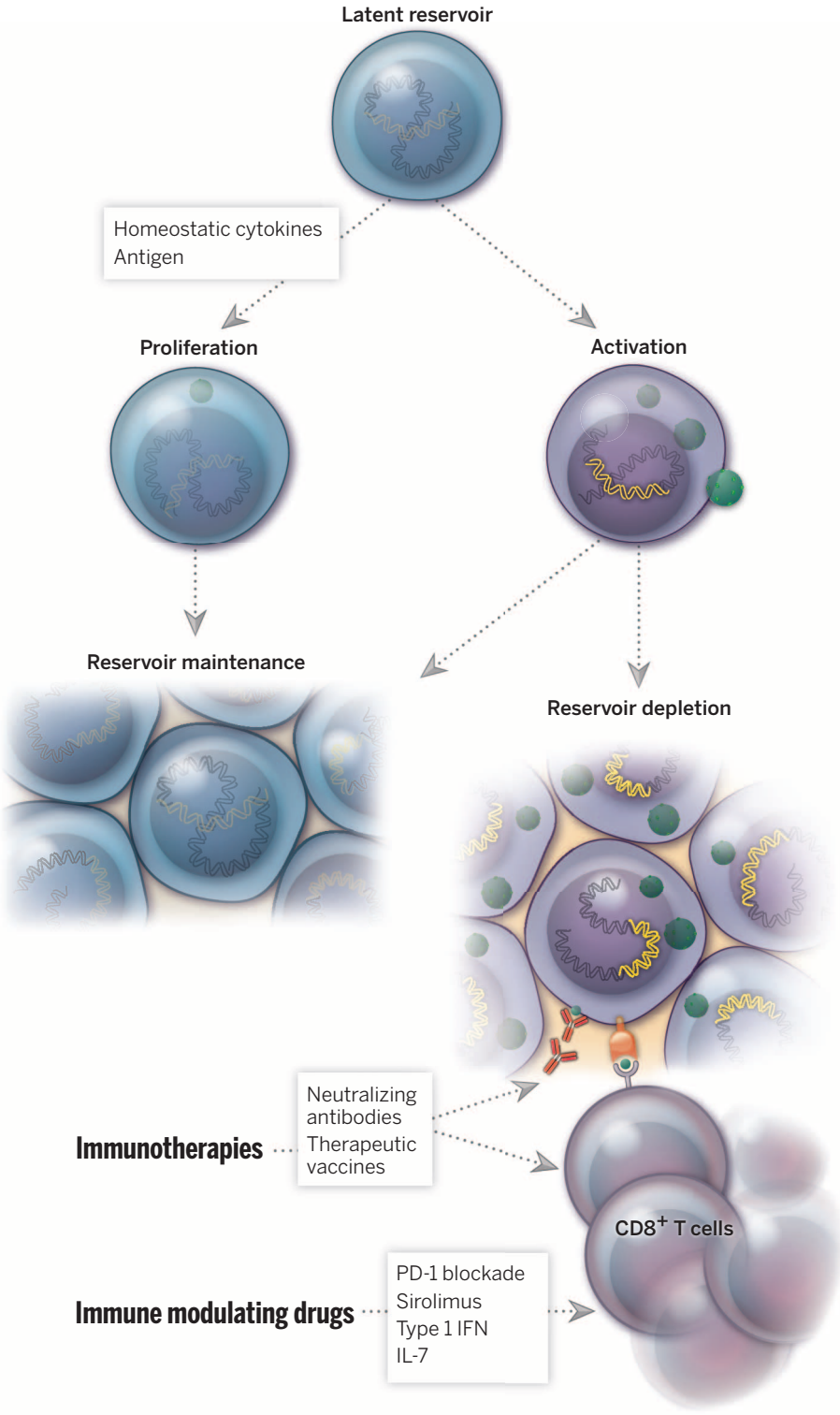

Fig. 2. Immunotherapeutic strategies. T cell proliferation and activation have complex effects on the size and distribution of the viral reservoir. Homeostatic cytokines and antigen-driven proliferation of T cells maintain a population of latently infected cells. Activation of T cells can either lead to virus production and virus spread (reservoir maintenance) or death of these cells because of virus-induced cytopathic effect or host clearance mechanisms (reservoir depletion). Therapies that alter the proliferation, maturation, activation, and effector functions of T cells could impact these processes. Immunotherapies, such as neutralizing antibodies and therapeutic vaccines, as well as immune modulating drugs, such as PD-1 inhibitors, sirolimus, type I interferon (IFN), and IL-7, may lead to reservoir depletion.

accelerating the decay of the reservoir during ART or improving the control of viral rebound after interruption of ART. Several therapeutic vaccines have been evaluated in HIV-1–infected subjects, including vector-based vaccines that express HIV-1 antigens from harmless or attenuated viruses such as canary pox (ALVAC) or adenovirus serotype 5 (Ad5), as well as plasmid DNA vaccines (*46*–*51*). Although these vaccines generally proved immunogenic, most therapeutic vaccines have to date failed to show virologic or clinical benefit, and a few have suggested harm, potentially as a result of increasing immune activation. Infusion of antigen-pulsed autologous dendritic cells has shown potentially greater promise but requires confirmation (*52*).

Most of these early-generation therapeutic vaccines involved relatively weak or suboptimal immunogens. Moreover, as was demonstrated in a study of DNA priming followed by Ad5 boosting, these therapeutic vaccines typically expand preexisting T cell clones, which by definition had already failed to control virus replication before ART (*53*), either because they were dysfunctional or because they selected for a virus population containing $CD8^+$ T cell escape mutations. A successful therapeutic vaccine would ideally induce functional $CD8^+$ T cells specific for novel HIV-1 epitopes. The next generation of therapeutic vaccines will also likely be combined with reservoir-activating agents.

Several novel therapeutic vaccines may be evaluated in clinical trials over the next several years. Such strategies include CMV vectors; Ad26 prime, modified vaccinia Ankara (MVA) boost regimens; and lymph node–targeted amphiphilic peptide vaccines. Prophylactic vaccination with CMV vectors has been shown to result in the induction of broad cellular immune responses against novel epitopes and apparent clearance of a stringent challenge with simian immunodeficiency virus (SIV) in about half of vaccinated rhesus monkeys (*54*–*56*). The persistently replicative nature of CMV vectors is likely critical for the highly functional effector memory T cells that appear to persist indefinitely. Moreover, the ability of CMV vectors to induce unconventional class II–restricted $CD8^+$ T cell responses provides a potentially important benefit because they target novel epitopes that likely were not previously subject to immune selection pressure (*56*). Clinical development of CMV vectors will presumably require attenuated vectors, and manufacturing and regulatory issues for CMV vectors remain to be determined.

Another therapeutic vaccine platform that will likely be evaluated in clinical trials involves Ad26 vectors. Prophylactic vaccination with Ad26-based prime-boost vaccine regimens, such as priming with Ad26 and boosting with the pox virus MVA, has proven highly immunogenic and has afforded partial protection against acquisition of infection as well as reduced setpoint viral loads after stringent SIV challenges in rhesus monkeys (*57*, *58*). Ad26 has several advantages over Ad5 as a vaccine vector, including the induction of different innate immune profiles that may reduce undesirable inflammatory responses and result in more

functional T cell phenotypes. Moreover, Ad26-based prime-boost regimens have demonstrated partial protective efficacy in the stringent rhesus monkey challenge models in which Ad5-based regimens have failed (*57*–*59*), suggesting their potential for greater clinical utility.

Use of amphiphilic peptides, which have been shown to target antigen to lymph nodes and aim to induce cellular immune responses simultaneously to two or more coevolving regions of immunologic vulnerability of HIV-1, is another potential therapeutic vaccine strategy (*60*, *61*). The extent to which these and other next-generation vaccine candidates will afford therapeutic efficacy in preclinical and clinical studies remains to be determined.

Broadly neutralizing monoclonal antibodies

Potent broadly neutralizing HIV-1–specific monoclonal antibodies (mAbs) are also being explored as a potential HIV-1 eradication strategy. Prior studies using the earlier generation of neutralizing mAbs were generally unsuccessful in both preclinical and clinical studies (*62*–*64*), but the identification of a new generation of mAbs with improved potency and breadth has led to a resurgence of interest in this approach. In particular, two studies in rhesus monkeys demonstrated that infusion of mAb cocktails, as well as certain individual mAbs, in chronically SHIV-infected rhesus monkeys resulted in substantial, albeit transient, suppression of viremia (*65*, *66*), building on previous studies in humanized mice (*67*). Moreover, a subset of animals with the lowest starting viral loads did not exhibit viral rebound even after mAb titers declined to undetectable levels, suggesting the potential for a durable therapeutic effect in certain circumstances (*65*). Infusion of one particular mAb, PGT121, resulted in not only rapid and profound suppression of plasma viral RNA but also substantial reductions of proviral DNA in peripheral blood, lymph nodes, and gastrointestinal mucosa (*65*). These data suggest that certain mAbs may be able to target virus-infected cells in tissues, although it remains to be determined whether these mAbs can impact the viral reservoir.

A growing number of potent and broadly neutralizing mAbs now exist that target various epitopes on the HIV-1 envelope protein. However, a central question for HIV-1 eradication strategies is whether mAbs will be able to target the viral reservoir and clear virally infected cells, potentially via Fc-mediated mechanisms such as antibody-dependent cellular cytotoxicity or antibody-dependent cell-mediated virus inhibition. Another possibility is that direct neutralization of free virions will reduce chronic antigen stimulation and augment the functionality of host virus-specific T cell responses, resulting in improved virologic control. Supporting this latter possibility is the observation that, after PGT121 infusion in SHIV-infected rhesus monkeys, HIV-1 Gag–specific T cells exhibited decreased activation and exhaustion and improved capacity to suppress virus replication in vitro (*65*). A potential caveat regarding broadly neutralizing mAbs is their limited accessibility to certain anatomic reservoir sites, such as the central nervous system.

Immune checkpoint blockade

Another potential strategy to augment host immune control involves the blockade of immune checkpoint molecules. Activated T cells express a series of receptors that when engaged by their ligands result in suppression of function and return to a nonactivated state. The best-characterized immune checkpoint molecule is PD-1, which is a marker of functional T cell exhaustion. The ligands for PD-1, PDL-1 and PDL-2, are widely expressed in tissues. Inhibitors of the PD-1 pathway restore T cell function and have shown efficacy in the cancer field (*68*). These inhibitors may also enhance the capacity of the host immune system to clear chronic viral infections. Indeed, a single dose of an antibody against PD-1 appeared to cure hepatitis C virus infection in a small subset of individuals (*69*). It is thought that inhibitors of other immune checkpoint molecules (such as CTLA-4, LAG-3, TIM-3, TIGIT, and 2B4) may also prove effective.

PD-1 inhibitors and other checkpoint blockers may also have direct effects on the establishment and maintenance of the viral reservoir (*11*). Because activated cells are more likely to become infected than resting cells, previously activated cells—including those expressing PD-1—might be expected to be enriched for HIV-1 (*11*). Indeed, the size of the reservoir is positively correlated with the frequency of PD-1–expressing cells (*11*, *22*), and HIV-1 is enriched in PD-1–expressing memory cells (*11*). Clinical trials of PD-1 inhibitors in treated HIV-1 disease have been initiated.

Immune-modulating drugs

After years of suppressive ART, the vast majority of the residual population of replication-competent virus resides in long-lived memory $CD4^+$ T cells. The estimated size of the reservoir during ART is directly associated with the frequency of activated and proliferating cells (*11*, *12*, *22*, *23*, *25*), and in some studies activated and proliferating cells also contain more HIV-1 (*11*, *70*). Therapeutic interventions that target T cell activation or proliferation may therefore impact the viral reservoir (Fig. 2).

T cell activation and proliferation are controlled by a number of signaling pathways, including those involving the mammalian target of rapamycin (mTOR), signal transducer and activator of transcription 5a (STAT5a), and forkhead box O3a (*71*). Specific inhibitors of these pathways might therefore reduce the size of the latent viral reservoir. For example, sirolimus (rapamycin) is a naturally occurring macrolide that inhibits mTOR, and as a consequence it blocks cell cycle progression from G_1 to S phase in activated T cells and reduces CCR5 expression (*72*). Sirolimus also enhances memory T cell formation in response to vaccines in preclinical studies (*73*). We performed a retrospective analysis of ART-treated HIV-1–infected kidney transplant recipients who received sirolimus or non–mTOR-targeting drugs to prevent graft rejection. Only treatment with sirolimus was temporally associated with lower levels of cell-associated HIV-1 DNA (*74*), suggesting that mTOR inhibition may prove useful in a combination eradication strategy. A prospective clinical trial is being developed to evaluate this concept further. Other drugs that limit T cell activation, including those that inhibit the Janus kinase/STAT pathway (*75*), are also being developed. Because chronic inflammation may contribute to excess morbidity in ART-suppressed, HIV-1–infected individuals (*9*), a number of therapies that target the inflammatory pathways are being developed as adjuncts to therapy (e.g., methotrexate, antifibrotic drugs, anti-CMV therapy, and a number of agents aimed at gut mucosa and microbial translocation). Measures of the viral reservoir are increasingly being incorporated into these studies.

The role of the type I interferon family of cytokines in the context of chronic viral infections is currently a focus of intense investigation and debate. An acute viral infection triggers immediate and potent type I interferon production by a variety of cells, leading to up-regulation of hundreds of genes (the interferon-stimulated genes) (*76*). In the context of chronic HIV-1 infection, persistent interferon signaling has been associated with increased CCR5 and PD-1 expression, up-regulation of indoleamine 2,3-dioxygenase and other inflammatory pathways, reduced thymopoieses, the generation of dysfunctional T cells, and altered T cell homeostasis (*77*–*80*). Higher levels of interferon signaling are also correlated with poor immune reconstitution (*80*, *81*). In murine models of chronic lymphocytic choriomeningitis virus (LCMV) infection, inhibition of type I interferon leads to decreased immune activation, decreased PD-1 and PD-L1 activity, decreased amounts of the immunomodulatory cytokine IL-10, restored lymphoid architecture, improved $CD4^+$ T cell responses, and ultimately enhanced viral clearance (*82*, *83*). Although chronic type I interferon stimulation might be harmful, supratherapeutic doses of type I interferon have also been shown to have sustained anti–HIV-1 effects in untreated chronic infection (*84*) and may affect reservoir size in treated disease (*85*). Proof-of-concept studies involving interferon-α and inhibitors of interferon-α are both planned.

As a result of the correlation between markers of T cell activation or dysfunction and the size of the viral reservoir, it is possible that immunosuppressive interventions may also contribute to a cure. It should be noted, however, that the most direct way to "shock" HIV-1 out of a state of latency may be nonspecific and potent activation of infected $CD4^+$ T cells (*40*, *86*–*87*). The first generation of HIV-1 eradication studies performed over a decade ago involved the use of antibodies against CD3 (*88*), which trigger T cell activation, but the inflammatory response proved too toxic to pursue. An ideal immune modifying regimen would reverse HIV-1 latency in a specific manner while preventing the negative consequences of T cell activation and T cell proliferation. Given the inherent complexity of the immune response and the fact that any immune-modifying

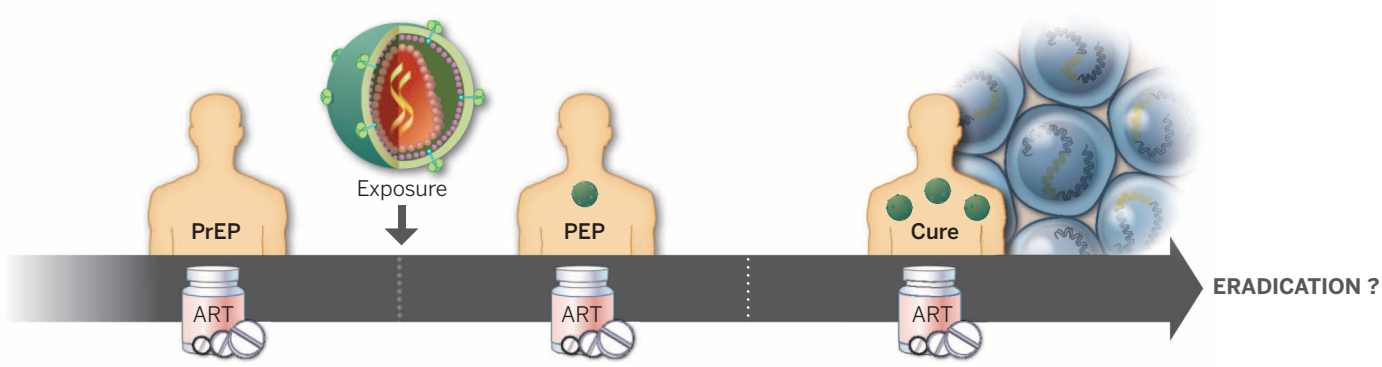

Fig. 3. PrEP/PEP/cure continuum. ART initiated before exposure is termed preexposure prophylaxis (PrEP), whereas ART initiated shortly after exposure is postexposure prophylaxis (PEP) and forms a continuum with efforts aimed at virus eradication (cure). Even if early ART is not curative, it may reduce the size of the viral reservoir and preserve immune function.

therapeutic agent will invariably lead to complex and difficult-to-predict counterregulatory responses, it is difficult to predict how such interventions will affect the viral reservoir. The complexity of attempting to use an activating agent to reverse latency is illustrated by recent studies with IL-7. Preclinical studies suggested that this approach would reverse latency (*89*). Although a proof-of-concept clinical study found that IL-7 caused production of virions in vivo (*90*), the overall impact of the approach was an increase in the estimated reservoir size, presumably because of proliferation and expansion of infected cells (*12*). Experiments in improved preclinical models of ART-suppressed virus infection and proof-of-concept clinical trials will hopefully provide clarity on these and other issues.

The PrEP, PEP, and cure continuum

Treating HIV-1 with ART shortly after infection may also contribute to HIV-1 eradication. ART during acute HIV-1 infection reduces the size of the reservoir (*91*, *92*), limits the generation of escape mutants, and preserves immune function. For these reasons, it is thought that HIV-1–infected individuals who initiate ART during acute infection have the best chance for HIV-1 eradication, although this group represents only a small fraction of total HIV-1–infected individuals. It is also possible that very early ART may even be curative, as illustrated by the case of the HIV-1–infected infant who was started on ART at 30 hours of life. Therapy was discontinued after 18 months, and virus remained undetectable (through at least month 30), suggesting that very early initiation of ART may prevent establishment of a long-lived reservoir (*28*). However, the applicability of these findings to sexual HIV-1 transmission in adults remains uncertain.

The potentially curative role of ART when administered within days of infection blurs the traditional distinction between preexposure prophylaxis (PrEP), postexposure prophylaxis (PEP), and a cure (Fig. 3). It is well established that treating adults with ART within hours of HIV-1 exposure (e.g., a needlestick injury in a healthcare worker) substantially reduces the risk of acquiring HIV-1. However, antiretroviral drugs inhibit active virus replication in host cells, and thus the clinical success of PEP strategies indicates that the first HIV-1–infected cells after viral exposure can be eradicated. Indeed, if intensive virologic monitoring were used in these individuals, then it is possible that some might exhibit transient low levels of virus in blood or tissues and thus would be considered "cured." From this perspective, the use of very early ART to eradicate HIV-1 infection may not be uncommon.

Early ART that fails to block the establishment of the viral reservoir might still prevent some of the immunologic damage that typically occurs during acute HIV-1 infection, thus augmenting the capacity of the host immune system to control viral replication. Such an ART-induced shift toward a more effective host immune response and a smaller viral reservoir may in rare cases lead to sustained control of the virus (a functional cure). Among a cohort of adults in France who started ART during acute HIV-1 infection and then discontinued therapy after several years (the VISCONTI cohort), about 10 to 15% did not exhibit detectable viral rebound, although replication-competent virus still persisted in these individuals and they lacked protective HLA haplotypes (*93*). This observation has not yet been confirmed, and the mechanism for the posttreatment controller phenotype remains to be determined. As compared with elite controllers who naturally control HIV-1 infection without ART, the posttreatment controllers demonstrate remarkably small viral reservoirs and low levels of T cell activation, both of which may have contributed to the lack of rebound viremia when therapy was discontinued.

Conclusions and perspectives

Advances over the past several years have suggested that HIV-1 might be eradicated or controlled under specific conditions. Thus, the increasing enthusiasm for HIV-1 eradication research and the growing public and private investment in the HIV-1 cure agenda are justifiable. However, as described in detail elsewhere (*94*, *95*), major scientific challenges remain. A more detailed understanding of the biology of the latent viral reservoir and the partially effective virus-specific immune responses is critical. As the Boston patients demonstrate, improved assays are needed to quantify the viral reservoir, and predictive biomarkers for viral rebound are also needed. Reliable and predictive animal models should also be developed to evaluate concepts and to inform clinical research strategies.

The establishment and maintenance of the viral reservoir appears to be affected at least in part by the immune system. Immunotherapy approaches will therefore likely have an increasing role in HIV-1 eradication strategies in the future. However, the optimal strategies to stimulate viral release from latency, to augment host immune responses, and to limit negative inflammatory responses remain to be determined. Although a small number of case reports suggest that it might be possible to eradicate HIV-1 infection in unusual circumstances, no proof of concept yet exists that chronic HIV-1 infection can be cured by a safe and scalable intervention. Over the next few years, multiple novel and promising HIV-1 eradication concepts will be evaluated. It is likely that progress will be steady but unpredictable, and reaching the final goal may take many years. Regardless, substantial expansion of rigorous basic research, preclinical studies, and clinical trials in this field will undoubtedly lead to important advances in our understanding of the biology of the HIV-1 reservoir and the challenges that face HIV-1 eradication strategies.

REFERENCES AND NOTES

1. D. Finzi *et al.*, *Science* **278**, 1295–1300 (1997).
2. D. Persaud, Y. Zhou, J. M. Siliciano, R. F. Siliciano, *J. Virol.* **77**, 1659–1665 (2003).
3. T. W. Chun *et al.*, *Proc. Natl. Acad. Sci. U.S.A.* **94**, 13193–13197 (1997).
4. T. W. Chun *et al.*, *Proc. Natl. Acad. Sci. U.S.A.* **95**, 8869–8873 (1998).
5. T. W. Chun *et al.*, *Nature* **387**, 183–188 (1997).
6. T. W. Chun, R. T. Davey Jr., D. Engel, H. C. Lane, A. S. Fauci, *Nature* **401**, 874–875 (1999).
7. D. Finzi *et al.*, *Nat. Med.* **5**, 512–517 (1999).
8. Y. C. Ho *et al.*, *Cell* **155**, 540–551 (2013).
9. S. G. Deeks, R. Tracy, D. C. Douek, *Immunity* **39**, 633–645 (2013).
10. G. Doitsh *et al.*, *Nature* **505**, 509–514 (2013).
11. N. Chomont *et al.*, *Nat. Med.* **15**, 893–900 (2009).
12. C. Vandergeeten *et al.*, *Blood* **121**, 4321–4329 (2013).

13. M. J. Buzón *et al.*, *Nat. Med.* **16**, 460–465 (2010).
14. J. Cohen, *Science* **343**, 1188 (2014).
15. L. Josefsson *et al.*, *Proc. Natl. Acad. Sci. U.S.A.* **110**, E4987–E4996 (2013).
16. C. V. Fletcher *et al.*, *Proc. Natl. Acad. Sci. U.S.A.* **111**, 2307–2312 (2014).
17. M. J. Buzon *et al.*, *Nat. Med.* **20**, 139–142 (2014).
18. S. A. Yukl *et al.*, *J. Infect. Dis.* **208**, 1212–1220 (2013).
19. T. W. North *et al.*, *J. Virol.* **84**, 2913–2922 (2010).
20. A. Sigal *et al.*, *Nature* **477**, 95–98 (2011).
21. V. A. Evans *et al.*, *PLOS Pathog.* **9**, e1003799 (2013).
22. H. Hatano *et al.*, *J. Infect. Dis.* **208**, 50–56 (2012).
23. J. M. Murray *et al.*, *J. Virol.* **88**, 3516–3526 (2014).
24. H. Hatano *et al.*, *J. Infect. Dis.* **208**, 1436–1442 (2013).
25. N. R. Klatt, N. Chomont, D. C. Douek, S. G. Deeks, *Immunol. Rev.* **254**, 326–342 (2013).
26. M. F. Chevalier, L. Weiss, *Blood* **121**, 29–37 (2013).
27. M. Zeng *et al.*, *PLOS Pathog.* **8**, e1002437 (2012).
28. D. Persaud *et al.*, *N. Engl. J. Med.* **369**, 1828–1835 (2013).
29. K. Luzuriaga *et al.*, *J. Infect. Dis.* (2014).
30. J. E. Mold *et al.*, *Science* **330**, 1695–1699 (2010).
31. R. F. Siliciano, *Nat. Med.* **20**, 480–481 (2014).
32. G. Hütter *et al.*, *N. Engl. J. Med.* **360**, 692–698 (2009).
33. S. A. Yukl *et al.*, *PLOS Pathog.* **9**, e1003347 (2013).
34. P. Tebas *et al.*, *N. Engl. J. Med.* **370**, 901–910 (2014).
35. N. Holt *et al.*, *Nat. Biotechnol.* **28**, 839–847 (2010).
36. P. M. Younan *et al.*, *Blood* **122**, 179–187 (2013).
37. T. J. Henrich *et al.*, *J. Infect. Dis.* **207**, 1694–1702 (2013).
38. P. M. Cannon, D. B. Kohn, H. P. Kiem, *Nat. Biotechnol.* **32**, 315–316 (2014).
39. N. M. Archin *et al.*, *Nature* **487**, 482–485 (2012).
40. C. K. Bullen, G. M. Laird, C. M. Durand, J. D. Siliciano, R. F. Siliciano, *Nat. Med.* **20**, 425–429 (2014).
41. J. Blazkova *et al.*, *J. Infect. Dis.* **206**, 765–769 (2012).
42. A. M. Spivak *et al.*, *Clin. Infect. Dis.* **58**, 883–890 (2014).
43. C. Katlama *et al.*, *Lancet* **381**, 2109–2117 (2013).
44. L. Shan *et al.*, *Immunity* **36**, 491–501 (2012).
45. S. A. Migueles *et al.*, *Immunity* **29**, 1009–1021 (2008).
46. E. S. Rosenberg *et al.*, *PLOS ONE* **5**, e10555 (2010).
47. R. T. Schooley *et al.*, *J. Infect. Dis.* **202**, 705–716 (2010).
48. J. B. Angel *et al.*, *AIDS* **25**, 731–739 (2011).
49. R. T. Gandhi *et al.*, *Vaccine* **27**, 6088–6094 (2009).
50. B. Autran *et al.*, *AIDS* **22**, 1313–1322 (2008).
51. J. M. Kilby *et al.*, *J. Infect. Dis.* **194**, 1672–1676 (2006).
52. F. García *et al.*, *Sci. Transl. Med.* **5**, 166ra2 (2013).
53. J. P. Casazza *et al.*, *J. Infect. Dis.* **207**, 1829–1840 (2013).
54. S. G. Hansen *et al.*, *Nature* **473**, 523–527 (2011).
55. S. G. Hansen *et al.*, *Nature* **502**, 100–104 (2013).
56. S. G. Hansen *et al.*, *Science* **340**, 1237874 (2013).
57. D. H. Barouch *et al.*, *Cell* **155**, 531–539 (2013).
58. D. H. Barouch *et al.*, *Nature* **482**, 89–93 (2012).
59. N. L. Letvin *et al.*, *Sci. Transl. Med.* **3**, 81ra36 (2011).
60. H. Liu *et al.*, *Nature* **507**, 519–522 (2014).
61. V. Dahirel *et al.*, *Proc. Natl. Acad. Sci. U.S.A.* **108**, 11530–11535 (2011).
62. P. Poignard *et al.*, *Immunity* **10**, 431–438 (1999).
63. A. Trkola *et al.*, *Nat. Med.* **11**, 615–622 (2005).
64. S. Mehandru *et al.*, *J. Virol.* **81**, 11016–11031 (2007).
65. D. H. Barouch *et al.*, *Nature* **503**, 224–228 (2013).
66. M. Shingai *et al.*, *Nature* **503**, 277–280 (2013).
67. F. Klein *et al.*, *Nature* **492**, 118–122 (2012).
68. S. L. Topalian *et al.*, *N. Engl. J. Med.* **366**, 2443–2454 (2012).
69. D. Gardiner *et al.*, *PLOS ONE* **8**, e63818 (2013).
70. T. W. Chun *et al.*, *J. Clin. Invest.* **115**, 3250–3255 (2005).
71. C. Riou *et al.*, *J. Exp. Med.* **204**, 79–91 (2007).
72. A. Heredia *et al.*, *Proc. Natl. Acad. Sci. U.S.A.* **100**, 10411–10416 (2003).
73. K. Araki *et al.*, *Nature* **460**, 108–112 (2009).
74. P. G. Stock *et al.*, *Am. J. Transplant.* **14**, 1136–1141 (2014).
75. C. Gavegnano *et al.*, *Antimicrob. Agents Chemother.* **58**, 1977–1986 (2014).
76. M. J. de Veer *et al.*, *J. Leukoc. Biol.* **69**, 912–920 (2001).
77. C. A. Stoddart, M. E. Keir, J. M. McCune, *PLOS Pathog.* **6**, e1000766 (2010).
78. D. Favre *et al.*, *Blood* **117**, 2189–2199 (2011).
79. D. Favre *et al.*, *Sci. Transl. Med.* **2**, 32ra36 (2010).
80. C. Le Saout *et al.*, *PLOS Pathog.* **10**, e1003976 (2014).
81. S. Fernandez *et al.*, *J. Infect. Dis.* **204**, 1927–1935 (2011).
82. E. B. Wilson *et al.*, *Science* **340**, 202–207 (2013).
83. J. R. Teijaro *et al.*, *Science* **340**, 207–211 (2013).
84. S. K. Pillai *et al.*, *Proc. Natl. Acad. Sci. U.S.A.* **109**, 3035–3040 (2012).
85. L. Azzoni *et al.*, *J. Infect. Dis.* **207**, 213–222 (2013).
86. A. Bosque, M. Famiglietti, A. S. Weyrich, C. Goulston, V. Planelles, *PLOS Pathog.* **7**, e1002288 (2011).
87. A. R. Cillo *et al.*, *Proc. Natl. Acad. Sci. U.S.A.* **111**, 7078–7083 (2014).
88. J. Kulkosky *et al.*, *J. Infect. Dis.* **186**, 1403–1411 (2002).
89. F. X. Wang *et al.*, *J. Clin. Invest.* **115**, 128–137 (2005).
90. I. Sereti *et al.*, *Blood* **113**, 6304–6314 (2009).
91. N. M. Archin *et al.*, *Proc. Natl. Acad. Sci. U.S.A.* **109**, 9523–9528 (2012).
92. J. Ananworanich *et al.*, *PLOS ONE* **7**, e33948 (2012).
93. A. Sáez-Cirión *et al.*, *PLOS Pathog.* **9**, e1003211 (2013).
94. D. D. Richman *et al.*, *Science* **323**, 1304–1307 (2009).
95. S. G. Deeks *et al.*, *Nat. Rev. Immunol.* **12**, 607–614 (2012).

ACKNOWLEDGMENTS

The authors thank B. Walker, N. Michael, J. Kim, M. Robb, R. Geleziunas, M. McCune, R. Sekaly, N. Chomont, and S. Lewin for helpful discussions. The authors acknowledge support from the NIH [AI078526, AI084794, AI095985, AI096040, AI096109 (Delaney AIDS Research Enterprise), AI100663, and OD011170]; the Bill and Melinda Gates Foundation (OPP1033091, OPP1040741, and OPP1083689); the Ragon Institute of MGH, MIT, and Harvard; the Henry M. Jackson Foundation; and the American Foundation for AIDS Research. D.H.B. is a co-inventor on Ad26 vector, mosaic antigen, and Env immunogen patents. S.G.D. has served as an ad hoc consultant for Bristol-Myers Squib, GlaxoSmithKline, and Janssen on HIV cure–related activities.

10.1126/science.1255512

RESEARCH

Neutron crystallography reveals cytochrome c peroxidase's secrets
Casadei et al., p. 193

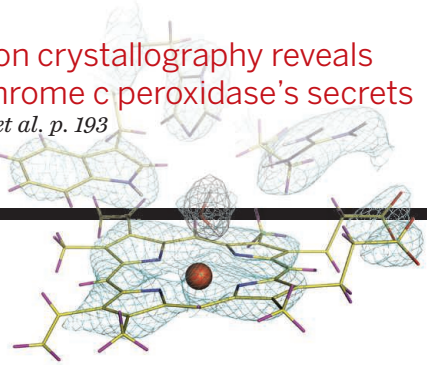

IN *SCIENCE* JOURNALS

Edited by **Stella Hurtley**

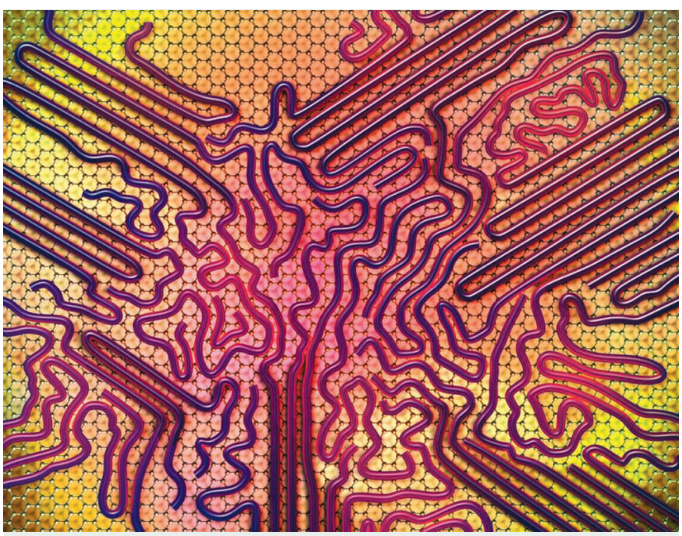

Idealized model of a folded-chain polymer ordering on a graphene surface

IMAGING TECHNIQUES

Probing interfaces with electrons

When molecules move on surfaces, they behave differently from when inside a solid. But surface layers give off limited signals, so to probe these systems, scientists need to act fast. Gulde *et al.* developed an ultrafast low-energy electron diffraction technique and used it to study how a polymer moved and melted on a graphene substrate (see the Perspective by Nibbering). After hitting the sample with a laser pulse, energy transferred across the graphene-polymer interface, the polymer film became less orderly, and an amorphous phase appeared. — MSL

Science, this issue p. 200; see also p. 137

MICROECONOMICS

Balancing your incomings and outgoings

Economic theory predicts that when someone receives money should have little effect on their spending patterns. Gelman *et al.* constructed a data set of 60 million transactions made by 75,000 people to test this theory. People do seem to go on a mini–spending spree after they get their paychecks or pensions. However, closer inspection reveals that that's mostly explained by the convenience of linking regular payments, such as rent and utilities, to regular income. Unsurprisingly, cash-strapped people are more likely to increase their spending in response to receiving income. — GJC

Science, this issue p. 212

OCEAN MICROBES

Up and down go the cyanobacteria

Plankton move together in strikingly coordinated daily patterns, sinking at night to avoid being eaten and rising to the surface in daylight to photosynthesize. Otteson *et al.* found similar activity patterns in even the smallest of planktonic organisms, such as photosynthetic bacteria (see the Perspective by Armbrust). Because it's hard to take regular samples in the open ocean, the authors built a robotic sampler and set it adrift for several days in the mid-Pacific. The captured bacteria showed immediate responses to changes in light, temperature, and salinity in ways that could affect the ocean's carbon and nitrogen cycles. — CA

Science, this issue p. 207; see also p. 134

CANCER

Chloride causes seizures in glioma

Gliomas, a common brain tumor, frequently induce epileptic seizures as they grow, but it is not clear why. Pallud *et al.* show that the epileptic activity in the brain around gliomas happens because neurons respond anomalously to the neurotransmitter γ-aminobutyric acid (GABA). Usually GABA turns neurons off, but when gliomas are nearby, it turns them on instead. Also seen in temporal lobe epilepsy, this unusual cell behavior happens because the neurons take up too many chloride ions. Glioma tumor cells also take up too much chloride, which helps them spread and invade into normal brain tissue. Perhaps drugs that block chloride uptake could interfere with both glioma-induced seizures and tumor growth, a two-for-one hit. — YN

Sci. Transl. Med. **6**, 244ra89 (2014).

CANCER THERAPY

Staying one step ahead of tumors

Cancer treatments require continual adjustment. A drug that works initially will lose its

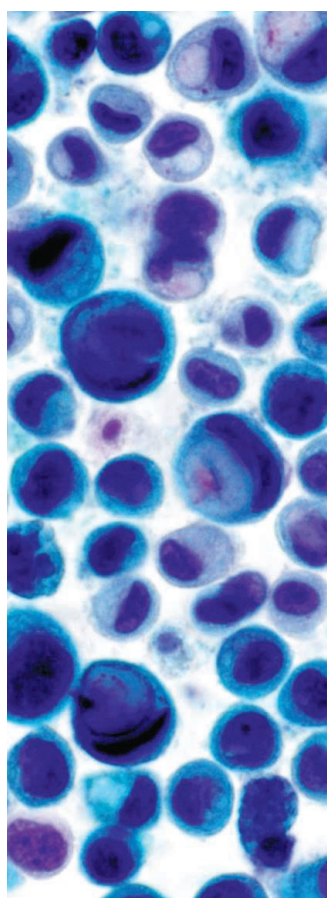

Ex vivo expansion of circulating breast cancer cells, nuclei stained blue

PHOTOS: (COUNTERCLOCKWISE FROM TOP) CASADEI *ET AL.*; ROSS URIEN/UNIVERSITY OF GÖTTINGEN; YU *ET AL.*

Downloaded from www.sciencemag.org on July 11, 2014

Published by AAAS

potency as the tumor acquires new mutations that allow it to bypass the drug's lethal effects. To stay ahead of the tumor, oncologists need a noninvasive way to collect tumor cells from patients over the course of their treatment. Analyzing the mutations in these samples may help them choose the right drugs as the tumors change. In a small study of breast cancer patients, Yu *et al*. show that rare tumor cells circulating in the blood can be captured in viable form and used for this purpose. — PAK

Science, this issue p. 216

PHYSIOLOGY

Interfering with the signal to relax

In people with high blood pressure, tissue perfusion is often reduced. In response to specific stimuli, endothelial cells that line arteries instruct the surrounding smooth muscle cells to relax, increasing blood flow into the tissue. Endothelial cells extend small processes called myoendothelial projections (MEPs) to communicate with smooth muscle cells. Sonkusare *et al*. found that the calcium-conducting ion channel TRPV4 and the scaffold protein AKAP150 concentrated at MEPs and visualized calcium signals at these sites. In a mouse model of hypertension, AKAP was not concentrated in MEPs, and the endothelial cells failed to tell the smooth muscle to relax, reducing tissue perfusion. — NRG

Sci. Signal. **7**, ra66 and pe16 (2014).

SPACE WEATHER

How the ionosphere gains influence

In Earth's upper atmosphere, the reconnection of magnetic field lines converts latent magnetic energy into the thermal and kinetic energy of plasma flows. But reconnection appears to produce faster flows before midnight compared with after. To find out why, Lotko *et al*. simulated this energy exchange. Challenging common assumptions about our space weather environment, they conclude that the ionosphere plays an active role when coupled to the magnetosphere in driving the behavior of the magnetotail. — MMM

Science, this issue p. 184

SUPERCONDUCTIVITY

Optically probed superconductor

The exotic superconductor UPt_3 has two superconducting phases that appear at different temperatures, but their nature remains unclear. Schemm *et al*. shone circularly polarized light on a crystal of UPt_3 and studied its reflection (see the Perspective by van der Marel and Sawatzky). In the low-temperature phase, the pairs of electrons that make the material superconducting have a handedness to them. The finding narrows down the possible descriptions of the electron-pair wave function. — JS

Science, this issue p. 190; see also p. 138

HIV LATENCY

For HIV: Location, location, location

HIV-infected cells linger even in the face of therapy, and this persistence, termed the latent reservoir, is a major hurdle for curing HIV. HIV integrates itself into the DNA of its host cells. Could that affect the latent reservoir? To find out, Maldarelli *et al*. drew blood from five HIV patients on antiretroviral therapy and analyzed sites where HIV had inserted itself into the blood cells' DNA (see the Perspective by Margolis and Bushman). In many cases, these sites were not random; HIV often weaseled its way into genes that help cells grow and proliferate. Where HIV integrates into the host genome may thus determine the size of the latent reservoir. — KLM

Science, this issue p. 179; see also p. 143

IN OTHER JOURNALS

Edited by **Kristen Mueller** *and* **Jesse Smith**

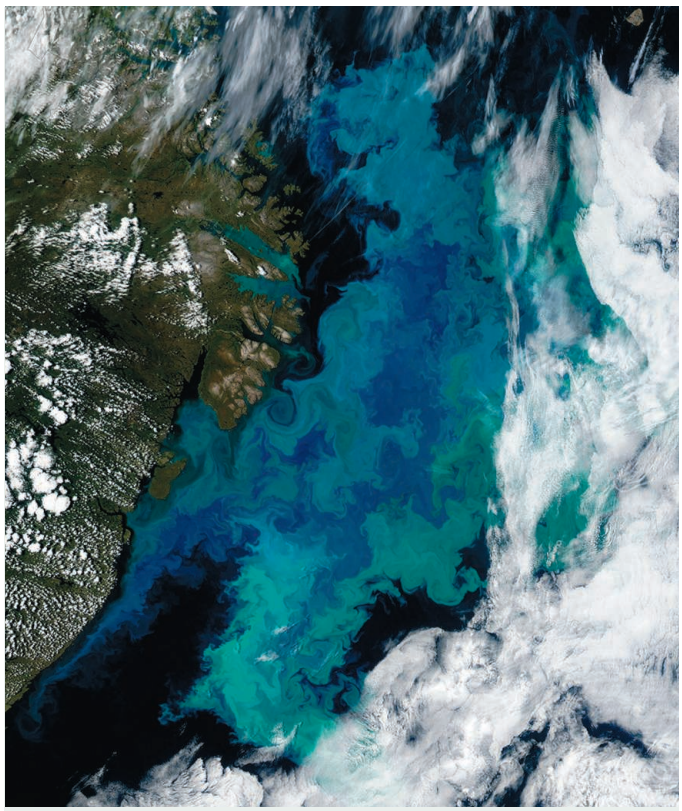

Satellite image of *Emiliania huxleyi* blooms in the Barents Sea

PHOTO: JEFF SCHMALTZ/MODIS RAPID RESPONSE TEAM/ASA GSFC

MARINE MICROBIOLOGY

A virus that enslaves ocean algae

The algal blooms that flourish near the ocean surface feed ecosystems and remove carbon from the atmosphere. But algal blooms can get sick. Rosenwasser *et al*. studied metabolism and gene transcription in the coccolithophore *Emiliania huxleyi* and a virus that attacks it. They fo und that the virus hijacked the algae's metabolic pathway and used it to build more virus particles. The virus carries information for its own lipid biosynthetic pathway. No shrinking violet, this physically large virus shut down and supplanted the parallel metabolic pathway in its algal host, forcing the algae to synthesize lipids that the virus needed. The host, deprived of its own lipids, faded into oblivion, sinking into the ocean and taking its resident carbon with it. — PJH

Plant Cell 10.1105/tpc.114.125641 (2014).

NEUROSCIENCE

Hearing and imagination shape what we see

Hearing sounds helps our visual system to predict incoming information and may give us a survival advantage. Vetter *et al*. blindfolded people and scanned their brains while they listened to birds singing, traffic noise, or people talking. Using sophisticated algorithms, the researchers were able to identify the category of sounds just by examining the pattern of activity

Published by AAAS

in the primary visual cortex, a brain area previously believed to process nothing but input from the eyes. And when the people imagined the specific sound categories in the complete absence of sight and sound, their primary visual cortices also showed activity. These results highlight the interconnectedness of the brain's sensory systems. — PRS

Curr. Biol. 10.1016/j.cub.2014.04.020 (2014).

CELL ADHESION

Forces inside the cell control adhesion

When tissues undergo change—when they're growing or healing, for example—the contact between cells changes too. Mechanical forces play an important role in remodeling these connections. The protein cadherin sticks cells together by spanning the cell membrane, making contacts with the network of actin filaments inside one cell and cadherins on another cell. Engl et al. watched junctions grow between pairs of cells. The dynamics of the actin cytoskeleton affected how cadherin moved to the junctions. During actin turnover, when opposite ends of the filament add and lose actin monomers simultaneously, contacts between cells shrank, whereas stable actin filaments stabilized the contacts between cells. Forces inside the cell stabilize the actin filaments and thus influence cell adhesion. — VV

Nat. Cell Biol. **16**, 584 (2014).

VIRAL CELL BIOLOGY

NEC helps herpesvirus escape from nucleus

Viruses must move out of their host cells before they can infect new ones. To make the break, newly created viruses form infectious virus particles by enshrouding themselves in the host cell's membrane, which eventually pinches off in a process called scission. For herpesviruses, this "budding" occurs in the inner nuclear membrane and requires a special protein

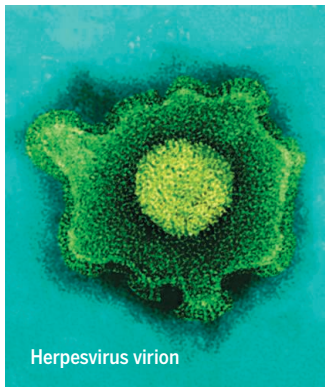

Herpesvirus virion

tool, called a nuclear egress protein complex (NEC). Bigalke *et al.* asked whether the NEC itself tells the membrane to bud and pinch off, or whether it needs to recruit host-cell proteins to get the message across. Using only purified NEC and lipids, the authors found that NEC works alone, by forming a coat-like hexagonal array inside the budding membrane. This array forms a scaffold for the bud and helps the neck of the budding point narrow so scission occurs. — SMH

Nat. Commun. 10.1038/ncomms5131 (2014).

DIFFRACTION METHODS

Locking into surface structure

Knowing the surface structure of functional materials such as catalysts is an essential part of understanding how they work. Lock-in amplifiers are instruments that extract weak signals from noisy data, which can help investigators who employ high-energy x-ray diffraction techniques to probe surfaces. Ferri *et al.* studied palladium nanoparticles on cerium-zirconium oxides, which are similar to catalysts used to control automotive exhaust emissions. They detected reduced Pd nanocrystals, as well as changes in oxygen coordination around the cerium cations, using phase-sensitive detection of diffraction peaks. Exposing the sample to alternating pulses of reducing CO and oxidizing O_2 led to those phase shifts. — PDS

Angew. Chem. Int. Ed. 10.1002/ange.201403094 (2014).

PHYSICS

Making larger numbers count more

Some measurements make better use of a larger number of particles than others. To make very precise measurements, physicists often increase the number of particles they use as probes—the more particles, the more precise the measurement. Sewell *et al.* sent light pulses through a cloud of ^{87}Rb atoms to measure the spin alignment of the atomic cloud. They found that the precision of the measurement grew more quickly as the number of photons was increased than it does when more conventional methods are employed. The key to this improvement was making an indirect measurement in which the output was a nonlinear function of the number of photons used. — JS

Phys. Rev. X **4**, 021045 (2014).

GEOPHYSICS

Different faults with the same risks

Everyone knows that buildings near traditional earthquake faults need careful engineering, but what about ones near faults that deform slowly over time? Most earthquakes occur on faults that are locked in place and resist motion; faults that deform slowly and continuously are traditionally considered less seismically hazardous. Harris and Abrahamson analyzed the San Andreas fault system in detail and report that ground shaking from earthquakes on slowly deforming faults looks the same as that from traditional earthquakes. The authors conclude that seismic hazard maps should not discount the potential for ground shaking from slowly deforming faults. — BG

Geophys. Res. Lett. 10.1002/2014GL060228 (2014).

PALEONTOLOGY

In the footsteps of duckbilled dinos

Thousands of fossilized footprints left on a 180-m-long stretch of flood plain in Alaska's Denali National Park and Preserve offer news clues to the lives of hadrosaurs, commonly called duck-billed dinosaurs. The impressions, made between 69 million and 72 million years ago, cluster within four size ranges that represent specific age groups in a multigenerational herd, report Fiorillo *et al*. About 84% of the tracks were made by adult and near-adult hadrosaurs, 13% by young probably less than 1 year old, and only 3% by juveniles—a rarity that suggests the species experienced a rapid growth spurt. The presence of juveniles also hints that the creatures spent their lives in the Arctic; the young would not have been able to migrate to and from warmer climates during wintertime. — SP

Geology 10.1130/G35740.1 (2014).

The hazards from slowly deforming faults are similar to those of rapidly deforming ones

PHOTOS: (TOP TO BOTTOM) LINDA M. STANNARD/UNIVERSITY OF CAPE TOWN/SCIENCE SOURCE; © WILL & DENI MCINTYRE/CORBIS

Published by AAAS

ALSO IN *SCIENCE* JOURNALS

Edited by **Stella Hurtley**

HIV TRANSMISSION

HIV needs to be fit to transmit

Although you might not think it, it's hard to catch HIV. Less than 1% of unprotected sexual exposures result in infection. What then leads to transmission? Carlson *et al*. determined the amino acid sequence of viruses infecting 137 Zambian heterosexual couples in which one partner infected the other (see the Perspective by Joseph and Swanstrom). The authors then used statistical modeling and found that transmitted viruses are typically the most evolutionarily fit. That is, compared to other viral variants in the infected person, the transmitted virus most closely matches the most common viral sequence found in the Zambian population. — KLM

Science, this issue p. 178; see also p. 136

BACTERIAL CELL WALL

Building the cell wall is flipping difficult

The cell wall of bacteria is constructed from a polysaccharide called peptidoglycan (PG). It forms a matrix that surrounds cells and is essential for the integrity of the cytoplasmic membrane. Many of our most successful antibiotics target PG synthesis. The synthetic pathway involves the assembly of sugar building blocks on a lipid carrier at the inner face of the cytoplasmic membrane. The reactions that produce this so-called lipid II precursor and the enzymes that catalyze them have been known for decades. However, the identity of the flippase enzyme that "flips" lipid II in the membrane to expose the sugar building blocks on the cell surface for polymerization has remained highly controversial. Sham *et al.* now show that the essential protein MurJ is the long sought-after flippase responsible for the translocation of lipid-linked cell wall precursors across the bacterial cytoplasmic membrane (see the Perspective by Young). The work completes the cell wall biogenesis pathway and defines the function of an attractive target for new antibiotics. — SMH

Science, this issue p. 220; see also p. 139

SUPERCONDUCTIVITY

Identifying a cuprate look-alike

Superconductivity in cuprate compounds remains poorly understood. Recreating its features in an unrelated material may provide insight. Kim *et al.* used a spectroscopic technique to study the electronic states of the material Sr_2IrO_4 at relatively high temperatures. They observed phenomenology similar to that of cuprates as they varied the surface carrier concentration. The study highlights the essential properties a material needs in order to exhibit cuprate-like features in the normal (nonsuperconducting) state. — JS

Science, this issue p. 187

CATALYSIS

Assessing calculated DFT properties

Density functional theory (DFT) is now widely used to calculate molecular and material properties. DFT's reliability is usually assessed by comparison with experimental values and higher-level theoretical methods. Medford *et al.* used the BEEF-vdW, an exchange-correlation density functional tailored for surface chemistry, and looked at uncertainties with ensembles of functionals. For the specific case of ammonia synthesis catalyzed by transition-metal surfaces, relative rates between different catalysts had lower errors than the absolute rates. — PDS

Science, this issue p. 197

HEME ENZYMES

Peroxidase proton placement

Heme enzymes catalyze a variety of biochemical oxidations through the activation of oxygen by iron. Casadei *et al.* used neutron crystallography to elucidate the mechanism of cytochrome c peroxidase (see the perspective by Groves and Boaz). In the highly reactive intermediate state termed compound I, the iron(IV) oxo, or ferryl, fragment was not protonated, whereas a nearby histidine residue was protonated. The sensitivity of neutron scattering to proton locations revealed these protonation states, where more common techniques, such as x-ray diffraction, have yielded more ambiguous results. — JSY

Science, this issue p. 193; see also p. 142

EARTHQUAKE DYNAMICS

Supershear rupture down below

Deep earthquakes occur in complex fault zones more than 70 kilometers below Earth's surface. Although they do not pose much of a hazard, they can still provide valuable insight into how earthquakes rupture. Zhan *et al.* found that a magnitude 6.7 aftershock of the largest deep earthquake recorded to date—the 2013 magnitude 8.3 Sea of Okhotsk earthquake—ruptured faster than the velocity of its seismic waves. This so-called "supershear" rupture shows that deep earthquakes have diverse rupture mechanisms and have several routes to dissipate energy. — NW

Science, this issue p. 204

GENETIC OSCILLATIONS

Observing an embryonic Doppler effect

The sound of an oncoming train changes as it passes you, a phenomenon termed the Doppler effect. Soroldoni *et al.* propose a similar event during the formation of vertebrate embryo body segments. It is generally thought that the internal timing of a genetic oscillator called the "segmentation clock" sets the rhythm of body segments called somites. However, time-lapse microscopy of the spatial waves of oscillations and the timing of body segment formation showed segments forming faster than spatial genetic oscillations. This "Doppler effect" occurs because the end of the oscillating tissue moves steadily into the oncoming waves. Thus, the rhythm of sequential body segmentation is a function of genetic oscillations, their changing wave pattern, and tissue shortening. — BAP

Science, this issue p. 222

MARINE POLLUTION

Seas are awash with microplastics

Plastics litter beaches and the open ocean. Scientists are increasingly concerned about a less visible form of plastic pollution: microplastics. Microplastics arise from the deterioration of larger plastic items and from microbeads used in cosmetics. In their Perspective, Law and Thompson explain that because marine currents distribute the pollutants in unpredictable ways, trends in microplastic pollution are difficult to measure. Microplastics can contain harmful chemicals and may also release toxic additives used in their manufacture. They are ingested by and can poison many marine organisms. We are currently unable, and may never be able, to remove microplastics from the oceans. We thus need to understand the environmental effects of this major pollutant in the hope of mitigating its worst effects. — JFU

Science, this issue p. 144

Published by AAAS

EXTENDED PDF FORMAT
SPONSORED BY
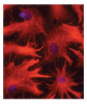
Travel Grants Available
Neuroscience 2014
Application Deadline: July 31st
>Apply Now
R&D systems
a bio-techne brand
www.rndsystems.com

Selection bias at the heterosexual HIV-1 transmission bottleneck

Jonathan M. Carlson *et al.*

Science **345**, (2014);
DOI: 10.1126/science.1254031

This copy is for your personal, non-commercial use only.

If you wish to distribute this article to others, you can order high-quality copies for your colleagues, clients, or customers by clicking here.

Permission to republish or repurpose articles or portions of articles can be obtained by following the guidelines here.

The following resources related to this article are available online at www.sciencemag.org (this information is current as of July 10, 2014):

Updated information and services, including high-resolution figures, can be found in the online version of this article at:
http://www.sciencemag.org/content/345/6193/1254031.full.html

Supporting Online Material can be found at:
http://www.sciencemag.org/content/suppl/2014/07/09/345.6193.1254031.DC1.html

A list of selected additional articles on the Science Web sites **related to this article** can be found at:
http://www.sciencemag.org/content/345/6193/1254031.full.html#related

This article **cites 70 articles**, 37 of which can be accessed free:
http://www.sciencemag.org/content/345/6193/1254031.full.html#ref-list-1

This article has been **cited by** 1 articles hosted by HighWire Press; see:
http://www.sciencemag.org/content/345/6193/1254031.full.html#related-urls

This article appears in the following **subject collections:**
Medicine, Diseases
http://www.sciencemag.org/cgi/collection/medicine

Downloaded from www.sciencemag.org on July 11, 2014

Science (print ISSN 0036-8075; online ISSN 1095-9203) is published weekly, except the last week in December, by the American Association for the Advancement of Science, 1200 New York Avenue NW, Washington, DC 20005. Copyright 2014 by the American Association for the Advancement of Science; all rights reserved. The title *Science* is a registered trademark of AAAS.

RESEARCH ARTICLE SUMMARY

HIV TRANSMISSION

Selection bias at the heterosexual HIV-1 transmission bottleneck

Jonathan M. Carlson,* Malinda Schaefer, Daniela C. Monaco, Rebecca Batorsky, Daniel T. Claiborne, Jessica Prince, Martin J. Deymier, Zachary S. Ende, Nichole R. Klatt, Charles E. DeZiel, Tien-Ho Lin, Jian Peng, Aaron M. Seese, Roger Shapiro, John Frater, Thumbi Ndung'u, Jianming Tang, Paul Goepfert, Jill Gilmour, Matt A. Price, William Kilembe, David Heckerman, Philip J.R. Goulder, Todd M. Allen, Susan Allen, Eric Hunter*

INTRODUCTION: Heterosexual HIV-1 transmission is an inefficient process with rates reported at <1% per unprotected sexual exposure. When transmission occurs, systemic infection is typically established by a single genetic variant, taken from the swarm of genetically distinct viruses circulating in the donor. Whether that founder virus represents a chance event or was systematically favored is unclear. Our work has tested a central hypothesis that founder virus selection is biased toward certain genetic characteristics.

RATIONALE: If HIV-1 transmission involves selection for viruses with certain favorable characteristics, then such advantages should emerge as statistical biases when viewed across many viral loci in many transmitting partners. We therefore identified 137 Zambian heterosexual transmission pairs, for whom plasma samples were available for both the donor and recipient partner soon after transmission, and compared the viral sequences obtained from each partner to identify features that predicted whether the majority amino acid observed at any particular position in the donor was transmitted. We focused attention on two features: viral genetic characteristics that correlate with viral fitness and clinical factors that influence transmission. Statistical modeling indicates that the former will be favored for transmission, while the latter will nullify this relative advantage.

RESULTS: We observed a highly significant selection bias that favors the transmission of amino acids associated with increased fitness. These features included the frequency of the amino acid in the study cohort, the relative advantage of the amino acid with respect to the stability of the protein, and features related to immune escape and compensation. This selection bias was reduced in couples with high risk of transmission. In particular, significantly less selection bias was observed in men with genital inflammation and in women (regardless of inflammation status), compared to healthy men, suggesting a more permissive environment in the female than male genital tract. Consistent with this observation, viruses transmitted to women were characterized by lower predicted fitness than those in men. The presence of amino acids favored during transmission predicted which individual virus within a donor was transmitted to their partner, while chronically infected individuals with viral populations characterized by a predominance of these amino acids were more likely to transmit to their partners.

CONCLUSION: These data highlight the clear selection biases that benefit fitter viruses during transmission in the context of a stochastic process. That such biases exist, and are tempered by certain risk factors, suggests that transmission is frequently characterized by many abortive transmission events in which some target cells are nonproductively infected. Moreover, for efficient transmission, some changes that favored survival in the transmitting partner are frequently discarded, resulting in overall slower evolution of HIV-1 in the population. Paradoxically, by increasing the selection bias at the transmission bottleneck, reduction of susceptibility may increase the expected fitness of breakthrough viruses that establish infection and may therefore worsen the prognosis for the newly infected partner. Conversely, preventive or therapeutic approaches that weaken the virus may reduce overall transmission rates via a mechanism that is independent from the quantity of circulating virus, and may therefore provide long-term benefits to the recipient if transmission does occur. ■

ON OUR WEBSITE

Read the full article at http://dx.doi.org/10.1126/science.1254031

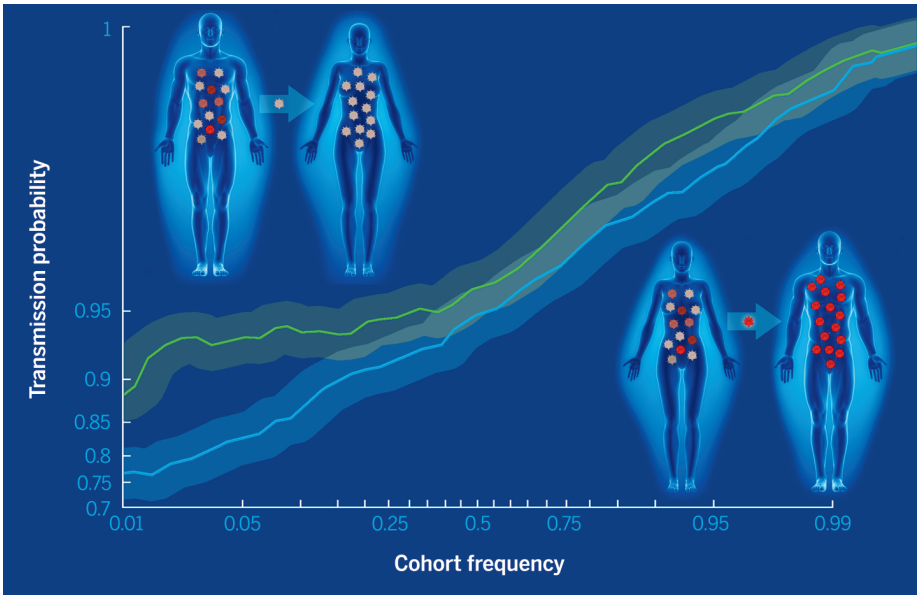

Fitter viruses (red) are favored more in woman-to-man (bottom curve) than in man-to-woman (top curve) transmission. The probability that a majority donor amino acid variant is transmitted is a function of relative fitness, here estimated by the frequency of the variant in the Zambian population. Even residues common in the population are less likely to be transmitted to healthy men than to women, indicative of higher selection bias in woman-to-man transmission.

RELATED ITEMS IN SCIENCE

S. B. Joseph, R. Swanstrom, A fitness bottleneck in HIV-1 transmission. *Science* **345**, 136–137 (2014).

The list of author affiliations is available in the full article online.
***Corresponding author. E-mail: carlson@microsoft.com (J.M.C.); ehunte4@emory.edu (E.H.)**
Cite this article as J. M. Carlson *et al.*, *Science* 345, 1254031 (2014). DOI: 10.1126/science.1254031

CREDIT: J. M. C., E. H., AND MICROSOFT RESEARCH

RESEARCH ARTICLE

HIV TRANSMISSION

Selection bias at the heterosexual HIV-1 transmission bottleneck

Jonathan M. Carlson,[1*†] Malinda Schaefer,[2†] Daniela C. Monaco,[2] Rebecca Batorsky,[3] Daniel T. Claiborne,[2] Jessica Prince,[2] Martin J. Deymier,[2] Zachary S. Ende,[2] Nichole R. Klatt,[2‡] Charles E. DeZiel,[1] Tien-Ho Lin,[1§] Jian Peng,[1¶] Aaron M. Seese,[3] Roger Shapiro,[4] John Frater,[5,6,7] Thumbi Ndung'u,[3,8,9,10] Jianming Tang,[11] Paul Goepfert,[11] Jill Gilmour,[12,13] Matt A. Price,[14,15] William Kilembe,[16] David Heckerman,[17] Philip J. R. Goulder,[8,18] Todd M. Allen,[3] Susan Allen,[16,19,20] Eric Hunter[2,16,19*]

Heterosexual transmission of HIV-1 typically results in one genetic variant establishing systemic infection. We compared, for 137 linked transmission pairs, the amino acid sequences encoded by non-envelope genes of viruses in both partners and demonstrate a selection bias for transmission of residues that are predicted to confer increased in vivo fitness on viruses in the newly infected, immunologically naïve recipient. Although tempered by transmission risk factors, such as donor viral load, genital inflammation, and recipient gender, this selection bias provides an overall transmission advantage for viral quasispecies that are dominated by viruses with high in vivo fitness. Thus, preventative or therapeutic approaches that even marginally reduce viral fitness may lower the overall transmission rates and offer long-term benefits even upon successful transmission.

Heterosexual HIV-1 transmission is characterized by a severe genetic bottleneck, in which infection is typically established by a single genetic variant selected from the large and diverse quasispecies typically present in the donor (*1*–*7*). The source of this bottleneck is likely mediated by multiple physical and immunologic factors that limit which virus particles can reach the genital tract, penetrate the mucosal barrier, productively infect target cells, and then traffic out of the mucosa for systemic dissemination—the sum total of which effectively blocks transmission in >99% of unprotected sexual exposures (*8*, *9*).

One potential source of this bottleneck is the unique environment of the male and female genital tracts, which may feature different target cell populations from those the majority of viruses face in systemic infection. The envelope (Env) protein, expressed on the surface of virus particles, determines target cell specificity; thus, variations in target cell populations are likely to exert selection pressure on the virus. Indeed, selection pressure appears to favor viruses encoding Env proteins that use CCR5 as a co-receptor (*10*), that favor target cells more likely to be trafficked out of the gut (*11*), and that have higher Env concentrations (*12*). There is also evidence that Env proteins with lower levels of glycosylation (*1*–*3*, *13*) and that are closer to ancestral sequences (*14*, *15*) are similarly favored. Glycosylation serves as a steric shield from the humoral immune response (*16*), whereas the move toward an ancestral state may involve the reversion of immunological escape mutations. Because the naïve host lacks an HIV-specific adaptive immune response, these escape features are no longer necessary, and any fitness cost associated with them may become a hindrance in transmission.

If general fitness plays a role in transmission, then fitness preferences will manifest themselves in non-Env proteins as well, the possibility of which has been recently suggested by observations that transmitted founder viruses are relatively more resistant to α-interferon (*12*, *17*), a phenotype that is unlikely to be dependent on Env. The ability of virus particles to grow and efficiently infect target cells has clear pathological consequences, with in vitro measurements of viral replicative capacity correlating with viral loads (VLs) and CD4 decline in both acute and chronic infection (*18*–*21*). VL is also closely linked with the odds of transmission, raising the possibility that general in vivo viral fitness could play a significant role in the transmission process as well.

The severe nature of the transmission bottleneck suggests that the selection of the breakthrough virus is a stochastic process in which a virus with a modest growth advantage in the mucosal compartments would be more likely to succeed in establishing infection. When viewed across many linked transmission partners, such viral advantages should emerge as measurable statistical biases. We provide evidence here that the genetic bottleneck imposes a selection bias for transmission of amino acids that are consensus in the cohort and are predicted to confer increased in vivo fitness on viruses in the newly infected, immunologically naïve recipient. This bias is tempered by transmission risk factors, such as donor VL, genital inflammation, and recipient gender, and provides an overall transmission advantage for viral quasispecies that are dominated by viruses with high in vivo fitness.

Results

Consensus residues are preferentially transmitted

If some viruses with a general growth advantage are more likely to establish infection, then transmission of minority variants will be more frequent when the majority variant has lower fitness. To test this hypothesis, we collected plasma samples from 137 donors and their virologically linked seroconverting partners (recipients) a median of 46 days beyond the estimated date of infection (table S1) and compared the amino acid variants determined by Sanger sequencing at each position in the Gag, Pol, and Nef proteins. Restricting our analysis to the 228,362 instances in which a dominant (non-mixture) residue was observed at a given position in both partners, we observed a clear bias for transmission of cohort consensus (≥50%) residues, with 99.65% of donor variants that matched cohort consensus transmitted to the partner compared with 92.61% of variants that were defined as polymorphisms (216,589 of 217,348 versus 10,200 of 11,014; $P < 1 \times 10^{-16}$, Fisher's exact test), indicating that donor minority variants are more likely to be

[1]Microsoft Research, Redmond, WA 98052, USA. [2]Emory Vaccine Center at Yerkes National Primate Research Center, Emory University, Atlanta, GA 30329, USA. [3]Ragon Institute of Massachusetts General Hospital, Massachusetts Institute of Technology and Harvard University, Cambridge, MA 02114, USA. [4]Division of Infectious Diseases, Beth Israel Deaconess Medical Center, Boston, MA 02215, USA. [5]Nuffield Department of Clinical Medicine, University of Oxford, Oxford OX1 7BN, UK. [6]National Institute of Health Research, Oxford Biomedical Research Centre, Oxford OX3 7LE, UK. [7]Oxford Martin School, University of Oxford, Oxford OX1 3BD, UK. [8]HIV Pathogenesis Programme, Doris Duke Medical Research Institute, Nelson R. Mandela School of Medicine, University of KwaZulu-Natal, Durban 4013, South Africa. [9]KwaZulu-Natal Research Institute for Tuberculosis and HIV (K-RITH), Nelson R. Mandela School of Medicine, University of KwaZulu-Natal, Durban 4001, South Africa. [10]Max Planck Institute for Infection Biology, D-10117 Berlin, Germany. [11]Department of Medicine, University of Alabama at Birmingham, Birmingham, AL 35294, USA. [12]International AIDS Vaccine Initiative, London SW10 9NH, UK. [13]Imperial College of Science Technology and Medicine, London SW10 9NH, UK. [14]International AIDS Vaccine Initiative, San Francisco, CA 94105, USA. [15]Department of Epidemiology and Biostatistics, University of California, San Francisco, San Francisco, CA 94105, USA. [16]Rwanda-Zambia HIV Research Group: Zambia-Emory HIV Research Project, Lusaka, Zambia. [17]Microsoft Research, Los Angeles, CA 98117, USA. [18]Department of Paediatrics, University of Oxford, Oxford OX1 3SY, UK. [19]Department of Pathology and Laboratory Medicine, Emory University, Atlanta, GA 30322, USA. [20]Department of Global Health, Rollins School of Public Health, Emory University, Atlanta, GA 30322, USA.
***Corresponding author. E-mail: carlson@microsoft.com (J.M.C.); ehunte4@emory.edu (E.H.)** †These authors contributed equally to this work. ‡Present address: Department of Pharmaceutics, Washington National Primate Research Center, University of Washington, Seattle, WA 98121, USA. §Present address: Google Inc., Venice, CA 90291, USA. ¶Present address: Department of Mathematics and Computer Science and Artificial Intelligence Laboratory, Massachusetts Institute of Technology, Cambridge, MA 02139, USA.

transmitted when the donor majority variant differs from the cohort consensus. An example of this bias was observed at Nef71, which is adjacent to the critical PxxP motif implicated in SH3 (Src homology 3) domain binding and major histocompatibility complex (MHC) class I down-regulation (*22*, *23*). Among the 114 donors where the consensus arginine was observed as the dominant donor variant, arginine was transmitted to 112 recipients; in contrast, the dominant residue was transmitted from only 7 of 14 donors where polymorphic lysine or threonine was dominant ($P = 1 \times 10^{-6}$, Fisher's exact test), suggesting a bias toward the transmission of consensus arginine at this site.

Within each couple, a median of 99.69% of donor sites matching cohort consensus were transmitted, compared to only 94.38% for polymorphic donor sites ($P < 1 \times 10^{-16}$, signed-rank test) (Fig. 1A). Similar results were observed for sites in the donor where we observed a mixture of two amino acids in the population sequences but a single amino acid in the recipient; in these instances, consensus was still preferentially transmitted (median, 60%; $P = 1.9 \times 10^{-10}$, signed-rank test), suggesting that this result was not driven by perfectly conserved sites that may be similarly conserved in the host (Fig. 1B).

Selection bias can be modeled by a binomial process

To further investigate the apparent bias against the transmission of non-consensus amino acids, we modeled transmission as a binomial mixture process, which assumes that each virus in the donor quasispecies is part of a subpopulation, and each virus within that subpopulation is equally and independently likely to establish infection (see Methods). Assuming a low probability of transmission, the odds that a donor amino acid a at a given position is observed in the recipient founder virus F is approximately the relative frequency of a in the donor quasispecies multiplied by the relative selection advantage of a, given by

$$\frac{\Pr(a \in F)}{\Pr(a \notin F)} \approx \frac{f_a}{1 - f_a} \times \frac{p_a}{p_{\overline{a}}}$$

where f_a is the frequency of viruses with a in the donor quasispecies, and $p_a/p_{\overline{a}}$ is the relative advantage for transmission that viruses with a have over viruses without a ($\overline{a}$) (p_a is the a priori probability that a virus of type a will establish infection, and similarly for $\overline{a}$). We refer to this latter ratio as the "selection bias" and say that the transmission bottleneck is "unbiased" if the ratio is one (that is, if there is no selection advantage for or against a). The log of this approximation yields the following linear relationship:

$$\text{logodds}(a \in F) \approx \text{logodds}(f_a) + \text{bias}_a \quad (1)$$

in which the log-odds that the founder virus F includes a virus with a is approximately the log-odds of the frequency of a in the donor quasispecies, shifted by the extent of selection bias [$\text{bias}_a = \log(\frac{p_a}{p_{\overline{a}}})$] for or against a. We use "increased selection bias" to refer to an increase in the absolute value of the bias, and "decreased selection bias" to mean the bias moves toward zero. The bias can be modeled as a linear function of fixed or random effects, allowing the estimation of the effects of features of interest on overall selection bias.

Deep sequencing confirms the statistical model for selection bias

We confirmed the above relationship by deep sequencing of viruses from five linked transmission pairs, treating a as an indicator that a virus matches the donor dominant variant in the virus quasispecies at a particular site, then treating each site as an independent set of observations, to obtain sensitive estimates of the frequency of each site (f_a) in each donor. We observed a linear relationship between the log-odds of f_a and the observed log-odds of the transmission probability, with a clear bias against transmission of non-consensus polymorphisms (Fig. 2A), consistent with Eq. 1. For example, an amino acid observed in 85% of the donor viruses will be transmitted with 85% probability if it matches cohort consensus, compared to only a 65% probability if it does not.

Odds of transmission are predicted by factors related to viral fitness

Although the frequency of the amino acid in the cohort (cohort frequency) and that in the donor's quasispecies (quasispecies frequency) were weakly correlated (Spearman $\rho = 0.18$, $P < 1 \times 10^{-16}$; fig. S1), each was a significant predictor in a multivariable logistic regression model of transmission ($P < 5 \times 10^{-9}$; Table 1), consistent with cohort frequency serving as a marker of selection bias. We therefore examined the relationship between the cohort frequency of each donor amino acid and the odds of its transmission in all 137 linked transmission couples, and observed a strong continuous relationship between cohort frequency and transmission probability, both at sites where a mixture of amino acids was observed in the donor (Fig. 2B) and at sites where a single residue was observed (Fig. 2C). The continuous nature of these transmission/frequency curves is striking and indicates that even small changes in the relative cohort frequency of an amino acid will have a measurable effect on the odds that that amino acid will be transmitted.

Although cohort frequency is not a direct measure of in vivo fitness, as it may also reflect founder effects or genetic drift, it likely correlates with population-wide in vivo fitness. We thus hypothesized that features that independently predict in vivo fitness would modulate the frequency/transmission curve. First, we found that the in silico predicted protein stability costs of amino acid substitutions modulated the transmission curve, such that amino acids with minimal impact on the protein structure were most likely to be transmitted (Fig. 2D). Our in silico measure of protein stability was, by construction, biased toward consensus residues, which were most likely to match the sequence of the protein used to define the crystal structure. Nevertheless, we found that, for any given cohort frequency, an amino acid that did not affect the structure was more likely to be transmitted than an amino acid with a large impact (in the case of polymorphisms), or than a residue that occurred at a site where many other residues were equally well suited for the structure. Similarly, we found that the number of putative compensatory mutations associated with a given amino acid residue [as estimated from statistical linkage (*24*)] was correlated with an increased probability of transmission, consistent with such mutations being fixed by the compensations, or of compensatory mutations reducing

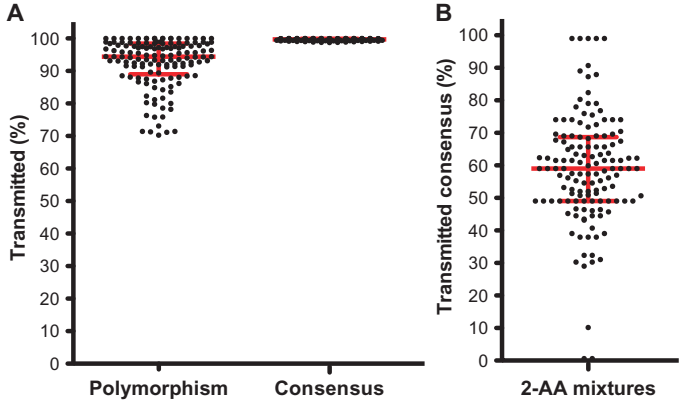

Fig. 1. HIV-1 viruses with amino acid residues matching the consensus of the study population are preferentially transmitted. For each linked transmission couple, the proportion of sites that were transmitted was defined to be the proportion of sites in which the variant observed in the recipient matched that observed in the donor. Sites with a mixture in the recipient were excluded. (**A** and **B**) Donor variants that matched cohort consensus were more likely to be transmitted among all non-mixture sites in the donor (A), whereas a consensus residue that was observed in mixture with one other variant was more likely to be transmitted than was the other variant (B). A nucleotide mixture was called if more than one base resulted in a >25% Sanger peak height. An amino acid (AA) mixture was called if the nucleotide mixture resulted in a mixture of amino acids. Dashed gray line represents the expected frequency of transmission of consensus. Consensus was defined to be any amino acid observed in at least 50% of chronically infected individuals in the Zambian cohort.

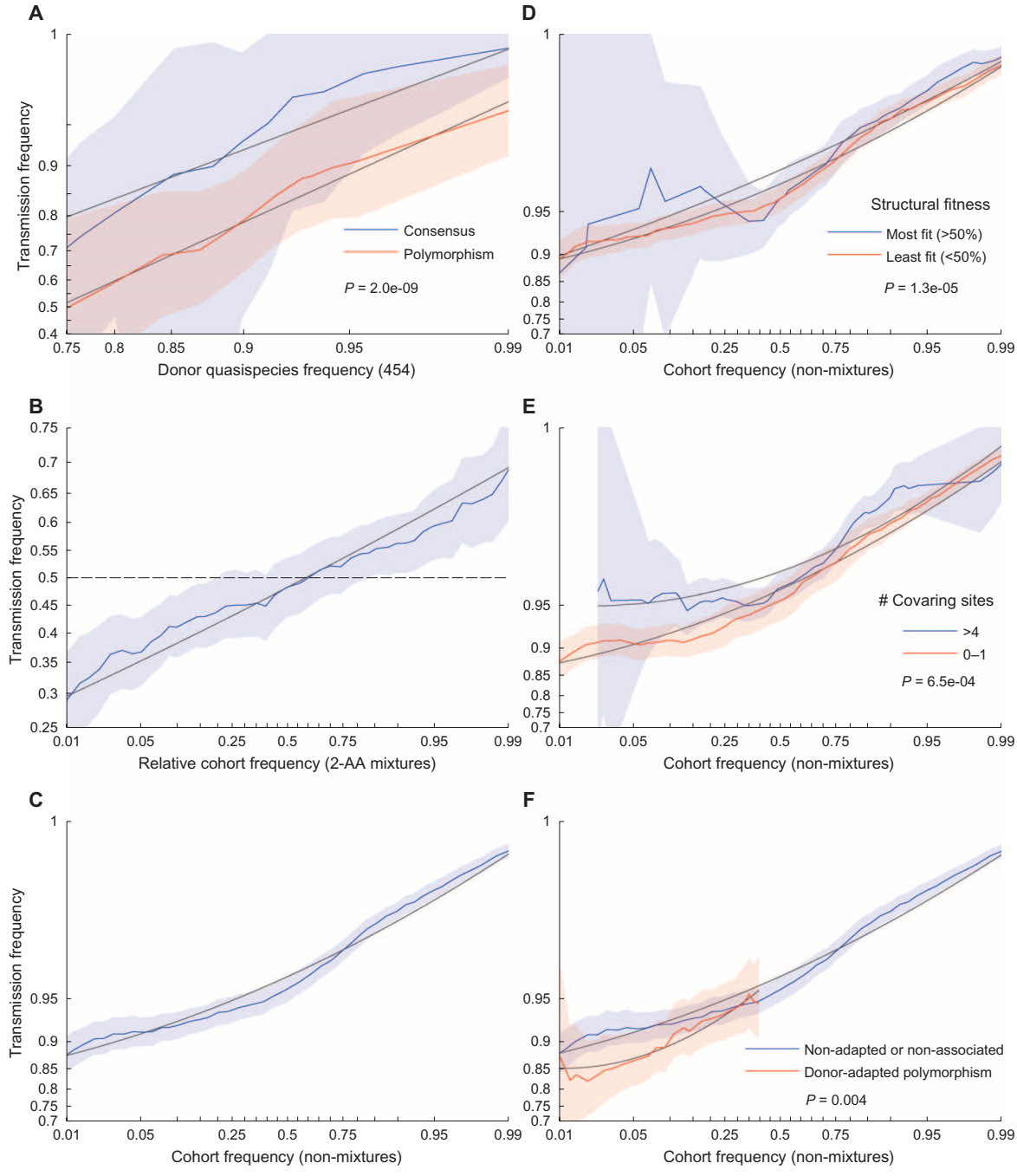

Fig. 2. Viral fitness modulates selection bias in heterosexual HIV-1 transmission. The odds that the donor's amino acid will be transmitted to the recipient is a function of the relative frequency of the amino acid in the quasispecies as well as the fitness of that amino acid, as estimated here by several independent metrics. Each plot shows the empirical transmission probability (odds on a $\log_{10}$ scale) of a variant as a function of one or more parameters. Empirical transmission probabilities (solid colored lines) are estimated counting the proportion transmitted within a continuous sliding window of width 1 log-odds with respect to the feature represented on the abscissa. All log-odds values are smoothed by adding a pseudo-count. Gray lines represent a quadratic fit to the sliding window averages; shaded areas represent 95% confidence intervals estimated using the percentile-*t* method on 1000 multilevel bootstraps. *P* values are taken from Table 1 (A) or Table 2 (D to F) and represent the *P* value from a multilevel logistic regression model in which all features are treated as continuous variables, as described in Methods. (**A**) The log-odds of transmission is linearly related to the relative in vivo frequency of the variant in the donor quasispecies, with a near 1-to-1 mapping for variants that match cohort consensus. In contrast, polymorphisms are uniformly less likely to be transmitted (N = 8314 observations over 5 couples). (**B**) Among N = 3115 donor sites containing two–amino acid mixtures from 137 couples, the probability of transmission is also strongly predicted by the relative cohort frequency of the amino acid. Transmission probability is with respect to a randomly chosen member of the mixture; the abscissa represents the relative frequency of that amino acid in the cohort compared to the other amino acid in the mixture. (**C** to **F**) Among N = 228,362 non-mixture donor sites from 137 couples, the odds of transmission is predicted by (C) the frequency of the amino acid in the cohort, (D) the relative impact of the variant on the stability of the protein structure (low impact implies high fitness), (E) the number of covarying sites statistically linked with the variant, and (F) whether the variant is consistent with immune escape from one of the donor's HLA alleles (only polymorphic sites are shown). See Methods for feature definitions.

the fitness cost that would otherwise be predicted by cohort frequency (Fig. 2E). Finally, sites consistent with immune escape from the donor's human leukocyte antigen (HLA) alleles (Fig. 2F and fig. S2, A to C) were less likely to be transmitted, consistent with replicative costs frequently associated with uncompensated immune escape mutations (*18*, *19*, *25*). We also observed a bias against transmission of residues that could be targeted by the recipient's HLA alleles (fig. S2D). This may suggest a selection advantage for pre-escaped viral sequences, though rapid escape and fixation after transmission could not be ruled out as an alternative cause. Differences were also observed among viral proteins (fig. S2, E and F), though such differences may primarily reflect differences in quasispecies diversity.

Each of these features was significant in a multilevel, multivariable logistic regression model (*26*) that included per-couple random effects to account for correlated regression residuals among sites taken from the same couples (Table 2). Thus, because each of these features is consistent with in vivo fitness, the transmission bottleneck appears to favor viruses with replicative advantages (that is, $\text{bias}_a \neq 0$).

Transmission risk factors reduce selection bias

The selection bias is defined above as the relative ability of viruses of type a to establish infection. Some risk factors increase the odds that any virus will establish infection. If a risk factor increases the ability of each virus to establish infection by a constant factor c, as opposed to simply increasing the frequency of exposure or the viral dosage upon exposure, then the resulting selection bias is approximately $\log\frac{p_a+c}{p_{\bar{a}}+c}$, which tends toward zero as c becomes large relative to p_a and $p_{\bar{a}}$. Such risk factors will therefore reduce the selection bias. To test for a reduction in selection bias during transmission, we analyzed three previously reported risk factors: donor VL (*27*, *28*), male-to-female transmission (*29*), and the presence of genital ulcers or inflammation (GUI) in the recipient partners over the 12-month period before the event of transmission (*30*, *31*). We observed a significant reduction in selection bias (most easily seen as a reduction in the effect of cohort frequency on transmission) for couples in which the donor had a high VL (Fig. 3A) or the recipient was a female (Fig. 3D). Although the presence of GUI had no effect on female recipients, GUI eliminated the increased selection bias experienced by male recipients (Fig. 3D). Consistent with prior observations that donor VL is a more important risk factor for male than for female recipients (*27*), increased donor VL reduced the bottleneck in female-to-male (Fig. 3B), but not male-to-female (Fig. 3C), transmission, with high donor VL eliminating the increased selection bias experienced by GUI-negative male recipients (Fig. 3, D to F). A composite risk index (standardized donor VL plus one if the recipient is female or a male with GUI) was significant in a multilevel, multivariable logistic regression model ($P = 6 \times 10^{-5}$; Table 2).

Under the assumption that the number of transmitted viruses is binomially distributed (that is, the per-virus particle probability of transmission is independent and identically distributed), the size of the donor viral population will not substantially affect selection bias (see notes S1 and S2 and fig. S3 for further discussion on this topic). Thus, these results suggest that the increased risk of transmission among male recipients that is linked with higher donor VL is attributable, at least in part, to increased in vivo viral fitness, consistent with the observation that donor VL is correlated with higher in vitro replicative capacity and higher early set-point VL in recipient partners (*32*–*34*). In contrast, the reduction in selection bias experienced by female recipients and male recipients with GUI suggests an overall reduced selection bias, which is more conducive to infection by lower-fitness variants.

Variable reversion rates compensate for variations in selection bias

Transmission of immune escape amino acids characterized by low fitness often results in gradual reversion to high-fitness (consensus) amino acids (*35*–*39*), suggesting that relative reversion rates can serve as a marker for the transmission of low-fitness variants. We hypothesized that, if the selection bias acts against the transmission of less-fit polymorphisms and such bias is reduced in female recipients, then the founder viruses of women will include a higher number of costly variants, which will revert more quickly than the variants transmitted to men. We therefore collected longitudinal plasma samples for 81 of the transmission pairs at an average interval of 3 months out to 24 months after infection. Consistent with the selection bias analysis, consensus residues were transmitted at a greater proportion of polymorphic donor sites to male recipients compared to female recipients (5.98% versus 4.22%); as hypothesized, the rate at which transmitted polymorphisms reverted to consensus was significantly faster among female (0.24%/month) than male recipients (0.12%/month) ($P = 0.016$; Fig. 4A and fig. S4), providing further evidence that selection bias is less stringent in male-to-female than in female-to-male transmission (Fig. 3D).

When we included all selection bias features in a Cox proportional hazard model of reversion from the early founder sequences through 24 months after infection, the relative hazard of all but one feature (the structural impact of an amino acid, which had no significant effect on reversion) was consistent with what would be predicted from selection bias: Selection features consistent with increased viral fitness predicted slower reversion, and selection features consistent with increased susceptibility predicted faster reversion (table S2). In addition, recipients who were transmitted a higher number of polymorphisms at sites where their donor was polymorphic had lower early set-point VL (Spearman $\rho = -0.34$, $P = 0.002$; Fig. 4B), consistent with previous reports that the in vitro *gag* fitness of early viral isolates (*19*, *21*), as well as the transmission of HLA-B escape variants (*40*, *41*), predicts early set-point VL. This further corroborates the in vivo fitness costs of polymorphisms that are actively selected against during the transmission bottleneck and is consistent with our previous observation of a significantly lower VL in these women early in infection (*34*).

Amino acid features predict odds of transmission of viral sequences and populations

The selection bias models described above result in a predicted log-odds that a given residue at a given site will be transmitted. If we treat all sites within an individual as independent (conditioned on the protein), then the mean of the predicted log-odds over a given viral sequence yields a transmission index that estimates how likely overall an individual sequence is to be transmitted. Given the observed selection bias, we expect that founder viruses will tend to have above-average transmission indices relative to the donor quasispecies. Using limiting dilution single genome amplification (SGA), we obtained a median of 19 (range, 4 to 27) Gag sequences for each of 17 donors and compared the transmission indices of donor amplicons to those of the linked founder sequences. Overall, founder sequences had higher than expected Gag transmission indices (Fig. 5, A and B; $P = 0.02$), though viruses with even higher transmissibility indices were frequently observed in the donor quasispecies, highlighting the stochastic nature of transmission.

The observed variation in mean donor transmissibility suggests that some quasispecies are,

Table 1. Donor quasispecies and cohort frequencies as additive predictors of transmission.

Feature	γ estimate*	SE	z	Pr(>|z|)	Likelihood ratio test†	
					χ^2 (df)	Pr(>χ^2)
(Intercept)	7.63	0.557	13.70	$<1 \times 10^{-16}$		
Donor quasispecies frequency‡	0.56	0.053	10.65	$<1 \times 10^{-16}$		
Cohort frequency (cfreq)§	1.98	0.541	3.66	2.5×10^{-4}	40.1 (2)	2.0×10^{-9}
cfreq^2	0.30	0.121	2.45	0.014		

*Fixed effect parameters. Model was fit using logistic regression. Model fit was not improved by the addition of protein domain features or random effects. Compare to Fig. 2A. †Combined significance for sets of features was estimated using the likelihood ratio test. ‡The standardized smoothed log-odds of the frequency of the amino acid in the donor from deep sequencing. Smoothing factor is $q = 1/50$. §The standardized smoothed log-odds of the frequency of the amino acid in the cohort. Smoothing factor is $q = 1/350$.

on average, more transmissible than others and may therefore be more likely to establish infection. To test this, we obtained Gag, Pol, and Nef sequences from 181 risk-matched, chronically infected individuals who had not transmitted to their partners. Overall, chronically infected partners who had transmitted exhibited higher median transmission indices than individuals who had not yet transmitted (P = 0.009; Fig. 5C), an effect that remained significant when controlling for the donor VL, recipient gender, and GUI risk factors (table S3).

Discussion

The recognition that a single virus, or at most a handful of viruses, establishes infection led to great optimism that the defining characteristics of transmitted founder viruses would be readily identified, leading to a clear vaccine strategy. Although selection bias has been observed to act on the Env protein (*1*–*3*, *10*, *12*, *42*), and may favor viruses that are relatively resistant to interferon-α (*12*), no deterministic features have yet been identified. Rather, the bottleneck appears to act at a stochastic level, favoring, though not exclusively, viruses with higher overall fitness in the context of the mucosal compartment. Here, we show that selection bias also acts on non-Env proteins and can be estimated by such generic features as the effect of a variant on protein stability, dependency of the variant on compensation, and the overall frequency of the variant in the cohort. That each of these features also predicts rates of reversion in the linked recipient further supports their role as markers of in vivo fitness. These observations confirm the hypothesis that minor fitness advantages play an important role in transmission beyond features that depend on the nature of target cells in the mucosa. Although the majority of these features likely correlate with fitness in many immunological compartments, the observation that variants linked to immune escape in the donor were less likely to be transmitted—and more likely to revert if they were transmitted—highlights the fact that in vivo fitness in chronic infection must account for immune pressures that may be absent at the site of transmission. As a result of selection bias, transmission often results in a step back in evolutionary time toward consensus, thereby slowing the rate of population-wide evolution, consistent with the low rate of population-wide evolution observed in the North American epidemic (*43*).

The observation that transmission risk factors reduce the selection bias further corroborates the role of fitness in transmission and provides important clues as to the mechanisms of increased risk. In the case of donor VL, whereas the quantity of virus during exposure likely plays a role in increased risk, it cannot explain the observed reduction in selection bias, suggesting that the underlying fitness typical of high VL is playing an important role as well (see note S1 and fig. S3 for simulation experiments and further discussion on this point). This in turn suggests that interventions that reduce VL without altering viral fitness (such as antiretroviral therapy in the absence of virologic escape) will have diminished effects on transmission compared to those that similarly reduce VL but additionally weaken the virus. Conversely, immunological escapes that confer a net advantage on the virus in the donor, and therefore result in higher VL, may nonetheless reduce the rate of transmission as a result of weakening the virus.

Selection bias was here measured by comparing genetic variants found in donor and recipient blood, and thus in principle could reflect selection occurring at any number of steps, including selection of viruses in the donor genital compartment or productive infection followed by reversion. Our previous SGA analysis of virus variants in the donor genital tract of Zambian transmission pairs argued against preferential selection in this compartment (*44*), and a deeper analysis of the reversion data also provides evidence that the selection bias observed above is

Table 2. Multilevel multivariable logistic regression model of transmission selection bias.

Feature	γ estimate*	SE	z	Pr(>|z|)	Likelihood ratio test†	
					χ^2 (df)	Pr(>χ^2)
(Intercept)	6.43	0.558	11.53	$<1 \times 10^{-16}$		
Cohort frequency (cfreq)‡	1.70	0.119	14.24	$<1 \times 10^{-16}$		
cfreq^2	0.24	0.019	12.28	$<1 \times 10^{-16}$		
No. of covarying sites	0.04	0.012	3.35	8.2×10^{-4}		
Susceptible to recipient HLA	−0.60	0.142	−4.18	2.9×10^{-5}		
Donor Esc polymorphism : Gag§¶	0.00	0.253	0.00	0.998		
Donor Esc polymorphism : Pol	−0.69	0.197	−3.49	4.9×10^{-4}	13.3 (3)	0.004
Donor Esc polymorphism : Nef	0.48	0.326	1.48	0.140		
Risk index**	0.15	0.084	1.74	0.081		
Risk index : cfreq	0.14	0.067	2.15	0.032	22.2 (3)	5.9×10^{-5}
Risk index : cfreq^2	0.06	0.015	3.65	2.6×10^{-4}		
Estimated time since infection	−0.16	0.132	−1.18	0.236		
p17††	0.22	0.228	0.97	0.333		
p17 : cfreq	0.19	0.103	1.83	0.067		
p24	1.72	0.285	6.03	1.7×10^{-9}		
p24 : cfreq	0.64	0.116	5.47	4.6×10^{-8}		
p15	0.65	0.241	2.71	0.007		
p15 : cfreq	0.28	0.106	2.66	0.008		
Protease	0.62	0.307	2.03	0.042		
Protease : cfreq	0.15	0.135	1.09	0.278		
RT	0.62	0.208	2.98	0.003		
RT : cfreq	0.15	0.095	1.60	0.109		
Integrase	0.50	0.225	2.23	0.026		
Integrase : cfreq	0.19	0.105	1.78	0.076		
Nef	0.97	0.236	4.12	3.8×10^{-5}		
Nef : cfreq	0.41	0.310	1.34	0.181		
Nef CD4/MHC domains	0.50	0.104	4.80	1.6×10^{-6}		
Nef CD4/MHC domains : cfreq	0.52	0.133	3.88	1.0×10^{-4}		
Structural frequency (sfreq)‡‡	0.33	0.144	2.29	0.022		
sfreq : cfreq	0.49	0.129	3.80	1.5×10^{-4}	24.2 (3)	2.2×10^{-5}
sfreq : cfreq^2	0.13	0.029	4.45	8.6×10^{-6}		
Random effects§§	**SD**	**Corr**				
(Intercept)	0.91					
cfreq	0.08	−1.00				

*Fixed effect parameters. Model was fit using multilevel logistic regression. Model fit was not improved by the addition of quadratic interaction effects between cohort frequency and protein domains or couple ID. See Methods for feature definitions. Compare to Figs. 2 and 3. †Likelihood ratio test performed between the full model and a model excluding the grouped set of features. ‡Cohort frequency was standardized (zero mean, unit variance). §Donor CTL escape features were scaled by 1 − cfreq to reflect the probability that de novo escape occurred in the donor. ¶Colon (:) signifies a multiplicative interaction. **Standardized (zero mean, unit variance) donor VL plus one if the recipient is female or a male with GUI. ††Protein domain features are treated as covariates. It is not clear whether significance implies a different relationship between cohort frequency and odds of transmission, or simply reflects variations in mean donor quasispecies diversity. ‡‡Defined as the expected frequency of an amino acid in the cohort based on the impact of that amino acid on the protein structure (see Methods; frequency was standardized). Structural features were evaluated separately from the rest of the model because crystal structures are available for only a subset of sites. Model estimates reflect model fit using all parameters. Likelihood ratio test is against a null model including only the main parameters, but fit on sites with structural information. §§Random effects were applied to each couple. The intercept and the slope of cohort frequency were allowed to vary as a bivariate Gaussian. Maximum likelihood SDs are reported. The maximum likelihood covariance term is presented as a correlation.

not an artifact of rapid reversion in the narrow time frame of acute infection. First, nonparametric estimates of reversion rates place the rate of reversion at 0.12% per month for males (0.24% for females), a rate that holds constant after 3 months of infection. In contrast, the inferred rate of reversion peaks during the transmission window with a maximum that is an order of magnitude higher than the constant rate observed

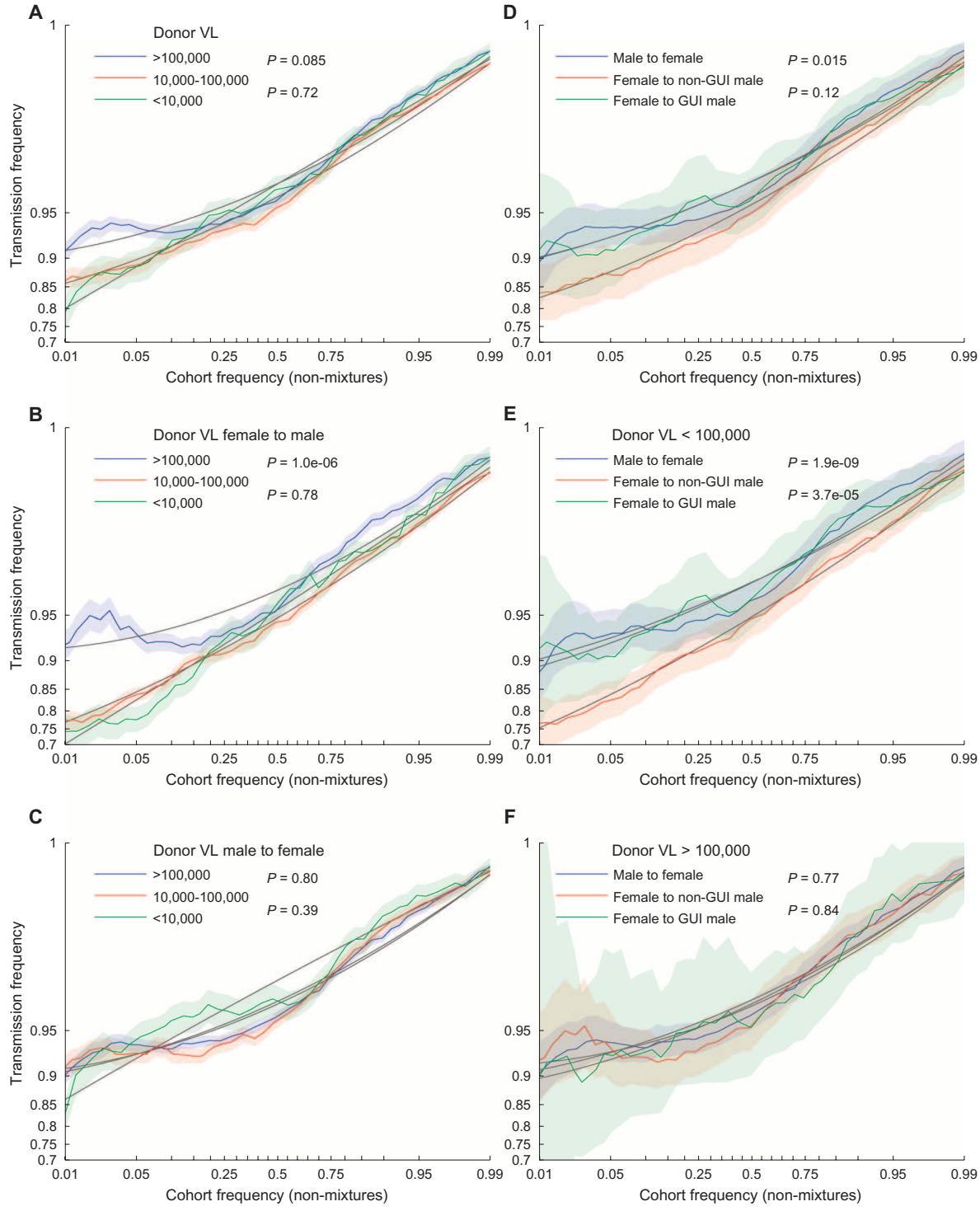

Fig. 3. Transmission risk factors reduce selection bias in heterosexual HIV-1 transmission. The empirical log-odds of transmission is plotted as a function of the frequency of each variant in the cohort, as defined in Fig. 2. Donor VL near the time of transmission, sex of the recipient, and presentation of GUI in male recipient partners each affect the selection bias. (**A** to **C**) Individuals are segregated by donor VL levels used in previous studies of transmission risk (*27*, *28*). High donor VL reduces transmission selection bias in (B) female-to-male, but not in (C) male-to-female, transmission. (**D** to **F**) Male recipients appear to have increased selection bias compared to female recipients, an effect that is mitigated by the presence of GUI (D and E) or high donor VL (F). Quadratic polynomial fit (solid gray lines) and 95% confidence intervals (shaded area) were estimated as in Fig. 2. *P* values are estimated from a nonparametric, block-bootstrap method that tests the null hypothesis that the normalized areas under two curves are identical (see Methods for details).

during the remainder of the sample period (fig. S4). It is unlikely that reversion rates would change so suddenly, and phylogenetic analyses of single genome amplified viral sequences from these early time points in this cohort (*3*, *6*, *44*) strongly argue against the founder virus undergoing significant rapid reversion in the first few days after transmission that must be enabled by rapid selective sweeps. Moreover, the observation in this study that features that reduced selection bias predict faster reversion is not consistent with the proposition that selection bias is an artifact of rapid reversion, as it would require reversion rates to be faster in men in the first month of infection and faster in women in the following years. These data thus argue that selection bias occurs primarily at the site of transmission, and suggest that sexual exposure frequently results in nonproductive infection of target cells until viruses with higher fitness gain a foothold for successful dissemination.

The observation that sequence features alone can predict the odds of transmission for a particular virus population highlights the importance of transmission selection bias and provides a clear mechanism for risk factors that reduce selection bias by increasing virulence or susceptibility. In addition, transmission of even subtly weaker viruses, either by increased susceptibility that allows transmission of less fit viruses from the donor quasispecies or because all variants in the donor quasispecies have lower fitness, may result in a clinical advantage for recipients (*40*, *41*). Although the advantage of such subtle effects may be short-lived because of increased reversion that typically restores viral fitness, previous reports indicate that the replicative fitness costs of early viral sequences result in a sustained clinical advantage for the linked recipient (*19*, *21*). Paradoxically, by increasing the selection bias at the transmission bottleneck, reduction of susceptibility would increase the expected fitness of breakthrough viruses that manage to establish infection and may therefore worsen the prognosis for the newly infected partner. Conversely, preventative or therapeutic approaches that even marginally weaken the virus may reduce overall transmission rates via a mechanism that is independent from the quantity of circulating virus and may provide long-term benefits even upon successful transmission.

Methods

Study subjects

All participants in the Zambia Emory HIV Research Project (ZEHRP) discordant couples cohort in Lusaka, Zambia, were enrolled in human subjects protocols approved by both the University of Zambia Research Ethics Committee and the Emory University Institutional Review Board. Before enrollment, individuals received counseling and signed a written informed consent form agreeing to participate. The subjects selected from the cohort were initially HIV-1 serodiscordant partners in cohabiting heterosexual couples with subsequent intracouple (epidemiologically linked) HIV-1 transmission (*45*–*47*). Epidemiological linkage was defined by phylogenetic analyses of HIV-1 *gp41* sequences from both partners (*48*). Viral isolates from each partner in the transmission pair were closely related, with median and maximum nucleotide substitution rates of 1.5 and 4.0%, respectively. In contrast, the median nucleotide substitution rate for unlinked HIV-1 C viruses from the Zambian cohort and elsewhere was 8.8% (*48*). The algorithm used to determine the estimated date of infection was previously described by Haaland *et al.* (*3*). All patients in this cohort were antiretroviral therapy naïve. Zambian linked recipients were identified with a median (interquartile range) estimated time since infection (ETI) of 46 (42 to 60.5) days, at which time plasma samples were obtained from both the transmitting source partner (donor) and the linked seroconverting partner (recipient). All of the transmission pairs included in this study are infected with subtype C HIV-1.

A control group of 181 not yet transmitting (NYT) HIV-positive partners were selected from discordant couples enrolled for a minimum of 1 year, and matched as a group with the transmitting couples for a risk factor score derived from data on recent (i) sexual activity with the primary partner, (ii) sperm count in vaginal wash of female partner, (iii) pregnancy history, and (iv) GUI disease. These factors were used to create a risk profile for every transmission pair, and then NYT partners in each of four successive risk strata were selected in the same proportion to the representation of donor in each of the four strata, so that the two sets of HIV-positive partners were frequency-matched by their risk profile. Summary statistics for donor and NYT individuals are available in table S1.

Parameter definitions and methods

Amplification and sequencing of gag, pol, and nef genes

Viral RNA was extracted from 140 μl of plasma samples using the Viral RNA Extraction Kit

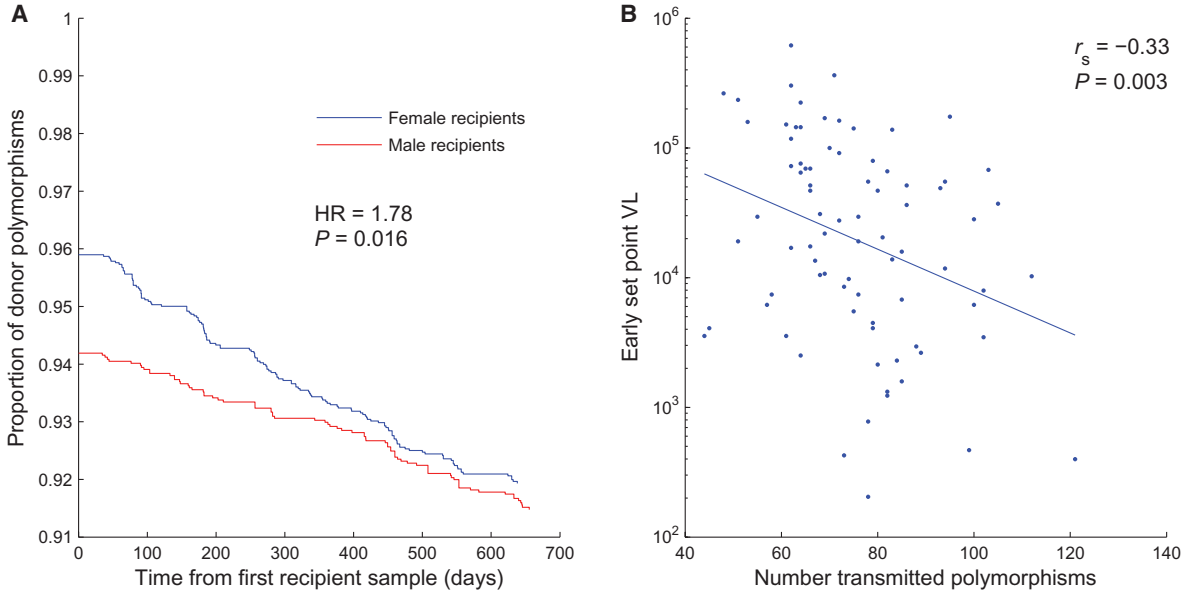

Fig. 4. Transmission of low-fitness viruses changes reversion dynamics and predicts lower early set point VL in the recipient. (**A**) The proportion of donor non-consensus polymorphisms that remain polymorphic is plotted as a function of days after the first available recipient sample (N = 6220 polymorphisms from 81 couples). The ordinate at time 0 represents the fraction of donor polymorphisms that were transmitted. Female recipients permit transmission of more polymorphisms than males, but these revert at a faster rate. HR and P value were taken from a multivariable Cox proportional hazard model (see table S2). See fig. S4 for estimates of instantaneous reversion rates as a function of time since the estimated date of infection. (**B**) The number of transmitted polymorphisms at sites that were polymorphic in the linked donor negatively correlates with early set point VL in the recipient (N = 81), corroborating the fitness cost imposed by many of these variants.

(Qiagen) and eluted in 60 µl of elution buffer. *Gag-pol* population sequences were generated using nested gene-specific primers. Combined reverse transcription polymerase chain reaction (RT-PCR) and first-round synthesis was performed using SuperScript III Platinum One-Step RT-PCR (Invitrogen) and 5 µl of viral RNA template. RT-PCR and first-round primers include GOF (forward) 5′-ATTTGACTAGCGGAGGCTAGAA-3′ and VifOR (RT-PCR and reverse) 5′-TTCTACGGAGACTCCATGACCC-3′. Second-round PCR was performed using Expand High Fidelity Enzyme (Roche) and 1 µl of the first-round PCR product. Nested second-round primers include GIF (forward) 5′-TTTGACTAGCGGAGGCTAGAAGGA-3′ and VifIR (reverse) 5′-TCCTCTAATGGGATGTGTACTTCTGAAC-3′. *Nef* sequences were generated in a similar fashion, using an additional set of nested gene-specific primers. RT-PCR and first-round primers include Vif1 (forward) 5′-GGGTTTATTACAGGGACAGCAGAG-3′ and OMF19 (RT-PCR and reverse) 5′-GCACTCAAGGCAAGCTTTATTGAGGCTTA-3′. Second-round primers include Vif2 (forward) 5′-GCAAAACTACTCTGGAAAGGTGAAGGG-3′ and OMF19 (reverse). An average of 800 RNA templates was added to the One-Step RT-PCR. Three positive amplicons per individual were pooled, representing on average 2400 input genomes, and purified with the PCR Purification Kit (Qiagen). Purified products were sequenced by the University of Alabama at Birmingham DNA Sequencing Core. Sequence chromatograms were analyzed using Sequencher 5.0 (Gene Codes Corp.), and degenerate bases were denoted using the International Union of Pure and Applied Chemistry (IUPAC) codes when minor peaks exceeded 25% of the total peak height in both forward and reverse reads. Codons containing degenerate bases were defined as "mixtures," whereas those with no evidence of degenerate bases or with minor peaks comprising less than 25% of the total were defined as "dominant variants."

Sequences were codon-aligned to the HXB2 reference sequence using HIVAlign (www.hiv.lanl.gov/content/sequence/VIRALIGN/viralign.html), followed by hand-editing. For all analyses, we considered sites where a dominant variant was identified, and we excluded sites where a gap or a stop codon was present. In cases where transmission was considered, a site was excluded if a mixture, gap, or stop codon was observed in either the donor or the recipient. For transmission indices, exclusion criteria were based on the sequence in question alone—no information was taken from the individual's partner. For a given couple, a residue was defined to have been transmitted if the same amino acid was observed in both donor and recipient. For Fig. 2B (transmission from mixtures), we limited the analysis to mixtures consisting of two amino acids in the donor, then randomly selected one of the residues to test if it transmitted. For Fig. 1B (proportion of mixtures that transmitted consensus), we limited the analysis to donor mixtures consisting of two amino acids, one of which matched cohort consensus, then measured the per-couple proportion of these sites in which the consensus residue was transmitted.

Protein domains were used as covariates in the modeling. Protein domains were defined as follows: Gag was split into p17, p24, and p15; Pol was split into protease (Pr), reverse transcriptase (RT), integrase, and the Gag-Pol transframe (GagPolTF) region. The CD4 and MHC down-regulation domains of Nef, here defined as HXB2 positions 2, 17–26, 57–58, 62–65, 69–81, 154–155, 164–165, and 174–175 (*49*), were treated as a separate Nef domain.

454 sequencing was performed on five donors to estimate the quasispecies frequency of donor variants. For each donor, we amplified from an average of 13,000 RNA templates and obtained two overlapping PCR amplicons spanning the entire protein-coding region of the HIV-1 genome. Pooled amplicons were acoustically sheared to produce fragments between 300 and 800 bases in length. Batched, barcoded samples were amplified by emulsion PCR and sequenced on a 454 Junior (Roche) as described previously (*50*). To achieve sufficient detection of minor variants, we required a targeted coverage per site of 250-fold. The raw sequence output ("reads") were assembled by Vicuna (*51*) and V-FAT (Broad Institute, www.broadinstitute.org/scientific-community/science/projects/viral-genomics/v-fat) to form a single genome that represents the majority base at each nucleotide position (the consensus assembly). The reads were then corrected for systematic 454 errors, such as homopolymer indels and carry forward/incomplete extensions (CAFIEs), and aligned to the consensus assembly using previously developed software RC454 and V-Phaser

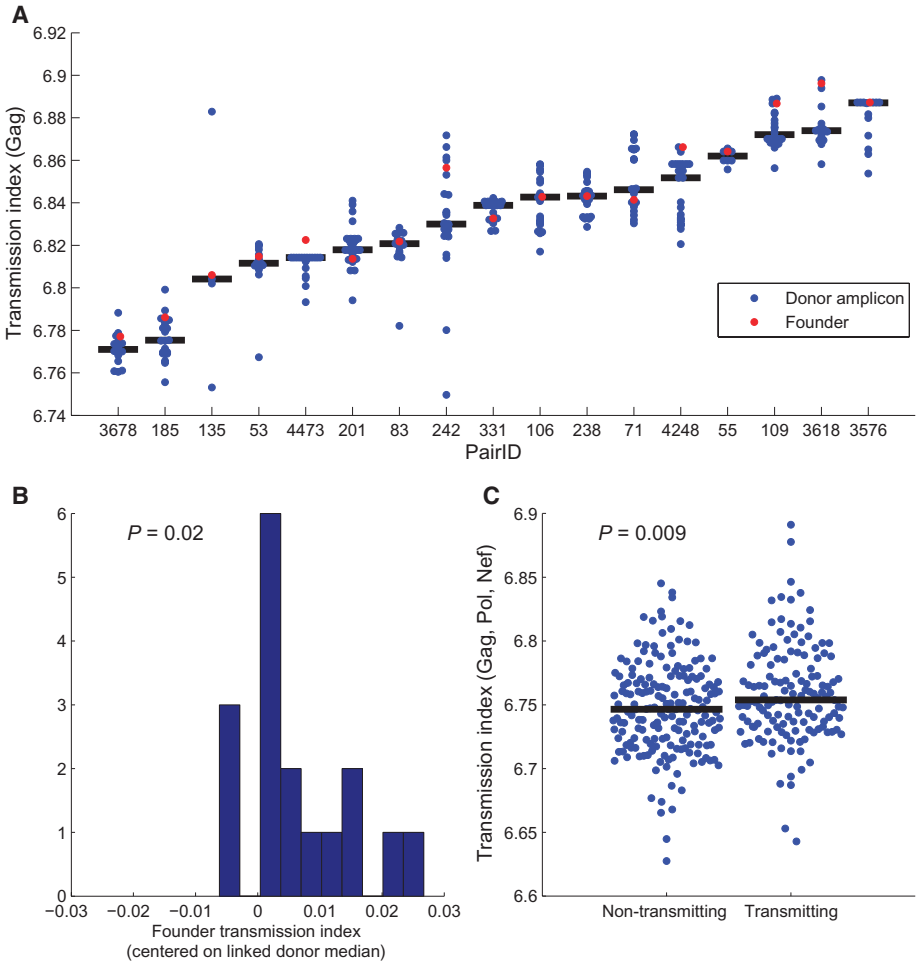

Fig. 5. Sequence-derived transmission index predicts transmission. The transmission index of a sequence was calculated as the mean of the expected log-odds of transmission for each site in the sequence, as estimated by a logistic regression model that included a second-order polynomial of cohort frequency, the number of covarying sites, and offsets and cohort-frequency interactions for each protein domain. Transmission indices were computed out-of-sample using leave-one-out cross-validation. (**A** and **B**) The transmission index for individual donor Gag amplicons compared to the transmission index for the linked founder Gag sequence. Models trained on Gag alone. (A) Transmission index for each couple. Black bar represents the median transmission index of donor sequences. Four sequences with transmission index <6.7 were excluded as outliers. (B) Transmission index of each founder virus, median-centered against the transmission indices for linked donor sequences (*P* value from two-tailed Wilcoxon signed-rank test). (**C**) The overall transmission index of Gag, Pol, and Nef is significantly different between donor and potential source partners in risk-matched discordant couples (*P* value from two-tailed Mann-Whitney rank-sum test).

(50), as well as with custom programs written in Perl. These alignments were hand-refined to match the corresponding population sequences. Codon positions in which the 454-derived dominant variant differed from the Sanger sequencing–derived amino acid were excluded. The quasispecies frequency of a codon was taken to be the fraction of reads spanning a codon position that contained the codon. Amino acid frequencies were defined to be the sum of the frequencies of codons encoding the same amino acid. Sites with a read depth of less than 10 were excluded.

Limiting dilution SGA sequencing of *gag* was performed on 11 donor-recipient pairs, as previously described (3), but using *gag*-specific primers. Briefly, full-length *gag* was amplified from peripheral blood mononuclear cell DNA by nested PCR using the following primers: outerfor1 5′-AAGTAAGACCAGAGGAGATCTCTCGAC-3′, gagR2b 5′-GCCAAAGAGTGATTTGAGGG-3′, innerfor1 5′-TTTGACTAGCGGAGGCTAGAAGGA-3′, and innerrev1 5′-GTATCATCTGCTCCTGTGTCTAAGAGAGC-3′. In addition, six pairs of *gag* SGA sequences were extracted from near–full-length genome sequences amplified by similar methods to those described previously (44). Sequences were aligned to the cohort Sanger sequence alignments.

Cohort frequencies were defined with respect to sequences taken from 375 (*gag*), 327 (*pol*), or 350 (*nef*) chronically infected individuals in the Zambian cohort. The donor and NYT individuals studied here were the subset for whom *gag*, *pol*, and *nef* sequences were available. The cohort frequency was taken to be the proportion of individuals with a given amino acid, excluding all individuals with gaps, stop codons, or missing data at the site in question. Amino acid mixtures containing k amino acids contributed $1/k$ observations to each amino acid in the mixture. Cohort consensus was defined to be residues observed in a majority (≥50%) of sequences, whereas polymorphism was defined as all nonmajority (<50%) residues. All residues at highly polymorphic sites in which no residue was observed in at least half the population were thus defined as polymorphisms.

Smoothed log-odds ratios were used to transform cohort and quasispecies frequencies as input variables for the logistic regression models, as well as for visualization of cohort, in vivo, and transmission frequencies. The smoothed log-odds account for finite sampling by including a prior that pushes log-odds ratios toward 0. For a probability p with smoothing factor q, $q \in [0, 1]$, the smoothed log odds ratio is defined as $\mathrm{slod}(p) = \log(p + q) - \log(p + q)$, which is equivalent to adding a pseudo-count of qN if the probability is a proportion derived from N observations. Here, we use $q = 1/350$ for cohort frequencies and $q = 1/50$ for quasispecies frequencies. For visualization, empirical transmission frequencies are smoothed by the same factor as the variable to which it is being compared.

Virologic and clinical parameters

HIV plasma VL was determined at the Emory Center for AIDS Research Virology Core Laboratory using the Amplicor HIV-1 Monitor Test (version 1.54, Roche). Early set-point VL in recipients was defined as the earliest stable nadir VL value measured between 3 and 9 months after infection and which did not show a significant increase in value within a 3- to 4-month window, as previously described (19). Donor VL was defined as the VL determined at or near the time of seroconversion in the previously HIV-negative partner.

GUI in the linked recipient was defined as at least one instance where genital inflammation or ulceration was noted on a physical examination or was treated between enrollment and seroconversion or during the 12-month period before seroconversion for individuals enrolled for more than 12 months, as previously described (52). Recipient GUI data were missing for three men and three women.

Physics-based estimation of structural impact of point mutations

One possible mechanism by which a mutation can reduce overall fitness is by altering the stability of the viral protein. We therefore used an in silico estimate of protein stability to estimate the impact of a point mutation on the viral structure, then used these estimates to define the energy-based expected frequency of each amino acid. In particular, we first estimated the thermodynamic stability changes caused by each of the 20 amino acids at each site using the FoldX software package (http://foldx.crg.es), as previously described (53). Briefly, the structures of p17 [Protein Data Bank (PDB) code: 2GOL] (54), p24 hexamer (PDB: 3H4E) (55), protease dimer (PDB: 3IXO) (56), RT (PDB: 1DLO) (57), integrase (PDB: 1BIS) (58), and Nef (PDB: 1EFN) (59) were mutated to the clade C consensus sequence (as defined by the consensus of our combined southern African cohort), and the FoldX optimization procedure and probability-based rotamer libraries were used to remove steric clashes and other estimation errors and to reconstruct missing side-chain atoms (60). Then the absolute changes $|\Delta\Delta G|$ in the Gibbs free energy were estimated using the FoldX software for each of the 20 amino acids. Next, we converted these predicted changes in free energy into a probability distribution for each site. The structurally based expected frequency $E_s[f_{ij}]$ (structural frequency) of amino acid j and site i was defined using a normalized negative exponential (Boltzmann distribution)

$$E_s[f_{ij}] = \frac{\exp(-|\Delta\Delta G_{ij}|)}{\sum_{k=1}^{20}\exp(-|\Delta\Delta G_{ik}|)}$$

This measure thus captures the relative impact on the structure of the 20 amino acids at a given site: If all amino acids result in roughly the same protein stability, then the expected frequency of each amino acid will be 1/20. We use the absolute value of the change in Gibbs free energy on the assumption that the structural stability of the viral protein is optimized in vivo. Thus, by construction, all consensus residues will have $|\Delta\Delta G_{ij}| = 0$. Nevertheless, the expected frequency of consensus residues at different sites will vary on the basis of the predicted impact of the other residues at each site.

The smoothed log-odds of $E_s[f_{ij}]$, with smoothing factor $q = 1/350$ to match cohort frequency smoothing, was then used as a feature in the models. Estimated values for structural frequency ($E_s[f_{ij}]$) are available in table S4.

HLA-HIV associations and covariation

For HLA class I genotyping, genomic DNA was extracted from whole blood or buffy coats (QIAamp blood kit, Qiagen). HLA class I genotyping relied on a combination of PCR-based techniques, involving sequence-specific primers (Invitrogen) and sequence-specific oligonucleotide probes (Innogenetics), as described previously (61). Ambiguities were resolved by direct sequencing of three exons in each gene, using kits (Abbott Molecular Inc.) designed for capillary electrophoresis and the ABI 3130xl DNA Analyzer (Applied Biosystems).

Correlations between HIV amino acids and HLA types were estimated using a phylogenetic dependence network, as previously described (24). Briefly, a maximum likelihood phylogeny was estimated for each protein using Phyml [version 3.0; (62)], using the general time reversible substitution model, a γ distribution over substitution rates, and inferred nucleotide and constant site probabilities. A phylogenetically corrected logistic regression model (63), conditioned on the PhyML-inferred phylogenies, was then used to assess the significance of an HLA allele in determining the amino acid for a given site. Forward selection was used to identify HLA alleles that correlate with a given amino acid at a given site. The model was run twice: once including other sites as covariates (covariation), and once without. To increase power, all variables were treated as binary, and all residues were tested against all HLAs (at "4-digit" subtype and "2-digit" type levels). All associations significant at $q < 0.2$ (corresponding to a false discovery rate of 20%) in either run are available in table S4.

An amino acid at a given site in a given individual was defined to be consistent with escape in that individual if (i) the individual expresses an HLA with an association at that site, and (ii) either the residue is positively correlated (referred to as "Adapted" in the literature) with the HLA, or any other residue is negatively correlated (referred to as "NonAdapted" in the literature) with the HLA. "Donor escape" is thus a binary variable that indicates whether the residue is consistent with escape from the donor. In multivariable models, we weight the donor escape binary variable by the probability that escape was selected in the donor, which is estimated as one minus the frequency of the residue in the cohort. A residue is susceptible to an individual if (i) the individual expresses an HLA with an association at that site, and (ii) the residue is negatively correlated (NonAdapted) with that HLA. "Recipient susceptible" is thus a binary variable that indicates whether an amino acid is putatively susceptible to an HLA expressed by the recipient. We limited analyses to associations identified at $q <$ 0.01, indicating that 99% of the associations are

expected to be nonspurious. These generally represent the strongest associations and are characterized by higher escape frequencies in individuals expressing the HLA and lower background frequencies in individuals not expressing the HLA.

Covariation among HIV sites was determined using the phylogenetically corrected logistic regression. However, rather than building a dependency network using forward selection, we liberally kept all pairwise associations significant at $q < 0.01$. Thus, a mutation at site a that initiates a chain reaction of compensation at site b followed by site c will be picked up as two separate covarying sites in the pairwise analysis. Thus, this pairwise analysis, while identifying indirect associations, will characterize the breadth of downstream compensation events expected to result from a given point mutation. We defined the number of covarying sites of a particular amino acid at a particular site to be the number of unique positions that were significantly associated (positively or negatively) with that amino acid. The numbers of covarying sites for each amino acid are available in table S4.

HLA and covariation associations were trained on a multicohort data set of 2066 chronically clade C–infected, antiretroviral-naïve individuals with HIV sequence and high-resolution HLA type information. These cohorts have been previously described, but were here merged together for the first time to yield greater statistical power. Briefly, in addition to the Zambian individuals described above (n = 360), the cohort consists of individuals from Durban, South Africa (n = 968) (*64*, *65*), Bloemfontein, South Africa (n = 260) (*66*), Kimberley, South Africa (n = 26) (*67*), Gaborone, Botswana (n = 386) (*68*), and southern African subjects attending outpatient HIV clinics in the Thames Valley area of the United Kingdom (n = 66), originally from Botswana, Malawi, South Africa, and Zimbabwe (*67*). From these individuals, population sequences were available for Gag-p17/p24 (n = 1897), Gag-p15 (n = 1135), Pol-Pr (n = 1315), Pol-RT (n = 1364), Pol-Int (n = 698), and Nef (n = 1336). High-resolution HLA types were missing or ambiguous for at least one allele in 239 of 2066 (11.5%) non-Zambian individuals. For these, a probability distribution over haplotypes was estimated using a machine learning approach that infers haplotype frequencies, as previously described (*69*) and extensively validated for this purpose (*70*). The inferred HLA completion probability distributions were used as a prior for the phylogenetic-logistic regression analysis, as previously described (*70*).

Statistical modeling of transmission selection bias

Infection as a binomial process

The observation that the majority (>99%) of sexual encounters among heterosexual partners do not result in transmission, coupled with the observation that the majority of transmissions are established by a single founder virus, implies that this process is stochastic. Here, we assume that the number of transmitted founder viruses is distributed binomially, parameterized by the number of viruses in the donor genital compartment and the probability that each virus will establish infection. We then build on this model to estimate the probability that the founder virus population contains a particular genotype, and use this to model selection bias.

Suppose the average sexual encounter is characterized by n viruses present in the infected partner's genital compartment, and that the a priori probability that any particular virus will establish infection is p. If the probability that a given virus establishes productive infection is independent of the state of other viruses, then the total number T of viruses establishing infection is a binomially distributed random variable. Of particular interest is the probability that at least one virus establishes infection, providing the rate r of transmission, given by

$$r \stackrel{\text{def}}{=} \Pr(T > 0; n, p) = 1 - (1-p)^n \approx np \quad (2)$$

where the approximation follows from a Taylor series expansion because the rate is small: observed rates of transmission have been reported in the range 0.01 to 0.001 (*9*).

A model for selection bias

The question of selection bias can now be phrased as the question of whether p depends on the type of viruses. Suppose the population of viruses in the infected donors is grouped into two types: type a and type $\bar{a}$. Such binarization can be defined arbitrarily, but in this study, we categorize the viruses on the basis of whether they contain the dominant amino acid variant at a particular site (a) or not ($\bar{a}$). Extending the above formulation, we can write $n = n_a + n_{\bar{a}}$ and $p = f_a p_a + (1 - f_a) p_{\bar{a}}$, where $n_a = f_a n$ is the number of viruses of type a, written in terms of the frequency f_a of a in the quasispecies; $n_{\bar{a}} = (1 - f_a) n$ is the number of viruses of type $\bar{a}$; and $p_a, p_{\bar{a}}$ are the a priori probabilities that a virus of type a or $\bar{a}$ will establish infection, respectively. Then the total number of transmitted viruses becomes $T = T_a + T_{\bar{a}}$, for binomially distributed random variables T_a and $T_{\bar{a}}$, which represent the total number of transmitted virons of type a and $\bar{a}$, respectively.

In the context of transmission selection bias, a natural quantity of interest is the odds that a virus of type a is in the population of viruses that establish infection, conditional on infection being established, which is approximately

$$\frac{\Pr(T_a > 0 | T > 0)}{\Pr(T_a = 0 | T > 0)} \approx \frac{\Pr(T_a > 0 | T > 0)}{\Pr(T_{\bar{a}} > 0 | T > 0)} \approx \frac{n_a p_a}{n_{\bar{a}} p_{\bar{a}}} = \frac{f_a p_a}{(1 - f_a) p_{\bar{a}}} \quad (3)$$

where the first step follows because a and $\bar{a}$ are mutually exclusive and complete and our assumptions of independence and low rates of infection imply that the probability of transmitting both a and $\bar{a}$ is negligible (see note S2).

The log of Eq. 3 fits nicely into the logistic regression framework:

$$\ln\left(\frac{\Pr(T_a > 0 | T > 0)}{\Pr(T_a = 0 | T > 0)}\right) = \ln\left(\frac{f_a}{1 - f_a}\right) + \ln\left(\frac{p_a}{p_{\bar{a}}}\right) \quad (4)$$

$$\equiv \beta_f + x\beta \quad (5)$$

where the offset term β_f estimates $\ln[f_a/(1 - f_a)]$, $x = (x_1, \ldots, x_L)$ is a row vector of features and $\beta = (\beta_1, \ldots, \beta_L)$ is a column vector of weights. From Eq. 4 we see that the ratio $p_a/p_{\bar{a}}$ has the effect of biasing the probability that a is in the founder virus, which is otherwise determined by the frequency of a in the donor quasispecies. Thus, we define the bias with respect to a to be

$$\text{bias}_a = \ln\left(\frac{p_a}{p_{\bar{a}}}\right)$$

and say transmission is "unbiased" if $\text{bias}_a = 0$. By fitting (β_f, β) to the observed data consisting of all dominant variants observed in all individuals, we can estimate the effects of our L features on selection bias and test the null hypothesis that a given feature has no effect on selection bias (that is, $\beta_i = 0$).

A key observation of this formulation is that the log-odds that the majority variant is transmitted is equal to the log-odds of the frequency of that variant in the quasispecies, plus or minus some bias term. This is validated in Fig. 2A, where the log-odds transmission probability is equal (within the limits of estimation) to the log-odds quasispecies frequencies for consensus residues, but is shifted down for polymorphisms. This formulation further predicts that donor quasispecies frequency will be the primary determinant of transmission except in the most extreme cases of selection bias, consistent with previous reports (*7*).

The effect of transmission risk factors on selection bias

Transmission risk factors may increase the risk of transmission in one of two ways: (i) by increasing the number of viruses n that have an opportunity to establish infection, for example by increasing VL or increasing the number of sexual exposures, or (ii) by increasing the probability p that any one virus can establish infection, by either increasing the transmission fitness of all virus particles or increasing the susceptibility of the uninfected partner.

A key observation from Eq. 4 is that n is completely absent, indicating that the number of exposures or quantity of virus present at the time of exposure will not alter the selection bias. In contrast, suppose all individual viruses are equally more likely to establish infection (for example, due to increased susceptibility in the uninfected partner), by a quantity c. Then, the selection bias with respect to a becomes

$$\text{bias}_a = \ln\left(\frac{p_a + c}{p_{\bar{a}} + c}\right) \quad (6)$$

which converges toward 0 as c becomes relatively large. Thus, individuals with high risk

factors will experience a reduced selection bias, as observed in Fig. 3. Our observation that VL reduces selection bias in female-to-male transmission indicates that VL increases transmission risk in this population, at least in part, by serving as a marker of increased transmission fitness, and not simply because of exposure to a higher quantity of virus particles.

The absence of n and the simple form of Eq. 6 are the result of our assumptions of independence of transmission among virions and of a low overall rate of transmission. These assumptions warrant further exploration and are discussed in supplementary notes.

Multilevel logistic regression (generalized linear mixed models)

Parameter estimation and hypothesis testing under logistic regression assumes independence of observations: in this case, each site in each individual is treated independently. However, as observed in fig. S2, the relationship between cohort frequency and transmission probability differs among proteins (indicating non-independence among sites within the same protein), and as suggested by Eq. 6, all sites within a couple may experience higher or lower transmission probabilities as a result of couple-specific risk factors (indicating non-independence among sites within the same couple). In this section, we describe our specification of a multilevel, multivariable logistic regression model (also known as a generalized linear mixed model) to account for these non-independences (*26*). A multilevel logistic regression is similar to a standard logistic regression, but with random variables embedded in the definition of some of the coefficients. In the current context, an instantiation of a random variable is indexed by the transmission couple, allowing the coefficients to be constant among observations drawn from the same individual, but to vary randomly between individuals.

For N total observations over J proteins in M couples, let p_{ijk} be the probability that the dominant variant observed at position i (i = 1,..., N) in protein j (j = 1,..., J) in couple k (k = 1,..., M) is transmitted. Let $X = \{x_{il}\}$ be an $N \times L$ data matrix of L features. The features of the model are given in Table 2 and described in detail in the "Parameter definitions and methods" section. Here, we call attention to two features of particular interest: let the column vectors X_c and X_r be the cohort frequencies and risk indices (the aggregate of sex, VL, and GUI, defined above) for the observations. Because we call special attention to these features, we define a new $N \times (L - 2)$ predictor matrix W, such that $X = [W\ X_c\ X_r]$. Then, the multilevel logistic regression is defined by level one:

$$\text{logodds}(p_{ijk}|X) = \beta^{(0)}_{ijk} + \beta^{(1)}_{ijk} x_{ic} + \beta^{(2)}_{i} x^2_{ic} \quad (7)$$

This model assumes a quadratic effect between cohort frequency and odds of transmission. (The quadratic polynomial was chosen by first testing a model that included only protein effects and cohort frequency as a cubic on cohort frequency, then observing that the linear and quadratic effects, but not the cubic effects, were significant.) Each of the β terms are composite, mixed-effect terms, defined by level two:

$$\beta^{(0)}_{ijk} = \gamma_{00} + W_i\Gamma + \gamma_{0r}x_{ir} + \gamma_{0j} + \varepsilon_{0k} \quad (8)$$

$$\beta^{(1)}_{ijk} = \gamma_{10} + \gamma_{1r}x_{ir} + \gamma_{1j} + \varepsilon_{1k} \quad (9)$$

$$\beta^{(2)}_{i} = \gamma_{20} + \gamma_{2r}x_{ir} \quad (10)$$

where Γ is a column vector of fixed effects, the γ terms are fixed effects, with separate γ_{0j} and γ_{1j} terms for each protein domain, and the ε terms are random effects, which are normally distributed as

$$\begin{bmatrix}\varepsilon_{0k}\\ \varepsilon_{1k}\end{bmatrix} \sim N\left(\begin{bmatrix}0\\0\end{bmatrix}; \sum_\theta\right), \theta = (\sigma_0, \sigma_1, \sigma_{01})$$

with an independent sample taken for each couple k. Thus, the offset $\beta^{(0)}_{ijk}$ (Eq. 8) is determined by a grand mean (γ_{00}), a linear combination of all predictors and their coefficients ($X_i\Gamma$), and protein- and couple-specific offsets; the linear term $\beta^{(1)}_{ijk}$ (Eq. 9) is determined by a grand mean (γ_{10}), the risk ($\gamma_{1r}\ x_{ir}$), and protein- and couple-specific slopes; and the quadratic term $\beta^{(2)}_{i}$ (Eq. 10) is determined by a grand mean (γ_{20}) and the risk ($\gamma_{2r}\ x_{ir}$). Proteins are treated as fixed effects. Because the couples in our study represent a random draw from an assumed population, the couple-specific offset and slope terms (ε_{0k}, ε_{1k}) are treated as random effects, with the effect for any given couple drawn from a bivariate normal distribution in which the offset and slope are allowed to be correlated. The final model learns the variance-covariance matrix Σ_θ, which specifies the level of variability in slope and offset among couples, then integrates out (ε_{0k}, ε_{1k}). The multilevel logistic regression was carried out using the glmer routine of the lme4 package (*71*) in R v3.0.2 (*72*). Protein- and couple-specific linear effects significantly improved the fit of the model ($P < 1 \times 10^{-8}$ by likelihood ratio test); quadratic effects did not improve the fit ($P > 0.4$ for both protein- and couple-specific terms). The final fit model is shown in Table 2.

Transmission index

Given a set of features $x = x_1,..., x_L$, and a trained model (β_0, β), β = $\beta_1,..., \beta_L$, we can compute the expected log-odds of transmission for any residue and any site. We define the transmission index of a sequence (or <Gag, Pol, Nef> tuple of sequences) to be the mean log-odds of transmission over all sites in the sequence. Sites containing mixtures, stop codons, or gaps are ignored. To avoid overfitting, models for the transmission index were estimated using leave-one-out cross-validation, such that the transmission index for each donor was computed using a model inferred from data that did not include that couple. The NYT transmissibility scores were taken from randomly selected models learned from the leave-one-out donor-recipient training runs to ensure that any differences in observed variance were not due to differential model variance. Transmission indices were computed using a subset of features: log-odds cohort frequency, and its square; the number of statistically linked covarying sites; and corrections for subproteins (p17, p24, p15, GagPolTF, protease, RT, integrase, and the Nef functional domain, as described above). SGA sequences were only available for Gag; we therefore used models trained on Gag alone for Fig. 5, A and B. For computational efficiency, random effects were not used in model inference for transmission indices.

Statistical analyses

Empirical transmission probability curves

To visualize the probability of transmission as a function of the frequency of a variant in the cohort or donor quasispecies (Figs. 2 and 3 and fig. S2), we used a sliding window approach in which we measure the observed proportion of sites that were transmitted within a given window. For example, for a given donor quasispecies frequency f, the empirical transmission probability corresponding to f is the proportion of all variants i such that $|\text{logodds}(f) - \text{logodds}(f_i)| < w$ for some window size w. The reported values are the empirical transmission frequency and the mean cohort frequency, over all observations within the window. We use w = 1, and only include values of f with at least 20 points in the window.

To estimate 95% confidence intervals for an empirical transmission probability curve, we use a block bootstrap approach using the percentile-t method (*73*). Briefly, for each of B = 1000 bootstrap replicates, we sample with replacement the couples, then the sites within each sampled couple. We then estimate the empirical transmission probability for each cohort frequency value observed in the complete data set. The percentile-t 95% confidence interval is then estimated independently for each cohort frequency value.

In Fig. 3, we report P values for comparing two empirical transmission probability curves (for example, comparing male-to-female versus female-to-male transmission). The statistic we used was the difference in the mean empirical transmission probability calculated over all cohort frequencies with at least 20 observations within the sliding window. Mean empirical transmission probabilities were calculated using the trapezoid method over the cohort and transmission frequencies output by the sliding window method. We then compared the observed difference in means to a normal distribution with mean 0 and SD $\hat{\sigma}$ to test the null hypothesis that the observed difference between the means of the two curves was zero. $\hat{\sigma}$ was estimated as the SD of the difference in means observed over the B = 1000 bootstrap replicates used to construct the confidence intervals.

Reversion analysis

The rates of reversion from polymorphism to consensus, for sites in which a polymorphism was present in both the donor and recipient,

were estimated as a function of fitness and susceptibility features. The date of reversion or loss to follow-up was determined relative to the date of the first available recipient sample. Thus, reversion rates are conditional on a polymorphism being present in both the donor sample and the first recipient sample. (Because we tracked reversion to consensus, the polymorphism in the recipient may differ from that in the donor.) The date of reversion was defined as the midpoint between the last non-mixture polymorphism and the first non-mixture consensus, minus the date of the first recipient sample. Mixtures were counted as missing data. Hazard ratios (HRs) were estimated using a Cox proportional hazard model. To account for assumed non-independence among sites sampled from the individuals, a multilevel bootstrap was performed (level 1 = sites, level 2 = individuals), with 1000 replicates. Reported HR values are those from the full model. *P* values are computed from the SEs of the bootstrap HR values, assuming a standard normal distribution. Only sites with available structures were used in the Cox proportional hazard model (table S2); all sites were used for Fig. 4. Statistical modeling was carried out using MATLAB (MATLAB and Statistics Toolbox Release 2012b, The MathWorks Inc.).

REFERENCES AND NOTES

1. M. R. Abrahams *et al*., Quantitating the multiplicity of infection with human immunodeficiency virus type 1 subtype C reveals a non-Poisson distribution of transmitted variants. *J. Virol.* **83**, 3556–3567 (2009). doi: 10.1128/JVI.02132-08; pmid: 19193811
2. C. A. Derdeyn *et al*., Envelope-constrained neutralization-sensitive HIV-1 after heterosexual transmission. *Science* **303**, 2019–2022 (2004). doi: 10.1126/science.1093137; pmid: 15044802
3. R. E. Haaland *et al*., Inflammatory genital infections mitigate a severe genetic bottleneck in heterosexual transmission of subtype A and C HIV-1. *PLOS Pathog.* **5**, e1000274 (2009). doi: 10.1371/journal.ppat.1000274; pmid: 19165325
4. B. F. Keele *et al*., Identification and characterization of transmitted and early founder virus envelopes in primary HIV-1 infection. *Proc. Natl. Acad. Sci. U.S.A.* **105**, 7552–7557 (2008). doi: 10.1073/pnas.0802203105; pmid: 18490657
5. B. Etemad *et al*., Human immunodeficiency virus type 1 V1-to-V5 envelope variants from the chronic phase of infection use CCR5 and fuse more efficiently than those from early after infection. *J. Virol.* **83**, 9694–9708 (2009). doi: 10.1128/JVI.00925-09; pmid: 19625411
6. J. F. Salazar-Gonzalez *et al*., Deciphering human immunodeficiency virus type 1 transmission and early envelope diversification by single-genome amplification and sequencing. *J. Virol.* **82**, 3952–3970 (2008). doi: 10.1128/JVI.02660-07; pmid: 18256145
7. A. J. Frater *et al*., Passive sexual transmission of human immunodeficiency virus type 1 variants and adaptation in new hosts. *J. Virol.* **80**, 7226–7234 (2006). doi: 10.1128/JVI.02014-05; pmid: 16809328
8. G. M. Shaw, E. Hunter, HIV transmission. *Cold Spring Harb. Perspect. Med.* **2**, a006965 (2012). doi: 10.1101/cshperspect.a006965; pmid: 23043157
9. R. A. Royce, A. Seña, W. Cates Jr., M. S. Cohen, Sexual transmission of HIV. *N. Engl. J. Med.* **336**, 1072–1078 (1997). doi: 10.1056/NEJM199704103361507; pmid: 9091805
10. E. A. Berger, P. M. Murphy, J. M. Farber, Chemokine receptors as HIV-1 coreceptors: Roles in viral entry, tropism, and disease. *Annu. Rev. Immunol.* **17**, 657–700 (1999). doi: 10.1146/annurev.immunol.17.1.657; pmid: 10358771
11. C. Cicala, J. Arthos, A. S. Fauci, HIV-1 envelope, integrins and co-receptor use in mucosal transmission of HIV. *J. Transl. Med.* **9** (Suppl. 1), S2 (2011). doi: 10.1186/1479-5876-9-S1-S2; pmid: 21284901
12. N. F. Parrish *et al*., Phenotypic properties of transmitted founder HIV-1. *Proc. Natl. Acad. Sci. U.S.A.* **110**, 6626–6633 (2013). doi: 10.1073/pnas.1304288110; pmid: 23542380
13. S. Gnanakaran *et al*., Recurrent signature patterns in HIV-1 B clade envelope glycoproteins associated with either early or chronic infections. *PLOS Pathog.* **7**, e1002209 (2011). doi: 10.1371/journal.ppat.1002209; pmid: 21980282
14. M. Sagar *et al*., Selection of HIV variants with signature genotypic characteristics during heterosexual transmission. *J. Infect. Dis.* **199**, 580–589 (2009). doi: 10.1086/596557; pmid: 19143562
15. J. T. Herbeck *et al*., Human immunodeficiency virus type 1 *env* evolves toward ancestral states upon transmission to a new host. *J. Virol.* **80**, 1637–1644 (2006). doi: 10.1128/JVI.80.4.1637-1644.2006; pmid: 16439520
16. X. Wei *et al*., Antibody neutralization and escape by HIV-1. *Nature* **422**, 307–312 (2003). doi: 10.1038/nature01470; pmid: 12646921
17. A. E. Fenton-May *et al*., Relative resistance of HIV-1 founder viruses to control by interferon-α. *Retrovirology* **10**, 146 (2013). doi: 10.1186/1742-4690-10-146; pmid: 24299076
18. M. A. Brockman *et al*., Early selection in Gag by protective HLA alleles contributes to reduced HIV-1 replication capacity that may be largely compensated for in chronic infection. *J. Virol.* **84**, 11937–11949 (2010). doi: 10.1128/JVI.01086-10; pmid: 20810731
19. J. L. Prince *et al*., Role of transmitted Gag CTL polymorphisms in defining replicative capacity and early HIV-1 pathogenesis. *PLOS Pathog.* **8**, e1003041 (2012). doi: 10.1371/journal.ppat.1003041; pmid: 23209412
20. J. K. Wright *et al*., Gag-protease-mediated replication capacity in HIV-1 subtype C chronic infection: Associations with HLA type and clinical parameters. *J. Virol.* **84**, 10820–10831 (2010). doi: 10.1128/JVI.01084-10; pmid: 20702636
21. J. K. Wright *et al*., Influence of Gag-protease-mediated replication capacity on disease progression in individuals recently infected with HIV-1 subtype C. *J. Virol.* **85**, 3996–4006 (2011). doi: 10.1128/JVI.02520-10; pmid: 21289112
22. M. E. Greenberg, A. J. Iafrate, J. Skowronski, The SH3 domain-binding surface and an acidic motif in HIV-1 Nef regulate trafficking of class I MHC complexes. *EMBO J.* **17**, 2777–2789 (1998). doi: 10.1093/emboj/17.10.2777; pmid: 9582271
23. A. Mangasarian, V. Piguet, J. K. Wang, Y. L. Chen, D. Trono, Nef-induced CD4 and major histocompatibility complex class I (MHC-I) down-regulation are governed by distinct determinants: N-terminal alpha helix and proline repeat of Nef selectively regulate MHC-I trafficking. *J. Virol.* **73**, 1964–1973 (1999). pmid: 9971776
24. J. M. Carlson *et al*., Phylogenetic dependency networks: Inferring patterns of CTL escape and codon covariation in HIV-1 Gag. *PLOS Comput. Biol.* **4**, e1000225 (2008). doi: 10.1371/journal.pcbi.1000225; pmid: 19023406
25. C. L. Boutwell, C. F. Rowley, M. Essex, Reduced viral replication capacity of human immunodeficiency virus type 1 subtype C caused by cytotoxic-T-lymphocyte escape mutations in HLA-B57 epitopes of capsid protein. *J. Virol.* **83**, 2460–2468 (2009). doi: 10.1128/JVI.01970-08; pmid: 19109381
26. G. Y. Wong, W. M. Mason, The hierarchical logistic regression model for multilevel analysis. *J. Am. Stat. Assoc.* **80**, 513–524 (1985). doi: 10.1080/01621459.1985.10478148
27. U. S. Fideli *et al*., Virologic and immunologic determinants of heterosexual transmission of human immunodeficiency virus type 1 in Africa. *AIDS Res. Hum. Retroviruses* **17**, 901–910 (2001). doi: 10.1089/088922201750290023; pmid: 11461676
28. R. H. Gray *et al*., Probability of HIV-1 transmission per coital act in monogamous, heterosexual, HIV-1-discordant couples in Rakai, Uganda. *Lancet* **357**, 1149–1153 (2001). doi: 10.1016/S0140-6736(00)04331-2; pmid: 11323041
29. Comparison of female to male and male to female transmission of HIV in 563 stable couples. European Study Group on Heterosexual Transmission of HIV. *BMJ* **304**, 809–813 (1992). doi: 10.1136/bmj.304.6830.809; pmid: 1392708
30. S. R. Galvin, M. S. Cohen, The role of sexually transmitted diseases in HIV transmission. *Nat. Rev. Microbiol.* **2**, 33–42 (2004). doi: 10.1038/nrmicro794; pmid: 15035007
31. J. Tang *et al*., Human leukocyte antigen class I genotypes in relation to heterosexual HIV type 1 transmission within discordant couples. *J. Immunol.* **181**, 2626–2635 (2008). doi: 10.4049/jimmunol.181.4.2626; pmid: 18684953
32. F. M. Hecht *et al*., HIV RNA level in early infection is predicted by viral load in the transmission source. *AIDS* **24**, 941–945 (2010). doi: 10.1097/QAD.0b013e328337b12e; pmid: 20168202
33. T. D. Hollingsworth *et al*., HIV-1 transmitting couples have similar viral load set-points in Rakai, Uganda. *PLOS Pathog.* **6**, e1000876 (2010). doi: 10.1371/journal.ppat.1000876; pmid: 20463808
34. L. Yue *et al*., Cumulative impact of host and viral factors on HIV-1 viral-load control during early infection. *J. Virol.* **87**, 708–715 (2013). doi: 10.1128/JVI.02118-12; pmid: 23115285
35. T. M. Allen *et al*., Selection, transmission, and reversion of an antigen-processing cytotoxic T-lymphocyte escape mutation in human immunodeficiency virus type 1 infection. *J. Virol.* **78**, 7069–7078 (2004). doi: 10.1128/JVI.78.13.7069-7078.2004; pmid: 15194783
36. Z. L. Brumme *et al*., Marked epitope- and allele-specific differences in rates of mutation in human immunodeficiency type 1 (HIV-1) Gag, Pol, and Nef cytotoxic T-lymphocyte epitopes in acute/early HIV-1 infection. *J. Virol.* **82**, 9216–9227 (2008). doi: 10.1128/JVI.01041-08; pmid: 18614631
37. H. Crawford *et al*., Compensatory mutation partially restores fitness and delays reversion of escape mutation within the immunodominant HLA-B*5703-restricted Gag epitope in chronic human immunodeficiency virus type 1 infection. *J. Virol.* **81**, 8346–8351 (2007). doi: 10.1128/JVI.00465-07; pmid: 17507468
38. A. Leslie *et al*., Transmission and accumulation of CTL escape variants drive negative associations between HIV polymorphisms and HLA. *J. Exp. Med.* **201**, 891–902 (2005). doi: 10.1084/jem.20041455; pmid: 15781581
39. J. Martinez-Picado *et al*., Fitness cost of escape mutations in p24 Gag in association with control of human immunodeficiency virus type 1. *J. Virol.* **80**, 3617–3623 (2006). doi: 10.1128/JVI.80.7.3617-3623.2006; pmid: 16537629
40. D. R. Chopera *et al*., Transmission of HIV-1 CTL escape variants provides HLA-mismatched recipients with a survival advantage. *PLOS Pathog.* **4**, e1000033 (2008). doi: 10.1371/journal.ppat.1000033; pmid: 18369479
41. P. A. Goepfert *et al*., Transmission of HIV-1 Gag immune escape mutations is associated with reduced viral load in linked recipients. *J. Exp. Med.* **205**, 1009–1017 (2008). doi: 10.1084/jem.20072457; pmid: 18426987
42. C. Cicala *et al*., The integrin $\alpha_4\beta_7$ forms a complex with cell-surface CD4 and defines a T-cell subset that is highly susceptible to infection by HIV-1. *Proc. Natl. Acad. Sci. U.S.A.* **106**, 20877–20882 (2009). doi: 10.1073/pnas.0911796106; pmid: 19933330
43. L. A. Cotton *et al*., Genotypic and functional impact of HIV-1 adaptation to its host population during the North American epidemic. *PLOS Genet.* **10**, e1004295 (2014). doi: 10.1371/journal.pgen.1004295; pmid: 24762668
44. J. F. Salazar-Gonzalez *et al*., Genetic identity, biological phenotype, and evolutionary pathways of transmitted/founder viruses in acute and early HIV-1 infection. *J. Exp. Med.* **206**, 1273–1289 (2009). doi: 10.1084/jem.20090378; pmid: 19487424
45. S. Allen *et al*., Promotion of couples' voluntary counselling and testing for HIV through influential networks in two African capital cities. *BMC Public Health* **7**, 349 (2007). doi: 10.1186/1471-2458-7-349; pmid: 18072974
46. M. C. Kempf *et al*. Enrollment and retention of HIV discordant couples in Lusaka Zambia. *J. Acquir. Immune Defic. Syndr.* **47**, 116–125 (2008). doi: 10.1097/QAI.0b013e31815d2f3f; pmid: 18030162
47. S. L. McKenna *et al*., Rapid HIV testing and counseling for voluntary testing centers in Africa. *AIDS* **11**, S103–S110 (1997). pmid: 9376093
48. S. A. Trask *et al*., Molecular epidemiology of human immunodeficiency virus type 1 transmission in a heterosexual cohort of discordant couples in Zambia. *J. Virol.* **76**, 397–405 (2002). doi: 10.1128/JVI.76.1.397-405.2002; pmid: 11739704
49. V. Piguet, D. Trono, in *Human Retroviruses and AIDS 1999*, C. L. Kuiken, B. Foley, B. Hahn, B. Korber, F. McCutchan, P. A. Marx, J. W. Mellors, J. I. Mullins, J. Sodroski, S. Wolinsky, Eds. (Theoretical Biology and Biophysics Group, Los Alamos National Laboratory, Los Alamos, NM, 1999), pp. 448–459.
50. M. R. Henn *et al*., Whole genome deep sequencing of HIV-1 reveals the impact of early minor variants upon immune recognition during acute infection. *PLOS Pathog.* **8**, e1002529 (2012). doi: 10.1371/journal.ppat.1002529; pmid: 22412369
51. X. Yang *et al*., De novo assembly of highly diverse viral populations. *BMC Genomics* **13**, 475 (2012). doi: 10.1186/1471-2164-13-475; pmid: 22974120
52. W. Song *et al*., Disparate associations of HLA class I markers with HIV-1 acquisition and control of viremia

in an African population. *PLOS One* **6**, e23469 (2011). doi: 10.1371/journal.pone.0023469; pmid: 21858133
53. C. L. Boutwell *et al*., Frequent and variable cytotoxic-T-lymphocyte escape-associated fitness costs in the human immunodeficiency virus type 1 subtype B Gag proteins. *J. Virol.* **87**, 3952–3965 (2013). doi: 10.1128/JVI.03233-12; pmid: 23365420
54. B. N. Kelly *et al*., Implications for viral capsid assembly from crystal structures of HIV-1 Gag_{1-278} and $CA^{N}_{133-278}$. *Biochemistry* **45**, 11257–11266 (2006). doi: 10.1021/bi060927x; pmid: 16981686
55. O. Pornillos *et al*., X-ray structures of the hexameric building block of the HIV capsid. *Cell* **137**, 1282–1292 (2009). doi: 10.1016/j.cell.2009.04.063; pmid: 19523676
56. A. H. Robbins *et al*., Structure of the unbound form of HIV-1 subtype A protease: Comparison with unbound forms of proteases from other HIV subtypes. *Acta Crystallogr. D Biol. Crystallogr.* **66**, 233–242 (2010). doi: 10.1107/S0907444909054298; pmid: 20179334
57. Y. Hsiou *et al*., Structure of unliganded HIV-1 reverse transcriptase at 2.7 Å resolution: Implications of conformational changes for polymerization and inhibition mechanisms. *Structure* **4**, 853–860 (1996). doi: 10.1016/S0969-2126(96)00091-3; pmid: 8805568
58. Y. Goldgur *et al*., Three new structures of the core domain of HIV-1 integrase: An active site that binds magnesium. *Proc. Natl. Acad. Sci. U.S.A.* **95**, 9150–9154 (1998). doi: 10.1073/pnas.95.16.9150; pmid: 9689049
59. C. H. Lee, K. Saksela, U. A. Mirza, B. T. Chait, J. Kuriyan, Crystal structure of the conserved core of HIV-1 Nef complexed with a Src family SH3 domain. *Cell* **85**, 931–942 (1996). doi: 10.1016/S0092-8674(00)81276-3; pmid: 8681387
60. R. Guerois, J. E. Nielsen, L. Serrano, Predicting changes in the stability of proteins and protein complexes: A study of more than 1000 mutations. *J. Mol. Biol.* **320**, 369–387 (2002). doi: 10.1016/S0022-2836(02)00442-4; pmid: 12079393
61. J. Tang *et al*., Favorable and unfavorable HLA class I alleles and haplotypes in Zambians predominantly infected with clade C human immunodeficiency virus type 1. *J. Virol.* **76**, 8276–8284 (2002). doi: 10.1128/JVI.76.16.8276-8284.2002; pmid: 12134033
62. S. Guindon *et al*., New algorithms and methods to estimate maximum-likelihood phylogenies: Assessing the performance of PhyML 3.0. *Syst. Biol.* **59**, 307–321 (2010). doi: 10.1093/sysbio/syq010; pmid: 20525638
63. J. M. Carlson *et al*., Widespread impact of HLA restriction on immune control and escape pathways of HIV-1. *J. Virol.* **86**, 5230–5243 (2012). doi: 10.1128/JVI.06728-11; pmid: 22379086
64. A. Leslie *et al*., Additive contribution of HLA class I alleles in the immune control of HIV-1 infection. *J. Virol.* **84**, 9879–9888 (2010). doi: 10.1128/JVI.00320-10; pmid: 20660184
65. P. C. Matthews *et al*., Central role of reverting mutations in HLA associations with human immunodeficiency virus set point. *J. Virol.* **82**, 8548–8559 (2008). doi: 10.1128/JVI.00580-08; pmid: 18596105
66. K. H. Huang *et al*., Prevalence of HIV type-1 drug-associated mutations in pre-therapy patients in the Free State, South Africa. *Antivir. Ther.* **14**, 975–984 (2009). doi: 10.3851/IMP1416; pmid: 19918101
67. P. C. Matthews *et al*., HLA-A*7401–mediated control of HIV viremia is independent of its linkage disequilibrium with HLA-B*5703. *J. Immunol.* **186**, 5675–5686 (2011). doi: 10.4049/jimmunol.1003711; pmid: 21498667
68. R. L. Shapiro *et al*., Antiretroviral regimens in pregnancy and breast-feeding in Botswana. *N. Engl. J. Med.* **362**, 2282–2294 (2010). doi: 10.1056/NEJMoa0907736; pmid: 20554983
69. J. Listgarten *et al*., Statistical resolution of ambiguous HLA typing data. *PLOS Comput. Biol.* **4**, e1000016 (2008). doi: 10.1371/journal.pcbi.1000016; pmid: 18392148.
70. J. M. Carlson *et al*., Correlates of protective cellular immunity revealed by analysis of population-level immune escape pathways in HIV-1. *J. Virol.* **86**, 13202–13216 (2012). doi: 10.1128/JVI.01998-12; pmid: 23055555
71. D. Bates, M. Maechler, B. Bolker, S. Walker, *lme4: Linear Mixed-Effects Models Using Eigen and S4. R Package* (2013).
72. R Core Team (R Foundation for Statistical Computing, Vienna, Austria, 2013).
73. B. Efron, Nonparametric standard errors and confidence intervals. *Can. J. Stat.* **9**, 139–158 (1981). doi: 10.2307/3314608

ACKNOWLEDGMENTS

We thank all the volunteers in Zambia who participated in this study and all the staff at the Zambia Emory HIV Research Project in Lusaka who made this study possible. We would like to thank J. Allen and M. Hurlston for technical assistance and sample management; P. Farmer, Ph.D., for database design and management; and I. Brill, K. Wall, X. Li, C. Lippert, N. Fusi, J. Listgarten, and Z. Brumme for helpful discussions. This study was funded by R01 AI64060 and R37 AI51231 (E.H.) and the International AIDS Vaccine Initiative (to S.A.), and made possible in part by the support of the American people through the U.S. Agency for International Development (USAID). The contents are the responsibility of the study authors and do not necessarily reflect the views of USAID or the U.S. government. This work was also supported, in part, by the Virology Core at the Emory Center for AIDS Research (grant P30 AI050409); the Yerkes National Primate Research Center base grant (2P51RR000165-51) through the National Center for Research Resources P51RR165 and by the Office of Research Infrastructure Programs/OD P51OD11132; NIAID grants P01-AI074415 (T.M.A.) and U01 AI 66454 (R.S.); and Multidisciplinary AIDS Training Grant NIH T32-AI007387 (R.B.). J.P., D.T.C., and M.S. were supported in part by Action Cycling Fellowships. T.N. was supported by the International AIDS Vaccine Initiative, the South African Department of Science and Technology and the National Research Foundation through the South Africa Research Chairs Initiative, by an International Early Career Scientist award from the Howard Hughes Medical Institute, and by the Victor Daitz Foundation. E.H. is a Georgia Eminent Scholar. All viral sequences not previously published have been submitted to GenBank—accession numbers JN014076-JN014465, JQ219842, and KM048382-KM050767. The data reported in this paper are tabulated in the supplementary online material.

SUPPLEMENTARY MATERIALS

www.sciencemag.org/content/345/6193/1254031/suppl/DC1
Text
Figs. S1 to S4
Tables S1 to S4
28 March 2014; accepted 13 June 2014
10.1126/science.1254031

RESEARCH ARTICLE

HIV LATENCY

Specific HIV integration sites are linked to clonal expansion and persistence of infected cells

F. Maldarelli,[1]* X. Wu,[2]* L. Su,[2] F. R. Simonetti,[1,3] W. Shao,[2] S. Hill,[1] J. Spindler,[1] A. L. Ferris,[1] J. W. Mellors,[4] M. F. Kearney,[1] J. M. Coffin,[5] S. H. Hughes[1]†

The persistence of HIV-infected cells in individuals on suppressive combination antiretroviral therapy (cART) presents a major barrier for curing HIV infections. HIV integrates its DNA into many sites in the host genome; we identified 2410 integration sites in peripheral blood lymphocytes of five infected individuals on cART. About 40% of the integrations were in clonally expanded cells. Approximately 50% of the infected cells in one patient were from a single clone, and some clones persisted for many years. There were multiple independent integrations in several genes, including *MKL2* and *BACH2*; many of these integrations were in clonally expanded cells. Our findings show that HIV integration sites can play a critical role in expansion and persistence of HIV-infected cells.

HIV replication is suppressed with combination antiretroviral therapy (cART), but infected cells persist in patients and are a critical obstacle to curing HIV infection (*1*, *2*). Analysis of HIV populations in vivo shows that after long-term suppressive cART, genetically identical HIV variants emerge (*3*, *4*). The source and mechanisms involved in the emergence of these identical variants are not understood. One possibility is that the identical variants arise from cells that have clonally expanded. Because HIV DNA integrates at many sites in the human genome, the site of integration can be used to identify clonally expanded cells that arose from a single infected progenitor.

Clonal expansion of HIV-infected cells in patients

We analyzed the integration sites in peripheral blood mononuclear cells (PBMCs) or $CD4^+$ T cells from patients on prolonged cART obtained by negative selection using a previously described technique (*5*–*7*). DNA from PBMCs or $CD4^+$ T cells was randomly sheared to ~400–base pair (bp) fragments, and linker-mediated polymerase chain reaction was used to selectively amplify fragments that contained viral/host DNA junctions (*8*). Both ends of the amplified junction fragments were sequenced on the Illumina platform (San Diego, CA) to determine the viral/host junctions and the breakpoints in the host DNA. The sequence of the viral/host junction identifies the exact position and orientation in which the HIV DNA was integrated. The breakpoints in the host DNA can be used to identify the integration sites in clonally expanded cells. If several cells with the same integration site are present, shearing their DNA will give rise to multiple fragments in which the integration site is the same, but the host DNA breakpoints differ.

Integration site analysis was performed by using PBMCs or $CD4^+$ T cells from five patients (table S1). A diverse population of viruses was present in each patient either before therapy or shortly after cART was initiated; however, after prolonged cART (mean duration of treatment, 11.7 years), identical viral sequences, defined at either the RNA or the DNA level, emerged (Fig. 1 and fig. S1). In total, 2410 integration sites were mapped; these represented 1632 different integration events. 1388 integration sites (57%) were detected once, and 1022 sites (43%) were associated with more than one host DNA breakpoint, revealing that a large fraction of the infected cells are from expanded clones (Fig. 2, tables S2 and S3, and fig. S2). We validated the method for identifying expanded clones by making two completely independent libraries from cells from the last time point from patient 1; the same highly expanded clones were identified in both libraries. In some cases, clonal expansion was extensive. For example, in patient 3 the initial analysis found the same site in the *HORMAD2* gene in 62 of 317 integrations, but because of overlaps in the breakpoint analysis, this figure is an underestimate. We also estimated the fraction of the total integration sites that were derived from this expanded clone (*8*). This analysis implied that ~58% of all the HIV-infected cells in this patient were derived from a single infected cell.

Among the five patients studied, HIV integration sites were found in 985 different genes (fig. S3). Most of the genes had only a single integrant (659 integrants, 67%); these integrants were not shown to be from clonally expanded cells. The remaining 326 genes (33%) either had a single integrant in a cell that underwent clonal expansion (126 genes) or had multiple integrants (200 genes), some of which (59 genes; 30%) were in cells that underwent clonal expansion (fig. S3). Approximately 70% (21 of 29) of the genes with multiple integrants in highly expanded clones (listed in table S4) are known to be directly involved in the regulation of cell growth. HIV proviruses (the integrated form of retroviral DNA is called a provirus) were also found in intergenic regions of the genome and in sites that could not be mapped to a single site in the human genome (ambiguous sites); some of the cells with such integrants were also highly expanded (fig. S2).

Persistence of clones of HIV-infected cells

Longitudinal sampling revealed that some of the clones that emerged on cART persisted for many years. Patient 1 had at least 13 different clones that were present in samples taken 11.2 years apart, and 11 other clones were present in samples taken 6.6 years apart (Table 1). A number of these persistent clones had integration sites in genes known to be associated with cell growth (*STAT5B*, *PARP8*, and *DDX6*), mitosis (*PKP4* and *MAP4*), or both. In patient 3, we analyzed a small set of integration sites (47 total sites) from a sample taken before the patient started cART. Most of the integration sites from this pre-cART sample were present only once, an observation that is consistent with the short half-life of infected cells during uncontrolled HIV replication (*9*). However, one site was from a clonally expanded cell, showing that there is clonal expansion in the absence of cART. Others have reported that there are HIV-infected clones that can persist for prolonged periods in patients on cART (*10*, *11*). Our data show that the prolonged persistence of expanded clones is common and frequently associated with specific integrations in genes involved in controlling cell growth and division. Although there was variation in integration sites among patients, all five patients showed evidence of clonal expansion of infected cells, even in the smallest data sets (35 and 46 distinct integration sites) (table S2).

Integration sites associated with clonal expansion or persistence of infected cells

Two genes with remarkable patterns of HIV integration were identified in patient 1 (Fig. 3). In the data set obtained from $CD4^+$ T cells after

[1]HIV Drug Resistance Program, National Cancer Institute, Frederick, MD 21702, USA. [2]Leidos Biomedical Research, Frederick, MD 21702, USA. [3]Department of Biomedical and Clinical Sciences L. Sacco, University of Milan, 20122 Milan, Italy. [4]Department of Medicine, University of Pittsburgh, Pittsburgh, PA 15261, USA. [5]Department of Molecular Biology and Microbiology, Tufts University, Boston, MA 02111, USA. *These authors contributed equally to this work. †Corresponding author. E-mail: hughesst@mail.nih.gov

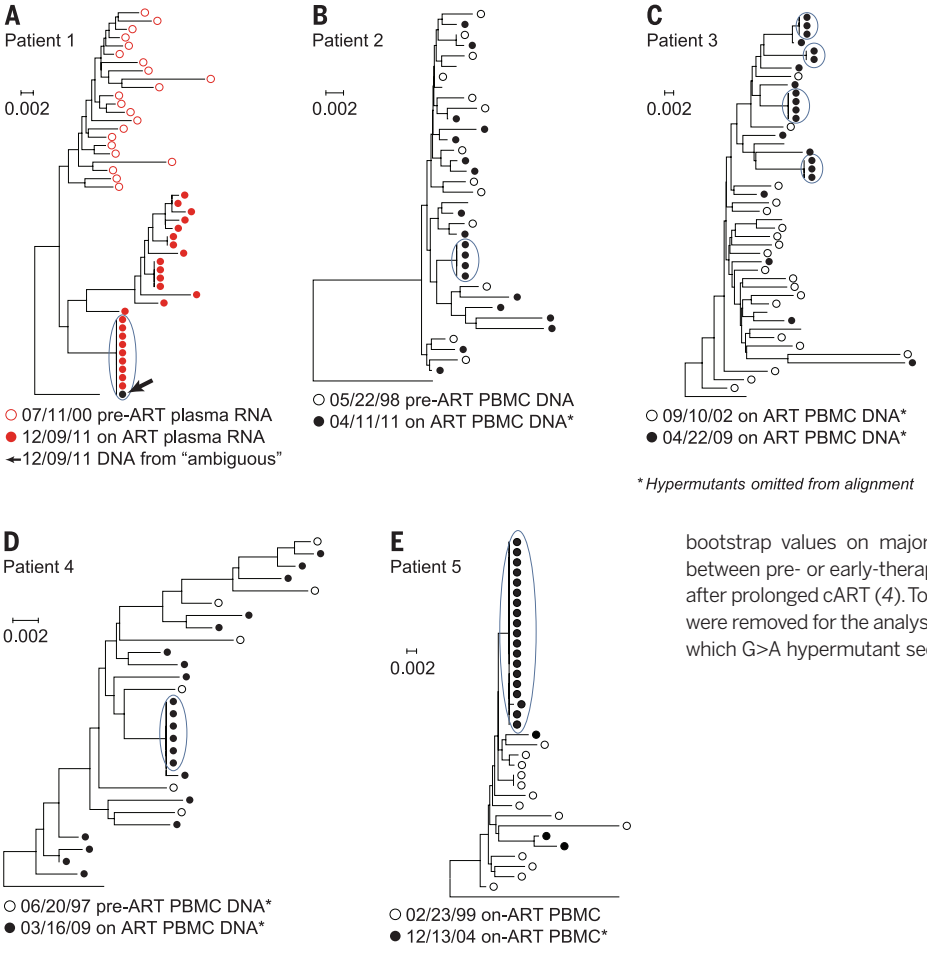

Fig. 1. Long-term cART reveals the presence in patients, at both the RNA and the DNA level, of HIV genomes that have identical sequences. (**A** to **E**) Single-genome sequences were obtained from plasma virion RNA or from PBMC DNA prior to or shortly after the initiation of cART, and after long-term cART. Sequences were aligned by using Clustal W (Clustal is maintained at the Conway Institute, Dublin, Ireland), and neighbor-joining trees were rooted on the consensus sequence of subgroup B HIV (*8*). Virus populations from pretherapy samples, or samples taken shortly after the initiation of cART, are shown as open circles (red, virion RNA; black, PBMC DNA); populations after prolonged cART are shown as solid circles (red, virion RNA; black, PBMC DNA). (A) In patient 1, the black dot (indicated with the arrow) represents DNA sequences from the provirus in a clone of expanded cells, whose integration site could not be mapped (Fig. 2, "ambiguous"). Short branches and low bootstrap values on major nodes of the trees support a lack of divergence between pre- or early-therapy sequences and populations of identical sequences after prolonged cART (*4*). To avoid distorting the trees, all hypermutant sequences were removed for the analysis shown in the figure. Asterisk denotes the trees from which G>A hypermutant sequences were removed.

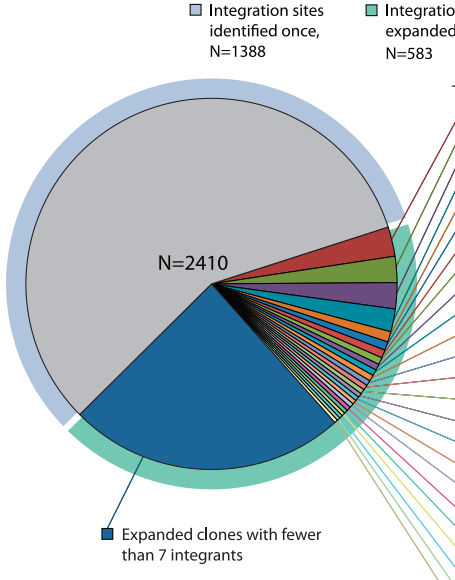

Genes	Patient	Highly expanded clones: Integrants	Total integrants in patient	%
HORMAD2	3	62	317	19.6
Ambiguous	1	55	1762	3.1
Intergenic-1	1	55	1762	3.1
MKL2a	1	48	1762	2.7
MKL2b	1	22	1762	1.2
HNRNPM	4	18	215	8.4
ATP6V1G3	1	17	1762	1.0
Intergenic-2	1	15	1762	0.9
TNFSF13B	1	13	1762	0.7
Intergenic-3	1	13	1762	0.7
UBE2D2	4	13	215	6.0
DDX6	1	11	1762	0.6
MKL2c	1	11	1762	0.6
FSIP1	1	10	1762	0.6
KIAA0319L	1	9	1762	0.5
MKL2d	1	9	1762	0.5
MKL2e	1	9	1762	0.5
Intergenic-4	1	9	1762	0.5
PABPC1L	1	9	1762	0.5
RBM15B	1	8	1762	0.5
CEPT1	1	7	1762	0.4
CKAP5	3	7	317	2.2
STAT5B	1	7	1762	0.4
PKP4	1	7	1762	0.4

Fig. 2. Distribution of integration sites in the five patients. A total of 2410 integration sites were obtained from PBMCs or negatively selected $CD4^+$ cells from the five patients. Genes in which we isolated a particular integration site seven or more times are shown. The table shows which patient harbored each of these expanded clones, how many times the different integrations sites were isolated, and the fraction of the infected cells the expanded clone represents in the patient. The MKL2 clones marked MKL2a, -b, -c, and -d correspond to the integration sites marked a, b, c, and d in Fig. 3. One provirus in a highly expanded clone in patient 1 was in a sequence that could not be unambiguously assigned in the human genome (denoted "ambiguous"). Our standard analysis (presented here) underestimated the fraction of the infected cells in patient 3 that had an integration site in HORMAD2 (*8*).

11.4 years of cART, there were 11 distinct integration sites in intron 6 of *MKL2* (intron 6 is ~3.5 kb), more than half of which were in clonally expanded cells; some of these cells were highly expanded (Figs. 2 and 3). There were also four nearby integration sites in intron 4, and none in any other part of *MKL2* (Fig. 3A). All 15 of these proviruses were integrated in the same transcriptional orientation as the host gene. Thus, ~7% of the infected cells in this patient had proviruses in a region that constitutes a very small fraction ($\sim 2 \times 10^{-6}$) of the human genome. In the same data set, there were 15 independent integration sites—also in the same transcriptional orientation as the host gene—in introns 4 and 5 of *BACH2* (Fig. 3B); two additional integration sites in *BACH2* were identified in earlier samples from this patient.

For comparison, we analyzed two large HIV integration site libraries made from acutely infected HeLa cells (~250,000 sites) and human CD34$^+$ hematopoietic stem cells (~150,000 sites). The frequencies of HIV integration in *MKL2* and *BACH2* in cells from patient 1 were much greater than in HeLa or CD34$^+$ cells. In cells from patient 1, integrations in *MKL2* were 7% of the total integrations, compared with 0.03% of total integrations in HeLa and CD34$^+$ cells. Similarly, integrations in *BACH2* in cells from patient 1 were 1.5% of the total integrations, compared with 0.002% in HeLa cells and 0.01% in CD34$^+$ cells. There was no preference for integrations in specific introns in these genes in HeLa cells or CD34$^+$ cells. Nor was there any indication, in either library, of preferential integration in one orientation in *MKL2* or *BACH2*. Across the entire patient data set (table S3), there was a weak, but significant preference for integrants in genes to be in an orientation opposite to the direction in which the gene is transcribed. Of the 1313 integrants that were in genes, 594 were in the same transcriptional orientation as the gene, and 719 were in the opposite orientation (P = 0.02, Fisher's exact test). These findings led us to conclude that the HIV DNA insertions in *MKL2* and *BACH2* were selected, after integration, because they altered the level of expression of the *MKL2* and *BACH2* proteins or gave rise to the expression of altered forms of the proteins, and that these alterations affected the expansion and survival of the infected cells. In the case of *BACH2*, all of the integrations were upstream of the initiation site for translation, which is consistent with the integrations altering the level of expression of *BACH2*. The integrations in *MKL2* were in introns that were between two coding exons, and these integrations were more likely to have affected the structure of the protein. Both of these mechanisms have been seen with other types of retroviruses and are known to be involved in oncogenic transformation in animals (*12*).

In all, we found that out of the 985 genes in which there were integrations in the patients, there were 200 genes that had multiple independent integrations; 59 of these were associated with expanded clones. The genes that had at least three independent integrants are shown in table S4; as mentioned earlier, many of these genes have roles in cell growth. In addition, there were integrations in more than one patient in more than 60% (18 of 29) of the genes listed in table S4. For example, a total of 10 independent integrants were found in *STAT5B* in four of the five patients; some of these integrants were in expanded clones. However, the proviruses integrated in *STAT5B* showed no orientation preference. Gene ontology analysis showed that the patient integration sites were enriched for genes in several pathways involved in cell growth. The HeLa and human CD34$^+$ cell data sets (which were similar to each other) were not enriched for genes in these pathways (fig. S4). This analysis also showed that the patient data set was related to leukemia and Burkitt's lymphoma; the HeLa and human CD34$^+$ data sets were not associated with any disease-related pathways.

Although as expected (*13*) most of the integration sites in the patients were in genes, 21% (509) were in intergenic regions or in sequences that could not be mapped to a single location in the human genome. Forty-four percent (226) of the integrants in the intergenic regions, or that could be mapped to a single site, were in cells that underwent clonal expansion, some of which were highly expanded (Fig. 2 and fig. S2). One of the proviruses in the two

Table 1. In patient 1, clones persist for many years.

Gene	Integration site	Detected in year*			Orientation†	Gene description
		0.2	4.8	11.4		
DDX6	chr11:118636877	+	+	+	Reverse	DEAD (Asp-Glu-Ala-Asp) box polypeptide 6
TNFSF13B	chr13:108927255	+	+	+	Forward	tumor necrosis factor (ligand) superfamily, member 13
PKP4	chr2:159370503	+	+	+	Forward	plakophilin 4
RBM15B	chr3:51434782	+	+	+	Reverse	RNA binding motif protein 15B
PARP8	chr5:50035007	+	+	+	Reverse	poly (ADP-ribose) polymerase family, member 8
ATP6V1G3	chr1:198506789	–	+	+	Forward	ATPase, H+ transporting, lysosomal 13 kD, V1 subunit G3
SLC30A7	chr1:101445575	–	+	+	Forward	solute carrier family 30 (zinc transporter), member 7
ZCCHC11	chr1:52956520	–	+	+	Reverse	zinc finger, CCHC domain containing 11
NUMA1	chr11:71744577	–	+	+	Forward	nuclear mitotic apparatus protein 1
CTAGE5	chr14:39760983	–	+	+	Reverse	CTAGE family, member 5
PATL2	chr15:44962782	–	+	+	Forward	protein associated with topoisomerase II homolog 2 (yeast)
P4HB‡	chr17:79800929	–	+	+	Reverse	prolyl 4-hydroxylase, beta polypeptide
ZC3H4	chr19:47603701	–	+	+	Reverse	zinc finger CCCH-type containing 4
COG5	chr7:107182849	–	+	+	Reverse	component of oligomeric golgi complex 5
GIMAP6‡	chr7:150318109	–	+	+	Reverse	GTPase, IMAP family member 6
ZNF16	chr8:146170620	–	+	+	Forward	zinc finger protein 16
R3HDM2‡	chr12:57731640	+	–	+	Forward	R3H domain containing 2 (R3HDM2), mRNA
FSIP1	chr15:39975096	+	–	+	Forward	fibrous sheath interacting protein 1
NLRC5	chr16:57030643	+	–	+	Forward	NLR family, CARD domain containing 5
STAT5B	chr17:40421711	+	–	+	Reverse	signal transducer and activator of transcription 5B
PABPC1L	chr20:43561100	+	–	+	Reverse	poly(A) binding protein, cytoplasmic 1–like
MAP4	chr3:47981132	+	–	+	Reverse	microtubule-associated protein 4
BTNL3‡	chr5:180401789	+	–	+	Forward	butyrophilin-like 3
SQLE	chr8:126012090	+	–	+	Forward	squalene epoxidase
CHD7	chr8:61594573	+	+	–	Reverse	chromodomain helicase DNA binding protein 7

*Relative to start of cART. †The orientation of the provirus relative to the direction of transcription of the gene. ‡Nearest gene.

most highly expanded clones in patient 1 [each site was identified 55 times, which is an underestimate because of breakpoint overlaps (*8*)] was in an intergenic region; the other could not be mapped to a single site in the human genome (Fig. 2). The predominant virus in the plasma of patient 1 late in therapy was clonal (Fig. 1 and fig. S1) and was insensitive to a switch in cART (Fig. 1 and fig. S1), suggesting that it was produced by a clone of infected cells, rather than from infection of new cells. More than 1 kb of sequence in *gag-pro-pol* from the RNA genome of this predominant virus exactly matched the sequence of the ambiguously mapped provirus, identifying this provirus as the source of the clonal viral RNA in the plasma (Fig. 1A, black arrow).

Discussion

Our results strongly imply that in at least some cases, sites of HIV integration play an important role in the expansion and persistence of infected cells in patients. This conclusion is particularly strong for the integrations into specific introns of the *MKL2* and *BACH2* genes. The integrations in *MKL2* and *BACH2* that were linked to clonal expansion were in internal introns, and in the same transcriptional orientation as the genes in which they are inserted. Even setting aside the fact that that it is extremely unlikely that such a large fraction of the integrations would have occurred in these two small segments of the genome, the probability that all 33 of the integrations we saw in *BACH2* and *MKL2* in the patients (table S4) would have been in the same orientation as

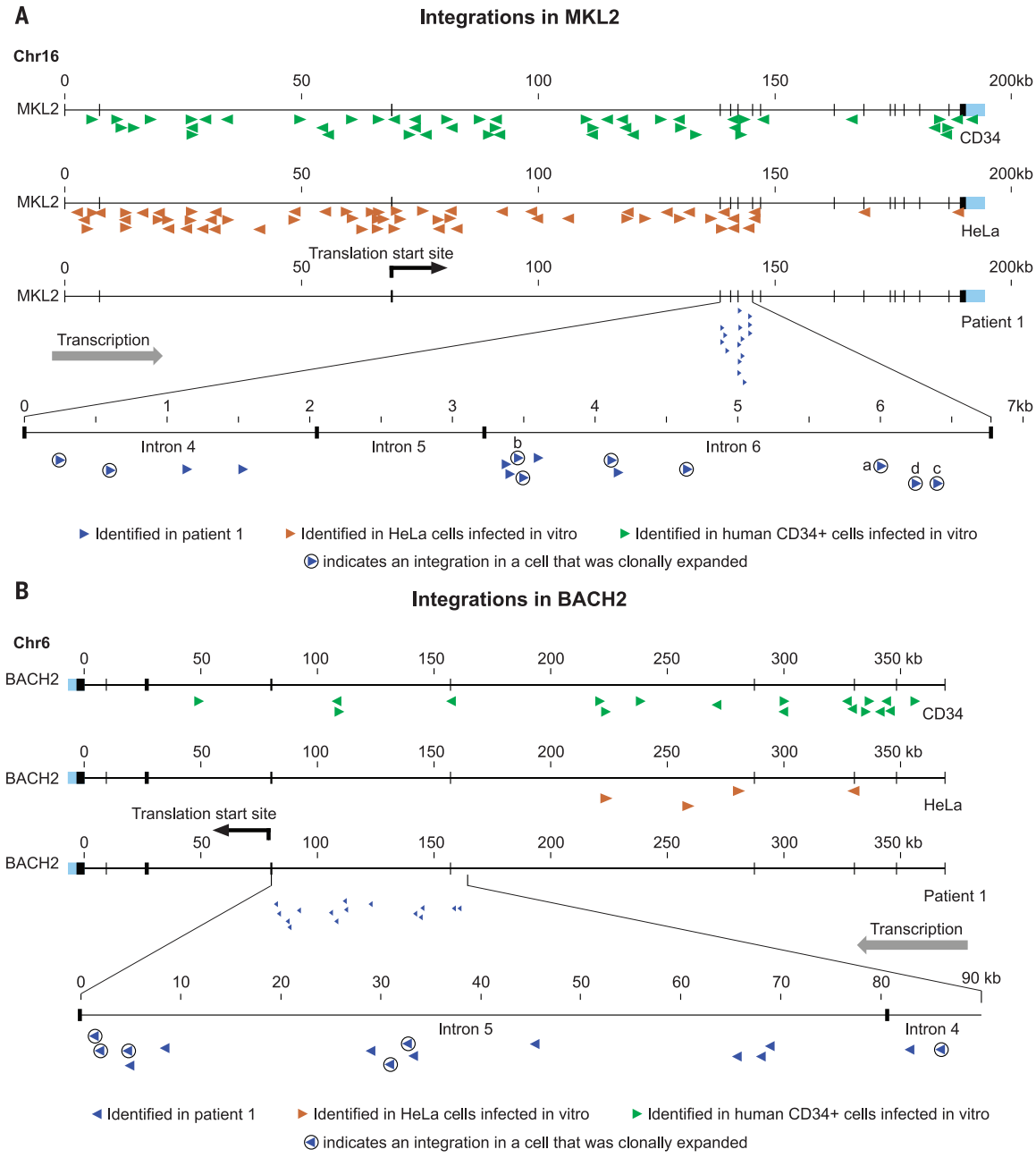

Fig. 3. Integration sites in the *MKL2* and *BACH2* genes in patient 1 after 11.4 years of cART. (**A**) There were 15 distinct integration sites (blue arrows) in a small region of the *MKL2* gene in patient 1. The arrows denote the transcriptional orientation of each provirus. The circled arrows indicate integration sites in clonally expanded cells. The arrows marked a, b, c, and d correspond to the clones marked MKL2a, -b, -c, and -d in Fig. 2. (**B**) There were 15 distinct integration sites in a small region of the *BACH2* gene in patient 1 (blue arrows). Some of these integration sites were in clonally expanded cells (circled arrows). (A) and (B) also show the HIV integration sites identified in the same two genes in acutely infected HeLa cells (total sites, 248,658; brown arrows) and $CD34^+$ cells (total sites, 159,484; green arrows).

the genes is ~10^{-10}. In prior studies, a limited number of HIV integration sites were identified in patients (*14*–*17*), and HIV proviruses were found in intron 6 of *MKL2* and intron 5 of *BACH2*, in the same orientation that the genes are transcribed. However, in the published studies the integration sites in these genes were not linked to the clonal expansion of the infected cells (table S5). Both *BACH2* and *MKL2* are involved in the growth and development of cells, and *BACH2* is known to play a key role in T cell development (*18*). Both genes [and the *MKL2*-related gene *MKL1*, in which there were four independent integration sites, some of which were associated with clonally expanded cells in patient 1 (table S4)] have been implicated in human cancers (*19*–*21*), in which they were activated by DNA rearrangements that created gene fusions. The pattern of multiple integrations in *MKL2* and *BACH2* found in the patients cannot be the result of preferential integration because HIV integration is neither intron-specific nor orientation-specific (*22*). Thus, the only plausible explanation for the data that is in accord with the rules for HIV integration is that the cells with the integrations in *MKL2* and *BACH2* were selected after integration because the integrations in these genes contributed to the expansion and persistence of the host cells. This interpretation is supported, for *BACH2*, by a report showing that this gene is a target for retroviral insertional activation in mice infected with mouse leukemia virus (*23*).

Most of our analyses were performed by using cells from patients on long-term cART, which blocks the infection of additional cells but has no effect on cells that have already been infected (*9*). During untreated HIV infections, ~10^9 cells are infected daily. The vast majority (99%) of the newly infected cells die within 24 to 48 hours, and a substantial proportion of the remaining cells die within 2 to 4 weeks (*24*–*26*). Viremia decreases by 4 to 5 logs when patients undergo cART; however, the number of cells containing HIV DNA decreases by approximately 1 log (*9*), indicating that a substantial fraction (~10%) of the cells that were infected before the initiation of cART persist. Most of these long-lived infected cells contain proviruses that are obviously defective; however, ~12% of the proviruses appear to be functional, although only a small fraction of these apparently functional proviruses can be induced to make virus in ex vivo experiments (*27*). Cells infected with highly defective or fully latent proviruses that produce little or no viral protein may have a survival advantage relative to cells that produce virions because cells that express viral proteins are more likely to be lysed by HIV-specific cytotoxic T lymphocyte or be subject to cytopathic effects of the viral proteins. This same logic applies to HIV-infected cells that undergo clonal expansion. Although we have not yet shown that clonally expanded cells produce replication-competent HIV, we have shown that a highly expanded clone of cells does produce HIV virions in sufficient quantity to cause viremia, which means that the selection against cells that produce viral proteins is not so strong that it prevents extensive clonal expansion of cells that express the viral proteins required to produce virions.

Our data show that many of the infected cells that persist have undergone clonal expansion; these clones were revealed but not created by cART. For some infected cell clones, it is likely that the integration site is only a passive marker of clonal expansions that are driven by another factor or factors, such as antigen stimulation or homeostatic proliferation signals (*28*). In contrast, we show here that some cells with HIV integration sites in specific genes are strongly selected because these integrations promote the survival and expansion of the infected cells. Although there are obvious similarities in the integration sites seen in the five patients, there is considerable heterogeneity from one patient to another, both in the extent of clonal expansion and in the genes in which proviruses are integrated in the clonally expanded cells (fig. S5). This complexity highlights the difficulty in attempting to extrapolate, from bulk HIV DNA quantification, the size and nature of the population of HIV proviruses that make up the reservoir that gives rise to HIV rebound after cessation of cART (*28*).

Our findings have relevance for three important areas. (i) To effectively target HIV persistence with the goal of achieving a cure, it will be important not only to suppress any replication of the virus, but also to block the expansion of infected cells. (ii) Although the HIV vectors used in gene therapy have safety features that the parental virus lacks, we now know that like many other retroviruses, HIV integration can lead to clonal expansion and persistence of infected cells. This discovery suggests that persons treated with HIV-based vectors should be carefully monitored for evidence of clonal expansion of vector-infected cells. (iii) We also suggest that it is time to reexamine the question of whether HIV integration can contribute to the development of malignancies. Although there are well-defined cancers in HIV-infected patients that are the result of uncontrolled expression of herpes viruses, there are reports of a small number of lymphomas with HIV proviruses integrated at defined sites; one lymphoma had a provirus integrated in BACH2 (*15*, *29*, *30*). Despite these published reports, it is widely believed that HIV DNA is not detectable in most cancers from HIV-infected patients; however, the experiments supporting this belief are not well-documented in the literature. It is possible that prior attempts to detect HIV DNA in cancers examined only a very small portion of the HIV genome and, as such, missed HIV proviruses having large deletions; large deletions are a characteristic of the proviruses that cause mouse and avian tumors. Thus, our findings have important implications for designing and implementing strategies to eliminate persistent HIV infection, for the use of lentiviral vectors for gene therapy in human patients and, possibly, for the origin of some HIV-related malignancies.

REFERENCES AND NOTES

1. S. G. Deeks *et al*., *Nat. Rev. Immunol.* **12**, 607–614 (2012).
2. S. Palmer, L. Josefsson, J. M. Coffin, *J. Intern. Med.* **270**, 550–560 (2011).
3. J. R. Bailey *et al*., *J. Virol.* **80**, 6441–6457 (2006).
4. M. F. Kearney *et al*., *PLOS Pathog.* **10**, e1004010 (2014).
5. C. C. Berry *et al*., *Bioinformatics* **28**, 755–762 (2012).
6. N. A. Gillet *et al*., *Blood* **117**, 3113–3122 (2011).
7. S. S. De Ravin *et al*., *J. Virol.* (2014).
8. Materials and methods are available as supplementary materials on *Science* Online.
9. J. Coffin, R. Swanstrom, *Cold Spring Harb. Perspect. Med.* **3**, a012526 (2013).
10. H. Imamichi *et al*., *AIDS* (2014).
11. L. Josefsson *et al*., *Proc. Natl. Acad. Sci. U.S.A.* **110**, E4987–E4996 (2013).
12. N. Rosenberg, P. Jolicoeur, in *Retroviruses*, J. M. Coffin, S. H. Hughes, H. E. Varmus, Eds. (Cold Spring Harbor Laboratory Press, Cold Spring Harbor, 1997), pp. 475–585.
13. A. R. Schröder *et al*., *Cell* **110**, 521–529 (2002).
14. T. Ikeda, J. Shibata, K. Yoshimura, A. Koito, S. Matsushita, *J. Infect. Dis.* **195**, 716–725 (2007).
15. K. D. Mack *et al*., *J. Acquir. Immune Defic. Syndr.* **33**, 308–320 (2003).
16. Y. Han *et al*., *J. Virol.* **78**, 6122–6133 (2004).
17. H. Katano *et al*., *Microbes Infect.* **9**, 1581–1589 (2007).
18. G. Hu, J. Chen, *Nat. Commun.* **4**, 2830 (2013).
19. S. Kobayashi *et al*., *Genes Chromosomes Cancer* **50**, 207–216 (2011).
20. U. Flucke *et al*., *Histopathology* **62**, 925–930 (2013).
21. S. Muehlich *et al*., *Oncogene* **31**, 3913–3923 (2012).
22. R. Craigie, F. D. Bushman, *Cold Spring Harb. Perspect. Med.* **2**, a006890 (2012).
23. J. Liu *et al*., *BMC Mol. Biol.* **10**, 2 (2009).
24. D. D. Ho *et al*., *Nature* **373**, 123–126 (1995).
25. X. Wei *et al*., *Nature* **373**, 117–122 (1995).
26. J. M. Coffin, *Science* **267**, 483–489 (1995).
27. Y. C. Ho *et al*., *Cell* **155**, 540–551 (2013).
28. N. Chomont *et al*., *Nat. Med.* **15**, 893–900 (2009).
29. B. Shiramizu, B. G. Herndier, M. S. McGrath, *Cancer Res.* **54**, 2069–2072 (1994).
30. B. G. Herndier *et al*., *Blood* **79**, 1768–1774 (1992).

ACKNOWLEDGMENTS

The authors are indebted to the study participants and to the clinical staff of the National Institute of Allergy and Infectious Diseases/Critical Care Medicine Department clinic who cared for them. We thank C. Lane, H. Malech, H. Imamichi, S. Matsushita, and L. Frenkel for stimulating discussions. We are grateful to J. Meyer and A. Kane for help with the figures and T. Burdette for help in preparing the manuscript. The data presented in this work is tabulated in the main paper and in the supplementary materials. The integration sites are compiled in table S3; the data can also be accessed using the National Center for Biotechnology Information accession no. PRJNA241020. Funding for this research was provided with Federal funds from the National Cancer Institute, an NIH Bench to Bedside award (F.M.), and by funds from the National Cancer Institute under contract HSSN261200800001E (X.W. and L.S.). J.M.C. was supported by a Research Professorship from the American Cancer Society with additional support from the F. M. Kirby Foundation and by funding from the National Cancer Institute (Leidos contract 25XS119). J.W.M. was supported by funding from the National Cancer Institute (Leidos contract 25XS119). The content of this publication does not necessarily reflect the views or policies of the Department of Health and Human Services, nor does mention of trade names, commercial products, or organizations imply endorsement by the U.S. government.

SUPPLEMENTARY MATERIALS

www.sciencemag.org/content/345/6193/179/suppl/DC1
Materials and Methods
Figs. S1 to S5
Tables S1 to S5
References (*31*–*35*)

1 April 2014; accepted 13 June 2014
Published online 26 June 2014;
10.1126/science.1254194

REPORTS

SPACE WEATHER

Ionospheric control of magnetotail reconnection

William Lotko,[1,2]* Ryan H. Smith,[1] Binzheng Zhang,[1] Jeremy E. Ouellette,[1,3] Oliver J. Brambles,[1] John G. Lyon[4]

Observed distributions of high-speed plasma flows at distances of 10 to 30 Earth radii (R_E) in Earth's magnetotail neutral sheet are highly skewed toward the premidnight sector. The flows are a product of the magnetic reconnection process that converts magnetic energy stored in the magnetotail into plasma kinetic and thermal energy. We show, using global numerical simulations, that the electrodynamic interaction between Earth's magnetosphere and ionosphere produces an asymmetry consistent with observed distributions in nightside reconnection and plasmasheet flows and in accompanying ionospheric convection. The primary causal agent is the meridional gradient in the ionospheric Hall conductance which, through the Cowling effect, regulates the distribution of electrical currents flowing within and between the ionosphere and magnetotail.

Plasma flows with bulk velocities up to 1000 km/s perpendicular to the local magnetic field are observed in Earth's nightside central plasmasheet beyond geostationary orbit (*1*–*7*). The earthward-directed flows transport the magnetic flux required to maintain the magnetosphere-ionosphere convection cycle (*3*). They are produced by time-variable magnetic reconnection wherein magnetic energy in the magnetotail is converted to plasma kinetic and thermal energy. The average spatial distribution of the flows exhibits a prominent asymmetry, with faster flows occurring more frequently in the premidnight (dusk) sector of the plasmasheet relative to those observed in the postmidnight (dawn) sector (*2*, *4*–*7*). An example (*5*) is shown in Fig. 1. The nightside plasmasheet was uniformly sampled across the tail in this data set, yet fast flows were found predominantly in the premidnight sector.

This asymmetry is attributed to a higher rate of magnetic reconnection in the premidnight sector (*4*), but the mechanism(s) controlling the distribution are unknown. Geospace phenomena are strongly influenced by the distribution and rate of reconnection, so this deficiency impedes our ability to interpret and predict geospace weather and its climatology. Imagine trying to describe tropospheric climate and weather without knowing what determines the location and intensity of the polar jet streams. Resolving this issue is a high priority for geospace science, and it has implications for magnetic activity in other planetary magnetospheres.

Asymmetries in the reconnection rate can be caused by dawn-dusk asymmetry in external driving, e.g., in interplanetary conditions. However, the observed asymmetry in high-speed flows and associated effects on plasmasheet properties persists even when interplanetary conditions are selectively sampled to minimize asymmetric driving, corrected to account for the aberration due to Earth's orbital motion, and averaged over residual asymmetry to eliminate its influence (*6*).

At least three internal mechanisms can produce an asymmetric distribution in reconnection and associated flows. (i) Variations in local conditions: The local Alfvén speed influences the local reconnection rate, which is slower when the plasma is an admixture of protons and heavy ions such as O^+ (*8*). Asymmetry in the Alfvén speed may arise from inhomogeneous outflows of ions from Earth's ionosphere (*9*, *10*). (ii) Magnetic x-line spreading: Hall magnetohydrodynamic simulations show that magnetic reconnection expands in the direction of the dominant current carriers in a neutral sheet—duskward or dawnward in the magnetotail neutral sheet when carried mainly by ions or electrons, respectively (*11*). The electron current evidently dominates in reconnection diffusion regions in the magnetotail (*12*), so this effect alone produces the wrong type of asymmetry. (iii) Magnetosphere-ionosphere coupling: The electrical currents flowing between the magnetosphere and ionosphere can produce global asymmetry in magnetospheric geometry and dynamos (*13*), which influences the transport and reconnection of magnetic flux. All three processes may be active in controlling the observed asymmetry. We show here that the large-scale interaction between the magnetosphere and ionosphere has a major impact on magnetotail reconnection.

Convective flows observed in the ionosphere also exhibit a dawn-dusk asymmetry (*14*). In classical magnetohydrodynamics, flows in the ionosphere and magnetosphere are nearly ideal, which means that magnetic field lines connecting the two regions are practically "frozen into" the fluid. The resulting magnetic shear stresses force the flows in the nightside ionosphere to move synchronously with the flows in the plasmasheet. The streamlines in the ionosphere (equivalent to electric equipotentials) exhibit

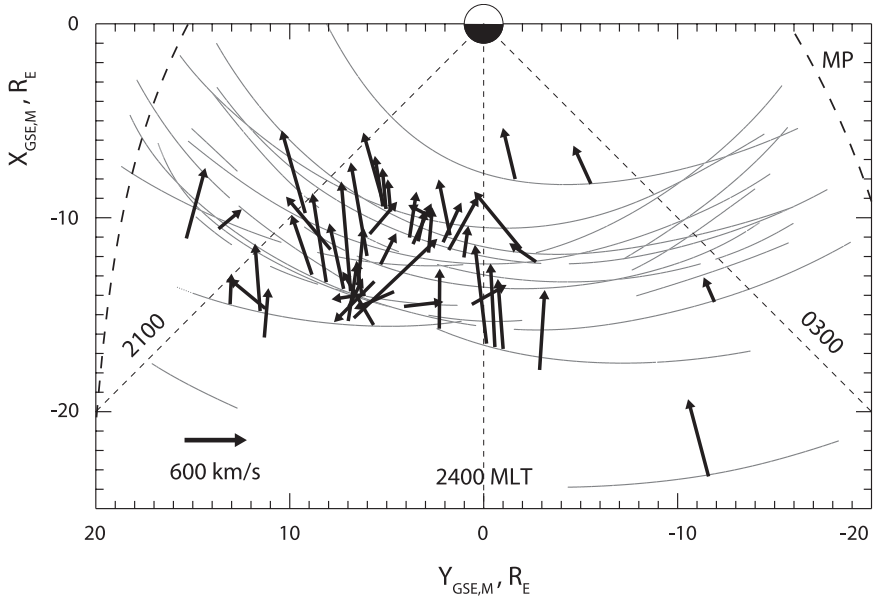

Fig. 1. Distribution of plasma flows with velocity >250 km/s observed near Earth's magnetotail neutral sheet (*5*). Vectors and their locations are resolved in geocentric solar magnetospheric (GSM) coordinates (*26*). Measurements are from the 17 perigee passes of the Wind spacecraft during 1995–1997 with gray orbit tracks in geocentric solar ecliptic (GSE) coordinates (*26*). The long dashed lines delineate a typical magnetopause (MP) boundary.

[1]Thayer School of Engineering, Dartmouth College, Hanover, NH, USA. [2]Research Affiliate, High Altitude Observatory, National Center for Atmospheric Research, Boulder, CO, USA. [3]Department of Computer and Information Systems, Vermont Technical College, Randolph Center, VT, USA. [4]Department of Physics and Astronomy, Dartmouth College, Hanover, NH, USA.
*Corresponding author. E-mail: wlotko@dartmouth.edu

antisunward convection over the polar cap and a return sunward flow at lower latitudes (Fig. 2). Two features of the ionospheric convection pattern in Fig. 2 are noteworthy: (i) It is rotated 16.1° clockwise (CW) about the magnetic pole, as determined by the angle between the line connecting the potential minimum and maximum and the dawn-dusk meridian; and (ii) more magnetic flux circulates in the dusk cell than in the dawn cell, which is manifest in the −6-kV offset in the dusk cell relative to the dawn cell.

Simple models of the distribution of high-latitude Hall and Pedersen conductance and field-aligned currents flowing between the magnetosphere and ionosphere show that the rotation in ionospheric convection is due to an auroral band of enhanced Hall conductance (*15*, *16*). However, these idealized ionospheric models do not yield asymmetry in magnetic flux circulation between the dawn and dusk convection cells. In specifying a given field-aligned current distribution as input to the well-known Poisson equation for ionospheric electrodynamics (*17*), the models do not self-consistently couple the magnetosphere and ionosphere and cannot be used to analyze linkages between asymmetries in the ionosphere and magnetosphere. For a better understanding of the relationship between the fast flows observed in the plasmasheet and convection in the ionosphere, we ran global simulations of the solar wind–magnetosphere–ionosphere (SW-M-I) interaction (*18*–*20*).

Each simulation was run for 8 hours (*18*). The upwind boundary conditions during the last 4 hours for the solar wind (SW) and interplanetary magnetic field in solar magnetic coordinates (8) were N_{SW} = 5/cm^3, T_{SW} = 8.5 eV, V_x = −300 km/s, B_z = −4 nT, and $V_{y,z}$ = $B_{x,y}$ = 0. We then calculated 1-hour average states (Figs. 3 and 4) during the last hour of the simulation.

Our first simulation (Fig. 3, left panels) has uniform Pedersen (5 S) and Hall (10 S) conductance in the ionosphere. The resulting ionospheric convection pattern and plasmasheet fast flows are dawn-dusk symmetric. The second simulation (Fig. 3, center panels) uses a causally regulated, empirical conductance model (*21*), including contributions from extreme ultraviolet (EUV)–induced ionization (day-to-night gradient in conductance) and auroral electron precipitation, which is noticeable as an approximately circular band offset toward midnight from the magnetic pole with greatest intensity near 69° magnetic latitude and 2300 magnetic local time (MLT). The nightside ionospheric convection pattern is rotated CW 7° relative to the uniform conductance run, and the magnitude of the dusk-cell potential is 8.2 kV larger than that of the dawn cell. Similar ionospheric effects are seen in other global simulation models when realistic ionospheric conductance distributions are included (*22*). The fast flows in the plasmasheet are concentrated in the premidnight sector (Fig. 3, bottom center panel). The final simulation (Fig. 3, right panels) has a time-independent, artificially depleted Hall conductance in a band centered on the magnetic pole. This simulation illustrates how an axisymmetric Hall conductance gradient controls rotation of the convection pattern [counterclockwise (CCW) 6° in contrast to the CW rotation in the causal conductance run] and moves the concentration of fast flows to the postmidnight sector.

Although the distributions of conductances in the uniform (Fig. 3, left) and auroral depletion (Fig. 3, right) simulations are unrealistic, their comparison with the simulation using a more realistic, causally regulated conductance (Fig. 3, center) illustrates the important effect of ionospheric Hall conduction in controlling convection in the coupled M-I system. The simulation with causally regulated conductance produces plasmasheet flows with an average distribution similar to that of satellite observations (Fig. 1) and ionospheric convection resembling empirical patterns (Fig. 2).

We performed additional simulations to isolate the effects of the night-to-day conductance gradient from EUV ionization and from the auroral enhancement in Hall conductance due to electron precipitation. Including the EUV contribution only produces a weak CCW rotation and a large asymmetry in the polar cap potentials with the dusk potential ≈35% larger in magnitude than the dawn potential. A band of enhanced Hall conductance distributed similarly to the Hall-depletion case in Fig. 3 produces rotation and asymmetry opposite to that of the Hall-depletion case: CW with larger dawn than dusk polar cap potentials. Combining EUV and a contrived Hall-enhancement band produces a configuration resembling the causal-empirical results (Fig. 3, center). A meridional gradient in Pedersen conductance does not produce rotation or asymmetry. The ratio of background Pedersen to Hall conductance has a modest effect on the asymmetry and significantly diminishes the asymmetry only for unrealistically large ratios. More controlled experiments are needed to fully resolve cause and effect, but the comparisons indicate that the meridional gradient in Hall conductance at the dayside convection throat (ionospheric projection of dayside x-line) regulates the asymmetry in polar cap potentials and dayside rotation, whereas the meridional gradient in Hall conductance at the nightside convection throat regulates the nightside rotation. These two effects combine to determine the distribution of magnetotail reconnection and the plasmasheet transport of magnetic flux.

We derived the simulated reconnection potential Φ_R by integrating the reconnection electric

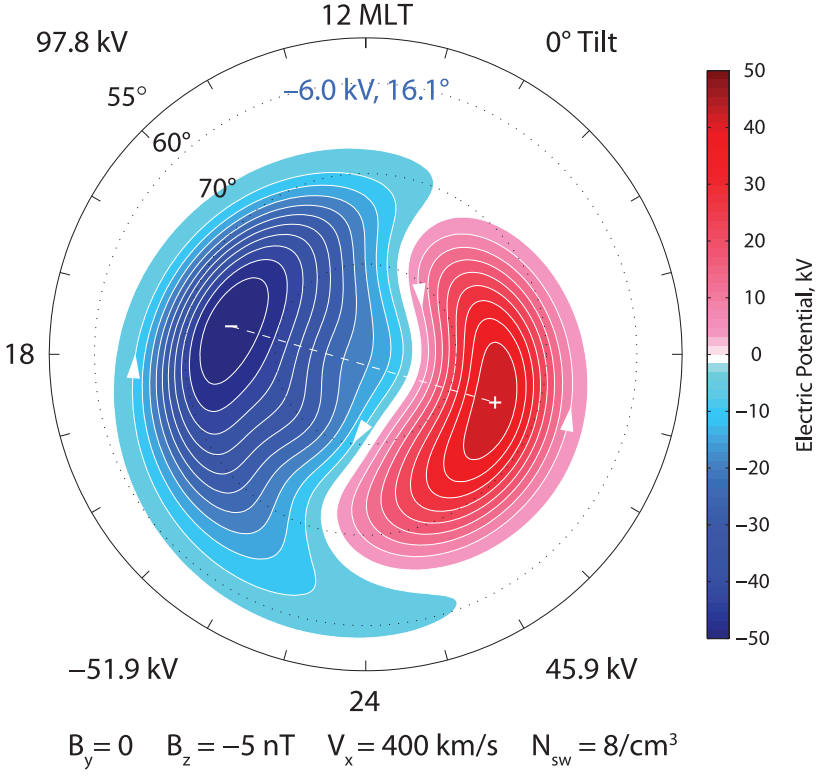

Fig. 2. Polar distribution of ionospheric convection and electric potential. Dependence on magnetic latitude and local time (MLT) is derived from the widely used Weimer empirical model (*27*) with 0° dipole tilt for solar wind and interplanetary magnetic field input variables indicated in GSM coordinates below the plot.

Table 1. Asymmetry in reconnection rates.

Run	Average rate (mV/m)	
T_O = MLT at Φ_R = 0	T_O − 1 hour	T_O + 1 hour
Causal (T_O = 23.91)	0.96	0.83
Depletion (T_O = 24.30)	0.68	0.93

field along the x-line or magnetic null (*23*) where four topological classes of magnetic field lines intersect: field lines with both ends in the interplanetary medium, with one end in the interplanetary medium and the other intersecting either the northern or southern ionosphere, and with one end in the southern ionosphere and the other in the northern ionosphere. The 1-hour average simulated x-line (Fig. 3, white contour

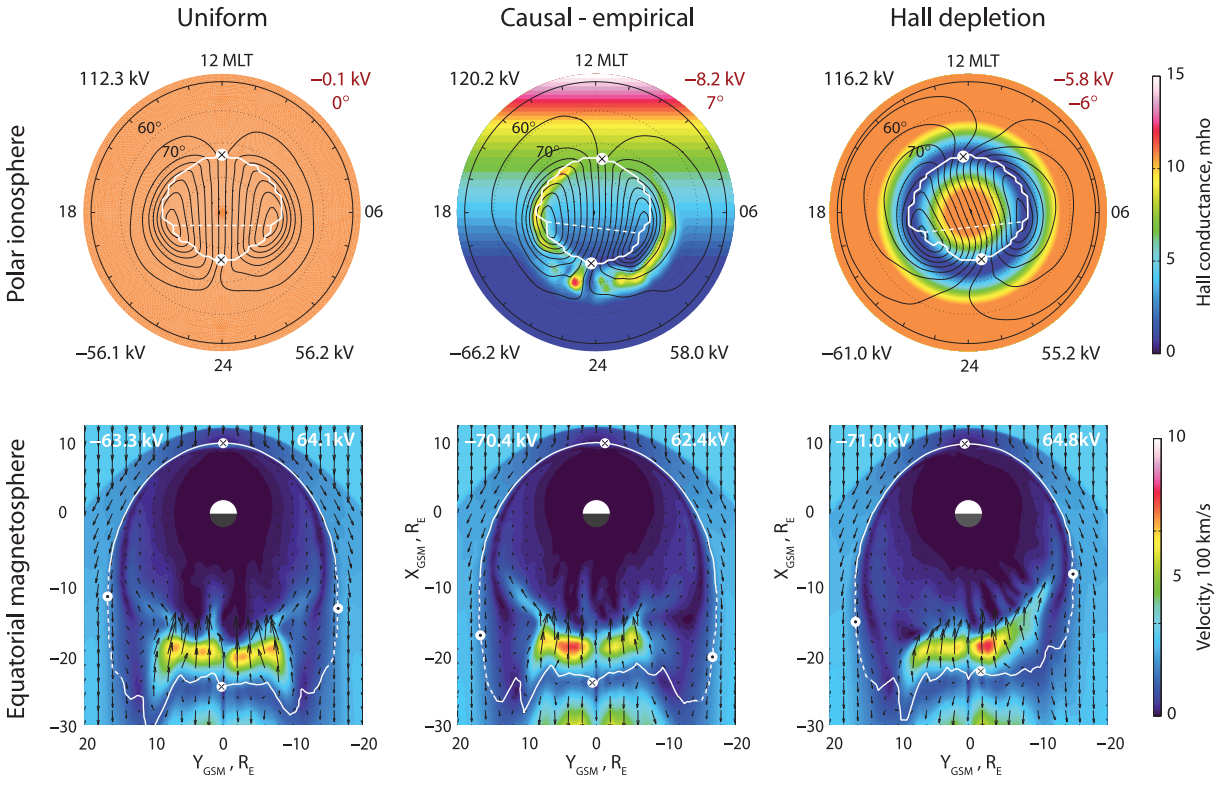

Fig. 3. Effect of ionospheric Hall conduction on convection in the ionosphere and plasmasheet. Top: Simulated ionospheric convection (8 kV contours) and Hall conductance distributions (color). The distribution of Pedersen conductance is a uniform 5 S for the simulations in the left and right panels and is similar to the Hall distribution in the causal conductance case but smaller in magnitude. Total cross polar cap potential is given in the upper left of each panel. The dusk minimum and dawn maximum are given below each panel. The white contour is the x-line mapped along magnetic field lines from the magnetosphere. The circled cross locates its intersection with the zero-potential contour. Bottom: Simulated equatorial magnetosphere with velocity vectors overlaid on velocity magnitude in color. B_z = 0 contour (magnetic x-line) is shown in white. Minimum and maximum reconnection potentials from Fig. 4 occur at circled dots, with location uncertainty confined to the dashed segments where the reconnection rate is nearly zero. The circled cross is the field-line mapping of the corresponding point in the ionosphere.

Fig. 4. Reconnection potential versus MLT. Different offset potentials are applied for each run so that Φ_R = 0 on the magnetic field line connecting the x-line in the magnetotail to the zero potential contour in the ionosphere (Fig. 3). Numerical uncertainty due to the finite simulation grid limits the precision in determining the local time of the extrema in potential on the x-line (gray segments here, dashed in Fig. 3).

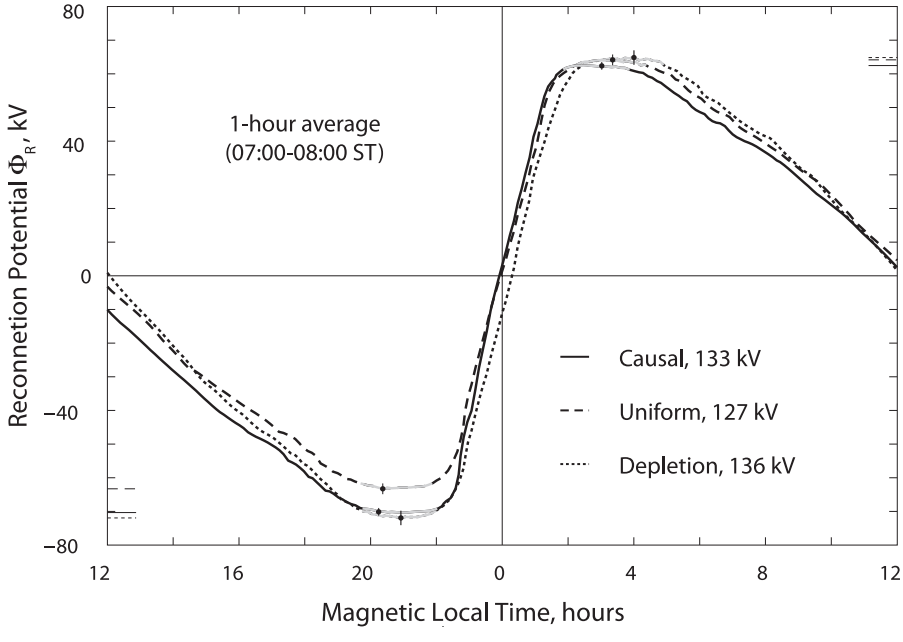

in lower panels) lies in the magnetic equatorial plane. The reconnection potential is arbitrary up to a constant of integration, which was chosen to ensure that, for each run, the zero value of reconnection potential in the magnetotail is magnetically connected to the zero potential in the ionosphere (*18*).

The reconnection potentials versus MLT with offsets chosen in this way (Fig. 4) exhibit the same dusk-to-dawn ratios of extrema as the ionospheric potentials (to within 1% for the values in Fig. 3). The minimum (duskside) potential is larger in magnitude than maximum (dawnside) potential for the causal and auroral depletion runs and equal in magnitude (within numerical error) for the uniform run. The average reconnection rate is higher on the nightside than on the dayside and more spatially limited. As expected from the distribution of fast flows (Fig. 3), the reconnection rate, per unit length x-line, averaged over a 1-hour MLT segment to either side of $\Phi_R = 0$ (Table 1), is larger in the premidnight sector, tailward of the fast flow, in the causal-empirical run and larger postmidnight in the Hall depletion run. The reconnection potential difference calculated as $\Delta\Phi_R = \Phi_{R,dawn} - \Phi_{R,dusk}$ exceeds the cross polar cap potential ($\Delta\Phi_{PC}$) in the ionosphere by 12, 6, and 14% for the uniform, causal, and auroral depletion runs, respectively (*18*).

Hall currents flow antiparallel to convection streamlines in the ionosphere (Fig. 3). If the Hall conductance develops a gradient parallel to a streamline—e.g., due to an enhancement in electron precipitation—the Hall current becomes discontinuous if other effects do not intervene. Its excess current could be diverted into a field-aligned current flowing through the magnetosphere to alleviate charge accumulation at the discontinuity, or a charge accumulation could polarize the ionospheric plasma and introduce a secondary electric field orthogonal to the primary convection electric field **E** (directed equatorward in a nightside auroral conductance band and sunward poleward of it). The resulting field, when added to the primary field, locally rotates the direction of convection and the Hall currents while driving secondary meridional Pedersen currents. This so-called Cowling effect produces the Harang reversal (*24*) in the nightside convection throat and increases the Joule dissipation in a zonally limited channel of enhanced conductance (*25*).

The Cowling effect dominates the electrodynamics of M-I coupling on the 100-km-scale ionospheric resolution of the global simulations. The sunward electric field in the polar cap produces a CW rotation of polar convection and a duskward drift in the magnetotail lobes. The secondary Pedersen current flowing equatorward in the nightside conductance band is supplied by a plasmasheet dynamo that generates field-aligned currents from a tailward current system (*24*). The resulting duskward, bulk Lorentz force presumably moves the otherwise symmetric plasmasheet flows toward the premidnight sector to produce the observed asymmetry in reconnection rates and plasmasheet fast flows. These results demonstrate the intricate interplay between the SW-M-I interaction and ionospheric Hall conduction in regulating magnetotail reconnection.

REFERENCES AND NOTES

1. E. W. Hones Jr., K. Schindler, *J. Geophys. Res.* **84**, 7155–7169 (1979).
2. M. Nakamura, G. Paschmann, W. Baumjohann, N. Sckopke, *J. Geophys. Res.* **96**, 5631–5649 (1991).
3. V. Angelopoulos *et al*., *J. Geophys. Res.* **99**, 21257–21280 (1994).
4. T. Nagai, S. Machida, in *New Perspectives on the Earth's Magnetotail*, Geophysical Monograph Series 105, A. Nishida, D. N. Baker, S. W. H. Cowley, Eds. (American Geophysical Union, Washington, DC, 1998), pp. 211–224.
5. A. Raj, T. Phan, R. P. Lin, V. Angelopoulos, *J. Geophys. Res.* **107** (A12), 1419 (2002).
6. L. Juusola, N. Østgaard, E. Tanskanen, *J. Geophys. Res.* **116**, A08201 (2011).
7. R. L. McPherron, T.-S. Hsu, J. Kissinger, X. Chu, V. Angelopoulos, *J. Geophys. Res.* **116**, A00I33 (2011).
8. M. A. Shay, M. Swisdak, *Phys. Rev. Lett.* **93**, 175001 (2004).
9. O. W. Lennartsson, H. L. Collin, W. K. Peterson, *J. Geophys. Res.* **109**, A12212 (2004).
10. O. J. Brambles *et al*., *Science* **332**, 1183–1186 (2011).
11. T. K. M. Nakamura, R. Nakamura, A. Alexandrova, Y. Kubota, T. Nagai, *J. Geophys. Res.* **117**, A03220 (2012).
12. T. Nagai *et al*., *J. Geophys. Res. Space Physics* **118**, 1667–1678 (2013).
13. B. Zhang *et al*., *J. Geophys. Res.* **117**, A09205 (2012).
14. Y. Kamide, S.-I. Akasofu, *J. Geophys. Res.* **86**, 3665–3668 (1981).
15. F. Yasuhara, R. Greenwald, S.-I. Akasofu, *J. Geophys. Res.* **88**, 5773–5777 (1983).
16. D. D. Barbosa, *J. Geophys. Res.* **89**, 2881–2890 (1984).
17. R. L. Lysak, *Space Sci. Rev.* **52**, 33–87 (1990).
18. Supplementary materials are available on *Science* Online.
19. J. G. Lyon, *Science* **288**, 1987–1991 (2000).
20. J. G. Lyon, J. A. Fedder, C. M. Mobarry, *J. Atmos. Sol. Terr. Phys.* **66**, 1333–1350 (2004).
21. M. Wiltberger *et al*., *J. Atmos. Sol. Terr. Phys.* **66**, 1411–1423 (2004).
22. A. J. Ridley, T. I. Gombosi, D. L. DeZeeuw, *Ann. Geophys.* **22**, 567–584 (2004).
23. J. E. Ouellette, B. N. Rogers, M. Wiltberger, J. G. Lyon, *J. Geophys. Res.* **115**, A08222 (2010).
24. P. L. Israelevich, A. I. Ershkovich, N. A. Tsyganenko, *J. Geophys. Res.* **106**, 25919–25927 (2001).
25. G. Haerendel, *J. Geophys. Res.* **114**, A06214 (2009).
26. C. T. Russell, *Cosmic Electrodyn.* **2**, 184–196 (1971).
27. D. R. Weimer, *J. Geophys. Res.* **110**, A05306 (2005).

ACKNOWLEDGMENTS

G. Haerendel provided helpful suggestions on the research. Support was provided by the NASA HTP Program (grant NNX11AO59G), NASA Geospace SR Program (grant NNX11AJ10G), and NSF NSWP (grant AGS-1023346). Computing resources were provided by the Computational and Information Systems Laboratory of the National Center for Atmospheric Research (grants 36761008 and 2761009). Simulation data are available from W. Lotko.

SUPPLEMENTARY MATERIALS

www.sciencemag.org/content/345/6193/184/suppl/DC1
Methods
Supplementary Text
Table S1
References (*28*, *29*)

4 March 2014; accepted 5 June 2014
10.1126/science.1252907

SUPERCONDUCTIVITY

Fermi arcs in a doped pseudospin-1/2 Heisenberg antiferromagnet

Y. K. Kim,[1] O. Krupin,[1] J. D. Denlinger,[1] A. Bostwick,[1] E. Rotenberg,[1] Q. Zhao,[2] J. F. Mitchell,[2] J. W. Allen,[3] B. J. Kim[2,3,4]*

High-temperature superconductivity in cuprates arises from an electronic state that remains poorly understood. We report the observation of a related electronic state in a noncuprate material, strontium iridate (Sr_2IrO_4), in which the distinct cuprate fermiology is largely reproduced. Upon surface electron doping through in situ deposition of alkali-metal atoms, angle-resolved photoemission spectra of Sr_2IrO_4 display disconnected segments of zero-energy states, known as Fermi arcs, and a gap as large as 80 millielectron volts. Its evolution toward a normal metal phase with a closed Fermi surface as a function of doping and temperature parallels that in the cuprates. Our result suggests that Sr_2IrO_4 is a useful model system for comparison to the cuprates.

Although the mechanism of high-temperature superconductivity (HTSC) remains an open question, it is commonly believed that certain distinct features of cuprates are essential to HTSC: spin-1/2 moment on a quasi–two-dimensional (2D) square lattice, Heisenberg antiferromagnetic coupling, and no orbital degeneracy. A minimal model based on this assumption can reproduce much of the phenomenology of the cuprates (*1*). Within this framework, it would be informative to realize the key features of cuprates in a different material (*2*). The 5d transition metal oxide Sr_2IrO_4, with a t_{2g}^5 valence shell, is a Mott insulator in which the orbital degeneracy is removed through strong spin-orbit coupling (*3*, *4*). Despite strong entanglement of spin and orbital degrees of freedom, the resulting pseudospins (with $J_{eff} = 1/2$ quantum number) exhibit the spin

[1]Advanced Light Source, Lawrence Berkeley National Laboratory, Berkeley, CA 94720, USA. [2]Materials Science Division, Argonne National Laboratory, Argonne, IL 60439, USA. [3]Randall Laboratory of Physics, University of Michigan, Ann Arbor, MI 48109, USA. [4]Max Planck Institute for Solid State Research, Heisenbergstraße 1, D-70569 Stuttgart, Germany.
*Corresponding author. E-mail: bjkim@fkf.mpg.de

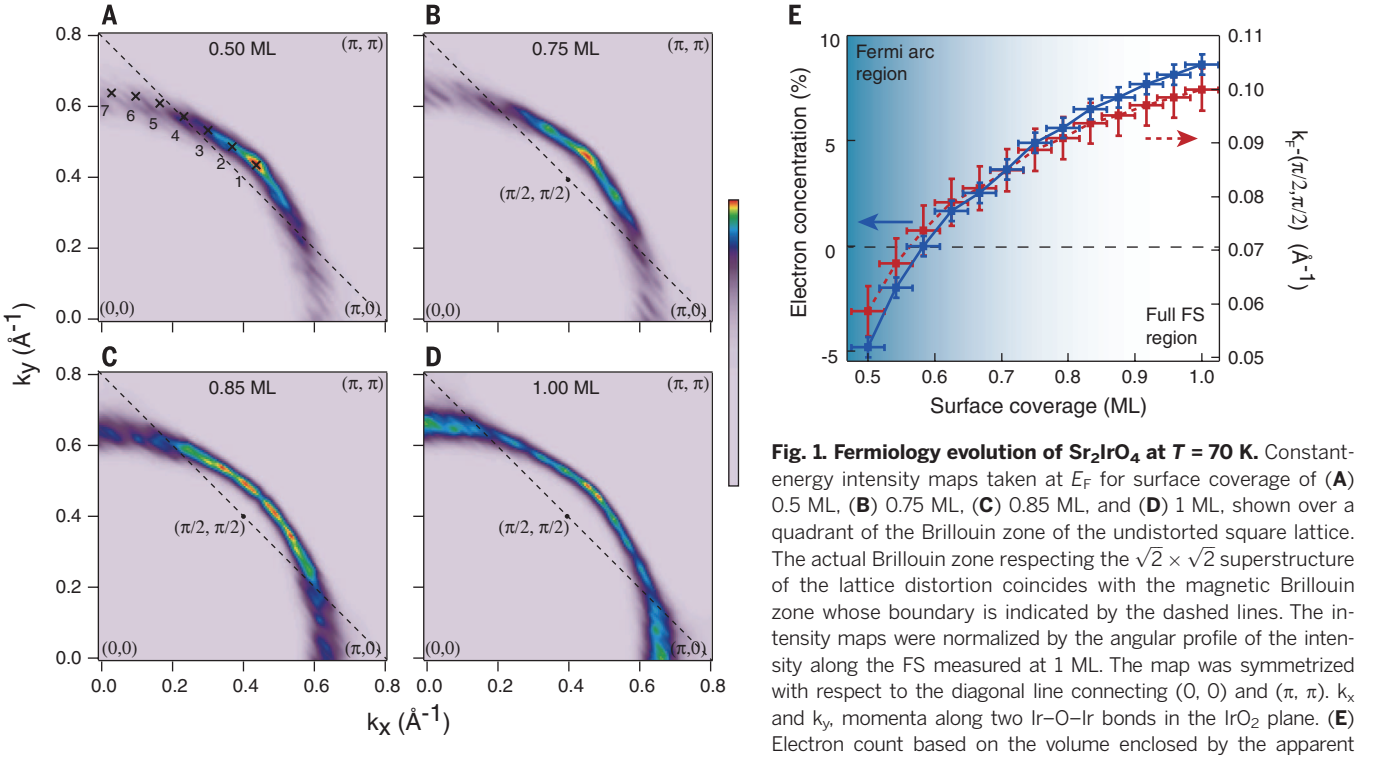

Fig. 1. Fermiology evolution of Sr_2IrO_4 at T = 70 K. Constant-energy intensity maps taken at E_F for surface coverage of (**A**) 0.5 ML, (**B**) 0.75 ML, (**C**) 0.85 ML, and (**D**) 1 ML, shown over a quadrant of the Brillouin zone of the undistorted square lattice. The actual Brillouin zone respecting the $\sqrt{2} \times \sqrt{2}$ superstructure of the lattice distortion coincides with the magnetic Brillouin zone whose boundary is indicated by the dashed lines. The intensity maps were normalized by the angular profile of the intensity along the FS measured at 1 ML. The map was symmetrized with respect to the diagonal line connecting (0, 0) and (π, π). k_x and k_y, momenta along two Ir–O–Ir bonds in the IrO_2 plane. (**E**) Electron count based on the volume enclosed by the apparent large FS centered at the Γ point and the distance from the node to (π/2, π/2) as a function of coverage. Zero of the left vertical axis corresponds to the case of a half-filled band. k_F, Fermi momentum along the diagonal line.

dynamics of a Heisenberg antiferromagnet (*5*) with the nearest-neighbor magnetic exchange coupling having an energy scale on the order of 60 to 100 meV (*6*, *7*). As a result, despite the very different starting electronic structures, the effective low-energy physics of Sr_2IrO_4 can be described by the same minimal model as developed for the cuprates, with comparable magnitudes of coupling constants, suggesting possible unconventional HTSC upon carrier doping of this material (*8*). Indeed, a recent Monte Carlo study predicts a d-wave superconducting phase for the electron-doped case (*9*).

However, thus far, little is known experimentally about the nature of the electronic phases that derive from carrier doping of Sr_2IrO_4 (*10*, *11*). One of the outstanding questions is whether the analogy to cuprates can be extended to the case of a metallic phase, because Sr_2IrO_4 may evolve differently with doping. In particular, weakening of spin-orbit coupling may cause the system to revert to a multiband metal. On the other hand, if the single-band picture remains intact, one may expect the generic cuprate phenomenology to be reproduced in this material. To address this issue, we used an in situ surface doping technique, an approach that has been proven effective for surface doping control of complex oxides (*12*), to reveal the doping evolution of the electronic structures via the use of angle-resolved photoemission. By varying the surface coverage of potassium atoms deposited on the surface of the parent insulator Sr_2IrO_4, we follow the electronic evolution across the entire phase diagram from a Mott insulating state to a normal metallic state,

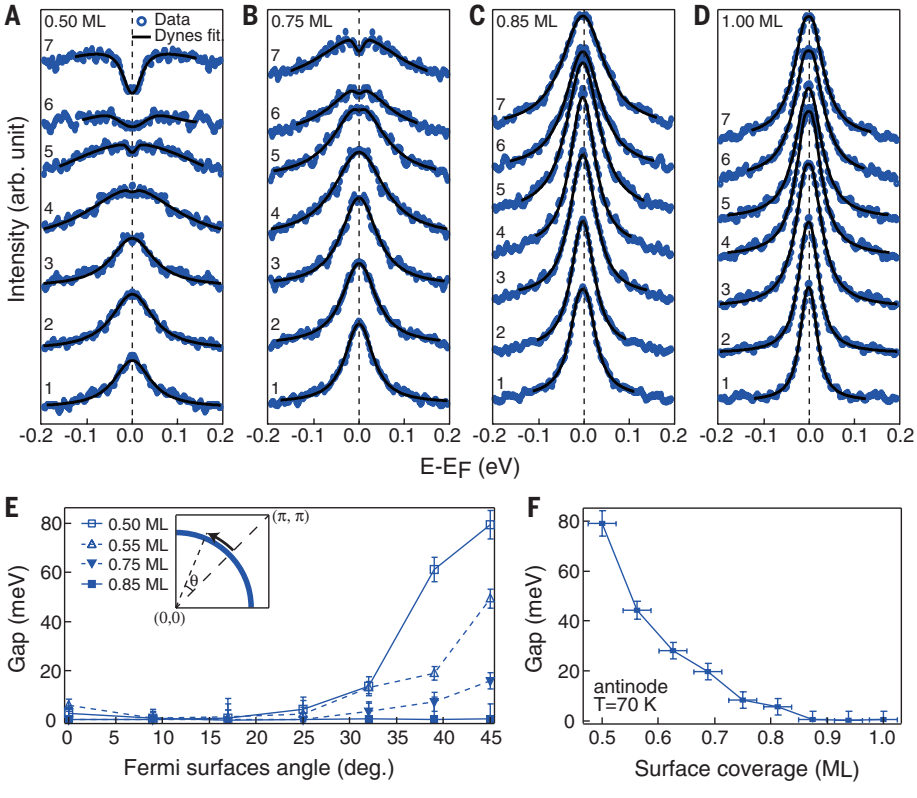

Fig. 2. Momentum and surface coverage dependences of the gap at T = 70 K. Symmetrized EDCs (blue circles) fit to the Dynes formula (black solid lines) along the arc at seven k_F points labeled in Fig. 1A for surface coverage of (**A**) 0.5 ML, (**B**) 0.75 ML, (**C**) 0.85 ML, and (**D**) 1 ML. (**E**) The gap magnitude Δ as a function of FS angle (θ; defined in the inset). (**F**) The gap magnitude Δ at the antinode as a function of surface coverage.

via a "strange" metallic phase that bears marked spectral similarities to those observed for the cuprates. We present our data in units of surface coverage rather than in electron doping concentration because of a highly nonlinear relation between the two.

Figure 1, A to D, shows the constant-energy intensity maps at the Fermi level (E_F) at T = 70 K for surface coverage ranging from 0.5 to 1 monolayer (ML). At 1 ML, we observe a closed, large Fermi surface (FS) indicative of a normal metal phase with the enclosed area of 54.3% of the 2D Brillouin zone (BZ) corresponding to 8.6% electron doping relative to a half-filled band. With decreasing coverage, however, we observe two gradual but conspicuous spectral changes that indicate formation of a distinct electronic phase. First, the intensity is much suppressed in an extended region near (π, 0), breaking up the large FS into disconnected segments of Fermi arcs (*13*, *14*). [Hereafter, we refer to the maximum (or minimum) intensity point as a "node" (or "antinode") in analogy to cuprates.] Second, the locus of the node shows a large shift toward (π/2, π/2) (Fig. 1E). As a result, an attempt to interpret the arc as a part of the large FS encounters a qualitative inconsistency in the electron count based on Luttinger's sum rule: The volume enclosed by the apparent large FS becomes less than half of the BZ for coverage below ≈0.6 ML (Fig. 1E), in clear contradiction with electron doping. These results imply either a global change in the FS topology or an inconsistency with the notion of FS as the system departs from the normal metal phase observed at 1 ML. We note that an analogous qualitative inconsistency in the hole count occurs (*15*) when interpreting the arcs in cuprates (*16*) as part of an underlying large FS—an initial hint that the analogy to cuprates extends to the case of a metallic phase.

The Fermi arc metal phase can be characterized by an order parameter that depends on both the coverage and the temperature. Figure 2, A to D, shows the energy distribution curves (EDCs) for T = 70 K, symmetrized to remove the effect of the Fermi function. In the antinodal region, the symmetrized EDCs show a clear opening of a gap at 0.5 and 0.75 ML, which closes as the system enters the normal metal state at higher coverage. We use a phenomenological Dynes formula (*17*), widely used to fit superconducting gaps (*18*, *19*), to quantify the gap. Thereby, we find for T = 70 K and 0.5 ML a gap as large as ≈80 meV, which rapidly decreases away from the antinode and becomes zero over a finite length of the contour that defines an arc (Fig. 2E). The gap at the antinode continuously diminishes with increasing surface coverage and becomes undetectable within the energy resolution (≈18 meV) beyond 0.85 ML (Fig. 2F).

Figure 3, A to C, shows the E_F intensity map taken at T = 30, 70, and 110 K for surface coverage of 0.7 ML. Similar to the surface coverage dependence, with increasing temperature the arc expands its enclosed volume (when extrapolated to a large FS), crossing from less than half-filling at T = 30 K (48.9%) to more than half-filling (52.1% of BZ) at T = 110 K. Concomitantly, the arc elongates (Fig. 3F) with increasing temperature and evolves to a closed FS at T = 110 K. On cooling down to T = 30 K, the length of the arc shortens considerably, but a finite length of arc still remains (Fig. 3F), which is incompatible with a d-wave gap indicative of superconductivity. Unfortunately, measurement at lower temperatures to check for possible emergence of a d-wave gap was precluded by the high resistance of the sample, the bulk of which remains an insulator.

Consistent with the formation of a closed FS at high temperature, the antinode gap magnitude decreases with increasing temperature, as indicated by the gradual shift of the leading edge in the EDC (Fig. 3E and 3F, inset), in clear contrast to the temperature evolution at the node that shows only a minor thermal broadening (Fig. 3D). The gap starts to emerge below T = 110 K but grows slowly with decreasing temperature, in contrast to the typical behavior of an order parameter that sets in at a well-defined transition temperature. However, the substantial temperature dependence indicates a nontrivial origin and a many-body nature of the gap. We remark that the overall momentum (*19*) and temperature (*20*, *21*) dependences of the gap closely follow those observed for the pseudogap in cuprates.

All of the preceding results—carrier counting inconsistency and gap behavior—indicate that the parallel between Sr_2IrO_4 and cuprates persists in the metallic phase induced by electron doping and that the breaking up of a FS into disconnected segments is a general phenomenon of a system containing certain generic characteristics of cuprates. The formation of an arc, as opposed to "hot spots" at intersections with a magnetic zone boundary, indicates that the correlation strength in Sr_2IrO_4, which has been intensely debated (*22*–*26*), is in the intermediate-to-strong coupling regime (*27*). Thus, Mott physics and local correlations are essential for understanding of the physics of Sr_2IrO_4. Taking all results together, we conclude that the phenomenology of the Fermi arc must be accountable within the minimal description of the physics of doping a single-band, spin-1/2 antiferromagnetic Mott insulator, as shared by Sr_2IrO_4 and cuprates. Their differences in microscopic electronic structures help separate essential features of HTSC from material-specific features. In particular, whether the charge gap is of Mott-insulating (Sr_2IrO_4) or charge-transfer (cuprates) nature seems to have little bearing on the properties discussed here.

The nature of the electronic phase manifesting Fermi arcs in electron-doped Sr_2IrO_4 remains unclear at this point. A growing body of evidence that Fermi arcs are associated with distinct phases in cuprates that compete with HTSC—such as density waves (*28*), stripes (*29*, *30*), and checkerboard orders (*31*)—prompts investigation of competing phases in carrier-doped Sr_2IrO_4. This, in turn, will help clarify which of these phases, if any, occur generically in proximity to HTSC. If,

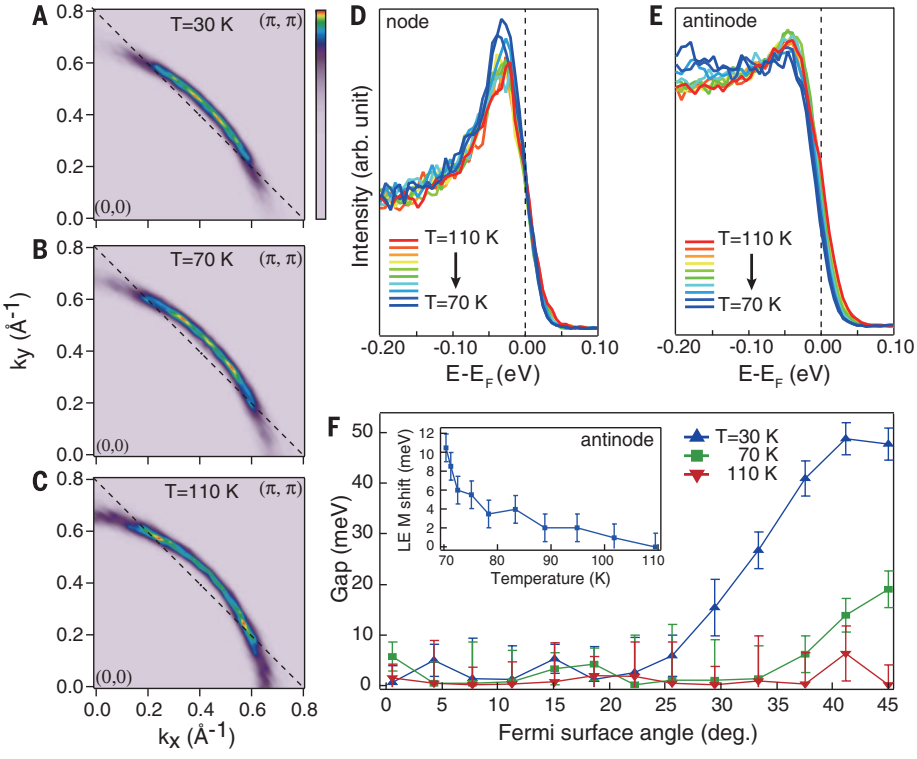

Fig. 3. Evolution of the Fermi arc as a function of temperature at 0.7 ML. E_F intensity map for (**A**) T = 30 K, (**B**) T = 70 K, and (**C**) T = 110 K. EDCs are shown at the (**D**) node and (**E**) antinode in the temperature range between 70 and 110 K. (**F**) The gap magnitude Δ as a function of FS angle for T = 30, 70, and 110 K. The inset shows the temperature dependence of the antinode leading edge midpoint (LEM) shift, which tracks approximately one-half of the antinode gap magnitude (*32*, *33*).

on the other hand, Fermi arcs are a precursor signature of d-wave superconductivity, Sr_2IrO_4 may superconduct at lower temperatures. Further inquiries into these questions will shed new light on the long-sought connection between the pseudogap and HTSC.

REFERENCES AND NOTES

1. P. A. Lee, N. Nagaosa, X.-G. Wen, *Rev. Mod. Phys.* **78**, 17–85 (2006).
2. J. Chaloupka, G. Khaliullin, *Phys. Rev. Lett.* **100**, 016404 (2008).
3. B. J. Kim *et al.*, *Phys. Rev. Lett.* **101**, 076402 (2008).
4. B. J. Kim *et al.*, *Science* **323**, 1329–1332 (2009).
5. G. Jackeli, G. Khaliullin, *Phys. Rev. Lett.* **102**, 017205 (2009).
6. J. Kim *et al.*, *Phys. Rev. Lett.* **108**, 177003 (2012).
7. S. Fujiyama *et al.*, *Phys. Rev. Lett.* **108**, 247212 (2012).
8. F. Wang, T. Senthil, *Phys. Rev. Lett.* **106**, 136402 (2011).
9. H. Watanabe, T. Shirakawa, S. Yunoki, *Phys. Rev. Lett.* **110**, 027002 (2013).
10. M. Ge *et al.*, *Phys. Rev. B* **84**, 100402 (2011).
11. O. B. Korneta *et al.*, *Phys. Rev. B* **82**, 115117 (2010).
12. M. A. Hossain *et al.*, *Nat. Phys.* **4**, 527–531 (2008).
13. Note that the positive sign of next-nearest hopping t' renders a FS topology with a large electron pocket around the Γ point, as opposed to a hole pocket centered at (π, π) in cuprates with a negative t' (*8*).
14. A. Damascelli, Z. Hussain, Z.-X. Shen, *Rev. Mod. Phys.* **75**, 473–541 (2003).
15. T. M. Rice, *AIP Conf. Proc.* **816**, 92–99 (2006).
16. K. M. Shen *et al.*, *Science* **307**, 901–904 (2005).
17. R. C. Dynes, V. Narayanamurti, J. P. Garno, *Phys. Rev. Lett.* **41**, 1509–1512 (1978).
18. K. Okazaki *et al.*, *Science* **337**, 1314–1317 (2012).
19. T. Yoshida, M. Hashimoto, I. M. Vishik, Z.-X. Shen, A. Fujimori, *J. Phys. Soc. Jpn.* **81**, 011006 (2012).
20. A. Kanigel *et al.*, *Nat. Phys.* **2**, 447–451 (2006).
21. T. J. Reber *et al.*, *Nat. Phys.* **8**, 606–610 (2012).
22. C. Martins, M. Aichhorn, L. Vaugier, S. Biermann, *Phys. Rev. Lett.* **107**, 266404 (2011).
23. R. Arita, J. Kuneš, A. V. Kozhevnikov, A. G. Eguiluz, M. Imada, *Phys. Rev. Lett.* **108**, 086403 (2012).
24. D. Hsieh, F. Mahmood, D. H. Torchinsky, G. Cao, N. Gedik, *Phys. Rev. B* **86**, 035128 (2012).
25. Q. Li *et al.*, *Sci. Rep.* **3**, 3073 (2013).
26. A. Yamasaki *et al.*, Bulk nature of layered perovskite iridates beyond the Mott scenario: An approach from bulk sensitive photoemission study. http://arxiv.org/abs/1310.7160.
27. D. Sénéchal, A.-M. S. Tremblay, *Phys. Rev. Lett.* **92**, 126401 (2004).
28. G. Ghiringhelli *et al.*, *Science* **337**, 821–825 (2012).
29. J. M. Tranquada, B. J. Sternlieb, J. D. Axe, Y. Nakamura, S. Uchida, *Nature* **375**, 561–563 (1995).
30. P. Abbamonte *et al.*, *Nat. Phys.* **1**, 155–158 (2005).
31. T. Hanaguri *et al.*, *Nature* **430**, 1001–1005 (2004).
32. T. Yoshida *et al.*, *Phys. Rev. Lett.* **103**, 037004 (2009).
33. D. L. Feng *et al.*, *Phys. Rev. Lett.* **88**, 107001 (2002).

ACKNOWLEDGMENTS

We thank J. H. Shim, K. Haule, G. Kotliar, C. Kim, M. Norman, and G. Khaliullin for helpful discussions. Work at the University of Michigan was supported by the U.S. NSF under grant no. DMR-07-04480. B.J.K. acknowledges the Institute for Complex Adaptive Matter for a travel grant that enabled a visit and helpful discussions at Rutgers University. Work in the Materials Science Division of Argonne National Laboratory (sample preparation and characterization) was supported by the U.S. Department of Energy (DOE) Office of Science, Basic Energy Sciences, Materials Science and Engineering Division. The Advanced Light Source is supported by the Director, Office of Science, Office of Basic Energy Sciences of the U.S. DOE under contract no. DE-AC02-05CH11231. Y.K.K. is supported through the National Research Foundation (grant no. 20100018092).

SUPPLEMENTARY MATERIALS

www.sciencemag.org/content/345/6193/187/suppl/DC1
Materials and Methods
Supplementary Text
Figs. S1 and S2
References (*34*–*36*)

22 January 2014; accepted 28 May 2014
10.1126/science.1251151

SUPERCONDUCTIVITY

Observation of broken time-reversal symmetry in the heavy-fermion superconductor UPt_3

E. R. Schemm,[1,2,3]* W. J. Gannon,[4]† C. M. Wishne,[4] W. P. Halperin,[4] A. Kapitulnik[1,2,3,5]

Models of superconductivity in unconventional materials can be experimentally differentiated by the predictions they make for the symmetries of the superconducting order parameter. In the case of the heavy-fermion superconductor UPt_3, a key question is whether its multiple superconducting phases preserve or break time-reversal symmetry (TRS). We tested for asymmetry in the phase shift between left and right circularly polarized light reflected from a single crystal of UPt_3 at normal incidence and found that this so-called polar Kerr effect appears only below the lower of the two zero-field superconducting transition temperatures. Our results provide evidence for broken TRS in the low-temperature superconducting phase of UPt_3, implying a complex two-component order parameter for superconductivity in this system.

The heavy-fermion metal UPt_3 (*1*) is one of only a handful of unconventional superconductors (*2*, *3*) exhibiting multiple superconducting phases (*4*–*6*). In the normal state, strong hybridization between itinerant platinum 5d electrons and localized uranium 5f moments results in an effective mass that is ~50 times that of free electrons (*2*). Below the Néel temperature $T_N \sim 5$ K, the local U moments order antiferromagnetically in the *a*-*b* plane (*7*). In zero magnetic field, two peaks in the specific heat at $T_{c+} \sim 550$ mK and $T_{c-} \sim 480$ mK indicate the presence of two superconducting states of differing symmetry, called the A and B phases, respectively (*4*–*6*). Pressure studies suggest that these two phases couple to, and are stabilized by, the antiferromagnetic order parameter (*8*). In finite magnetic fields, three distinct vortex phases are also observed (*9*–*11*). The phase diagram of UPt_3 therefore presents a particular challenge for models of unconventional superconductivity.

In the absence of a detailed understanding of the microscopic origins of unconventional superconductivity, theoretical and experimental efforts center on identifying the structure of the macroscopic superconducting order parameter—the pair wavefunction, or gap. In the case of UPt_3, acceptable candidate order parameters should respect the D_{6h} point-group symmetry of the underlying crystal lattice and should therefore transform under one or more representations of this group.

[1]Department of Physics, Stanford University, Stanford, CA 94305, USA. [2]Geballe Laboratory for Advanced Materials, Stanford University, Stanford, CA 94305, USA. [3]Stanford Institute for Materials and Energy Sciences (SIMES), SLAC National Accelerator Laboratory, 2575 Sand Hill Road, Menlo Park, CA 94025, USA. [4]Department of Physics and Astronomy, Northwestern University, Evanston, IL 60208, USA. [5]Department of Applied Physics, Stanford University, Stanford, CA 94305, USA.
*Corresponding author. E-mail: eschemm@stanford.edu
†Present address: Department of Physics and Astronomy, Stony Brook University, Stony Brook, NY 11794, USA.

In this framework, many—but not all—experimental studies of the superconducting states (*1*) favor an E_{2u} odd-parity triplet representation in which the gap is given by

$$\Delta(\mathbf{k}_F) = \hat{z}[\eta_1(T)(k_x^2 - k_y^2)k_z \pm 2i \cdot \eta_2(T)k_x k_y k_z] \quad (1)$$

in a coordinate system where $\hat{z} \parallel c$. Here, $\eta_1(T) \propto \sqrt{1-(T/T_{c+})^2}$ is the real component of the superconducting order parameter, marking the onset of the A phase at T_{c+}, whereas $\eta_2(T) \propto \sqrt{1-(T/T_{c-})^2}$ introduces an additional imaginary component in the B phase at T_{c-} (*12*, *13*). An order parameter of this form first breaks gauge symmetry in the A phase, in which it also exhibits fourfold rotational symmetry in the *a*-*b* plane distinct from the hexagonal symmetry of the crystal lattice. In the B phase, the order parameter becomes isotropic in the *a*-*b* plane as $T \to 0$ K, and the phase difference between the real and imaginary components imparts an overall angular momentum to the pair wave function. Hence, time-reversal symmetry (TRS) is broken in this phase, with the sign of the imaginary component determining the orientation (chirality) of the internal angular momentum of the pair along $\pm \hat{z}$.

The results of Josephson interferometry experiments (*13*, *14*) are consistent with the spatial symmetries of the E_{2u} order parameter of Eq. 1. However, attempts to observe TRS-breaking (TRSB) in UPt_3 via muon spin relaxation measurements have yielded conflicting results (*15*, *16*). Moreover, recent thermal conductivity data (*17*) have been interpreted to support a gap function belonging to an E_{1u} representation that precludes TRSB in the B phase. Thus, the unresolved question of whether TRS is indeed broken in the B phase has become critical to determining the symmetry and hence the proper classification of the superconducting order parameter of UPt_3.

A general consequence of a TRSB order parameter (with a net moment oriented along the *c*

axis) in the presence of particle-hole asymmetry is the appearance of a finite difference between the complex indices of refraction for right (n_R) and left (n_L) circularly polarized light, resulting in ellipticity and circular birefringence (*12*). In particular, the polar Kerr angle, which measures the degree of rotation of linearly polarized light at normal incidence, is related to the off-diagonal terms of the optical conductivity (*18*) by

$$\theta_K = -\Im\left(\frac{n_R - n_L}{n_R n_L - 1}\right) \approx \frac{4\pi}{\omega d} \cdot \frac{\sigma''_{xy}(\omega)}{\tilde{n}(\tilde{n}^2 - 1)} \quad (2)$$

where $\tilde{n}$ is the average complex index of refraction of the material, d is a microscopic length scale, and ω is the frequency of the incident light. The off-diagonal term of the conductivity tensor, $\sigma_{xy} = \sigma'_{xy} + i\sigma''_{xy}$, is nonzero if TRS is broken (*19*), and the second equality holds for weak absorption (*21*). In the simplest estimate, σ_{xy} will have the natural scale of the Hall conductivity e^2/h, where h is Planck's constant, reduced by a factor that reflects the large difference between the superconducting gap and probe energies: $\Delta_0 << \hbar\omega$ in the optical regime, where Δ_0 is the magnitude of the order parameter at the Fermi level and h is h divided by 2π. Because the current response to the incident electric field involves a product of the wave function and its gradient, the conductivity must be proportional to Δ_0^2, yielding $\sigma''_{xy}(\omega) \sim \frac{e^2}{hd}(\Delta_0/\hbar\omega)^2$ (*21*). As a result, the degree of optical rotation expected from TRSB in unconventional superconductors is expected to be on the order of 1 microradian (μrad) or less (*12*). Measurements of such small rotations pose challenges to experiment; nevertheless, high-resolution measurements of polar Kerr effect (PKE) have been used to place limits on anyon superconductivity in the high-T_c cuprates (*22*) and to establish TRSB in the order parameter of the spin-triplet superconductor Sr_2RuO_4 (*23*).

The requirement to resolve optical rotation below 1 μrad without application of an external TRSB field (such as a magnetic field) prevents us from using the modulation techniques commonly used to detect small signals in magnetic materials. Thus, to measure Kerr rotation in UPt_3 we have constructed a fiber-based zero-area loop Sagnac interferometer operating at 1550 nm (*24*, *25*) with a focused spot size of 10.6 μm. The interferometer is designed and biased to reject optical signals attributable to nonreciprocal effects (such as linear birefringence and backscattering off of interfaces), allowing us to resolve changes in Kerr angle on the order of 50 nrad with a minimum of optical power incident on the sample. This latter quality is of particular relevance in this study because spot heating in the temperature range of interest (300 to 600 mK) can be substantial even for thermally well-anchored samples with high thermal conductivities. To optimize the signal-to-noise ratio (SNR), we typically applied 20 μW of optical power to the sample, of which ~40% is expected to have been absorbed (*26*). Lower incident powers (with inferior SNR) were also used to verify our results (*27*).

Our experiments were performed on a 4.5- by 3.3- by 0.91-mm single crystal of UPt_3 with residual resistivity ratio (RRR) of ~850 measured along the c axis (Fig. 1). The crystal was mounted with GE varnish to a copper stage attached to the cold finger of a helium-3 cryostat, with the optical probe beam incident on the a-b plane of the crystal. The sample was then cooled down to the cryostat's base temperature, and Kerr angle was measured in ambient magnetic field (H_{ext} < 0.3 Oe) as the sample was slowly warmed through T_{c-} and T_{c+}. In addition to measuring the Kerr angle, we installed a split-coil mutual inductance assembly (*28*) operating at 100 kHz with a drive amplitude of ~8.5 mG. Mutual inductance measurements of the sample could then be conducted under the same experimental conditions as the PKE measurements in order to verify the upper transition temperature of ~550 mK (Fig. 2).

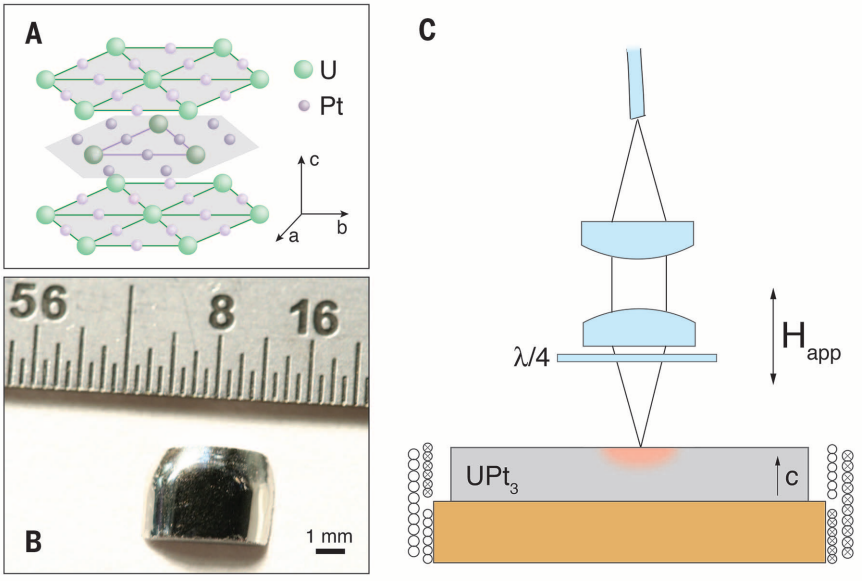

Fig. 1. Material information and experimental setup. (**A**) Crystal structure of UPt_3. In the image, the c axis is pointing out of the page. (**B**) Photograph of the single crystal used in this study. Length scale on ruler is in 1/64ths of an inch. (**C**) Experiment geometry of the Kerr rotation and mutual inductance measurements.

The main experimental result is summarized in Fig. 2. On the left-hand axis, we plot the Kerr angle versus temperature obtained in a typical zero-field warmup after a zero-field cooldown. A temperature-independent background, consisting of electrical and optical offsets in the instrument, has been averaged between 600 and 700 mK and subtracted from the plotted data as in (*23*); the equivalent magnitude of this offset varied between ~0.2 and ~3 μrad over all of the data taken on UPt_3, although for most experimental runs, the equivalent offset was of order 0.3 μrad (*27*). Above $T_{Kerr} \approx 460$ mK, the measured Kerr signal remains unchanged from the background. Below this temperature, however, a finite change in Kerr angle appears, which reaches ~400 nrad at 350 mK and falls to zero at T_{Kerr}. Finite element analysis using the thermal conductivity and heat capacity data of (*29*, *30*) allows us to estimate the degree of sample heating to be no more than 50 mK at the spot of illumination. The resulting uncertainty in the transition temperature in the limit of zero optical heating is indicated by the thick gray bar in Fig. 2.

Theoretical treatments of the optical response of chiral superconductors suggest that the Kerr effect varies as the product of the real and imaginary components of the order parameter (*31*). The Kerr effect may arise either via impurity scattering (*32*, *33*) or interband coupling (*34*), although for our measurements, the latter mechanism is more likely given the high purity of our sample and the involvement of five bands in the Fermi surface (*1*). Because the real and imaginary components of the proposed order parameter for UPt_3 have different transition temperatures, the phenomenological expression for θ_K involves both T_{c+} and T_{c-}

$$\theta_K \propto \sqrt{\left[1 - (T_c/T_{c+})^2\right] \cdot \left[1 - (T_c/T_{c-})^2\right]} \quad (3)$$

This functional form is plotted as a solid line in Fig. 2 and is consistent with measurement, although the scatter in the data is too large to exclude the possibility of a more complex relationship between θ_K, temperature, and the gap structure of UPt_3.

To compare the observed optical Kerr transition with the onset of A-phase superconductivity in UPt_3, a baseline magnetic susceptibility curve, taken with no incident light from the Kerr probe, is shown in Fig. 2 on the right-hand axis of the plot. We identify the upper superconducting transition temperature T_{c+} ~ 550 mK with the departure of the susceptibility from the normal state linear background, as in (*35*). The absorption of light from the Kerr measurement results in bulk sample heating that depresses the measured mutual inductance T_c from the 0-μW curve by no more than ~8.5 mK for the optical powers used in this study (fig. S3). This offset is indicated by the thin gray band in Fig. 2. The transitions at

T_{c+} and T_{Kerr} are clearly separated in temperature; in the absence of any other structural or electronic phase transitions in this temperature range, we ascribe the additional broken symmetry at T_{Kerr} to the onset of B phase superconductivity at T_{c-}.

A defining characteristic of spontaneous symmetry-breaking is the sensitivity of the order parameter to alignment by a small symmetry-breaking field as the transition temperature is crossed. In the case of UPt_3, the TRSB state is expected to couple to magnetic fields applied along the *c* axis (*12*); therefore, it should be possible to train the sign of the TRSB Kerr signal with an arbitrarily small external field oriented in this direction. We show the results of field-training measurements of the Kerr effect in Fig. 3. For these experiments, the sample was cooled to base temperature in an applied field of +50 or −50 G. At base temperature, the field was switched off, and Kerr angle was again measured upon warm-up. The residual magnetic field with the magnet off was identical to that of the zero-field cooled measurements to within the resolution of a commercial Hall sensor installed in the sample space.

There are several features in the data that are of note. First, the signal tracks the direction of the training field, indicating that the TRSB order parameter couples to magnetic fields as expected. Second, the maximum size of the field-trained signal matches that of the zero-field measurements to within our experimental resolution. Although in general one would expect TRSB domains to form with random alignments, leading to partial or even complete cancellation of Kerr signal in the area sampled by the probe beam, our repeated observation of maximal Kerr signal even in the absence of field training is consistent with observations elsewhere that UPt_3 tends to spontaneously form very large superconducting domains, possibly spanning the entire crystal (*13*, *14*, *17*). Last, the absence of a discernable additional Kerr signal in the field-cooled measurements implies that the TRSB signal originates from the superconducting order parameter itself, rather than from vortices induced by an external field.

To properly analyze broken TRS in the superconducting state, one must also consider the potential influence of magnetic effects already present at higher temperatures. In UPt_3, antiferromagnetic (AF) correlations associated with magnetic moments on the uranium sites appear at 20 K, with static in-plane AF order developing below $T_N \sim 5$ K (*7*, *36*). TRS is therefore broken well above T_{c+} and T_{c-}. However, one can still examine the superconducting condensate for additional TRSB that is ferromagnetic in character, that is, displaying a two-state degeneracy because of the presence of an imaginary component in the gap function, as discussed above. This additional out-of-plane signal can be considered independently from the in-plane TRSB arising from antiferromagnetism, although the AF order may still couple to superconductivity by acting as, for example, a symmetry-breaking field (*7*, *12*). We can verify the independence of these two sources of TRSB by measuring Kerr rotation through T_N. As expected for in-plane ordering with no net moment, we find no signature (within ±100 nrad) of the AF transition in the Kerr effect under both zero-field and field-cooled conditions (fig. S4), despite the enhancement provided by the large spin-orbit coupling present in the material (*12*). The null result at T_N suggests that the signal observed in the B phase is a true property of superconductivity in UPt_3, rather than a secondary effect of the background AF ordering in this system.

The appearance of broken TRS in the B phase carries with it several implications for the theory of superconductivity in UPt_3. Because a general multicomponent superconducting order parameter can break TRS only if it belongs to a multidimensional representation (*37*), our results taken alone imply that the superconducting order parameter belongs to one of the four two-dimensional representations of D_{6h}. In principle, the data are consistent with any choice of basis functions with relatively complex coefficients within these representations. However, the preponderance of other experimental evidence (*1*, *9*–*11*, *13*–*15*, *30*) narrows the possibilities further, leaving the E_{2u} order parameter of Eq. 1 as the likely candidate to describe the superconducting phases of UPt_3. Although a microscopic theory for PKE in UPt_3 is not available at present, the temperature dependence of our data appears to be consistent with the phenomenology developed in (*34*) to account for a finite Kerr rotation in a multiband superconductor with interorbital coupling ε_{12} and intraband pairing: $\theta_K \propto \varepsilon_{12}\eta_1\eta_2$. This in turn suggests that Kerr effect measurements can more generally

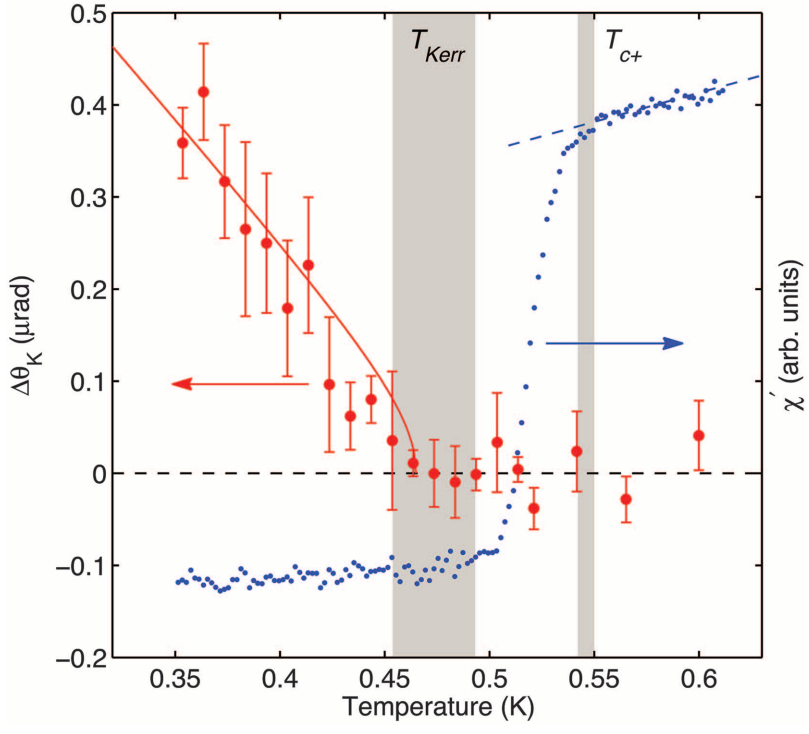

Fig. 2. Measurement of Kerr effect and T_{c+} in UPt_3. Kerr angle (red, left axis) and the real part of the mutual inductance (blue, right axis) are plotted as a function of temperature for a UPt_3 single crystal. The onset of superconductivity at T_{c+} is well removed from the onset of TRSB at $T_{Kerr} \sim 460$ mK $\sim T_{c-}$. The gray bands indicate uncertainties in T_{c+} and T_{c-} from the effects of optical heating. Error bars on the Kerr data are statistical. The solid line is a guide to the eye of the form $\theta_K \propto \sqrt{[1-(T_c/T_{c+})^2]\cdot[1-(T_c/T_{c-})^2]}$.

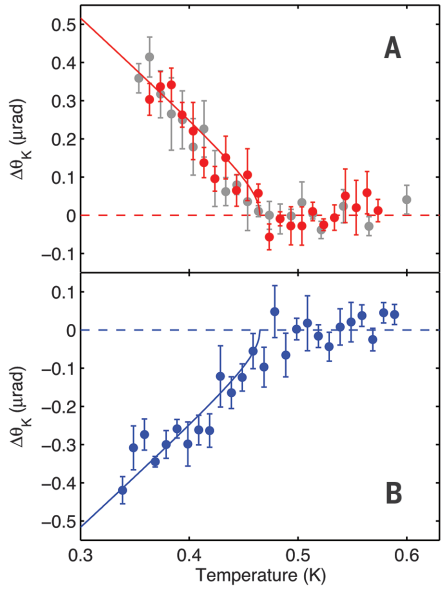

Fig. 3. Magnetic field training of the Kerr effect. Solid lines are guides to the eye of the form $\theta_K \propto \sqrt{[1-(T_c/T_{c+})^2]\cdot[1-(T_c/T_{c-})^2]}$. (**A**) Zero-field warmup data after cooling the sample through T_{c-} in a +50 G field (red) and in zero field (gray, replotted from Fig. 2). (**B**) Zero-field warmup data after cooling the sample down in a −50 G field, showing complete reversal of the TRSB signal.

be used to track the temperature dependence of the gap function in TRSB superconductors.

REFERENCES AND NOTES

1. R. Joynt, L. Taillefer, *Rev. Mod. Phys.* **74**, 235–294 (2002).
2. G. R. Stewart, Z. Fisk, J. O. Wills, J. L. Smith, *Phys. Rev. Lett.* **52**, 679–682 (1984).
3. M. R. Norman, *Science* **332**, 196–200 (2011).
4. R. A. Fisher *et al*., *Phys. Rev. Lett.* **62**, 1411–1414 (1989).
5. K. Hasselbach, L. Taillefer, J. Flouquet, *Phys. Rev. Lett.* **63**, 93–96 (1989).
6. S. Adenwalla *et al*., *Phys. Rev. Lett.* **65**, 2298–2301 (1990).
7. G. Aeppli, A. Goldman, G. Shirane, E. Bucher, M. Lux-Steiner, *Phys. Rev. Lett.* **58**, 808–811 (1987).
8. S. M. Hayden, L. Taillefer, C. Vettier, J. Flouquet, *Phys. Rev. B* **46**, 8675 (1992).
9. R. N. Kleiman *et al*., *Phys. Rev. Lett.* **69**, 3120–3123 (1992).
10. U. Yaron *et al*., *Phys. Rev. Lett.* **78**, 3185–3188 (1997).
11. A. Huxley *et al*., *Nature* **406**, 160–164 (2000).
12. J. A. Sauls, *Adv. Phys.* **43**, 113–141 (1994).
13. J. D. Strand *et al*., *Science* **328**, 1368–1369 (2010).
14. J. D. Strand, D. J. Van Harlingen, J. B. Kycia, W. P. Halperin, *Phys. Rev. Lett.* **103**, 197002 (2009).
15. G. M. Luke *et al*., *Phys. Rev. Lett.* **71**, 1466–1469 (1993).
16. P. D. de Réotier *et al*., *Phys. Lett. A* **205**, 239–243 (1995).
17. Y. Machida *et al*., *Phys. Rev. Lett.* **108**, 157002 (2012).
18. P. N. Argyres, *Phys. Rev.* **97**, 334–345 (1955).
19. Other mechanisms, such as chiral crystal structure or gyrotropic order, may also give rise to a finite Kerr effect; however, such sources of Kerr rotation do not exhibit the same magnetic field training behavior observed in TRS-breaking materials (*20*).
20. P. Hosur, A. Kapitulnik, S. A. Kivelson, J. Orenstein, S. Raghu, *Phys. Rev. B* **87**, 115116 (2013).
21. L. D. Landau, L. P. Pitaevskii, E. M. Lifshitz, *Electrodynamics of Continuous Media* (Elsevier, Burlington, MA, ed. 2, 1984).
22. S. Spielman *et al*., *Phys. Rev. Lett.* **68**, 3472–3475 (1992).
23. J. Xia, Y. Maeno, P. T. Beyersdorf, M. M. Fejer, A. Kapitulnik, *Phys. Rev. Lett.* **97**, 167002 (2006).
24. J. Xia, P. T. Beyersdorf, M. M. Fejer, A. Kapitulnik, *Appl. Phys. Lett.* **89**, 062508 (2006).
25. A. Kapitulnik, J. Xia, E. Schemm, A. Palevski, *New J. Phys.* **11**, 055060 (2009).
26. P. E. Sulewski *et al*., *Phys. Rev. B Condens. Matter* **38**, 5338–5352 (1988).
27. Materials and methods are available as supplementary materials on *Science* Online.
28. B. Jeanneret, G. L. Gavilano, G. A. Racine, C. Leemann, P. Martinoli, *Appl. Phys. Lett.* **55**, 2336 (1989).
29. J. P. Brison *et al*., *J. Low Temp. Phys.* **95**, 145 (1994).
30. B. Lussier, B. Ellman, L. Taillefer, *Phys. Rev. B Condens. Matter* **53**, 5145–5148 (1996).
31. V. M. Yakovenko, *Phys. Rev. Lett.* **98**, 087003 (2007).
32. J. Goryo, *Mod. Phys. Lett. B* **24**, 2831–2836 (2010).
33. R. M. Lutchyn, P. Nagornykh, V. M. Yakovenko, *Phys. Rev. B* **80**, 104508 (2009).
34. E. Taylor, C. Kallin, *Phys. Rev. Lett.* **108**, 157001 (2012).
35. P. J. C. Signore *et al*., *Phys. Rev. B Condens. Matter* **52**, 4446–4461 (1995).
36. S. Fujimoto, *Phys. Rev. B* **72**, 024515 (2005).
37. S. Yip, A. Garg, *Phys. Rev. B Condens. Matter* **48**, 3304–3308 (1993).

ACKNOWLEDGMENTS

Stimulating discussions with S. Kivelson, A. Huxley, and D. Agterberg; sample characterization by K. Avers (Northwestern); and instrument design assistance from G. Burkhard (Stanford) are greatly appreciated. This work was supported by the U.S. Department of Energy Office of Basic Energy Science, Division of Materials Science and Engineering, at Stanford under contract DE-AC02-76SF00515 and at Northwestern under contract DE- FG02-05ER46248. Construction of the Sagnac apparatus was partially funded by the Stanford Center for Probing the Nanoscale (NSF NSEC 0425897). E.R.S. received additional support from a Gabilan Stanford Graduate Fellowship and the DARE Doctoral Fellowship Program.

SUPPLEMENTARY MATERIALS

www.sciencemag.org/content/345/6193/190/suppl/DC1
Materials and Methods
Supplementary Text
Figs. S1 to S4

15 November 2013; accepted 21 May 2014
10.1126/science.1248552

HEME ENZYMES

Neutron cryo-crystallography captures the protonation state of ferryl heme in a peroxidase

Cecilia M. Casadei,[1,2] Andrea Gumiero,[3] Clive L. Metcalfe,[3] Emma J. Murphy,[3] Jaswir Basran,[1] Maria Grazia Concilio,[4] Susana C. M. Teixeira,[2,5] Tobias E. Schrader,[6] Alistair J. Fielding,[4] Andreas Ostermann,[7] Matthew P. Blakeley,[2] Emma L. Raven,[3]* Peter C. E. Moody[1]*

Heme enzymes activate oxygen through formation of transient iron-oxo (ferryl) intermediates of the heme iron. A long-standing question has been the nature of the iron-oxygen bond and, in particular, the protonation state. We present neutron structures of the ferric derivative of cytochrome c peroxidase and its ferryl intermediate; these allow direct visualization of protonation states. We demonstrate that the ferryl heme is an Fe(IV)=O species and is not protonated. Comparison of the structures shows that the distal histidine becomes protonated on formation of the ferryl intermediate, which has implications for the understanding of O–O bond cleavage in heme enzymes. The structures highlight the advantages of neutron cryo-crystallography in probing reaction mechanisms and visualizing protonation states in enzyme intermediates.

Aerobic organisms have evolved to use the intrinsic oxidizing power of oxygen from the atmosphere. This activation of oxygen is achieved by a catalytic metal center (usually iron or copper) buried within a protein. In the case of iron, high-valent iron-oxo (also known as ferryl) intermediates play a role in a large number of different, and sometimes difficult, biological oxidations catalyzed by various heme and non-heme iron-containing enzymes.

For the heme iron enzymes, the mechanism of oxidation involves initial formation of the iconic compound I intermediate (*1*, *2*). Compound I contains an oxidized ferryl heme, plus either a porphyrin π-cation radical or a protein radical; reduction of compound I by one electron yields the closely related compound II intermediate, which contains only the ferryl heme. These compound I and II intermediates are a defining feature across the heme enzyme family and appear in a diverse group of catalytic heme enzymes that include all the cytochrome P450s, the nitric oxide synthases, and the terminal oxidases, plus the heme dioxygenases and heme peroxidases. Indeed, they are such crucial intermediates in so many processes—including many involved in drug metabolism and other important oxidations—that their structure and reactivity has become a key question for both heme (*3*–*7*) and non heme iron enzymes where similarly transient iron-oxo species are also employed (*8*, *9*).

A long-standing and highly contentious question has been to clarify the bond order and protonation state of the ferryl heme. The question has focused on whether the ferryl is formulated as an Fe(IV)=O [iron(IV)-oxo] or Fe(IV)-OH [iron(IV)-hydroxide] species, but there are a number of reasons why previous methodologies—none of which can measure the protonation state directly—have failed to fully resolve the issue. To begin with, even capturing these transient intermediates in some enzymes [especially in the P450s (*10*, *11*)] has proved very difficult. Early approaches to the problem used both extended x-ray absorption fine structure and resonance Raman methods [reviewed in (*12*)] to examine the iron-oxygen bond as an indirect reporter on the protonation state. These studies indicate a short Fe-O bond length, but the data were not totally consistent, and the photolability of compound I during laser excitation is well documented (*13*) so that interpretation of stretching frequencies from Raman work has not been unambiguous either. More recently, x-ray crystallographic methods have been employed. These methods showed longer iron-oxygen bond lengths, but the x-ray structures of compounds I and II were subsequently shown to have been affected by photoreduction of the iron and are now considered to be unreliable. The more recent use of multiple crystals in x-ray analyses minimizes photoreduction but cannot entirely eliminate the problem. Moreover, hydrogen atoms are difficult to locate in electron density maps due to their weak scattering. Even if very high-resolution data (i.e., better than 1.2 Å) are available, hydrogen atoms can remain obscured due to their mobility. There is also the substantive question of whether such small changes in Fe-O

[1]Department of Biochemistry and Henry Wellcome Laboratories for Structural Biology, University of Leicester, Lancaster Road, Leicester LE1 9HN, UK. [2]Institut Laue-Langevin, 71 Avenue des Martyrs, 38000, Grenoble, France. [3]Department of Chemistry, University of Leicester, University Road, Leicester LE1 7RH, UK. [4]The Photon Science Institute, The University of Manchester, Manchester M13 9PL, UK. [5]EPSAM, Keele University, Keele, Staffordshire ST5 5BG, UK. [6]Jülich Centre for Neutron Science (JCNS), Forschungszentrum Jülich GmbH, Outstation at MLZ, Lichtenbergstraße 1, 85747 Garching, Germany. [7]Heinz Maier-Leibnitz Zentrum (MLZ), Technische Universität München, Lichtenbergstraße 1, D-85748 Garching, Germany.
***Corresponding author. E-mail: emma.raven@le.ac.uk (E.L.R.); peter.moody@le.ac.uk (P.C.E.M.)**

bond length (<0.2 Å) between Fe(IV)=O and Fe (IV)-OH species, even if measured at high resolution and without photoreduction, are determined accurately enough in x-ray experiments to report reliably on the protonation state.

For these reasons, we have adopted a different approach. Neutron diffraction offers a more reliable solution to the problem, because hydrogen and, particularly, its isotope deuterium (D) are visible at much lower resolutions than required with x-rays (*14*, *15*). The approach does present a number of challenges, particularly the need to cool the large crystals required for neutron crystallography down to the cryogenic temperatures required for the study of enzyme intermediates (*16*). But the fact that neutrons are non-ionizing and are scattered by the atomic nuclei (rather than by the electrons, as in x-ray crystallography) means that photoreduction, which has been the source of most of the confusion in previous x-ray work, does not occur at all. In the case of redox enzymes, the elimination of photoreduction is a considerable advantage if the other experimental challenges can be overcome.

In this work, we have used neutron crystallography to determine the structure of ferric cytochrome c peroxidase (CcP) and its transient ferryl intermediate. The structures allow us to visualize the positions of hydrogen and deuterium atoms in the enzyme, as well as to unambiguously identify the protonation state of the ferryl heme.

Cytochrome c peroxidase catalyzes the H_2O_2-dependent oxidation of cytochrome c. Compound I of CcP, formed rapidly from the reaction of ferric enzyme with peroxide, contains a ferryl heme plus a stable protein radical on Trp^{191} (*17*). It was the first peroxidase to be crystallized (*18*) and over many years has served as a model enzyme for the understanding of oxygen activation across the family of catalytic heme enzymes. We first solved the neutron structure of ferric CcP to 2.4 Å at room temperature. The structure was determined using x-ray and neutron diffraction data obtained from a D_2O-exchanged crystal (see supplementary materials and methods; data and refinement statistics are shown in table S1).

Figure 1 shows nuclear scattering and electron density of ferric CcP in the region of the heme and summarizes the positions of all the hydrogen and deuterium atoms. On the distal side of the heme (Fig. 1, A and C), His^{52} is neutral as N_δ is deuterated but N_ε is not. The N_ε of Trp^{51} is deuterated; Arg^{48} is fully deuterated and positively charged. The neutron structure unambiguously identifies W1 as a heavy water molecule (D_2O), rather than an OD^- ion, at a distance of 2.7 Å from the iron. We assign the heme as five-coordinate. On the proximal side (Fig. 1, B and D), N_ε of His^{175} is not deuterated and is 2.0 Å from the iron. The N_δ of His^{175} is deuterated and within hydrogen bond distance of the unprotonated $O_\delta 2$ of Asp^{235}; likewise, $O_\delta 1$ of Asp^{235} is unprotonated and within hydrogen bond distance of the deuterated N_ε of Trp^{191}. Both heme propionates are unprotonated.

Crystals of D_2O-exchanged CcP (see supplementary materials and methods) were reacted

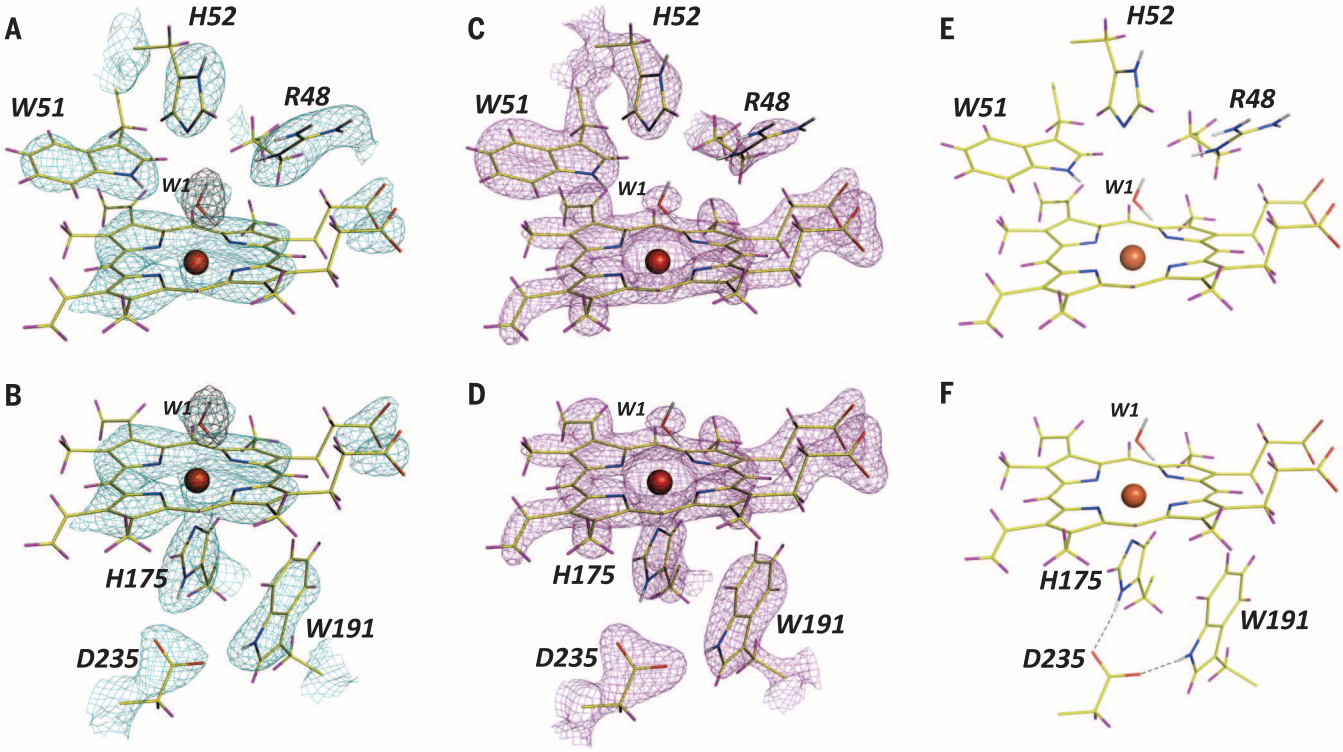

Fig. 1. The structure of ferric CcP in the region of the heme. In the neutron experiment, neutrons are diffracted by the atomic nuclei (in contrast to x-rays, which are scattered by electrons). Hydrogen atoms (shown in magenta) have a negative coherent neutron scattering length (–3.74 fm), whereas deuterium atoms (shown in white) have a positive coherent scattering length (6.77 fm). Exchangeable hydrogen atoms, therefore, show up with density similar to carbon (6.65 fm) and oxygen (5.85 fm), whereas nitrogen has a greater scattering length (9.37 fm). The scatter from a methylene (CH_2) group sums to nearly zero, so that at moderate resolution (~2 to 2.5 Å) cancellation of nuclear scattering density is observed, and the joint refinement allows use of the x-ray terms to place the nonhydrogen atoms in these regions. Nuclear scattering density [σA-weighted $2F_o$-F_c contoured at 2.6 root mean square (RMS)] in the (**A**) distal and (**B**) proximal heme pocket is shown in cyan. Electron density (σA-weighted $2F_o$-F_c contoured at 2.4 RMS) in the (**C**) distal and (**D**) proximal pocket is shown in magenta. The black contour (σA-weighted neutron F_o-F_c contoured at 5.0σ) shows the difference density calculated by omitting the bound water (W1). Protonation states are depicted for (**E**) distal and (**F**) proximal active site residues. The distal pocket shows an ordered water molecule (W1) 2.7 Å away from the five-coordinate heme iron. W1 donates a hydrogen bond to the π orbitals of the porphyrin ring and may be a potential hydrogen bond acceptor to the deuterated N_ε of Trp^{51}. W1 may also interact with a poorly ordered water (not shown) that displaces the guanidinium of Arg^{48}, which is seen in the "out" position (*19*). Color scheme: hydrogen atoms, magenta; deuterium, white; oxygen, red; nitrogen, blue; carbon, yellow; iron, orange sphere. Hydrogen bonds are shown as dashed lines. H, His; R, Arg; D, Asp; W (except W1), Trp.

with hydrogen peroxide as previously reported (*19*). Formation of compound I in CcP crystals is established [e.g., (*20*, *21*)] but was verified in several ways. Single-crystal microspectrophotometry at 100 K on similar (smaller) crystals showed the characteristic absorption peaks in the visible region (530, 560, and 632 nm) (fig. S1A), in agreement with the literature (*22*). Spectra of these crystals were unchanged on storage over 20 days (fig. S1B). Single-crystal electron paramagnetic resonance (EPR) on similar crystals prepared and reacted in the same way (see supplementary materials and methods) also showed the appearance of the characteristic $g = 2$ signal from the Trp^{191} radical (*17*) (fig. S2); in solution, compound I of CcP is stable for hours at room temperature (*23*) and indefinitely at 77 K (figs. S3 and S4).

We then used x-ray and neutron diffraction data to determine the 2.5 Å resolution neutron structure of compound I of CcP at 100 K (see supplementary materials and methods). Figure 2 shows nuclear scattering and electron density in the region of the heme and summarizes the positions of all the hydrogen and deuterium atoms. Data and refinement statistics are shown in table S2. Nuclear scattering and electron density maps for individual active site residues are shown in fig. S5. In comparison to the ferric enzyme, most of the protonation states are retained in the compound I structure, with the exception of His^{52}, which is now deuterated at both N_δ and N_ε (fig. S5D). We observe that the N_ε of the Trp^{191} radical is deuterated, which identifies the radical species as a (protonated) π-cation radical (*24*). Compared to the ferric enzyme, Arg^{48} has moved into the heme pocket.

Analysis of the nuclear scattering density maps indicates that the ferryl oxygen is not deuterated in the structure. This is confirmed by examination of the hydrogen bond structure: The ferryl oxygen acts as a hydrogen bond acceptor to the N_ε of Trp^{51} and to the N_ε of Arg^{48}, both of which are accordingly deuterated. We interpret this geometry as consistent with an unprotonated Fe(IV)=O species. An F_o–F_c neutron map calculated in the absence of the ferryl oxygen shows a peak (3.8σ) in nuclear scattering density at 1.6 Å from the iron atom (Fig. 2, A and B), which is consistent with the most recent x-ray data [reported as 1.63 Å (*19*) and 1.73 Å (*25*)]. However, bond lengths cannot be determined precisely at this resolution and, as we note above, report only indirectly on the protonation state. The unambiguous observation from the neutron structure is that the oxygen is not protonated, which establishes that the ferryl intermediate is an Fe(IV)=O species at this pH. The neutron data show that there is no hydrogen bond from the distal histidine to the ferryl heme, as has been suggested previously (*26*) in horseradish peroxidase to account for pH-dependent spectroscopic behavior of the ferryl intermediate.

Mechanisms for O–O bond cleavage in peroxidases are invariably drawn (*1*, *27*) showing the distal histidine (His^{52} in the case of CcP) as neutral in both ferric and compound I species, which assumes that both protons of H_2O_2 are used in the formation of a water molecule. Our data are not consistent with this long-standing description. His^{52} is indeed neutral in the ferric state (Fig. 1 and fig. S5E) but is deuterated on N_ε and N_δ in compound I (Fig. 2 and fig. S5D). We take this to mean that the widely assumed role of the distal histidine in compound I formation—acting first as a base catalyst (to deprotonate peroxide) and then as an acid catalyst (to protonate the peroxide oxygen and release water)—needs to be reassessed.

Possible alternative mechanisms showing movement of protons during O–O bond cleavage are shown in Fig. 3. Ferric CcP is unprotonated on the N_ε of His^{52}, and the N_ε lone-pair geometry does

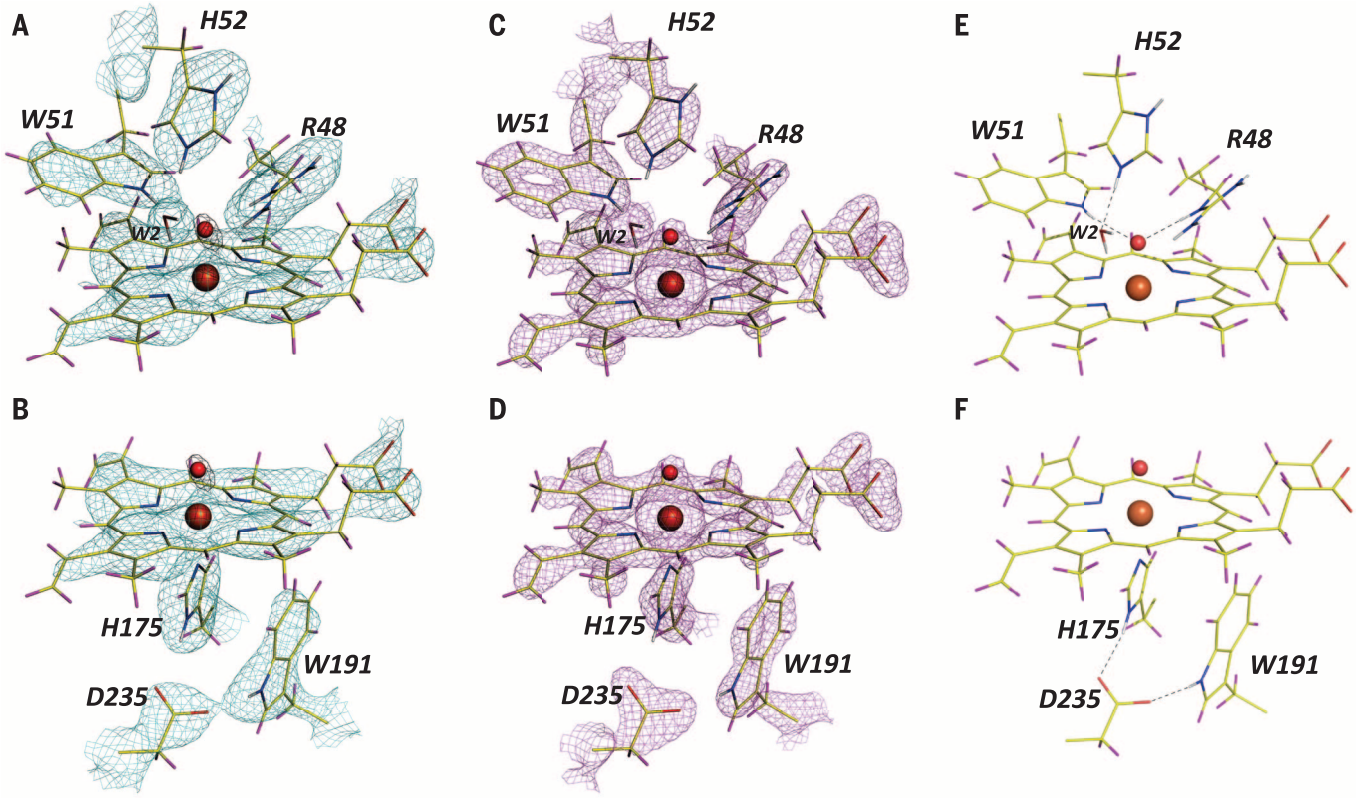

Fig. 2. The structure of compound I of CcP in the region of the heme. Nuclear scattering density (σA-weighted $2F_o$-F_c contoured at 2.2 RMS) in the (**A**) distal and (**B**) proximal heme pocket is shown in cyan. Electron density (σA-weighted $2F_o$-F_c contoured at 2.6 RMS) in the (**C**) distal and (**D**) proximal heme pocket is shown in magenta. The black contour (σA-weighted neutron Fo-Fc contoured at 3.5σ) shows the difference density calculated by omitting the ferryl oxygen. Protonation states are depicted for (**E**) distal and (**F**) proximal active site residues. In the distal pocket, the ferryl oxygen acts as an acceptor for hydrogen bonds from the deuterated N_ε of Arg^{48} and the deuterated N_ε of Trp^{51}. His^{52} is deuterated at both N_δ and N_ε, the latter acting as a hydrogen bond donor to a bound water molecule (W2). W2 donates a hydrogen bond to the π orbitals of the porphyrin ring. Color scheme is as in Fig. 1, with the iron and ferryl oxygen depicted as orange and red spheres.

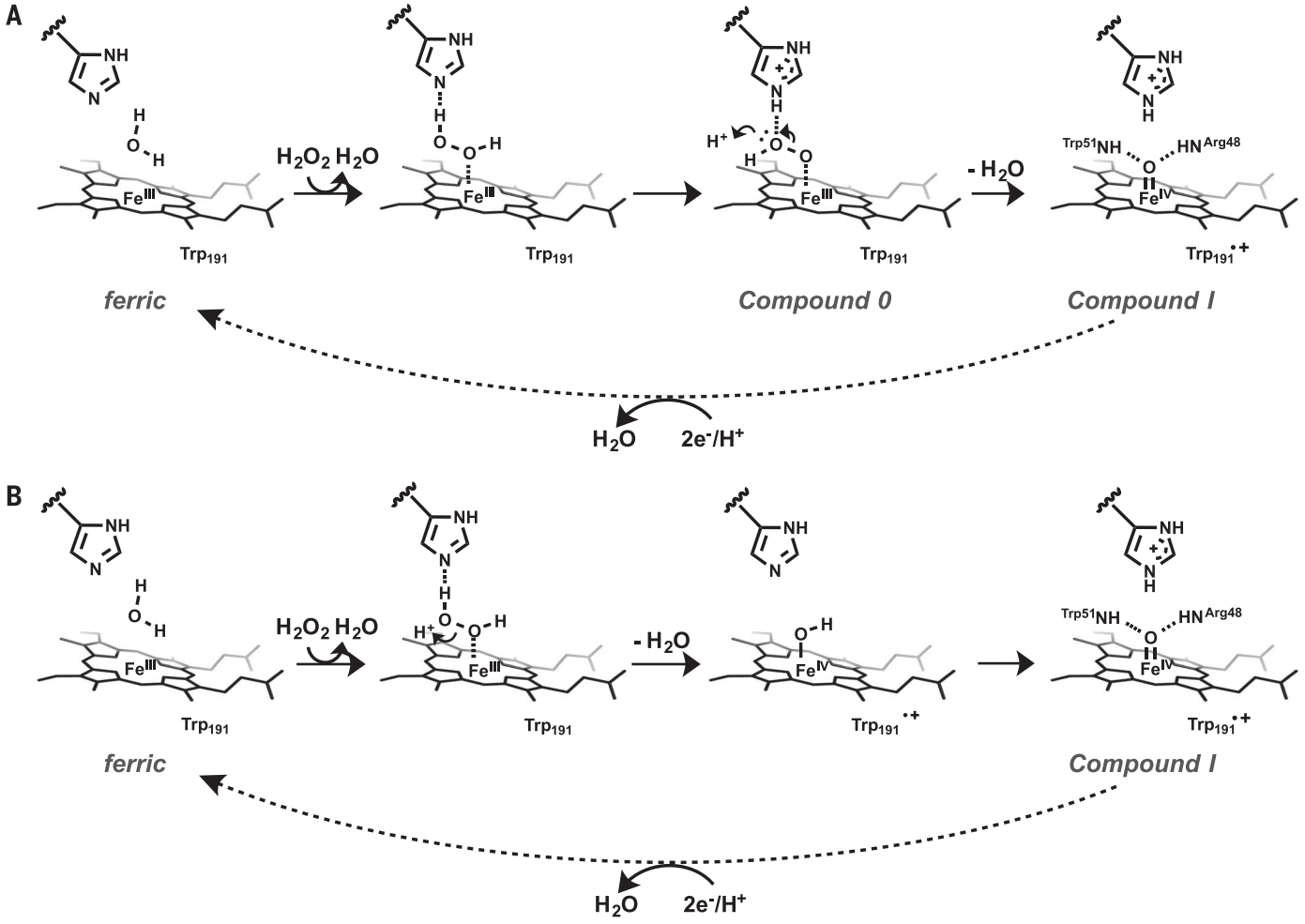

Fig. 3. Possible movement of protons during O–O bond activation. (**A**) Formation of a peroxide-bound complex and then compound 0 is followed by O–O bond cleavage. The distal histidine retains a proton upon formation of compound I, which means that an additional proton is required for release of water in both formation and reduction of compound I. (See text for detailed discussion.) The orientation of deuterium atoms on active site water molecules (Figs. 2 and 3) seems to preclude a water-mediated mechanism for O–O bond cleavage as suggested in horseradish peroxidase (*34*) because the deuterium atoms on W2 are oriented away from the ferryl oxygen atom and a hydrogen bond would not be possible (Fig. 2E). (**B**) An alternative mechanism from the same peroxide-bound complex. Cleavage of the peroxide bond may lead initially to formation of a transient iron(IV)-hydroxide species [Fe(IV)-OH], which, via proton transfer, leads to compound I, with Fe(IV)=O and a protonated distal histidine.

not interact ideally with any neighboring proton donors. This lack of ideal hydrogen bonding structure in the ferric form may favor formation of the peroxide complex and the deprotonated compound 0 (*28*), as structures of the closely related compound III (oxy) complexes all suggest that more favorable hydrogen bonding interactions with the bound peroxide are likely (fig. S6). Our data suggest that His^{52} retains a proton upon formation of compound I. In terms of proton count, this presumably means that delivery of an additional proton to compound 0 is needed for compound I formation if water is released as product (Fig. 3A), aligning the mechanism more closely with the related P450s in which delivery of a single proton to compound 0 is also widely assumed (*2*, *29*). Arg^{48}, which is protonated (Figs. 1 and 2), could act as the source of the additional proton required for release of water in both formation and reduction of compound I, as it is thought to play a role in proton-relay networks (*30*). Hydroxide (instead of water, Fig. 3A) formation is also possible; if this is the case, a role for Arg^{48} in charge stabilization of OH^- is easily envisaged and would be consistent with early predictions (*31*). Because the proton on His^{52} must be removed before a second turnover of the enzyme can occur, the acid-catalysis role of His^{52} must occur after compound I formation and not [as is often assumed (*1*)] before (Fig. 3A). An alternative and intriguing possibility (Fig. 3B), which could apply generally to any heme protein with a distal histidine in the heme pocket, is that O–O bond cleavage initially forms a transient Fe(IV)-OH species [as in the P450s (*32*)], but the presence of the distal histidine provides an escape route for the proton, thus disfavoring formation of Fe(IV)-OH. Proton transfer in this direction, to form Fe(IV)=O, would be consistent with published pK_as (K_a, acid dissociation constant) for the distal histidine across the peroxidase family [estimated $pK_a \approx 4$ to 5 (*1*, *33*)] if the pK_a of the ferryl heme, which is not known reliably for a heme peroxidase, was lower than that.

REFERENCES AND NOTES

1. H. B. Dunford, *Heme Peroxidases* (Wiley, Chichester, UK, 1999).
2. P. R. Ortiz de Montellano, *Cytochrome P450: Structure, Mechanism, and Biochemistry* (Kluwer Academic/Plenum, New York, ed. 3, 2005).
3. K. D. Karlin, *Nature* **463**, 168–169 (2010).
4. S. G. Sligar, *Science* **330**, 924–925 (2010).
5. J. T. Groves, *Nat. Chem.* **6**, 89–91 (2014).
6. I. Schlichting *et al.*, *Science* **287**, 1615–1622 (2000).
7. G. I. Berglund *et al.*, *Nature* **417**, 463–468 (2002).
8. L. Que Jr., W. B. Tolman, *Nature* **455**, 333–340 (2008).
9. A. R. McDonald, L. Que Jr., *Nat. Chem.* **3**, 761–762 (2011).
10. J. Rittle, M. T. Green, *Science* **330**, 933–937 (2010).
11. D. G. Kellner, S. C. Hung, K. E. Weiss, S. G. Sligar, *J. Biol. Chem.* **277**, 9641–9644 (2002).
12. R. K. Behan, M. T. Green, *J. Inorg. Biochem.* **100**, 448–459 (2006).
13. J. Terner *et al.*, *J. Inorg. Biochem.* **100**, 480–501 (2006).
14. M. P. Blakeley, *Crystallogr. Rev.* **15**, 157–218 (2009).
15. V. L. Davidson, *Nat. Chem.* **3**, 662–663 (2011).
16. M. P. Blakeley, A. J. Kalb, J. R. Helliwell, D. A. Myles, *Proc. Natl. Acad. Sci. U.S.A.* **101**, 16405–16410 (2004).
17. M. Sivaraja, D. B. Goodin, M. Smith, B. M. Hoffman, *Science* **245**, 738–740 (1989).
18. T. L. Poulos *et al.*, *J. Biol. Chem.* **255**, 575–580 (1980).
19. A. Gumiero, C. L. Metcalfe, A. R. Pearson, E. L. Raven, P. C. Moody, *J. Biol. Chem.* **286**, 1260–1268 (2011).

20. H. Hori, T. Yonetani, *J. Biol. Chem.* **260**, 349–355 (1985).
21. S. L. Edwards, H. X. Nguyen, R. C. Hamlin, J. Kraut, *Biochemistry* **26**, 1503–1511 (1987).
22. A. E. Pond, G. S. Bruce, A. M. English, M. Sono, J. H. Dawson, *Inorg. Chim. Acta* **275–276**, 250–255 (1998).
23. J. E. Erman, T. Yonetani, *Biochim. Biophys. Acta* **393**, 350–357 (1975).
24. J. E. Huyett *et al.*, *J. Am. Chem. Soc.* **117**, 9033–9041 (1995).
25. Y. T. Meharenna, T. Doukov, H. Li, S. M. Soltis, T. L. Poulos, *Biochemistry* **49**, 2984–2986 (2010).
26. A. J. Sitter, C. M. Reczek, J. Terner, *J. Biol. Chem.* **260**, 7515–7522 (1985).
27. H. B. Dunford, *Peroxidases and Catalases: Biochemistry, Biophysics, Biotechnology, and Physiology* (Wiley, Chichester, UK, ed. 2, 2010).
28. E. Derat, S. Shaik, *J. Phys. Chem. B* **110**, 10526–10533 (2006).
29. S. Shaik, D. Kumar, S. P. de Visser, A. Altun, W. Thiel, *Chem. Rev.* **105**, 2279–2328 (2005).
30. I. Efimov *et al.*, *J. Am. Chem. Soc.* **133**, 15376–15383 (2011).
31. T. L. Poulos, J. Kraut, *J. Biol. Chem.* **255**, 8199–8205 (1980).
32. T. H. Yosca *et al.*, *Science* **342**, 825–829 (2013).
33. J. E. Erman, L. B. Vitello, M. A. Miller, J. Kraut, *J. Am. Chem. Soc.* **114**, 6592–6593 (1992).
34. P. Vidossich *et al.*, *J. Phys. Chem. B* **114**, 5161–5169 (2010).

ACKNOWLEDGMENTS

We thank D. Collison for assistance with EPR, P. Ortiz de Montellano for discussions on the mechanisms, S. Fisher for assistance with the joint x-ray/neutron refinement, and the University of Leicester BioMedical Workshop for custom building of microspectrophotometry equipment, and J. Devos and the D-lab for experimental support. Atomic coordinates have been deposited in the Protein Data Bank under accession codes 4CVI for ferric CcP and 4CVJ for compound I. This work was supported by The Leverhulme Trust (grant F/00 212/Q to E.L.R./P.C.E.M.), Biotechnology and Biological Sciences Research Council (grant BB/C001184/1 to E.L.R./P.C.E.M., and a studentship to E.J.M.), The Wellcome Trust (grant WT094104MA to P.C.E.M./E.L.R.), an Institut Laue-Langevin studentship (to C.M.C.) and beam time at LADI-III and BIODIFF (EU FP7 NMI3-II grant 283883), Bruker UK (Sponsorship of A.J.F. and M.G.C.), and beam time at LADI-III and BIODIFF. P.C.E.M., M.P.B., and E.L.R. designed the research; C.M.C., A.G., M.P.B., A.O., S.C.M.T, T.E.S., C.L.M., E.J.M., and P.C.E.M. performed crystallographic experiments; C.M.C., A.G., M.P.B., S.C.M.T., A.O., T.E.S., E.L.R., and P.C.E.M. analyzed crystallographic data; C.M.C., A.J.F., M.G.C., J.B., and P.C.E.M. performed spectroscopic experiments; C.M.C., A.G., A.J.F., M.G.C., E.L.R., and P.C.E.M. analyzed spectra; and E.L.R., M.P.B., and P.C.E.M. wrote the paper, with contributions from all authors.

SUPPLEMENTARY MATERIALS

www.sciencemag.org/content/345/6193/193/suppl/DC1
Materials and Methods
Figs. S1 to S6
Tables S1 and S2
References (*35–48*)

4 April 2014; accepted 29 May 2014
10.1126/science.1254398

CATALYSIS

Assessing the reliability of calculated catalytic ammonia synthesis rates

Andrew J. Medford,[1,2] Jess Wellendorff,[1,2] Aleksandra Vojvodic,[1] Felix Studt,[1] Frank Abild-Pedersen,[1] Karsten W. Jacobsen,[3] Thomas Bligaard,[1] Jens K. Nørskov[1,2]*

We introduce a general method for estimating the uncertainty in calculated materials properties based on density functional theory calculations. We illustrate the approach for a calculation of the catalytic rate of ammonia synthesis over a range of transition-metal catalysts. The correlation between errors in density functional theory calculations is shown to play an important role in reducing the predicted error on calculated rates. Uncertainties depend strongly on reaction conditions and catalyst material, and the relative rates between different catalysts are considerably better described than the absolute rates. We introduce an approach for incorporating uncertainty when searching for improved catalysts by evaluating the probability that a given catalyst is better than a known standard.

With the surge in density functional theory (DFT) calculations of chemical and materials properties, the question of the reliability of calculated results becomes increasingly urgent (*1*), particularly when calculations are used to make predictions of new materials with interesting functionality (*2–5*). Evaluating the reliability of DFT calculations has relied mainly on comparisons to experiments or to data sets of higher-level calculations to provide a measure of the expected accuracy of directly calculated properties such as bond strengths, bond lengths, or activation energies of elementary processes. The question is how such intrinsic uncertainties in calculated microscopic properties transform into error bars on calculated complex properties, defined here as properties that depend on several microscopic properties in a complex way (*6*). Examples of such properties include mechanical strength (*7*), phase stability (*8*), and catalytic reaction rates (*5*).

We estimate the reliability of DFT energies by choosing an ensemble of exchange-correlation functionals to represent the known computational errors for a set of adsorption energies (*9–11*). This ensemble of energies is used to calculate the rates of the ammonia synthesis reaction via microkinetic modeling. We choose this process because it is well described both experimentally and theoretically (*12–16*) and has enough complexity to bring out important aspects of error propagation through multiple layers of simulation. This approach directly captures correlations between systematic errors in the underlying energetics, revealing that uncertainties on the calculated rates exhibit a nontrivial dependence on the reaction conditions as well as the material and that trends in catalytic activity are considerably better described than the absolute rates.

To calculate energies and estimated errors, we apply the Bayesian error estimation functional with van der Waals correlation (BEEF-vdW), a recent exchange-correlation density functional tailored for surface chemistry with built-in error estimation capabilities (*11*). The functional was fitted to describe several different properties, including common adsorbate-surface bond strengths, and an ensemble of density functionals around BEEF-vdW was generated. This Bayesian error estimation (BEE) ensemble was designed to reproduce known energetic errors by mapping them to uncertainties on the exchange-correlation model parameters. Figure 1 illustrates this. Uncertainties on new calculations may then be estimated by mapping back again: Random sampling of a probability distribution for fluctuations of the model parameters leads to a large ensemble of different predictions of the same quantity. The statistical variance of those predictions defines the error estimate on the BEEF-vdW result, $\sigma_{BEE} = \sqrt{Var(\vec{p})}$, where the ensemble predictions are stacked in vector $\vec{p}$. Further details are provided in (*11*, *17*). This approach to quantitative error estimation in DFT can be viewed as a structured analysis of the sensitivity of DFT results to the choice of exchange-correlation approximation. An appropriately designed ensemble also captures correlated variations between DFT total energies and offers a consistent approach to keeping track of possible sources of error when data from multiple calculations are folded in composite post-DFT frameworks, such as microkinetic models used to analyze catalytic reactions.

For the ammonia synthesis reaction, microkinetic models provide the link between the calculated microscopic properties and the reaction rate or turnover frequency (TOF). Here, we use a relatively simple kinetic model based on N_2 dissociation as the rate-limiting step, following the mechanism described by Honkala *et al.* (*16*). This model has previously been shown to capture the experimentally observed trends in catalytic activity for different catalysts (*18*); details of the model can be found in (*17*, *18*). We first consider in some detail the rates of ammonia synthesis over stepped Fe and Ru surfaces, which are the industry-standard catalysts (*14*, *19*, *20*). The calculated ammonia synthesis rate over iron per active (step) site (the TOF) is shown in Fig. 2A as an Arrhenius plot at industrial conditions. The red shaded area indicates that the estimated

[1]SUNCAT Center for Interface Science and Catalysis, SLAC National Accelerator Laboratory, Menlo Park, CA 94025, USA. [2]SUNCAT Center for Interface Science and Catalysis, Department of Chemical Engineering, Stanford University, Stanford, CA 94305, USA. [3]Center for Atomic-scale Materials Design (CAMD), Department of Physics, Technical University of Denmark, DK-2800 Lyngby, Denmark.
***Corresponding author. E-mail: norskov@stanford.edu**

error in TOF is generally less than one order of magnitude, although there is a nontrivial dependence on reaction conditions that results in larger uncertainties at extreme temperatures. We also investigated the ammonia synthesis rate over a stepped Ru surface for which there are detailed experiments for comparison (Fig. 2B). In this case, the magnitude of the prediction uncertainty is somewhat greater, around two orders of magnitude, and again varies with reaction conditions. The calculated apparent activation barrier (*17*) and N_2 dissociation barrier are compared with experimental results in the inset of Fig. 2B; the experimental value is within the uncertainty of the calculation, corroborating the surface and kinetic models employed.

One interesting feature of error propagation through the kinetic model is the cancellation of errors arising from correlation between model inputs. To assess this effect, we compared the uncertainty inferred by the BEE ensembles (red) to "uncorrelated" ensembles (gray) in Fig. 2 [see (*17*) for details]. The uncorrelated ensembles substantially overestimate the error at low temperatures because the TOF varies monotonically with the product of the rate constant (k) and the free site coverage (θ_*). The rate constant varies exponentially with the activation energy and, in regimes of intermediate adsorbate coverage, θ_* will be very sensitive to variations in the energy of the most abundant surface intermediate. A positive covariance between the transition-state energy and the energies of all intermediates (see table S2) implies that an exchange-correlation functional that predicts a strong binding of the surface-bound species (lower θ_*) will also yield a very stable transition state (higher k), hence the cancellation of possible errors. This reasoning is general to other surfaces, reactions, and kinetic models, although the magnitude of the effect will depend on the details of the system.

Next, we compare catalytic rates and error estimates for several different metal catalysts calculated using the chosen kinetic model (see Fig. 3A). As previously indicated, the uncertainty on the TOF depends considerably on the catalyst. For the unreactive metals, the uncertainty is large, whereas it is considerably smaller for the most active catalysts, Ru and, in particular, Fe. Furthermore, Fig. 3B demonstrates that error bars on relative TOFs $\left(\frac{\mathrm{TOF}}{\mathrm{TOF@Fe}}\right)$ and relative nitrogen adsorption energies ($E_N - E_N$@Fe) are substantially smaller than on the absolute materials properties. This decrease in uncertainty is the result of the correlation of errors between various transition-metal surfaces (see table S3). Exchange-correlation functionals that bind a given intermediate or transition state stronger on one metal are likely to bind it stronger on another, and the BEEF-vdW exchange-correlation ensemble captures this effect quantitatively. Figure 3B demonstrates that we can make statistically significant predictions about the relative ammonia synthesis rates on different metals. The predictions are in agreement with experimental data showing that Ru and Fe are the most active catalysts for ammonia synthesis at these conditions (*14*, *21*).

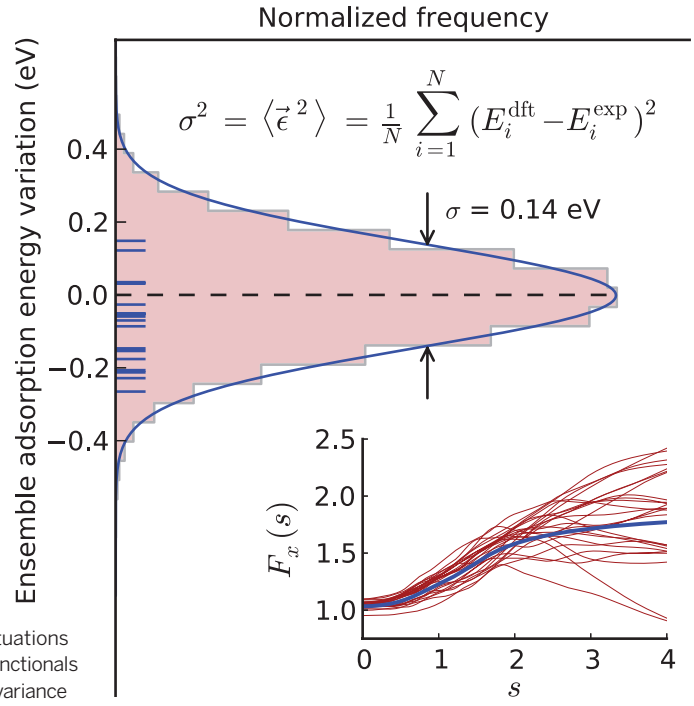

Fig. 1. BEEF-vdW functional and ensemble. BEEF-vdW prediction errors for 17 experimental adsorption energies (blue horizontal lines) and distribution of adsorption energy perturbations (shaded histogram) that result from applying perturbed exchange-correlation functionals from the BEEF-vdW ensemble to those systems. The inset illustrates the exchange part of the perturbed functionals (red lines) in terms of exchange enhancement factor, F_x, as a function of the reduced electron density gradient, s. The BEEF-vdW F_x is shown in blue. Fluctuations within the ensemble of functionals are scaled such that the variance of the resulting energy perturbations, σ^2, reproduces the average square prediction error realized by BEEF-vdW. The original ensemble from (*11*) reproduces errors on several properties. The present work concerns surface chemistry, so the fluctuations are rescaled to reflect the expected prediction error for surface adsorption energies only [see (*17*)].

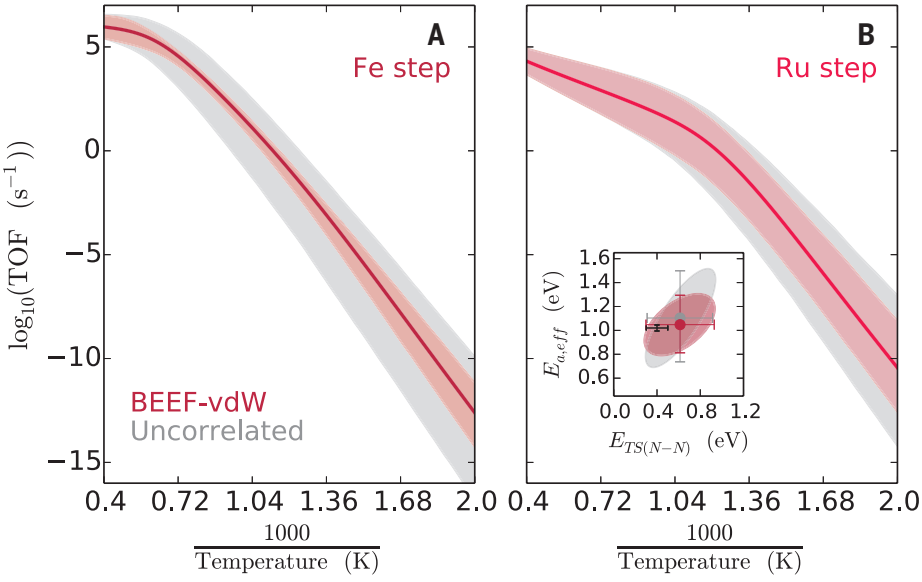

Fig. 2. Simulated Arrhenius plots. Arrhenius plot for ammonia synthesis on Fe(211) (**A**) and Ru(0001) (**B**) step site as calculated with BEEF-vdW and the described microkinetic model at industrial conditions (100 bar, 50% approach to equilibrium). The shaded red area corresponds to error estimates, and the gray area corresponds to an uncorrelated model [see (*17*)]. In the inset of (B), the N_2 dissociation barrier is plotted against the apparent Arrhenius activation barrier for the Ru(0001) step site under conditions comparable to (*15*). The principal component ellipses [see (*17*)] of the correlated (red) and uncorrelated (gray) ensembles are shown, and the predictions are compared to experimental measurements taken from (*15*, *19*) (black error bars).

The nitrogen adsorption energy at the active site is a good descriptor of ammonia synthesis activity due to a set of linear scaling relations between the adsorption energy of nitrogen and the adsorption energies of the other intermediates, H, NH, NH_2, and the N–N transition state

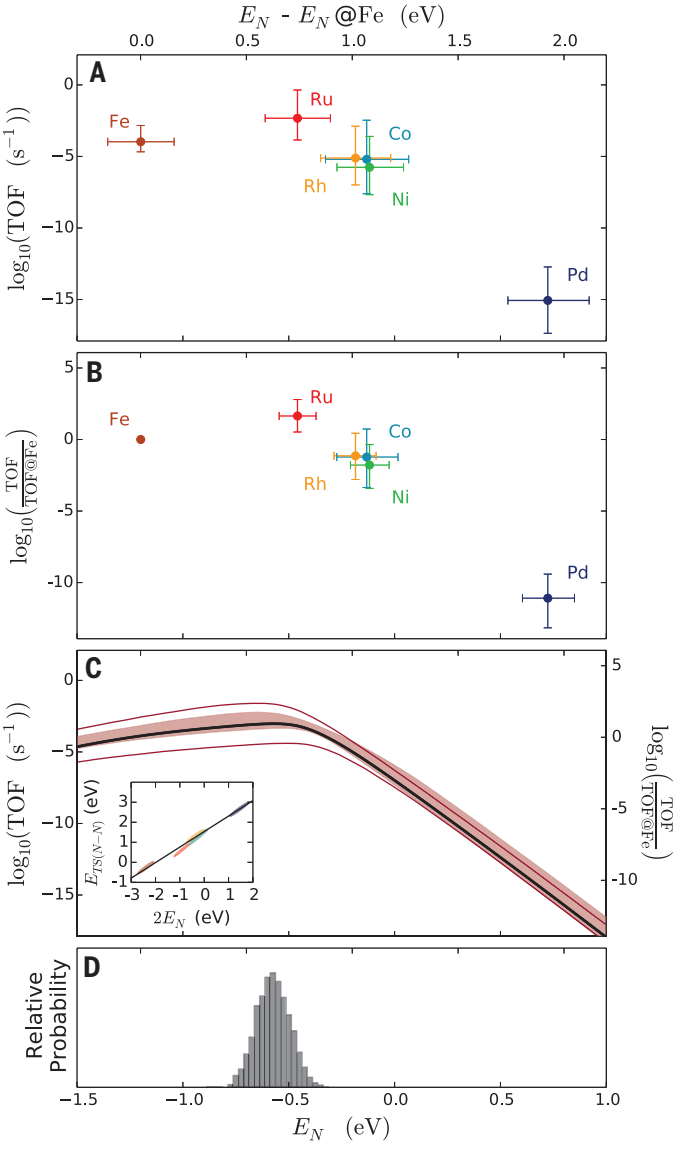

Fig. 3. Ammonia synthesis rate trends. Absolute TOFs on metallic step sites of selected metals plotted as a function of nitrogen adsorption energy (**A**) and TOFs divided by the TOF of Fe as a function of nitrogen adsorption energy relative to Fe (**B**). The rate activity map obtained from linear scaling relations between the adsorption energy of nitrogen and other intermediates is shown in (**C**), where the red line/area corresponds to the uncertainty on the absolute/relative rate, respectively. Linear regression between the dissociative adsorption energy of N_2 ($2E_N$) and the N–N transition-state energy is shown in the inset, along with principal component ellipses of the metal ensembles [see (*17*)]. The probability that a rate volcano has an optimum at a given nitrogen adsorption energy is presented in (**D**). The temperature is 673 K, total pressure is 100 bar, and approach to equilibrium is fixed at 10%.

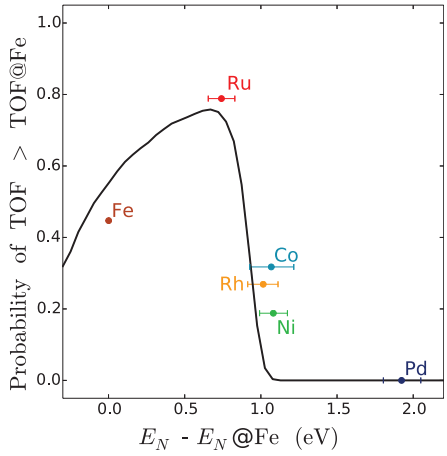

Fig. 4. Rate probability map. The probability that the ammonia synthesis TOF of a given catalyst is higher than the TOF of iron step sites (calculated with the self-consistent BEEF-vdW energetics) as a function of nitrogen adsorption energy relative to that of iron. Reaction conditions are given in Fig. 3. The line corresponds to linear regression between the adsorption energy of nitrogen and other intermediates as described in Fig. 3C and fig. S2.

(*18*, *22*–*24*). Given these relations, the nitrogen adsorption energy determines all other energies in the problem (to within the accuracy of the scaling relations), and the rate can be calculated as a function of nitrogen adsorption energy. In Fig. 3C, we apply such an approach to each density functional in the BEEF-vdW ensemble to evaluate the consequence of an imperfect representation of exchange-correlation effects on a descriptor-based model of surface chemistry. The linear regression parameters between the nitrogen adsorption energy and the N–N transition state exhibit much smaller standard deviations than the underlying energies used to construct them (Fig. 3C, inset). The lower uncertainty on scaling parameters results from cancellation of error due to correlated energetics (tables S2 and S3) and is general to the other intermediates in the system, as shown in fig. S2. The resulting ensemble of "rate maps" (Fig. 3C) shows that the "volcano"-type relation between rate and nitrogen adsorption energy is well determined by the calculations. Comparing Fig. 3, B and C, it is also evident that the calculated rates for individual metals agree with the descriptor-based model to within the BEE uncertainty.

The descriptor-based analysis provides a simple method for computational design of new catalysts (*3*, *5*). Once a set of descriptors is identified and a mapping between the descriptors and the catalytic activity has been constructed, the search for new catalysts is reduced to finding new materials with descriptor values near the optimum. An essential question is how well the position of the maximum in such activity maps is determined (*25*). Figure 3D shows the relative probability that the maximum of the ammonia synthesis rate occurs at a given nitrogen adsorption energy. The position of the maximum is –0.58 eV, with a standard deviation of 0.08 eV. This uncertainty in the predicted optimum is considerably smaller than the >2 eV range spanned by the nitrogen adsorption energies of the metals included in this study. The optimum descriptor value is therefore precisely determined relative to the energetic differences between transition-metal catalysts.

In computational materials design, the magnitude of the uncertainty associated with a given predicted property is of less importance than the confidence with which one can evaluate a hypothesis. For ammonia synthesis catalysts, for instance, we could look for materials that exhibit higher TOFs than the industry-standard iron catalyst. Our analysis allows an evaluation of the probability that a given catalyst has a TOF greater than that of iron. The results in Fig. 4 provide support to the notion that despite uncertainties of several orders of magnitude in absolute values of predicted TOFs, it is possible to draw strong scientific conclusions about which new materials are promising for ammonia synthesis. The probabilities shown in Fig. 4 reflect only the expected magnitude of uncertainty on energetics from exchange-correlation effects and neglect all other possible sources of error, such as the surface model, reaction mechanism, and descriptor-based dimensionality reduction. Nonetheless, the present analysis indicates an upper bound to the reliability of theoretical predictions for ammonia synthesis TOFs, and the probabilistic approach provides a convenient framework for including additional sources of uncertainty.

REFERENCES AND NOTES

1. K. Burke, *J. Chem. Phys.* **136**, 150901 (2012).
2. G. Ceder *et al.*, *Nature* **392**, 694–696 (1998).
3. S. Curtarolo *et al.*, *Nat. Mater.* **12**, 191–201 (2013).
4. L. Yu, A. Zunger, *Phys. Rev. Lett.* **108**, 068701 (2012).
5. J. K. Nørskov, T. Bligaard, J. Rossmeisl, C. H. Christensen, *Nat. Chem.* **1**, 37–46 (2009).
6. B. B. Machta, R. Chachra, M. K. Transtrum, J. P. Sethna, *Science* **342**, 604–607 (2013).

7. P. Liao, E. A. Carter, *Acta Mater.* **58**, 5912–5925 (2010).
8. K. Reuter, M. Scheffler, *Phys. Rev. B* **2**, 12 (2001).
9. S. L. Frederiksen, K. W. Jacobsen, K. S. Brown, J. P. Sethna, *Phys. Rev. Lett.* **93**, 165501 (2004).
10. J. J. Mortensen *et al.*, *Phys. Rev. Lett.* **95**, 216401 (2005).
11. J. Wellendorff *et al.*, *Phys. Rev. B* **85**, 235149 (2012).
12. G. Ertl, *Catal. Rev.* **21**, 201–223 (1980).
13. S. R. Bare, D. R. Strongin, G. A. Somorjai, *J. Phys. Chem.* **90**, 4726–4729 (1986).
14. R. Schlögl, *Angew. Chem. Int. Ed.* **42**, 2004–2008 (2003).
15. S. Dahl, P. A. Taylor, E. Törnqvist, I. Chorkendorff, *J. Catal.* **178**, 679–686 (1998).
16. K. Honkala *et al.*, *Science* **307**, 555–558 (2005).
17. Materials and methods are available as supplementary material on *Science* Online.
18. A. Vojvodic *et al.*, *Chem. Phys. Lett.* **598**, 108–112 (2014).
19. S. Dahl *et al.*, *Phys. Rev. Lett.* **83**, 1814–1817 (1999).
20. R. C. Egeberg *et al.*, *Surf. Sci.* **491**, 183–194 (2001).
21. K. Aika, A. Ozaki, in *Catalysis: Science and Technology Volume 1*, M. Boudart, J. R. Anderson, Eds. (Springer, Berlin, 1981), Chapter 3.
22. A. Logadottir *et al.*, *J. Catal.* **197**, 229–231 (2001).
23. F. Abild-Pedersen *et al.*, *Phys. Rev. Lett.* **99**, 016105 (2007).
24. S. Wang *et al.*, *Phys. Chem. Chem. Phys.* **13**, 20760–20765 (2011).
25. Z. Ulissi, V. Prasad, D. G. Vlachos, *J. Catal.* **281**, 339–344 (2011).

ACKNOWLEDGMENTS

Data reported herein are available in the supplementary materials. Support from the U.S. Department of Energy Office of Basic Energy Science to the SUNCAT Center for Interface Science and Catalysis is gratefully acknowledged. A.J.M. is grateful for support by the U.S. Department of Defense through the National Defense Science and Engineering Graduate Fellowship Program.

SUPPLEMENTARY MATERIALS

www.sciencemag.org/content/345/6193/197/suppl/DC1
Materials and Methods
Figs. S1 and S2
Tables S1 to S3
References (*26*–*28*)

17 March 2014; accepted 2 June 2014
10.1126/science.1253486

IMAGING TECHNIQUES

Ultrafast low-energy electron diffraction in transmission resolves polymer/graphene superstructure dynamics

Max Gulde,[1] Simon Schweda,[1] Gero Storeck,[1] Manisankar Maiti,[1] Hak Ki Yu,[2] Alec M. Wodtke,[2,3] Sascha Schäfer,[1] Claus Ropers[1]*

Two-dimensional systems such as surfaces and molecular monolayers exhibit a multitude of intriguing phases and complex transitions. Ultrafast structural probing of such systems offers direct time-domain information on internal interactions and couplings to a substrate or bulk support. We have developed ultrafast low-energy electron diffraction and investigate in transmission the structural relaxation in a polymer/graphene bilayer system excited out of equilibrium. The laser-pump/electron-probe scheme resolves the ultrafast melting of a polymer superstructure consisting of folded-chain crystals registered to a free-standing graphene substrate. We extract the time scales of energy transfer across the bilayer interface, the loss of superstructure order, and the appearance of an amorphous phase with short-range correlations. The high surface sensitivity makes this experimental approach suitable for numerous problems in ultrafast surface science.

The investigation of atomic-scale dynamics with high spatiotemporal resolution yields insights into ultrafast structural reorganizations associated with energy transfer or phase transitions. Substantial progress was made in establishing methods for the time-resolved structural analysis of bulk media, including ultrafast implementations of x-ray crystallography (*1*–*3*), high-energy electron diffraction (*4*–*6*), and microscopy (*7*–*9*), as well as time-resolved x-ray and electron spectroscopy (*10*, *11*). In contrast, structural dynamics at surfaces, interfaces, and ultrathin films remain largely elusive, as the surface signal in both x-ray and high-energy electron diffraction is typically masked by large bulk contributions. This limits our ability to study quasi–two-dimensional (2D) systems exhibiting characteristic phase transitions and topologically controlled ordering (*12*, *13*), as well as the dynamics of surface reconstructions and complex adsorbate superstructures (*14*, *15*). Ultrafast electron scattering in grazing incidence enhances the surface signal (*14*, *16*) but faces particular challenges in quantitative diffraction analysis.

Optimal surface sensitivity would be attained with an ultrafast implementation of low-energy electron diffraction (LEED). At electron energies of tens to a few hundreds of electron volts, scattering cross sections are strongly increased, which allows for probing depths of only a few monolayers and has made LEED a widely used tool for surface structure determination. However, at such low energies, it has proven exceedingly difficult to implement pulsed electron sources that fulfill the requirements of an ultrafast diffraction experiment (*17*–*19*), that is, short pulse duration and low beam emittance. Laser-triggered electron emission from nanoscale photocathodes (*20*, *21*) is expected to resolve some of these issues (*22*–*24*), providing well-collimated low-energy electron pulses and a temporal resolution that is comparable to state-of-the-art ultrafast x-ray or high-energy electron diffraction. Motivated by these prospects, we have undertaken the development of a new diffraction apparatus.

We have developed transmission ultrafast LEED (T-ULEED) based on a nanometric needle photocathode and demonstrate its capability to resolve atomic-scale structural dynamics of surfaces and monolayer films with a temporal resolution of a few picoseconds. Specifically, we studied the ultrafast laser-driven dynamics of a polymer superstructure on freestanding monolayer graphene.

In the laser-pump/electron-probe scheme (Fig. 1A), the sample is excited out of equilibrium by amplified femtosecond laser pulses (800 nm wavelength, 80-fs pulse duration, repetition rate 10 kHz, focal diameter about 100 μm). To minimize hot electron emission from graphene (*25*), the pump pulse is temporally stretched to 3 ps by dispersion, which, however, is still sufficiently short to resolve the processes described below. The pump-induced structural dynamics are probed by ultrashort electron pulses emitted from a sharp tungsten tip (50-nm radius of curvature), triggered by the second harmonic of the laser. These electron pulses (up to 100 electrons per pulse) are collimated and focused onto the sample at variable electron energies using an electrostatic lens assembly in a geometry that we have recently studied numerically (*22*). Scattered electrons are subsequently recorded in a transmission geometry by a phosphor screen microchannel plate detector (MCP, Hamamatsu F2226-24P). With our laser-triggered low-energy electron source, diffraction patterns can also be recorded in back-reflection and for a range of electron energies, as demonstrated in the supplementary materials (*26*) (figs. S6 to S8).

The electron pulse duration and the spatial and temporal overlap (delay time, $\Delta t = 0$) of the laser-pump and electron-probe pulses are determined via a transient-electric-field effect near a bare transmission electron microscopy (TEM) copper grid. Upon excitation of a single copper grid bar with high peak intensity (fluence up to 30 mJ/cm^2, unstretched pump pulses), a dense electron cloud is emitted (*25*, *27*), which may lead to a spatial deflection of the passing electron pulse (Fig. 2A). Projection images of the grid before and after $\Delta t = 0$ are shown in Fig. 2B, acquired by defocusing the pulsed electron beam. The central distortion in the lower image indicates the extension of the pump-induced electron cloud. Using a collimated electron beam passing a single mesh

[1]4th Physical Institute, University of Göttingen, 37077 Göttingen, Germany. [2]Max Planck Institute for Biophysical Chemistry, 37077 Göttingen, Germany. [3]Institute for Physical Chemistry, University of Göttingen, 37077 Göttingen, Germany.
***Corresponding author. E-mail: cropers@gwdg.de**

cell, the effective temporal resolution of the diffraction experiment can be evaluated. Figure 2C shows the delay-dependent electron signal within a detector segment corresponding to a few-micron-sized mesh region. The observed transient displays a 2-ps width for 450 eV electron energy. This represents an upper bound for the electron pulse duration when using a partial beam because both plasma-cloud formation and beam traversal times limit the probing speed of the transient-electric-field method at low energies to the order of a picosecond. Averaging over the deflection of the entire collimated beam yields an upper limit of about 6 ps.

Using these experimental capabilities, we have studied the dynamics of a freestanding polymer/graphene bilayer. The relevance of this model system entails at least two aspects. From the perspective of polymer physics, considerable interest exists in thin polymer films on solids and the role of spatial confinement on the dynamics or key characteristics of phase and glass transitions (*28*, *29*). Ultrathin films of monolayer dimensions, on the other hand, will exhibit structural and dynamical features governed by short-range polymer-substrate interactions involving in-plane atomic corrugation (*30*, *31*). Furthermore, increasing efforts are devoted to developing graphene-based heterostructures, with polymers serving both as important compounds in graphene transfer and as interface candidates (*32*, *33*).

We prepared an ultrathin atactic poly(methyl methacrylate) (PMMA) layer adsorbed to freestanding monolayer graphene on a TEM grid (*26*). A projection image of a partially covered grid is shown in Fig. 1C. Local diffraction images from selected sample regions, as shown in Fig. 1B, can be recorded by passing the electron beam through a single mesh cell. The diffraction pattern displays peaks corresponding to the sixfold symmetry of single crystalline graphene and additional spots closer to the central beam stop. The latter are associated with the polymer adsorbate, which forms a superstructure that is orientationally linked to the graphene substrate.

We use cryo-TEM in local diffraction mode to identify the polymer order on the scale of few tens of nanometers, finding a reduced symmetry of the diffraction pattern with only two superstructure peaks (fig. S4). This implies that the polymer chains locally exhibit a stripe-like order, registered to the graphene substrate, and with a well-defined periodicity a = 4.26 Å, doubled relative to that of the graphene lattice (Fig. 1, D and E). The angular correlation with the substrate allows for three equivalent superstructure domains rotated by 60° with respect to each other (Fig. 1F) (denoted by half-integer Miller indices). The stripe-like structure follows from the tendency of the polymer strands to adapt to the periodically corrugated adsorption potential by forming 2D folded-chain crystals on the substrate. Similar behavior has been reported for PMMA adsorption on graphite and mica surfaces (*34*, *35*), even for atactic polymers and with the microscopic structure depending on tacticity (*35*). In contrast to the ordering perpendicular to the chains (*36*), the diffraction images show no clear sign for pronounced order of the atactic polymer along the chains.

We have found that the polymer superstructure can be reversibly melted by laser excitation. Figure 3 summarizes the changes in the diffraction maps induced by the optical pump. The graphene and superstructure diffraction spots of the bilayer system before and after excitation are shown in Fig. 3A. A normalized difference image is displayed in Fig. 3B. Whereas no prominent changes are observed for the graphene peaks, the intensity of the superstructure spots substantially decreases. The structural evolution is illustrated in Fig. 3C, showing difference images at three pump-probe delays. These difference maps display two main features, namely a reduction of the superstructure intensity (blue spots) and an increase of diffraction at smaller scattering angles corresponding to an in-plane momentum transfer $k_{||}$ of less than 1.25 Å^{-1} (red disc).

To differentiate the evolution of the inner disc from that of the superstructure spots, we decompose the diffraction changes into an isotropic and a sixfold symmetric component in Fig. 3, D and E, respectively. Specifically, we compute angular averages of the images in azimuthal segments around and in between the spots, and plot the diffraction changes along the radial direction (fig. S2). The increase of small-angle scattering (Fig. 3D) is peaked around $k_{||}$ = 1.1 Å^{-1}, which is also discernible as a ring shape in Fig. 3C (central panel). The analysis in Fig. 3, D and E, shows a strong dependence on scattering angle in the time scales of positive and negative signal changes. For example, while the spot intensity decrease is nearly complete after 160 ps (Fig. 3E, blue line), substantial relaxation still occurs in the nearly isotropic small-angle region at later times (Fig. 3D).

Figure 4 presents a more quantitative picture of the diffraction changes based on time curves and fluence dependencies. The delay-dependent reduction of the superstructure diffraction intensity, representing the loss of crystalline order, occurs on a time scale of ~105 ps (Fig. 4A, blue triangles). This temporal evolution is accompanied

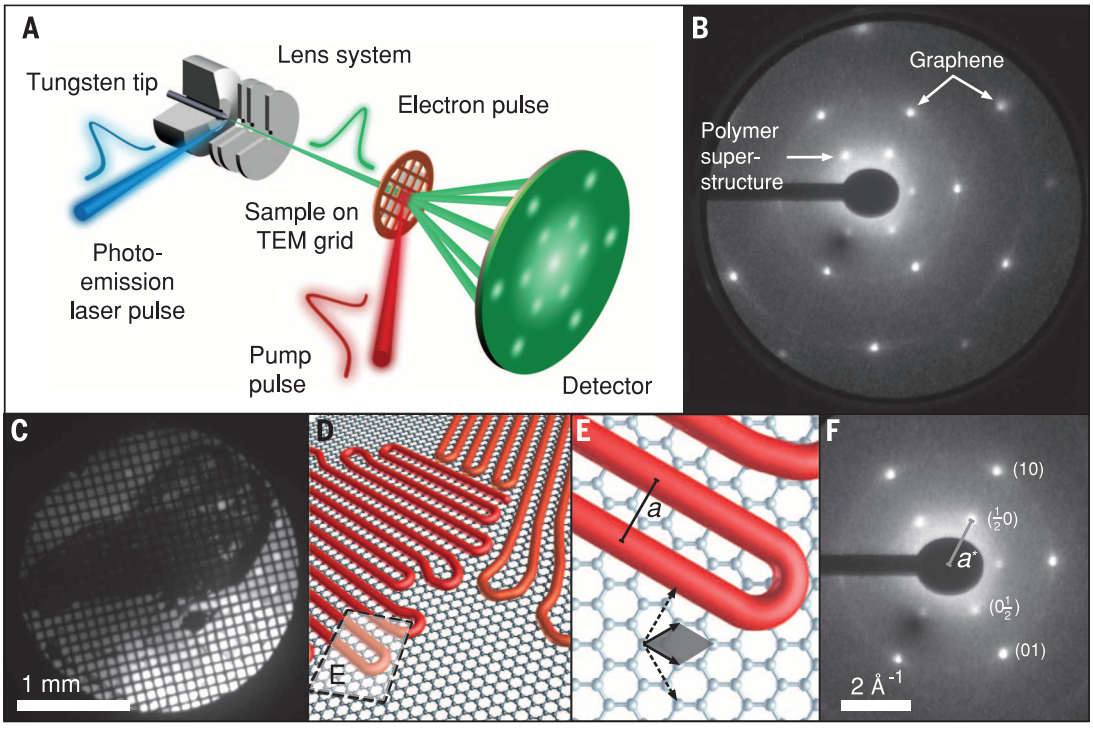

Fig. 1. Ultrafast low-energy electron diffraction in transmission and polymer/graphene bilayer system. (**A**) Schematic of the laser-pump/electron-probe setup. (**B**) Diffraction pattern of polymer/graphene bilayer system (at increased electron energy of 1 keV; integration time 1 s). (**C**) Projection image of one of the samples (450 eV). Dark areas indicate bilayer coverage. (**D**) Idealized sketch of stripe-like polymer superstructure domains of two different orientations. (**E**) Zoom into area denoted in (D). Solid (dashed) arrows indicate lattice vectors for real (reciprocal) space unit cell of graphene. Chain spacing denoted by a. (**F**) Central part of diffraction pattern indicating Miller indices and reciprocal distance $a^* = 2\pi/a$ = 1.47 Å^{-1}.

by an inward shift of the remaining spot intensity (Fig. 4B), which amounts to an increase of the polymer interchain distance of about 0.23 Å or 5%. The concurrent appearance of the small-angle diffraction disc is evaluated in Fig. 4A (red circles, averaged over the entire disc region). We find that the time scale of the diffraction increase is in fact a strong function of the scattering angle, with the slowest dynamics occurring at the smallest momenta, as quantified in the inset of Fig. 4A.

We have recorded similar dynamics for multiple samples and observe a distribution of characteristic superstructure melting-time constants of 95 ± 25 ps, which is likely caused by slight variations in sample preparation and storage times. Recrystallization after laser-induced melting of the superstructure occurs on time scales of few tens of microseconds, rendering the repetition rate of 10 kHz suitable for reversible studies.

To corroborate the notion of superstructure melting, we have carried out measurements as a function of pump fluence. Figure 4C displays the fluence-dependent change in superstructure peak intensity (green diamonds) relative to the unperturbed sample, together with the associated structural expansion of the crystalline phase (blue triangles), each evaluated at a delay of 600 ps. Both observables exhibit a threshold behavior at a fluence of 3 mJ/cm^2 (dashed line). Beyond this threshold, a strong linear decrease in diffraction intensity is found, and it is accompanied by a kink in the otherwise linear fluence-dependent lattice expansion. These marked changes in the physical properties of the superstructure upon differential energy deposition evidence the qualitative characteristics of a phase transition.

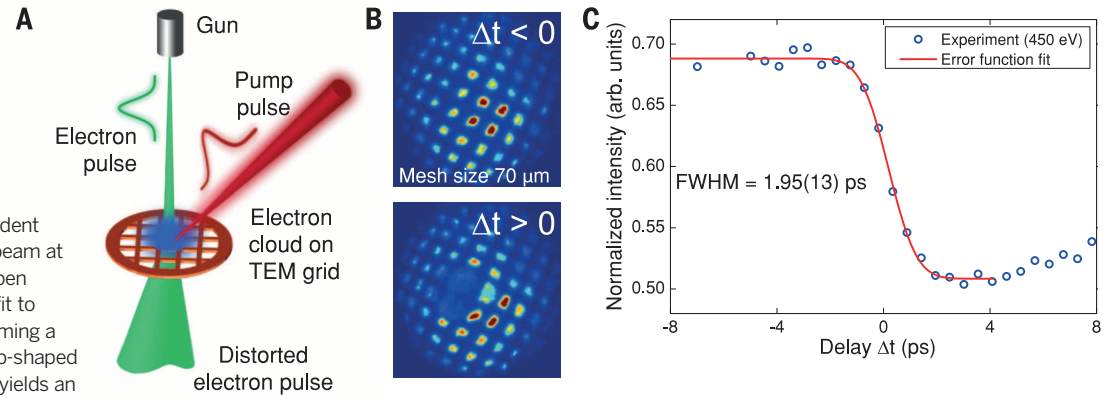

Fig. 2. Temporal characterization of low-energy electron pulses. (**A**) Schematic of the transient-electric-field effect used for determination of the electron pulse duration. (**B**) Projection images of bare TEM grid recorded before and after time zero. (**C**) Delay-dependent intensity change for collimated beam at an electron energy of 450 eV (open circles). Red line, error function fit to transient intensity change. Assuming a Gaussian pulse profile and a step-shaped transient-electric-field response yields an electron pulse duration (full width at half maximum) of about 2 ps.

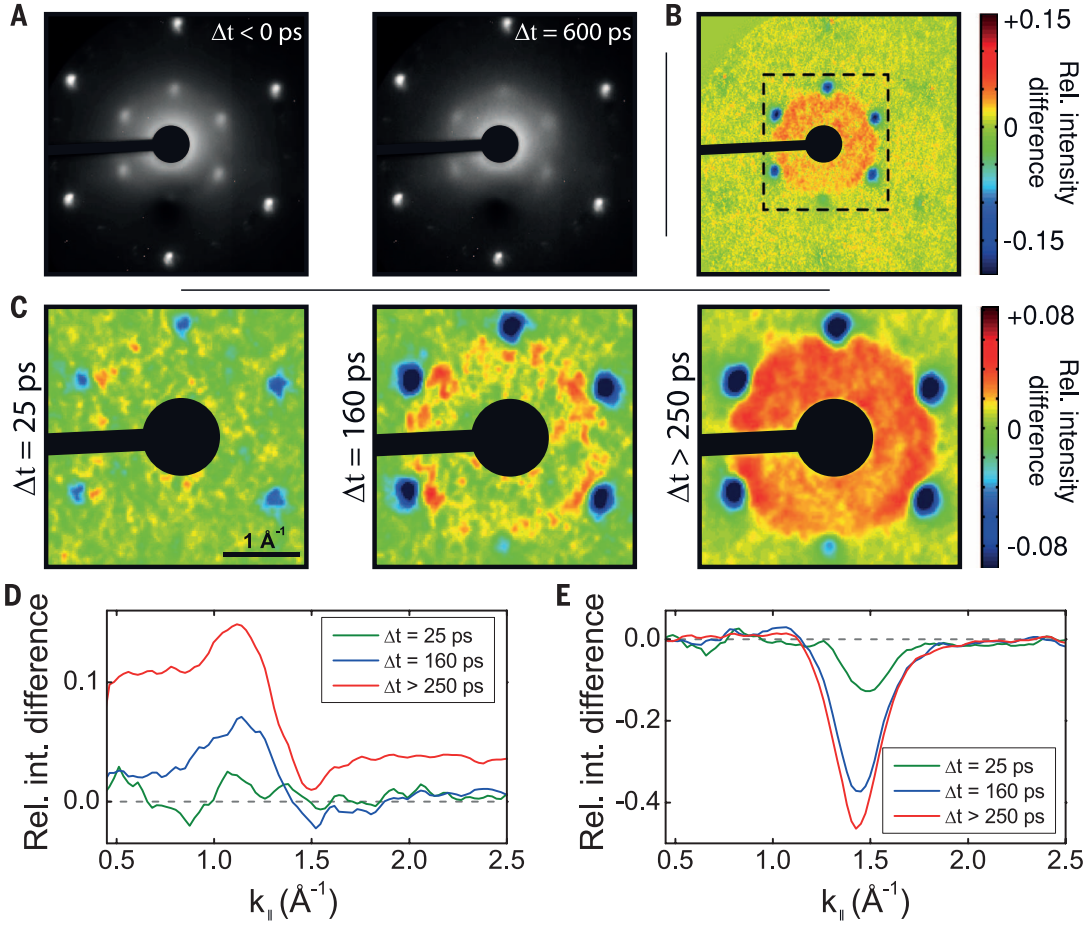

Fig. 3. Time-resolved diffraction maps of superstructure melting. (**A**) Diffraction images for negative delay (left) and Δt = 600 ps (right). Pump fluence: 6 mJ/cm^2. Electron energy: 450 eV. (**B**) Difference of images shown in (A) with intensity I_n normalized to the superstructure peak intensity I_0 = I(Δt < 0) at negative delay times: $I_n(\Delta t) = [I(\Delta t) - I_0]/I_0$. (**C**) Normalized difference images for central region [dashed rectangle in (B)] for several delay times. (**D** and **E**) Relative change of radial diffraction intensity (averaged over azimuthal angles) for isotropic (D) and sixfold symmetric (E) components (*26*). (The darker region around the bottom superstructure spot arises from reduced MCP quantum efficiency.)

We interpret the structural dynamics as follows: The initial state of the system is characterized by strongly physisorbed polymer chains within a periodic adsorption potential. The presence of both polymer-substrate and polymer interchain interactions determines the equilibrium state as displaying 2D folded-chain crystallites with three equivalent domains orientationally correlated to the graphene substrate. The widths of superstructure diffraction peaks from various samples indicate typical correlation lengths spanning at least 5 to 10 chain spacings of 4.26 Å each. The strength of the PMMA peaks relative to those of graphene suggests both considerable overall crystallinity and substrate coverage. Because the polymer is optically transparent, the laser excitation primarily deposits energy in the graphene, giving rise to a lattice temperature increase of about 540 K at an incident fluence of 3 mJ/cm^2 (*26*). Whereas the graphene degrees of freedom equilibrate on times comparable to the pulse duration used, coupling to the overlayer is considerably slower. The structural dynamics at fluences below the threshold for loss of crystalline order are valuable to estimate the threshold temperature for superstructure melting and the energy coupling times. In the absence of a phase transition, the energy transfer to the adsorbate causes thermal expansion of up to 0.05 Å. Using the thermal expansion coefficient of bulk PMMA for a rough estimate yields a threshold temperature of about 165°C (*26*), close to the melting temperature of the bulk polymer (values ranging from 130° to 160°C). This expansion occurs on a comparatively short time scale of about 43 ps (fig. S1). As the thermal expansion itself should be more rapid given the PMMA sound velocity and the estimated domain sizes, this time constant likely represents the actual energy transfer time across the graphene/polymer interface. Assuming a monolayer polymer film (about 5 Å thickness), this time constant implies thermal Kapitza resistances around 8×10^{-8} m^{2}K/W, which is well in the range of literature values for a polymer/carbon nanotube interface (*26*).

Above the fluence threshold for superstructure melting, qualitatively different structural features are observed, including (i) a loss of polymer-substrate registration, (ii) the appearance of an amorphous phase with enhanced low spatial frequency components, and (iii) an accelerated expansion of remaining crystallites. Notably, these processes occur on time scales longer than the mere layer heating and reflect the intrinsic polymer reorganization (see Table 1): (i) Crossing the threshold, increased thermal fluctuations release a growing fraction of mobile polymer chain segments out of substrate registration, in particular at domain boundaries and chain folds. Considering the diffraction peak decrease, this process occurs on a 100-ps time scale. (ii) Subsequently, mobile segments form expanded amorphous structures, which are no longer angle-correlated to the graphene substrate, and contribute to the appearance of the inner diffraction disc. Depending on their spatial frequencies, these rearrangements proceed over durations beyond 300 ps for the range of scattering momenta imaged here (Fig. 4A, inset). The peaked feature in the radial diffraction intensity of the amorphous phase implies a preferred spatial correlation period of 5.7 Å, which is substantially expanded by 25% with respect to the crystalline phase. (iii) The continuous expansion of the crystalline phase above the threshold excludes an interpretation of the melting process based on a gradual exchange between two coexisting thermodynamic phases at a pinned temperature.

The sequential relaxation processes observed here are a direct result of the hierarchy of coupling strengths, from the relatively weak interchain interaction over the substrate surface registration to the structural constraint given by the polymer backbone. Presently, it remains an open question whether the enhanced expansion of remaining crystallites above threshold is caused by a loss of crystallinity—e.g., by domain shrinkage—or if itself serves as a major driver of the melting process. The observed time scales are relatively short in comparison with very recently reported intrinsic fluctuations within polymer-graphene heterostructures at similar temperatures (*31*). This suggests that the loss of superstructure registration involves a release of considerable stress present in the ordered phase. We expect that a Frenkel-Kontorova–type model and dynamical excitations therein may lead to a detailed microscopic picture (*30*), provided that the dimensionality of the system and the internal polymer degrees of freedom are considered.

The compact experimental implementation of time-resolved LEED is adaptable to conventional ultrafast optics setups and ultrahigh vacuum apparatuses, rendering its application feasible in the broader surface science community. The present operation conditions (energies at the upper end of the LEED range and transmission geometry) were chosen for an optimal combination of low pulse duration and high scattering efficiency providing monolayer sensitivity. Time-resolved LEED measurements in back-reflection from surfaces, including reconstructions and adsorbate layers, will require lower energies than employed here. To demonstrate the suitability of our approach for more general ultrafast surface studies, we provide back-scattering diffraction images and a pulse characterization at lower energy in the supplementary materials (figs. S8 and S5, respectively). We anticipate that further developments toward miniaturized electron guns will in the future allow for femtosecond LEED studies of bulk surfaces at energies of 100 eV and below, opening up the exploration of a whole arena of unconventional phases and transitions in solid-state and molecular surface science.

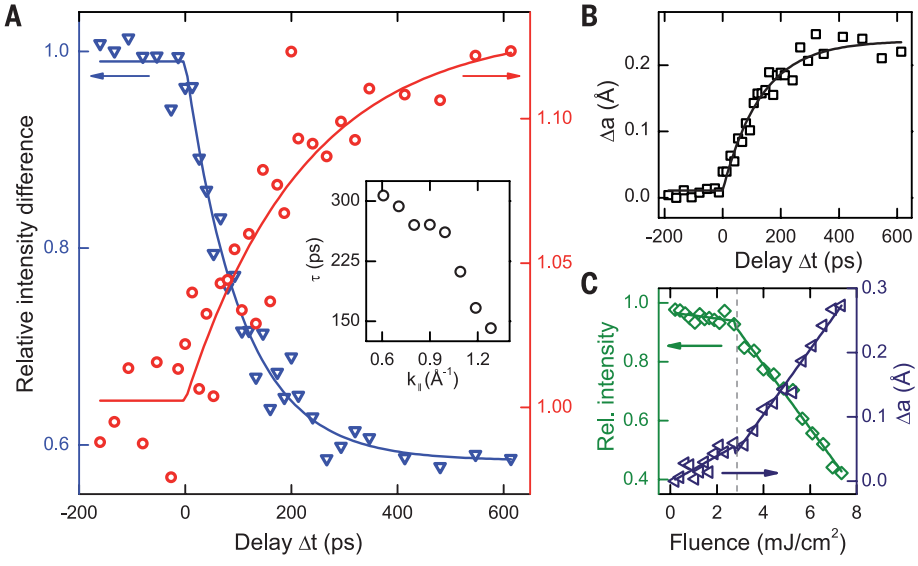

Fig. 4. Structural dynamics: Time constants and fluence threshold. (**A**) Delay-dependent superstructure diffraction spot (blue triangles) and disc (red circles) intensities, normalized to negative delay. Solid lines are exponential fits to experimental data. (Inset) Momentum-dependent time constants of small-angle scattering increase. (**B**) Expansion of crystalline PMMA component. Pump fluence for A and B: 6 mJ/cm^2. (**C**) Fluence-dependent superstructure diffraction intensity (green squares) and expansion (blue triangles), evaluated at Δt = 600 ps. Solid lines, guides to the eye. Dashed line, threshold fluence.

Table 1. Experimentally observed time scales in the PMMA/graphene bilayer system.

Dynamical process	Characteristic time (ps)
Bilayer temperature equilibration	43 (10)
Loss of PMMA crystallinity	105 (8)
Increase of PMMA chain spacing	133 (12)
Structural relaxation of amorphous phase	140–300

REFERENCES AND NOTES

1. S. L. Johnson, E. Vorobeva, P. Beaud, C. J. Milne, G. Ingold, *Phys. Rev. Lett.* **103**, 205501 (2009).
2. V. Juvé *et al.*, *Phys. Rev. Lett.* **111**, 217401 (2013).
3. D. M. Fritz *et al.*, *Science* **315**, 633–636 (2007).
4. B. J. Siwick, J. R. Dwyer, R. E. Jordan, R. J. D. Miller, *Science* **302**, 1382–1385 (2003).
5. P. Baum, D.-S. Yang, A. H. Zewail, *Science* **318**, 788–792 (2007).
6. M. Eichberger *et al.*, *Nature* **468**, 799–802 (2010).
7. A. H. Zewail, *Science* **328**, 187–193 (2010).
8. T. LaGrange *et al.*, *Ultramicroscopy* **108**, 1441–1449 (2008).
9. O. F. Mohammed, D.-S. Yang, S. K. Pal, A. H. Zewail, *J. Am. Chem. Soc.* **133**, 7708–7711 (2011).
10. M. Chergui, *Acta Crystallogr. A* **66**, 229–239 (2010).
11. F. Carbone, O.-H. Kwon, A. H. Zewail, *Science* **325**, 181–184 (2009).
12. J. M. Kosterlitz, D. J. Thouless, *J. Phys. Chem.* **6**, 1181–1203 (1973).
13. P. M. Chaikin, T. C. Lubensky, *Principles of Condensed Matter Physics* (Cambridge University Press, Cambridge, 2000).
14. A. Hanisch-Blicharski *et al.*, *Ultramicroscopy* **127**, 2–8 (2013).
15. M. A. Van Hove, W. H. Weinberg, C.-M. Chan, *Low-Energy Electron Diffraction* (Springer, Berlin Heidelberg, 1986).
16. S. Schäfer, W. Liang, A. H. Zewail, *J. Chem. Phys.* **135**, 214201 (2011).
17. R. S. Becker, G. S. Higashi, J. A. Golovchenko, *Phys. Rev. Lett.* **52**, 307–310 (1984).
18. C. Cirelli *et al.*, *Europhys. Lett.* **85**, 17010 (2009).
19. R. Karrer, H. J. Neff, M. Hengsberger, T. Greber, J. Osterwalder, *Rev. Sci. Instrum.* **72**, 4404 (2001).
20. M. Krüger, M. Schenk, P. Hommelhoff, *Nature* **475**, 78–81 (2011).
21. G. Herink, D. R. Solli, M. Gulde, C. Ropers, *Nature* **483**, 190–193 (2012).
22. A. Paarmann *et al.*, *J. Appl. Phys.* **112**, 113109 (2012).
23. E. Quinonez, J. Handali, B. Barwick, *Rev. Sci. Instrum.* **84**, 103710 (2013).
24. J. C. H. Spence, T. Vecchione, U. Weierstall, *Philos. Mag.* **90**, 4691–4702 (2010).
25. H. Park, J. M. Zuo, *Appl. Phys. Lett.* **94**, 251103 (2009).
26. Materials and methods are available as supplementary materials on *Science* Online.
27. R. K. Raman, Z. Tao, T.-R. Han, C.-Y. Ruan, *Appl. Phys. Lett.* **95**, 181108 (2009).
28. M. Tress *et al.*, *Science* **341**, 1371–1374 (2013).
29. J. A. Forrest, K. Dalnoki-Veress, *Adv. Colloid Interfac.* **94**, 167–195 (2001).
30. O. M. Braun, Y. S. Kivshar, *The Frenkel-Kontorova Model: Concepts, Methods, and Applications* (Springer, Berlin, Heidelberg, 2004).
31. A. N. Rissanou, V. Harmandaris, *J. Nanopart. Res.* **15**, 1589 (2013).
32. Y.-C. Lin *et al.*, *Nano Lett.* **12**, 414–419 (2012).
33. A. K. Geim, I. V. Grigorieva, *Nature* **499**, 419–425 (2013).
34. J. Kumaki, T. Kawauchi, E. Yashima, *J. Am. Chem. Soc.* **127**, 5788–5789 (2005).
35. J. S. Ha *et al.*, *J. Vac. Sci. Technol. B* **12**, 1977–1980 (1994).
36. Whereas the (10) diffraction spot of PMMA overlaps with that of graphene, the (3/2 0) PMMA spot is not observed, which is most likely a result of the chain form factor or disorder.

ACKNOWLEDGMENTS

We thank M. Müller for helpful discussions on polymer dynamics. Supporting sample characterizations by H. Schuhmann, M. Seibt, S. Strauch, H. Stark (TEM imaging), S. Dechert, and M. Sivis (Raman spectroscopy), as well as James E. Evans and Nigel D. Browning (high-resolution TEM, Pacific Northwest National Laboratory), are gratefully acknowledged. This work was partially funded by the Deutsche Forschungsgemeinschaft (DFG-ZuK 45/1 and DFG-SFB 1073). M.G. was financially supported by the German National Academic Foundation. A.M.W. and H.K.Y. gratefully acknowledge support from the Alexander von Humboldt Foundation.

SUPPLEMENTARY MATERIALS

www.sciencemag.org/content/345/6193/200/suppl/DC1
Materials and Methods
Figs. S1 to S8
References (*37*–*48*)

9 January 2014; accepted 22 May 2014
10.1126/science.1250658

EARTHQUAKE DYNAMICS

Supershear rupture in a M_w 6.7 aftershock of the 2013 Sea of Okhotsk earthquake

Zhongwen Zhan,[1,2]* Donald V. Helmberger,[2] Hiroo Kanamori,[2] Peter M. Shearer[1]

Earthquake rupture speeds exceeding the shear-wave velocity have been reported for several shallow strike-slip events. Whether supershear rupture also can occur in deep earthquakes is unclear, because of their enigmatic faulting mechanism. Using empirical Green's functions in both regional and teleseismic waveforms, we observed supershear rupture during the 2013 moment magnitude (M_w) 6.7 deep earthquake beneath the Sea of Okhotsk, an aftershock of the large deep earthquake (M_w 8.3). The M_w 6.7 event ruptured downward along a steeply dipping fault plane at an average speed of 8 kilometers per second, suggesting efficient seismic energy generation. Comparing it to the highly dissipative 1994 M_w 8.3 Bolivia earthquake, the two events represent end members of deep earthquakes in terms of energy partitioning and imply that there is more than one rupture mechanism for deep earthquakes.

Most earthquakes rupture at speeds less than the shear-wave speed (V_S). Theory and laboratory experiments indicate that rupture speeds in excess of V_S are possible (*1*–*3*), and supershear ruptures have now occasionally been reported for large strike-slip events (mode II), including the 1979 Imperial Valley (*4*), 1999 Izmit (*5*), 2001 Kunlun (*6*–*8*), 2002 Denali (*7*, *9*), 2010 Yushu (*10*), and 2013 Craig (*11*) earthquakes. All of these documented occurrences were shallow earthquakes with a simple fault geometry (*12*), and mostly with surface breaks, which is consistent with theoretical studies that the free surface helps promote supershear rupture (*13*, *14*).

No definitive evidence has yet been obtained for supershear rupture in deep earthquakes (depth > 300 km) (*15*). However, the rupture speeds of these events are difficult to estimate because of a general absence of near-field observations, and they appear highly variable. For example, the rupture speeds of the two largest deep earthquakes observed to date, the 1994 moment magnitude (M_w) 8.3 Bolivia earthquake and the 2013 M_w 8.3 Sea of Okhotsk earthquake (*16*–*18*), were about 0.2 to 0.4 and 0.7 V_S, respectively. About 80% of the rupture velocities for deep earthquakes fall between 0.3 and 0.9 V_S (*19*), a greater range than is seen for shallow earthquakes (*15*). The rupture speed may depend on the slab thermal state (*20*, *21*), with ruptures propagating more slowly in warm slabs than in cold slabs, but seismic observations have been inconclusive (*22*, *23*). The one previous example of observed supershear rupture during the 1990 M_w 7.1 Sakhalin deep earthquake neglected to take into account waveform changes from attenuation and the high-velocity subducted slab (*24*, *25*).

The 24 May 2013 M_w 8.3 Sea of Okhotsk event (depth, 607 km) was the largest deep earthquake ever recorded (Fig. 1), slightly larger than the 1994 Bolivia earthquake. On the same day, an M_w 6.7 earthquake at a depth of 642 km occurred about 300 km southwest of the mainshock and was recorded by many teleseismic stations and one regional station (Fig. 1). An extraordinary feature of the M_w 6.7 event was its sharp teleseismic *P* waves, which had displacement pulse widths at most azimuths of 1 to 2 s (Fig. 1). These are much less than the expected source duration of 8 s, based on its magnitude and previous studies of scaled durations of deep earthquakes (*26*, *27*). If taken as a rough estimate of the M_w 6.7 earthquake's source duration, these very short teleseismic *P*-wave durations imply extremely high stress drops in a range from 157 MPa to 5.856 GPa (*17*). On the other hand, the regional station PET (distance ≈ 495 km) on the Kamchatka Peninsula to the east displayed a much longer direct *P* wavetrain of about 5 s (Fig. 1). Because the *P* wave to the PET station left the source along an upgoing ray path, instead of the downgoing rays for the teleseismic stations, this longer *P*-wave duration at PET suggests possible downward rupture directivity during the M_w 6.7 earthquake. However, to test this possibility we first need to account for possible path effects such as wave diffractions along the high-velocity slab in which the earthquake occurred and site effects at the stations.

We used waveforms from two nearby smaller earthquakes (Fig. 1; the 24 June 2013 M_w 4.3

[1]Institute of Geophysics and Planetary Physics, Scripps Institution of Oceanography, University of California, San Diego, La Jolla, CA 92093–0225, USA. [2]Seismological Laboratory, California Institute of Technology, 1200 East California Boulevard, Pasadena, CA 91125, USA.
*Corresponding author. E-mail: zwzhan@ucsd.edu, zwzhan@gmail.com

event and the 30 August 1996 M_w 5.5 event) as empirical Green's functions (EGFs) to calibrate the paths. The M_w 4.3 earthquake's small moment, similar depth, and probably similar focal mechanism as the M_w 6.7 earthquake (fig. S1) make it an ideal EGF event. Its direct *P* wave recorded at the PET station displays two distinct arrivals separated by about 2 s (Fig. 2), due to diffraction along the dipping high-velocity slab in the upper mantle (*25*). Therefore, the apparent 5-s *P* duration of the M_w 6.7 earthquake at the PET station was partly caused by the structural path effect. We deconvolved the EGF waveform from the M_w 6.7 earthquake *P* wave to remove the path effect and obtained a more accurate source-time function (STF) (*28*). Most of the energy then concentrated in the first ~2 s, which we measured as the STF duration at the PET station (Fig. 2; red shading in top STF).

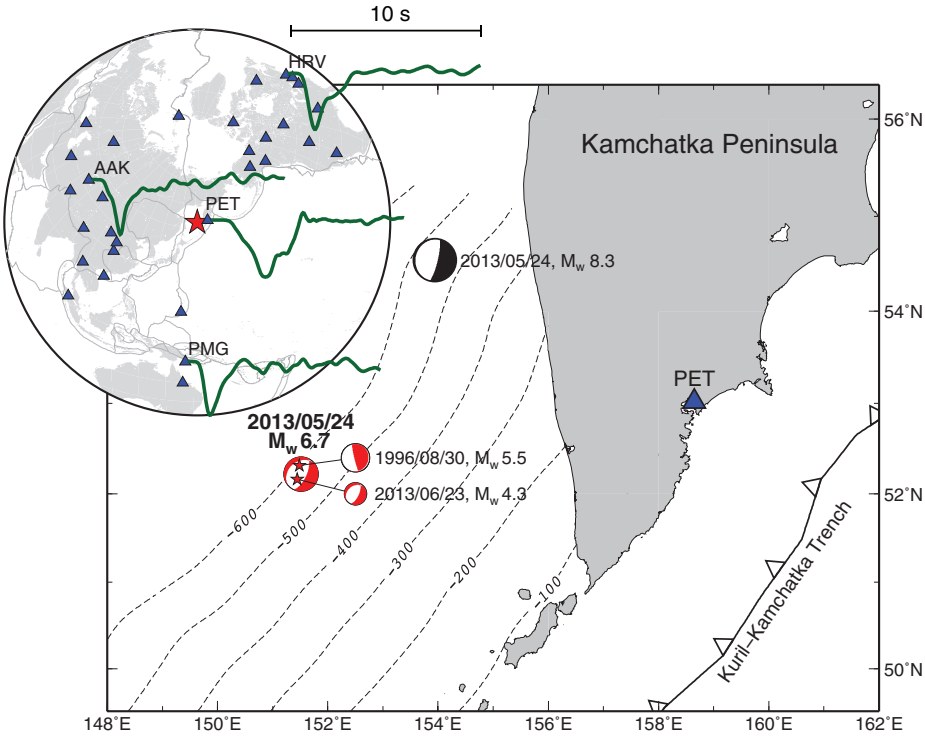

Fig. 1. Earthquake and station locations. The 2013 Okhostk M_w 8.3 mainshock and M_w 6.7 aftershock are displayed as the black and red beachballs, respectively. The two red stars connected with two smaller beachballs represent the EGF events used in this study. Slab contours from the Slab 1.0 model (*31*) are shown as dashed lines. The inset shows teleseismic and regional stations with four representative *P* vertical displacement seismograms (green lines).

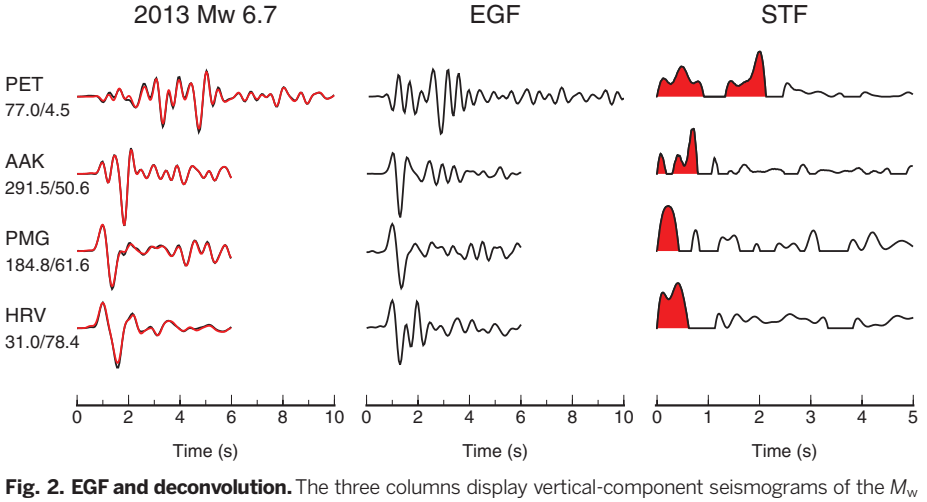

Fig. 2. EGF and deconvolution. The three columns display vertical-component seismograms of the M_w 6.7 earthquake, EGFs, and the deconvolved STFs. To ensure high signal-to-noise ratio and enhance high-frequency energy, we used acceleration seismograms filtered between 0.5 and 1 Hz. Seismograms of the M_w 6.7 event and EGFs are flipped to have the same polarity before deconvolution. The black and red traces in the first column are the data and predictions, respectively. The two numbers beneath station names are distances and azimuths in degrees. In the third column, we show the STF durations defined by the red shading, which includes most of the energy.

Because teleseismic records of the M_w 4.3 event are noisy, we used the 1996 M_w 5.5 event at somewhat shallower depth (~590 km) with a slightly rotated focal mechanism (Fig. 1) as the teleseismic EGF event. Because we only used teleseismic direct *P* waveforms (no absolute amplitude), these small differences in depth and radiation pattern did not significantly affect the accuracy of the EGFs. The M_w 4.3 and 5.5 EGF events had highly similar waveforms at the regional station PET and several quiet teleseismic stations (fig. S2), despite their difference in moment. This suggests that both EGF events can be regarded as delta-function–like point sources and their waveforms are mostly controlled by path effects. We chose teleseismic stations with clean direct *P* waves from both the M_w 6.7 and the M_w 5.5 earthquakes (Fig. 1 inset) and then deconvolved to estimate STFs and their durations (Fig. 2 and fig. S3). The resulting teleseismic STF durations range from ~0.5 to ~1 s. For both regional and teleseismic stations, relatively simple and compact STFs convolved with the EGFs produce good fits to the direct *P* and *P*-coda waveforms of the M_w 6.7 earthquake, which suggests effective correction of the path effects. We also attempted to include two more stations, MA2 and YSS, at distances of about 818 and 858 km, respectively (fig. S4). Direct *P* waves from these stations left the source along approximately horizontal ray paths. However, because of waveform complexities caused by triplications due to the 660-km discontinuity (figs. S4 to S6), we were unable to find an appropriate EGF event to correct for these structural effects.

After removing the path effects with EGFs, we inverted the resulting STF durations for earthquake rupture parameters. The path-corrected STF duration of the PET station (~2.1 s) is still more than two times longer than those of the teleseismic stations (0.5 to ~1 s), suggesting downward rupture directivity. For three-dimensional unilateral rupture (fig. S7), the STF duration of the *i*-th station T_i can be written as a function of rupture duration τ, horizontal rupture azimuth θ_r, and horizontal and vertical dimensions L and H, as $T_i = \tau + x_i(\theta_r)L + \eta_i H$, where $x_i(\theta_r)L$ and $\eta_i H$ are the corrections for azimuthal and vertical directivity, respectively. Note that $x_i(\theta_r) = -\frac{\cos(\theta_i - \theta_r)}{c_p^i}$ is the horizontal directivity parameter for the *i*-th station with azimuth θ_i and *P*-wave phase velocity $c_p^i = \frac{\alpha}{\sin\varphi_i}$ (*18, 29*). Here φ_i is the takeoff angle for the *i*-th station, and α is the *P*-wave speed. Therefore, the azimuthal variations in STF durations resolve the rupture direction θ_r and horizontal extent L. In the final term, $\eta_i = -\frac{\alpha}{\cos\varphi_i}$ is the vertical slowness, negative for teleseismic stations (with down-going rays) and positive for regional stations (with up-going rays). This sign

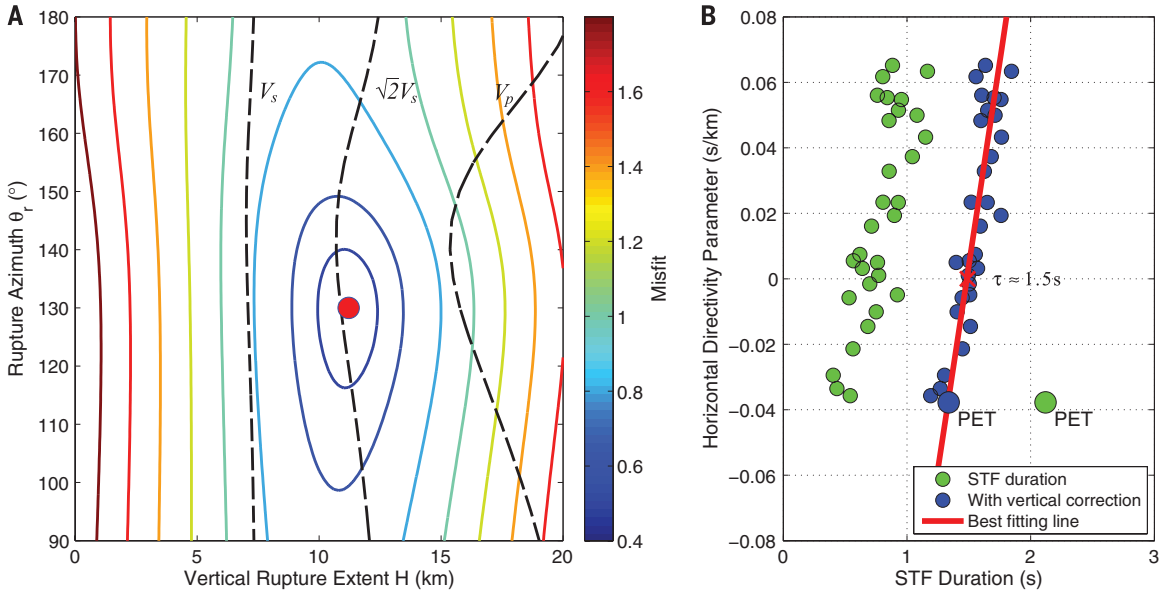

Fig. 3. Inversion for earthquake rupture parameters. (**A**) Misfit as a function of the grid-searched vertical rupture extent H and rupture azimuth θ_r. The red dot at (11 km, 130°) marks the optimal solution without a substantial tradeoff. The dashed contours show the rupture speeds for all grid-searched solutions at reference speeds of V_S, $\sqrt{2}\,V_S$, and V_P. (**B**) STF durations with and without vertical directivity corrections, assuming the optimal values from (A). The corrected STF durations (blue dots) fall near a straight line with a slope of L = 4 km, and zero-crossing duration of τ = 1.5 s (red cross). The green dots show the STF durations without the vertical directivity corrections, in which the PET station has a longer STF duration than all the teleseismic stations.

difference in η_i accounts for the major observed difference between teleseismic and regional STF durations.

We used a grid-search method to invert for the rupture parameters (τ, θ_r, L, and H). The least-squares misfit of the STF durations, as a function of rupture vertical extent H and rupture azimuth θ_r, has a well-defined global minimum at H = 11 km and θ_r = 130° (Fig. 3A). With these optimal values, the STF durations corrected for the downward vertical directivity (Fig. 3B) fall near a straight line with a slope of L = 4 km and zero-crossing duration of τ = 1.5 s. With L = 4 km and H = 11 km, we estimated the rupture dip to be ~70°, coincident with the steeper fault plane's dip of ~69° (*17*). Because the rupture direction θ_r = 130° is roughly perpendicular to the fault strike (~26°), we conclude that the M_w 6.7 earthquake features a downward mode II rupture on the fault plane dipping steeply to the southeast (Fig. 4A). The rupture propagated $\sqrt{L^2+H^2}$ or ~12 km in τ = 1.5 s, from which we estimate an average rupture speed of about 8 km/s. This speed is about $\sqrt{2}\,V_S$, which is substantially higher than the local shear wave speed (V_S ~5.5 km/s, based on the Preliminary Reference Earth Model). Contouring the average rupture speeds for all grid-searched rupture parameters (Fig. 3A) shows that within the region with reasonable misfit (inside the dark blue contours), the rupture speed is always higher than V_S and lower than V_P. Within 95% confidence limits, the average rupture speed is 8.0 ± 0.7 km/s. Anomalously broad teleseismic depth phases (*pP*) also are roughly consistent with the downward supershear rupture model (figs. S8 and S9). However, *pP* pulse widths exhibit much larger scatter than *P* pulse widths, and their behavior appears to be heavily influenced by complicated path effects, thus we cannot invert the *pP* waveforms for rupture parameters with any confidence.

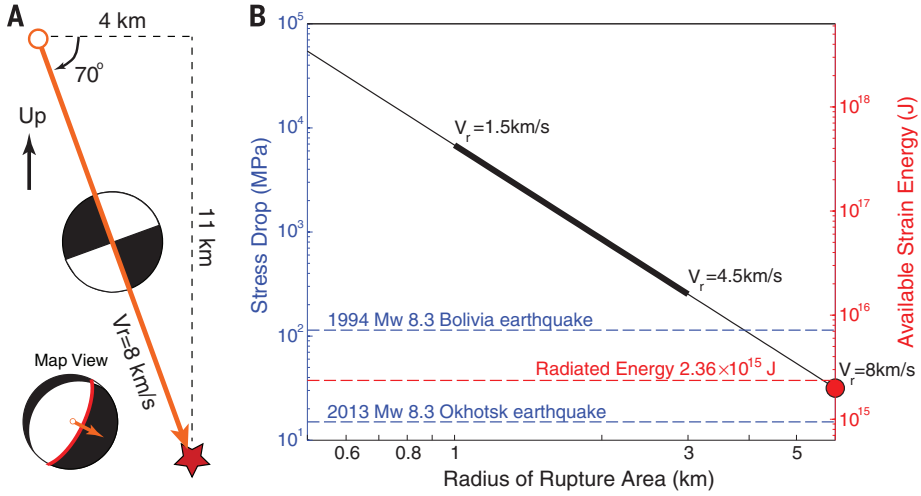

Fig. 4. Earthquake stress drop and energy partitioning. (**A**) Rupture geometry of the M_w 6.7 earthquake. In the focal mechanism in map view, the thick red line marks the steep fault plane on which the rupture is inferred to occur. The orange arrow shows the estimated rupture direction, almost perpendicular to the fault strike. In the side view along the fault strike from the southwest, the earthquake ruptured along the steeper fault plane downward at a speed of 8 km/s. The horizontal and vertical rupture extents are 4 and 11 km, respectively. (**B**) Stress drop and available strain energy as a function of rupture area radius. Assuming a rupture speed from 1.5 to 4.5 km/s, Ye *et al*. (*17*) obtained rupture radii of 1 to 3 km (thick black line), which correspond to stress drops higher than those of the 2013 Okhostk M_w 8.3 mainshock and the 1994 Bolivia earthquake (dashed blue lines as references, left vertical axis). The resulting available strain energy is also significantly higher than the radiated energy (dashed red line, right vertical axis) (*17*), which suggests low radiation efficiency. Our preferred result with a supershear rupture speed of 8 km/s is marked as the red dot, assuming a circular crack. The stress drop is about 32 MPa, and the available strain energy is close to the radiated energy, suggesting a radiation efficiency of near unity.

Previously identified extremely high-stress drops (157 MPa to 5.856 GPa) of the M_w 6.7 earthquake and subsequently low radiation efficiency ($0.005 < \eta_R < 0.15$) (*16*, *17*) depict this event as mechanistically distinct from the Okhotsk M_w 8.3 mainshock ($\Delta\sigma \approx 15$ MPa, $\eta_R \approx 0.6$) and more similar to the 1994 M_w 8.3 Bolivia earthquake ($\Delta\sigma \approx 114$ MPa, $\eta_R \leq 0.036$) in a warmer

slab (Fig. 4B). This complexity suggests strong stress heterogeneity in subducted slabs (*17*). However, supershear rupture during the M_w 6.7 earthquake brings its stress drop down to 32 MPa and its radiation efficiency to about 1.0 (Fig. 4B), which are much closer to values for the M_w 8.3 Okhotsk mainshock. Therefore, strong stress heterogeneity inside subducted slabs is not required to explain the 2013 Okhotsk mainshock and its M_w 6.7 aftershock. However, the difference in rupture speed (subshear versus supershear) indicates substantial spatial heterogeneity in the fracture strength or fracture energy within the slab.

Compared with shallow supershear events, this deep event has a relatively small rupture dimension and higher static stress drop (by a factor of ~10). Our estimate of high radiation efficiency ($\eta_R \approx 1.0$) during the M_w 6.7 event is also consistent with theoretical predictions of low fracture energy during supershear ruptures (*30*). This constraint of low fracture energy bears on the question of deep earthquake faulting mechanisms, which is still enigmatic (*15*, *19*). The 1994 Bolivia earthquake involved a large amount of fracture/thermal energy and radiated relatively little energy in seismic waves (*16*). In terms of energy partitioning, the supershear M_w 6.7 earthquake represents the opposite end member from the Bolivia earthquake, with almost all the available strain energy being radiated as seismic waves. This contrast is consistent with the idea of more than one rupture mechanism for deep earthquakes in slabs with different thermal states (*18*, *20*, *21*). The Okhotsk mainshock and aftershock in a cold slab ruptured with the transformational faulting mechanism, whereas the Bolivia earthquake in a warm slab was dominated by shear melting (*18*).

REFERENCES AND NOTES

1. R. Burridge, *Geophys. J. R. Astron. Soc.* **35**, 439–455 (1973).
2. D. Andrews, *J. Geophys. Res.* **81**, 5679–5687 (1976).
3. K. Xia, A. J. Rosakis, H. Kanamori, *Science* **303**, 1859–1861 (2004).
4. R. J. Archuleta, *J. Geophys. Res.* **89**, 4559–4585 (1984).
5. M. Bouchon *et al.*, *Geophys. Res. Lett.* **28**, 2723–2726 (2001).
6. M. Bouchon, M. Vallée, *Science* **301**, 824–826 (2003).
7. K. T. Walker, P. M. Shearer, *J. Geophys. Res.* **114** (B2), B02304 (2009).
8. M. Vallée, E. M. Dunham, *Geophys. Res. Lett.* **39**, L05311 (2012).
9. E. M. Dunham, R. J. Archuleta, *Bull. Seismol. Soc. Am.* **94**, S256–S268 (2004).
10. D. Wang, J. Mori, *Bull. Seismol. Soc. Am.* **102**, 301–308 (2012).
11. H. Yue *et al.*, *J. Geophys. Res.* **118**, 5903–5919 (2013).
12. M. Bouchon *et al.*, *Tectonophysics* **493**, 244–253 (2010).
13. H. Zhang, X. Chen, *Geophys. J. Int.* **167**, 917–932 (2006).
14. Y. Kaneko, N. Lapusta, *Tectonophysics* **493**, 272–284 (2010).
15. H. Houston, in *Treatise on Geophysics*, G. Schubert, Ed. (Elsevier, Amsterdam, 2007), pp. 321–350.
16. H. Kanamori, D. L. Anderson, T. H. Heaton, *Science* **279**, 839–842 (1998).
17. L. Ye, T. Lay, H. Kanamori, K. D. Koper, *Science* **341**, 1380–1384 (2013).
18. Z. Zhan, H. Kanamori, V. C. Tsai, D. V. Helmberger, S. Wei, *Earth Planet. Sci. Lett.* **385**, 89–96 (2014).
19. C. Frohlich, *Deep Earthquakes* (Cambridge Univ. Press, Cambridge, 2006).
20. D. A. Wiens, *Phys. Earth Planet. Inter.* **127**, 145–163 (2001).
21. R. Tibi, G. Bock, D. A. Wiens, *J. Geophys. Res.* **108**, 2091 (2003).
22. S.-C. Park, J. Mori, *J. Geophys. Res.* **113**, B08303 (2008).
23. M. Suzuki, Y. Yagi, *Geophys. Res. Lett.* **38**, L05308 (2011).
24. K. Kuge, *J. Geophys. Res.* **99** (B2), 2671–2685 (1994).
25. Z. Zhan, D. Helmberger, D. Li, *Phys. Earth Planet. Inter.* **232**, 30–35 (2014).
26. S. E. Persh, H. Houston, *J. Geophys. Res.* **109**, B04311 (2004).
27. A. Tocheport, L. Rivera, S. Chevrot, *J. Geophys. Res.* **112**, B07311 (2007).
28. Materials and methods are available in the supplementary materials.
29. C. J. Ammon *et al.*, *Science* **308**, 1133–1139 (2005).
30. R. Madariaga, K. B. Olsen, *Pure Appl. Geophys.* **157**, 1981–2001 (2000).
31. G. P. Hayes, D. J. Wald, R. L. Johnson, *J. Geophys. Res.* **117**, B01302 (2012).

ACKNOWLEDGMENTS

We thank two anonymous reviewers for their helpful comments. The Incorporated Research Institutions for Seismology (IRIS) provided the seismic data. This work was supported by NSF (grants EAR-1142020 and EAR-1111111). All data used are available from the IRIS data center at www.iris.edu.

SUPPLEMENTARY MATERIALS

www.sciencemag.org/content/345/6193/204/suppl/DC1
Materials and Methods
Figs. S1 to S9

27 February 2014; accepted 2 June 2014
10.1126/science.1252717

OCEAN MICROBES

Multispecies diel transcriptional oscillations in open ocean heterotrophic bacterial assemblages

Elizabeth A. Ottesen,[1,2,3] Curtis R. Young,[1,2] Scott M. Gifford,[1,2] John M. Eppley,[1,2] Roman Marin III,[4] Stephan C. Schuster,[5] Christopher A. Scholin,[4] Edward F. DeLong[1,2,6]*

Oscillating diurnal rhythms of gene transcription, metabolic activity, and behavior are found in all three domains of life. However, diel cycles in naturally occurring heterotrophic bacteria and archaea have rarely been observed. Here, we report time-resolved whole-genome transcriptome profiles of multiple, naturally occurring oceanic bacterial populations sampled in situ over 3 days. As anticipated, the cyanobacterial transcriptome exhibited pronounced diel periodicity. Unexpectedly, several different heterotrophic bacterioplankton groups also displayed diel cycling in many of their gene transcripts. Furthermore, diel oscillations in different heterotrophic bacterial groups suggested population-specific timing of peak transcript expression in a variety of metabolic gene suites. These staggered multispecies waves of diel gene transcription may influence both the tempo and the mode of matter and energy transformation in the sea.

The coordination of biological activities into daily periodic cycles is a common feature of eukaryotes and is widespread among plants, fungi, and animals, including man (*1*). Among single celled noneukaryotic microbes, diel cycles have been well documented in cyanobacterial isolates (*2*–*4*), one halophilic archaeon (*5*), and bacterial symbionts of fish and squid (*6*, *7*). Some evidence for diel cycling in microbial plankton has also been suggested on the basis of bulk community amino acid incorporation, viral production, or metabolite consumption (*8*–*10*). However, the existence of regular diel oscillations in free-living heterotrophic bacterial species has rarely been assessed.

Microbial community RNA sequencing techniques now allow simultaneous determination of whole-genome transcriptome profiles among multiple cooccurring species (*11*, *12*), enabling high-frequency, time-resolved analyses of microbial community dynamics (*12*, *13*). To better understand temporal transcriptional dynamics in oligotrophic bacterioplankton communities, we conducted a high-resolution multiday time series of bacterioplankton sampled from the North Pacific Subtropical Gyre (*14*).

To facilitate repeated sampling of the same planktonic microbial populations through time, automated Lagrangian sampling of bacterioplankton was performed every 2 hours over 3 days by using a free-drifting robotic Environmental Sample Processor (ESP) (*13*, *15*) (fig. S1). After instrument recovery, planktonic microbial RNA was extracted, purified, converted to cDNA, and sequenced to assess whole-genome transcriptome dynamics of predominant planktonic microbial populations (tables S1 and S2). The recovered cDNAs were dominated by transcripts from

[1]Department of Civil and Environmental Engineering, Massachusetts Institute of Technology, Cambridge, MA 02139, USA. [2]Center for Microbial Oceanography: Research and Education (C-MORE), University of Hawaii, Honolulu, HI 96822, USA. [3]Department of Microbiology, University of Georgia, Athens, GA 30602, USA. [4]Monterey Bay Aquarium Research Institute, Moss Landing, CA 95039, USA. [5]Singapore Centre on Environmental Life Sciences Engineering, Nanyang Technological University, 637551 Singapore. [6]Department of Biological Engineering, Massachusetts Institute of Technology, Cambridge, MA 02139, USA.
***Corresponding author. E-mail: edelong@hawaii.edu**

Prochlorococcus and several proteorhodopsin-containing or photoheterotrophic bacteria, including members of the *Pelagibacter* (SAR11), *Roseobacter*, SAR116, SAR86, and SAR324 clades (fig. S2).

Phylogenetic analysis of gene transcripts in the most abundant taxa revealed the presence of some microdiversity (figs. S3 to S8). However, the most abundant transcripts sampled at any given time point were dominated by only a few genotypes within each population that persisted throughout the sampling period. An exception was *Roseobacter*, with transcripts for two different genes (*groEL* and *dnaK*) indicating the presence of genotypes that started at a very low

Table 1. Harmonic regression results. Sequence reads are the total number assigned to each taxon bin. Transcripts are the total number of unique ortholog clusters (see table S1) with at least one mapped sequence. Periodic is the total number of sequences identified as showing 24-hour periodicity using harmonic regression. The next row shows the proportion of variance explained by 24-hour periodicity in constrained principal components analysis (PCA). The fifth row indicates the Procrustes correlation between the first two principal components from *Prochlorococcus* and other taxa (unconstrained principal components analysis as shown in Fig. 3); *P* values based on 999 permutations. Bottom row is the correlation between pairwise transcriptome similarities at each time point from *Prochlorococcus* and heterotrophic taxa based on Mantel test on Euclidean distance matrices; *P* value based on 999 permutations.

	Prochlorococcus	*Roseobacter* SAGs	SAR11	SAR116	SAR86	SAR324
Sequence reads	2,886,677	177,982	774,064	200,368	151,468	118,098
Transcripts	3045	2604	2802	2618	2367	4732
Periodic	1491	426	201	80	10	8
Constrained PCA versus 24-hour clock	0.68	0.49	0.24	0.15	0.13	0.10
	(P = 0.005)	(P = 0.005)	(P = 0.005)	(P = 0.005)	(P = 0.005)	(P = 0.01)
Procrustes test versus *Prochlorococcus* PCA		0.78	0.55	0.70	0.52	0.36
		(P < 0.001)	(P < 0.001)	(P < 0.001)	(P < 0.001)	(P = 0.031)
Mantel test versus *Prochlorococcus*		0.63	0.40	0.31	0.26	0.27
		(P < 0.001)	(P < 0.001)	(P = 0.003)	(P = 0.005)	(P = 0.002)

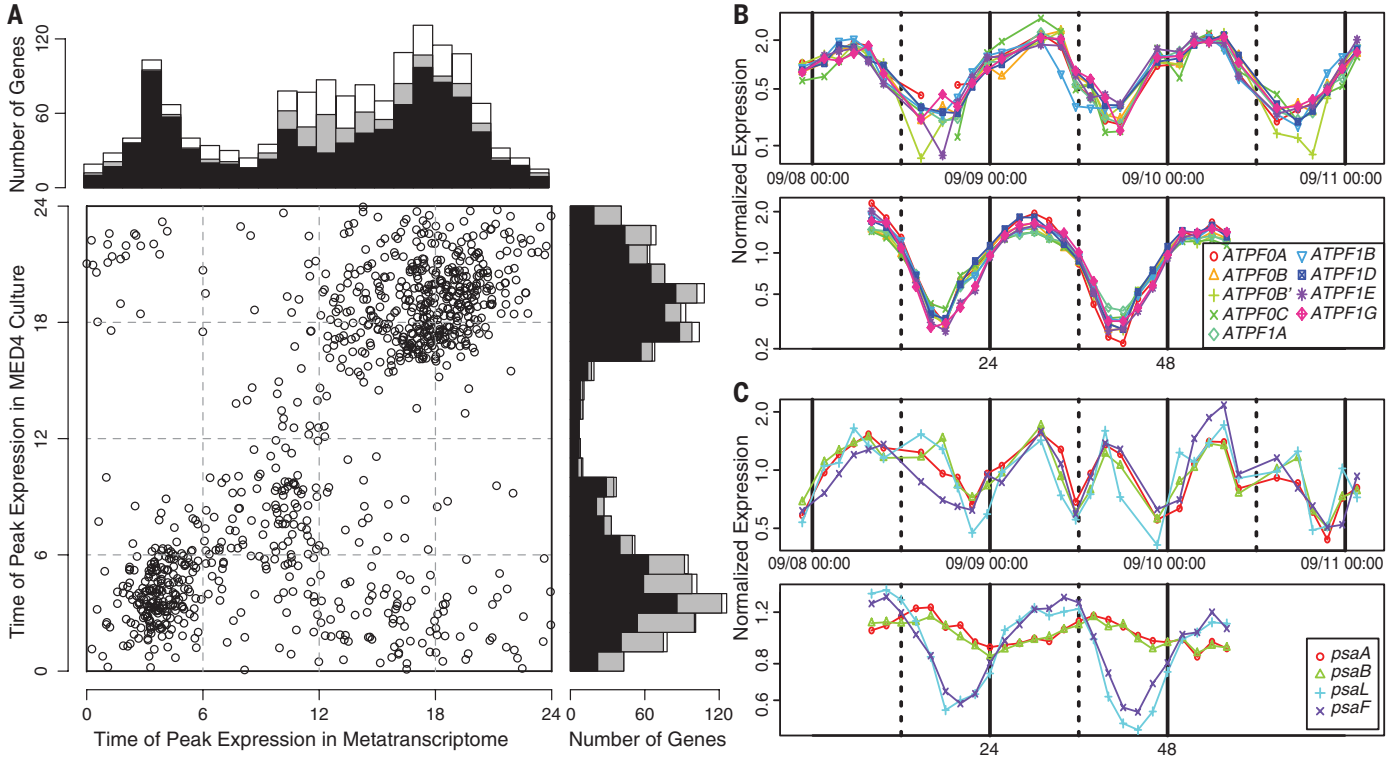

Fig. 1. Laboratory versus field comparisons of periodic expression patterns in *Prochlorococcus* populations. (**A**) Scatter plot shows time of peak abundance for 973 transcripts identified as significantly periodic in both studies. Histograms show the total number of genes peaking in 1-hour intervals in this study (top) and the laboratory experiment (side). Black bars represent genes identified as significantly periodic in both studies, gray bars represent genes expressed in both studies but significantly periodic in only one, and white bars represent significantly periodic transcripts that were not detected in the other data set. For this comparison, we used published significance cutoffs from the laboratory study (*4*) but for consistency generated new peak times by using our harmonic regression approach and the published normalized mean expression levels for each time point. In general, the peak times generated using our approach closely matched published values for that data set. (**B** and **C**) Plots showing relative expression (normalized to mean expression level) over time for our metatranscriptome (top trace) and in microarray data (bottom trace) for selected transcripts. For comparison, experimental midnights (24 and 48 hours) from the microarray study are aligned with the 12:00 midnight samples from 9 and 10 September, respectively. All adenosine triphosphate (ATP) synthase subunits (B) and selected subunits from photosystem I (C) are shown.

abundance and increased in representation over the course of the time series. This variability could be due to an injection of a new population as water masses mixed during the latter portion of the time series or to an alteration in the relative transcriptional activities of two ecotypes that are responding to changes in the surrounding environment.

Transcriptional activity in *Prochlorococcus* was highly dependent on the time of day. Harmonic regression analyses indicated that nearly half (1491) of all *Procholorococcus* population transcripts were significantly periodic (Table 1, table S3, and Fig. 1). The expression patterns observed were similar to those of monocultures growing in controlled laboratory settings (*4*), but there were also notable differences (Fig. 1). For example, photosystem I gene expression exhibited a double peak in the wild *Prochlorococcus* transcriptome around noon (Fig. 1). In contrast, under laboratory conditions most photosystem I genes, for example, *psaL* and *psaF*, were found to peak just before noon, and *psaA* and *psaB* peaked shortly after noon (*4*).

The largest discrepancy between *Prochlorococcus* laboratory studies and our field observations was that a considerable number of *Prochlorococcus* transcripts in our field populations peaked around midday (Fig. 1). Some of these genes did exhibit periodicity in cultures but peaked at a different time of day than in field populations. A larger fraction of the field midday-peaking transcripts were either not periodically expressed or were not present in the culture experiments. In addition, 62% of the 10 a.m.–to–4 p.m. peaking transcripts in our field study lacked Kyoto Encyclopedia of Genes and Genomes (KEGG) orthology annotations, as opposed to those peaking in the evening or late at night.

A number of factors may be responsible for differences in transcript dynamics between in laboratory cultures versus field *Prochlorococcus* populations. Maximal light levels at our study site at 23-m depth were frequently twofold higher (450 μmol Q m^{-2} s^{-1}) than those used in laboratory microarray experiments (232 μmol Q m^{-2} s^{-1}) (*4*). Fundamental genetic differences between our field populations and the *Prochlorococcus* strain used in laboratory culture experiments likely also contribute to the differences we observed. Other variables, including nutrient composition and organismal interactions, may also be factors in the observed differences. Although we could not identify obvious trends in the type or function of field population transcripts showing peak expression during the midday period, they did include a wide range of enzymatic functions that are more consistent with nutrient-responsive metabolic changes rather than a simple high-light stress response.

An abundant *Roseobacter* population also showed strong diel oscillations in its transcriptome profile, most notably in expressed genes involved in bacteriochlorophyll-associated aerobic anoxygenic photosynthesis. Overall, a large fraction of *Roseobacter* transcripts were periodically expressed (Table 1). Of these, the majority peaked during daylight hours, with only a few gene transcripts peaking at night (Fig. 2). Although this pattern contrasts with that observed in *Prochlorococcus*, where most diurnally regulated transcripts peaked at dawn or dusk, it was consistent with transcriptional regulation recently reported in *Dinoroseobacter shibae* (*16*).

Thirty-five of the 40 significantly periodic *Roseobacter* transcripts that peaked between 11 p.m. and 7 a.m. encoded genes belonging to a large photosynthetic "superoperon" (fig. S9). Nightly expression of these genes, followed by immediate repression upon light onset, is consistent with the *D. shibae* study (*16*) and may be preparing cells for efficient solar energy harvest in the early morning hours. Functions that peaked during the daytime hours included ribosomal proteins, respiratory transcripts, genes involved in amino acid metabolism, and transporters (Fig. 2).

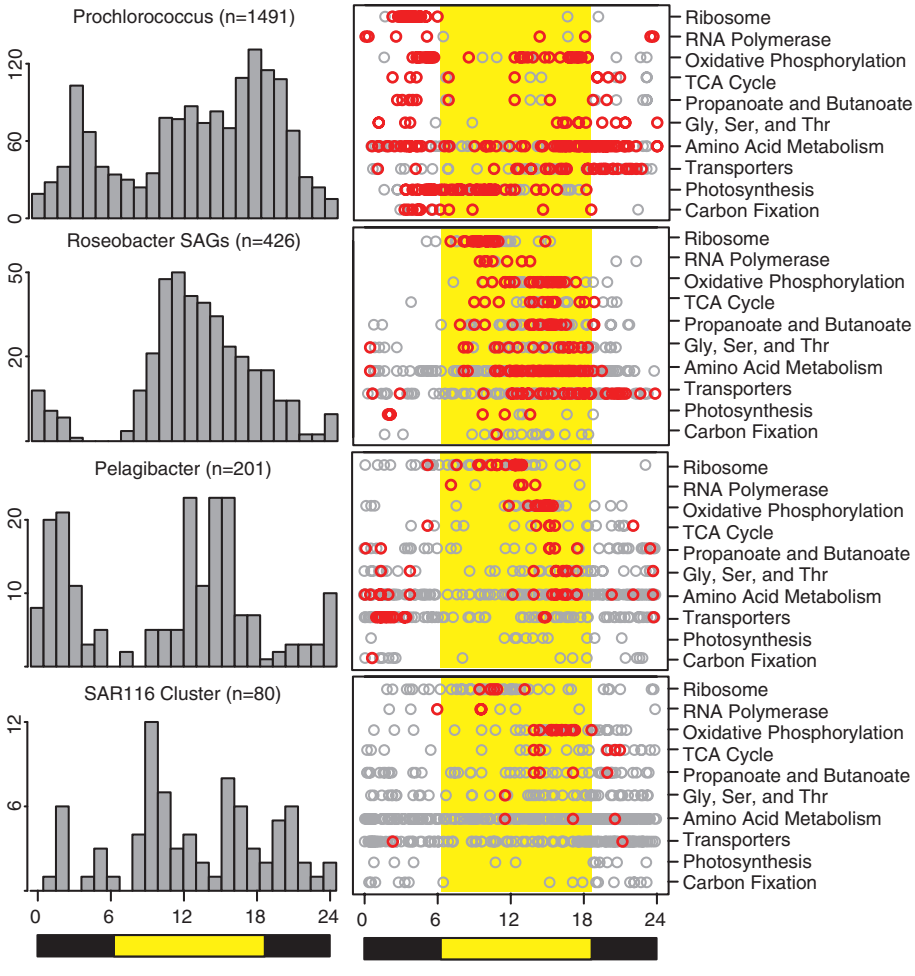

Fig. 2. Timing of periodically expressed transcripts. For each population, a histogram showing the number of periodically expressed diel transcripts with peak expression within 1-hour intervals throughout the day is shown (**left**). (**Right**) Time of peak expression of all transcripts assigned to selected KEGG pathways is plotted (gray circles). Red circles denote transcripts identified as significantly periodic (24-hour period). The transporters category includes both the ATP binding cassette transporters KEGG pathway and the transporters BRITE hierarchy; the photosynthesis category includes both the photosynthesis KEGG pathway and the BRITE photosynthesis proteins categorizations. Carbon fixation refers to genes assigned to the carbon fixation in photosynthetic organisms KEGG pathway. The photosynthesis and carbon fixation categories are present in heterotrophic organisms because of cross-assignment of ATP synthase genes and pentose phosphate cycle genes. Black and yellow bars depict the daily photoperiod (based on sunrise and sunset times). SAGs, single amplified genome-similar transcripts; TCA, tricarboxylic acid.

Proteorhodopsin-containing photoheterotrophs including Pelagibacter (SAR11), SAR116, and SAR86 also showed evidence of diel periodicity in many of their gene transcripts (Fig. 2 and Table 1). All opsin-containing bacteria analyzed (SAR11, SAR116, SAR86, and SAR324) exhibited statistically significant diel oscillations in their proteorhodopsin gene transcripts (table S3 and fig. S10). Peak expression of the opsin transcripts occurred near dawn in all these populations (fig. S10), potentially optimizing solar energy capture by the light-driven, proton-pumping rhodopsins.

Principal components analysis distinguished time series samples for each heterotroph by time of day (Fig. 3) and showed significant correlation with the light-driven behavior of *Prochlorococcus* (Table 1). Overall, these data are consistent with genome-wide transcriptional changes across the day-night cycle for each population. In addition, coclustering of transcripts using GeneARMA (GA) (*14*, *17*) revealed suites of gene transcripts that exhibited similar expression patterns among different taxa (Fig. 4, figs. S11 to S14, and table S4). For example, a group of transcripts that fit highly similar GA expression models across multiple species included Pro GA5, Pro GA7, Pro GA9, Pro GA23, SAR11 GA6, SAR11 GA18, SAR116 GA2, and *Roseobacter* GA8 (Fig. 4, fig. S14, and table S4). These multispecies, day-peaking transcripts (fig. S14 and table S4) included gene products associated with respiration (*Procholorococcus*, SAR11, SAR116, and *Roseobacter*), nitrogen metabolism (*Procholorococcus*, SAR11, and SAR116), glycine metabolism (*Procholorococcus*, SAR11, and *Roseobacter*), carbon monoxide metabolism (SAR116 and *Roseobacter*), and DNA synthesis (*Procholorococcus* and *Roseobacter*). The coclustering of gene transcripts revealed a complex pattern of expression through the day and across the time series and provides evidence for parallel trends in gene expression across multiple species (Fig. 4, fig. S11 to S14, and table S4).

Together, the transcriptional profiles of *Roseobacter*, SAR11, SAR116, and SAR86 indicate diel cycling of metabolic gene transcripts and suggest a multispecies wavelike progression of up-regulated gene suites across the day-night cycle (Fig. 4). Most conspicuously, a regular diel succession of translational, transcriptional, and respiratory gene transcripts was followed by peaks in transporter transcripts that possibly reflect a metabolic recovery phase (Fig. 2). Many of these metabolic pathway transcripts peaked earlier in the day in *Roseobacter* field populations relative to other bacterial heterotrophs (Figs. 2 and 4 and table S4).

The overall transcriptional profile of SAR324 did not show as many transcript diel oscillations as other heterotrophic taxa. Instead, principal components analysis clustered SAR324 transcripts according to the specific day that they were collected (Fig. 3). In particular, the SAR324 group showed a strong separation between the first portion of the time series and the second in principal components analysis (Fig. 3). This split appears to be associated with the increases in temperature and salinity observed across the time series (fig. S1).

The diurnal patterns reported here for open-ocean heterotrophic bacterioplankton were different from those observed in a previous study of phylogenetically related coastal bacterioplankton using similar methods (*12*). For example, coastal versus open-ocean SAR11 populations revealed differential expression levels among several orthologous transcript categories (fig. S15). Additionally, whereas the open-ocean SAR11 populations reported here exhibited statistically significant diel oscillations for many gene transcripts (Fig. 2), the coastal SAR11 populations did not.

Currently available data are insufficient to provide definitive mechanistic explanations for the diel behaviors we observed in different heterotrophic bacterioplankton species. It is possible that photoreceptors in these bacteria are involved in regulating light-dark cycles of transcriptional activity. Marine *Roseobacter* species have previously been shown to regulate their global transcriptional behavior in response to light (*16*), and laboratory cultures of *Pelagibacter* also exhibit light-responsive metabolic behaviors (*18*). However, differences between the behaviors of SAR11 coastal versus open ocean field populations (fig. S15), as well as comparisons of several taxa in our field study versus laboratory experiments on related cultivated isolates (Fig. 1), suggest that other factors may be at play in regulating diel behavior among these different bacterioplankton populations.

Previous studies have proposed that tight metabolic coupling between primary producers and consumers in microbial plankton might elicit conspicuous diel cycling in heterotrophic bacterial activities (*8*). The diel cycling we observed among different bacterioplankton species is consistent with this hypothesis, with multiple coexisting heterotroph populations exhibiting diurnal oscillations resembling those of their photoautotrophic neighbors. We postulate that the tightly coupled multispecies temporal expression patterns observed may elicit corresponding waves of species-specific metabolic responses at regular time intervals, potentially coordinating diverse biogeochemical activities in these complex microbial communities. Such temporal coordination of biogeochemical activities among multiple species may be important regulators of both the tempo and the mode of microbial matter and energy transformation in the sea.

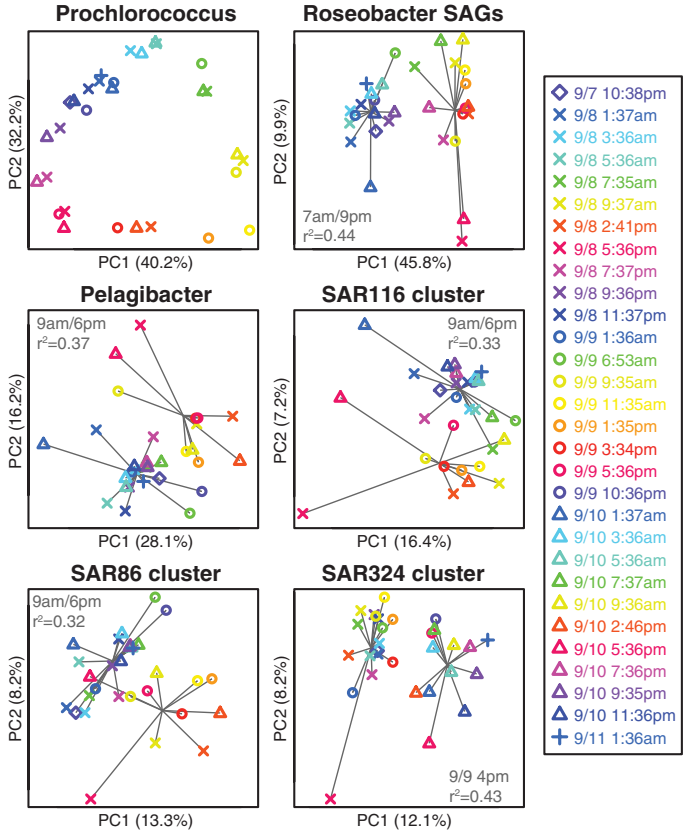

Fig. 3. Principal component (PC) analyses of population transcriptional profiles. Transcript abundances were normalized to total transcripts assigned to each population at each time point and arcsin-transformed to approximate normality (*19*). Symbol color denotes time of day, and shape denotes day of collection. Gray lines connect samples to centroids for selected sample groupings that separate points well. *Roseobacter* SAG represents samples that were collected between 7 a.m. and 9 p.m. (versus 9 p.m to 7 a.m.); Pelagibacter, SAR116, and SAR86 clusters represent samples that were collected between 9 a.m. and 6 p.m. (and vice versa); SAR324 cluster represents samples that were collected before or after 9 September 4 p.m. All factor correlations shown were highly significant (P = 0.001). Alternative time of day categories were also highly significant for *Roseobacter* SAGs, Pelagibacter, SAR116, and SAR86. SAR116 (r^2 = 0.10, P = 0.037) and SAR86 (r^2 = 0.12, P = 0.019) also correlated weakly with the grouping shown for SAR324. All analyses carried out by using functions in the vegan software package (*20*).

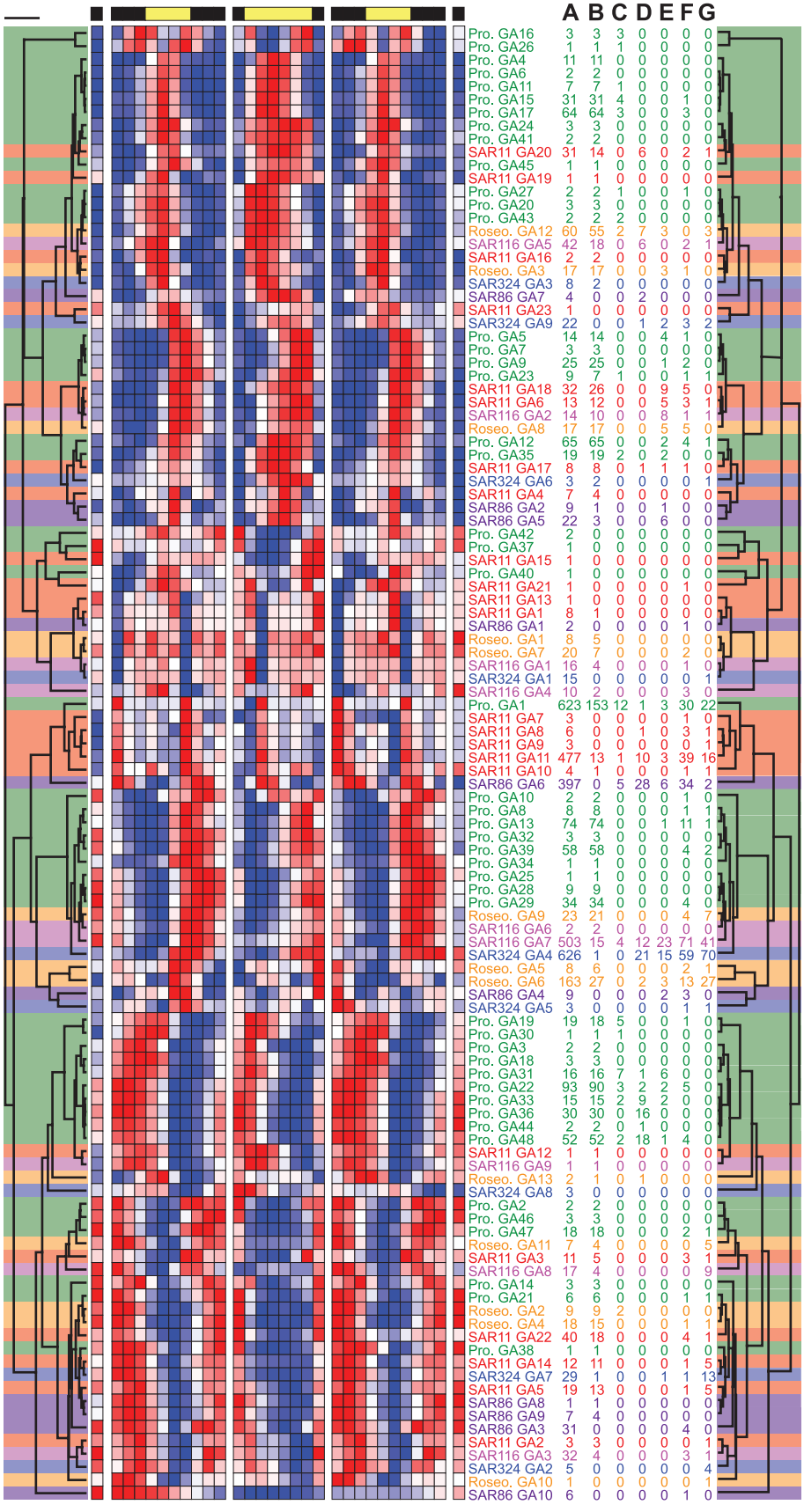

Fig. 4. Timing of expression of functional gene clusters among different taxa, clustered by the similarities of their temporal expression patterns. Heat map shows cluster models for all GA clusters, colored by mean-centered relative expression (red, high; blue, low). Black and yellow bars show the daily photoperiod. Each box represents a single sampling event; for sample times, see table S1. Dendrograms show cluster model similarity (Pearson correlations, average linkage clustering, scale bar at upper right represents a correlation of 0.5). The total number of genes (column A), significantly periodic genes (B), and genes associated with photosynthesis (C), ribosome (D), oxidative phosphorylation (E), amino acid metabolism (F), and transport (G) (defined as for Fig. 2), are listed for each cluster. See table S4 for the identities of genes found within any specific GeneARMA (GA) cluster.

REFERENCES AND NOTES

1. D. Bell-Pedersen *et al.*, *Nat. Rev. Genet.* **6**, 544–556 (2005).
2. I. M. Axmann, S. Hertel, A. Wiegard, A. K. Dörrich, A. Wilde, *Mar. Genomics*, (2014).
3. H. Ito *et al.*, *Proc. Natl. Acad. Sci. U.S.A.* **106**, 14168–14173 (2009).
4. E. R. Zinser *et al.*, *PLOS ONE* **4**, e5135 (2009).
5. K. Whitehead, M. Pan, K. Masumura, R. Bonneau, N. S. Baliga, *PLOS ONE* **4**, e5485 (2009).
6. J. F. Flint, D. Drzymalski, W. L. Montgomery, G. Southam, E. R. Angert, *J. Bacteriol.* **187**, 7460–7470 (2005).
7. A. M. Wier *et al.*, *Proc. Natl. Acad. Sci. U.S.A.* **107**, 2259–2264 (2010).
8. J. M. Gasol *et al.*, *Mar. Ecol. Prog. Ser.* **164**, 107–124 (1998).
9. C. Winter, G. J. Herndl, M. G. Weinbauer, *Aquat. Microb. Ecol.* **35**, 207–216 (2004).
10. M. Galí *et al.*, *Global Biogeochem. Cycles* **27**, 620–636 (2013).
11. S. M. Gifford, S. Sharma, M. Booth, M. A. Moran, *ISME J.* **7**, 281–298 (2013).
12. E. A. Ottesen *et al.*, *Proc. Natl. Acad. Sci. U.S.A.* **110**, E488–E497 (2013).
13. E. A. Ottesen *et al.*, *ISME J.* **5**, 1881–1895 (2011).
14. Materials and methods are available as supplementary materials on *Science* Online.
15. C. M. Preston *et al.*, *PLOS ONE* **6**, e22522 (2011).
16. J. Tomasch, R. Gohl, B. Bunk, M. S. Diez, I. Wagner-Döbler, *ISME J.* **5**, 1957–1968 (2011).
17. N. Li *et al.*, *PLOS ONE* **5**, e9894 (2010).
18. L. Steindler, M. S. Schwalbach, D. P. Smith, F. Chan, S. J. Giovannoni, *PLOS ONE* **6**, e19725 (2011).
19. Z. Liu, W. Hsiao, B. L. Cantarel, E. F. Drábek, C. Fraser-Liggett, *Bioinformatics* **27**, 3242–3249 (2011).
20. J. Okansen *et al.*, Package "vegan": Community ecology package (2012); http://cran.rproject.org/web/packages/vegan//vegan.pdf.

ACKNOWLEDGMENTS

We thank the officers and crew of the *Kilo Moana*, J. Robidart, S. Wilson, and the ESP engineering and science team (J. Ryan, J. Birch, C. Preston, G. Massion, S. Jensen, and B. Roman) for all of the able assistance. This work was supported by grants from the Gordon and Betty Moore Foundation GBMF nos. 492.01 and 3777 (E.F.D.) and NSF grant EF0424599 (E.F.D.). Development of the ESP was supported by NSF grant OCE-0314222 (to C.A.S.), NASA Astrobiology grants NNG06GB34G and NNX09AB78G (to C.A.S.), the Gordon and Betty Moore Foundation nos. 731 and 2728 (C.A.S.), and the David and Lucile Packard Foundation. This work is a contribution of C-MORE. Sequences reported in this paper have been deposited in the GenBank database (accession no. SRP041215). The Monterey Bay Aquarium Research Institute holds rights to C. A. Scholin *et al.*, U.S. Patent 6187530 (2001). C.A.S. is disqualified from receiving any royalties that might arise from licensing agreements. The ESP is available commercially from Spyglass Technologies and MacLane Research Laboratories; C.A.S. has no financial interest in either company and is not compensated in any way for giving advice on ESP technology transfer.

SUPPLEMENTARY MATERIALS

www.sciencemag.org/content/345/6193/207/suppl/DC1
Materials and Methods
Figs. S1 to S14
Tables S1 to S4
References (*21*–*35*)

20 February 2014; accepted 22 May 2014
10.1126/science.1252476

MICROECONOMICS

Harnessing naturally occurring data to measure the response of spending to income

Michael Gelman,[1] Shachar Kariv,[2] Matthew D. Shapiro,[1,3]* Dan Silverman,[3,4] Steven Tadelis[3,5]

This paper presents a new data infrastructure for measuring economic activity. The infrastructure records transactions and account balances, yielding measurements with scope and accuracy that have little precedent in economics. The data are drawn from a diverse population that overrepresents males and younger adults but contains large numbers of underrepresented groups. The data infrastructure permits evaluation of a benchmark theory in economics that predicts that individuals should use a combination of cash management, saving, and borrowing to make the timing of income irrelevant for the timing of spending. As in previous studies and in contrast to the predictions of the theory, there is a response of spending to the arrival of anticipated income. The data also show, however, that this apparent excess sensitivity of spending results largely from the coincident timing of regular income and regular spending. The remaining excess sensitivity is concentrated among individuals with less liquidity.

Economic researchers and policy-makers have long sought high-quality measures of individual income, spending, and assets from large and heterogeneous samples. For example, when policy-makers consider whether and how to stimulate the economy, they need to know how individuals will react to changes in their income. Will individuals spend differently? Will they save at a different rate or reduce their debt, and when? There are many obstacles to obtaining reliable answers to these important questions. One obstacle is that existing data sources on individual income and spending have substantial limits in terms of accuracy, scope, and frequency.

This paper advances the measurement of income and spending with new high-frequency data derived from the actual transactions and account balances of individuals. It uses these measures to evaluate the predictions of a benchmark economic theory that states that the timing of anticipated income should not matter for spending. Like previous research, it finds that there is a response of spending to the arrival of anticipated income. The data show that, on average, an individual's total spending rises substantially above average daily spending on the day that a paycheck or Social Security check arrives, and remains high for at least the next 4 days. The data also allow the construction of variables that show, however, that this apparent excess sensitivity of spending results in large part from the coincident timing of regular income and regular spending. The remaining excess sensitivity is concentrated among individuals who are likely to be liquidity-constrained.

Traditionally, researchers have used surveys such as the Consumer Expenditure Survey (CEX) to measure individual economic activity. Such surveys are expensive to implement and require considerable effort from participants and are therefore fielded infrequently, with modest-sized samples. Researchers have recently turned to administrative records, which are accurate and can be frequently refreshed, to augment survey research. So far, however, the administrative records have typically represented just a slice

Table 1. Check versus ACS demographics (percent). The sample size for Check is 59,072, 35,417, 28,057, and 63,745 for gender, age, education, and region, respectively. The sample size for ACS is 2,441,532 for gender, age, and region and 2,158,014 for education.

	Check	ACS
Sex		
Male	59.93	48.59
Female	40.07	51.41
Age		
18–20	0.59	5.72
21–24	5.26	7.36
25–34	37.85	17.48
35–44	30.06	17.03
45–54	15.00	18.39
55–64	7.76	16.06
65+	3.48	17.95
Highest degree		
Less than college	69.95	62.86
College	24.07	26.22
Graduate school	5.98	10.92
Census Bureau region		
Northeast	20.61	17.77
Midwest	14.62	21.45
South	36.66	37.36
West	28.11	23.43

[1]Department of Economics, University of Michigan, Ann Arbor, MI 48109, USA. [2]Department of Economics, University of California, Berkeley, Berkeley, CA 94720, USA. [3]National Bureau of Economic Research (NBER), Cambridge, MA 02138, USA. [4]Department of Economics, Arizona State University, Tempe, AZ 85287, USA. [5]Haas School of Business, University of California, Berkeley, Berkeley, CA 94720, USA.
*Corresponding author. E-mail: shapiro@umich.edu

of economic activities. They have not provided simultaneous information about various sources of income and forms of spending.

The data described here result from transactions that are captured in the course of business by Check (https://check.me), a financial aggregation and service application (app). The resulting income data are accurate and comprehensive, in that they capture income from several sources and can be linked to similarly accurate and comprehensive information on spending. These raw data present important technical and conceptual challenges. This paper describes protocols necessary for turning them into a data set with several features that are useful for research and policy analysis.

Check had approximately 1.5 million active users in the United States in 2012. Users can link almost any financial account to the app, including bank accounts, credit cards, utility bills, and more. The application logs into the Web portals for these accounts daily and obtains the user's primary financial data. The data are organized so that users can obtain a comprehensive view of their financial situation.

The data we analyzed are derived from a sample of approximately 75,000 Check users, selected at random from the pool of U.S.-based users who had at least one bank or credit card account, and cover 300 consecutive days spanning 2012 and 2013. The data were de-identified and the analysis was perfomed on normalized and aggregated user-level data as described in the text and supplementary materials (SM). Check does not collect demographic information directly, and instead uses a third party that gathers both publicly and privately provided demographic data, anonymizes them, and provides aggregate tabulations of demographic characteristics of users. Table 1 compares the gender, age, education, and geographic distributions in the Check sample that matched with an email address to the distributions in the U.S. Census Bureau's American Community Survey (ACS), representative of the U.S. population in 2012.

Table 1 shows that the data overrepresent males and those aged 25 to 44. Education levels are broadly similar to those of the U.S. population, and the geographic distribution of Check users is reasonably consistent with that of the U.S. population. Overall, the sample contains large numbers of even the most underrepresented sociodemographic groups. For example, the sample contains about 3000 individuals aged 65 and older. At a point in time, the CEX contains information on approximately 1100 individuals aged 65 and older. We note, however, that the willingness to provide login credentials may select on personal characteristics or increased need for financial organization. The extent of this selection could be assessed with surveys of Check users, the results of which could be compared to those from existing surveys of representative populations. Alternatively, random samples of the population could be encouraged to link their financial accounts to the app, and the transaction and balances of this population could be compared with those of Check users.

Summary statistics for the raw data are provided in tables S1 and S2 of the SM. The data allowed us to calculate total income and to separately identify paychecks and Social Security payments using the description fields of transactions. Similarly, we measured total spending and subcategories of spending. We identified recurring and nonrecurring income and spending by looking for transactions that occurred at regular periodicity and had regular amounts.

We derived two measures of income: The first sums all transactions that represent credits to a user's non–credit card accounts, excluding transfers from one account to another. The second isolates only those transactions that credit paychecks and Social Security payments, using a list of keywords commonly found in the description field. Figure 1 shows the distribution of average monthly income measures at the user level.

Total monthly income depicted in Fig. 1A has a median of $4800 and a mean of $8923. The long and heavy right tail reflects income inequality and also includes large one-off transactions from asset sales. Paycheck and Social Security income, shown in Fig. 1B, is less skewed, with a median of $2900 and a mean of $3951. The figure also displays a kernel density estimate of the distribution of monthly incomes reported in the U.S. Census Bureau's ACS. The income concepts in the ACS and Check data have important differences. Figure 1A shows the distribution of ACS monthly pre-tax household income. The Check data shown in Fig. 1A are net of any (tax) withholding and may be aggregated from either individual or household income. Despite these differences, the ACS and Check distributions are qualitatively similar. Figure 1B shows the ACS distribution of wages, salaries, and the sum of wages and salaries and Social Security payments, which are more closely aligned with their analogs in the Check data. The shape of the ACS distribution is again similar to Check's.

For credit card accounts, we identify spending as transactions that post debits to the account. Non–credit card accounts are similar, but a sum of their debits will overstate spending, because some may represent credit card payments or transfers between accounts. Consequently, spending measures exclude debits we can identify as such payments or transfers either by amount or by transaction description.

We considered three measures of spending: (i) total spending, calculated using the method just described; (ii) nonrecurring spending; and (iii) spending on fast food and coffee shops. See fig. S1 in the SM for the distribution of these average weekly spending measures at the user level. Nonrecurring spending subtracts from total spending both ATM cash withdrawals and expenditures of at least $30 that recur, in the exact same amount (to the cent), at regular frequencies, such as weekly or monthly. It isolates spending that, due to its irregularity, is not easily timed to match the arrival of income. This measure thus uses the amount and timing of spending rather than an a priori categorization based on goods and services, an approach

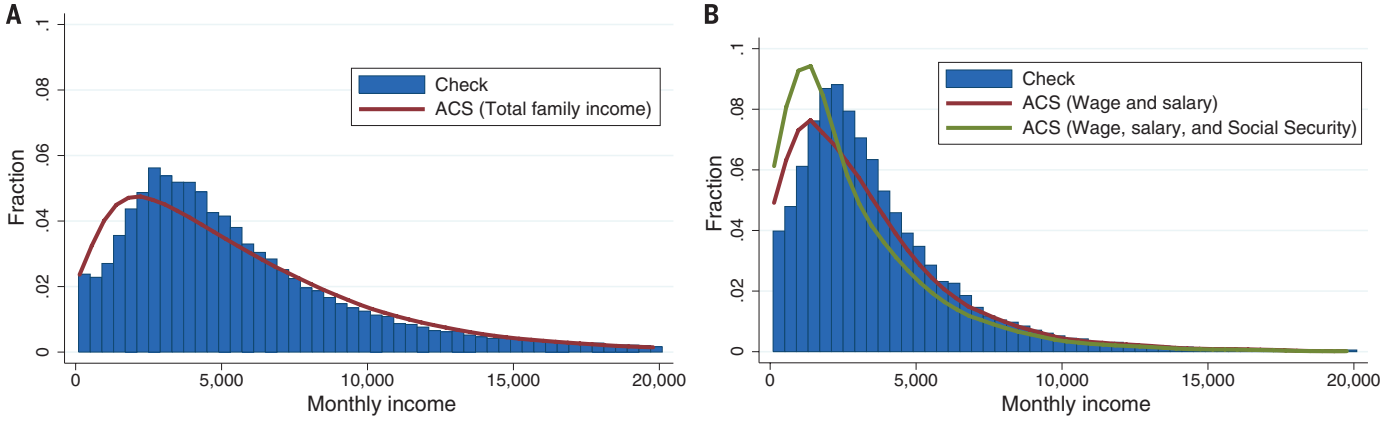

Fig. 1. Distribution of monthly income. (**A**) Total income. (**B**) Paycheck and Social Security income. The figure shows average monthly income across users. Any month in which the user had fewer than 20 days of data was dropped from computation of the average. In (A), the Check distribution represents 61,184 users who have at least one checking or savings account. In (B), both Check and ACS distributions are conditional on having paycheck and Social Security income (47,050 users).

made possible by the distinctive features of the data infrastructure. The fast food and coffee shop measure is identified using keywords from the transaction descriptions. This measure isolates an especially discretionary, nondurable, and highly divisible form of spending, which we used in the analysis of the spending response to anticipated income.

A benchmark theory indicates that the anticipated arrival of a payment should not affect the timing of spending. Specifically, spending should not rise after the arrival of a regular paycheck or Social Security payment. We estimated the excess sensitivity of total, nonrecurring, and coffee shop and fast food spending to the arrival of regular paychecks or Social Security payments. We thus evaluated the possibility that the benchmark theory describes behavior well and that excess sensitivity reflects either the convenience of coordinating recurring expenses with the arrival of regular income, or the intrinsic difficulty of smoothing some forms of spending. We also estimated the excess sensitivity of spending separately for users with different levels of liquidity and different levels of available credit. We thus evaluated the possibility that, as standard enhancements to the benchmark theory indicate, excess sensitivity is a phenomenon of those with inadequate liquidity or credit.

We restricted attention to approximately 23,000 users observed to receive paychecks or Social Security payments at a regular frequency and in regular amounts. A payment is classified as regular in frequency if the median number of days between its arrival is from 13 to 15 or from 26 to 34 and if its coefficient of variation is less than 0.5. The demographic characteristics of users who receive either regular paychecks or regular Social Security payments are remarkably similar to those of the entire sample, as are the distributions of their income, spending, and balances.

Our main econometric specification is

$$x_{ict} = \sum_{j=\text{Mon.}}^{\text{Sun.}} \delta_{jc} + \sum_{k=-7}^{6} \beta_{kc} I_i(\text{Paid}_{t-k}) + \varepsilon_{ict} \qquad (1)$$

where x_{ict} is the ratio of spending of individual i to i's average daily spending in category c, at date t, δ_{jc} is a day-of-week fixed effect, and $I_i(\text{Paid}_{t-k})$ is an indicator equal to 1 if i received a payment at time $t-k$, and equal to 0 otherwise. The β_{kc} coefficients thus measure the fraction by which individual spending in category c deviates from average daily spending in the days surrounding the arrival of a payment. The day-of-week dummies capture within-week patterns of both income and spending.

Figure 2 shows estimates of β_{kc} for the following categories of spending: (A) total, (B) nonrecurring, and (C) coffee shop and fast food spending. The dashed lines are the bounds of the 95% confidence intervals of these estimates based on heteroskedasticity-robust standard errors, with clustering at the individual level. Figure 2A shows that, on average, a user's total spending rises about 70% above its daily average on the day that a regular paycheck or Social Security payment arrives, and remains high for at least the next 4 days.

Total spending includes, however, expenditures such as rent, cable bills, or tuition that are recurring and predictable and whose timing can be adjusted to match the arrival of regular income. Figure 2B shows the excess sensitivity of only nonrecurring spending, confirming that a substantial part (40%) of the excess sensitivity of total spending can be attributed to the convenience of paying major bills automatically

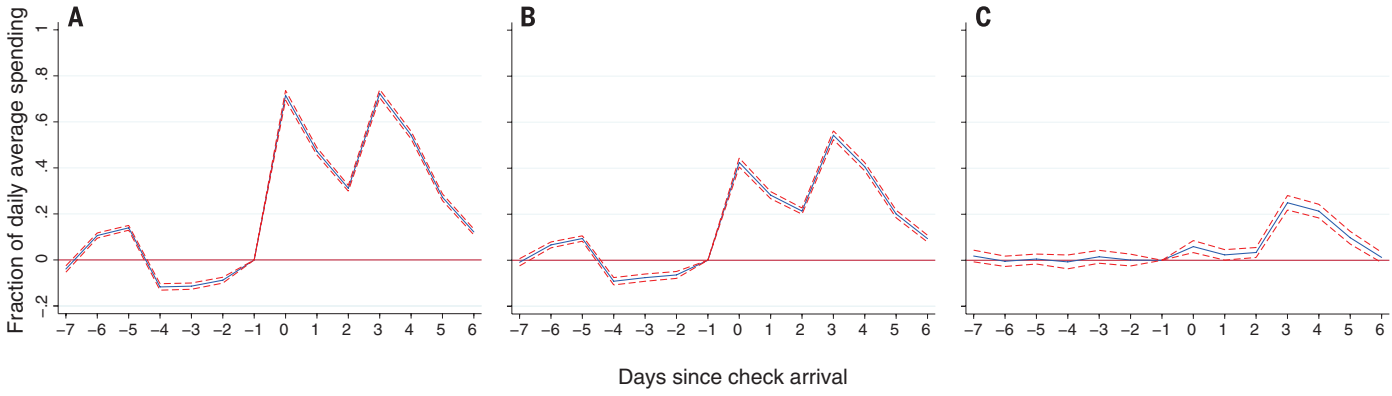

Fig. 2. Response of spending to income: Alternative components of spending. (**A**) Total spending. (**B**) Nonrecurring spending. (**C**) Fast food and coffee shop spending. The solid line represents regression coefficients from Eq. 1. The dashed lines are 95% confidence intervals. Estimates are based on 5,371,244, 5,371,244, and 5,173,594 total observations from 23,985, 23,985, and 23,021 users for panels (A), (B), and (C), respectively.

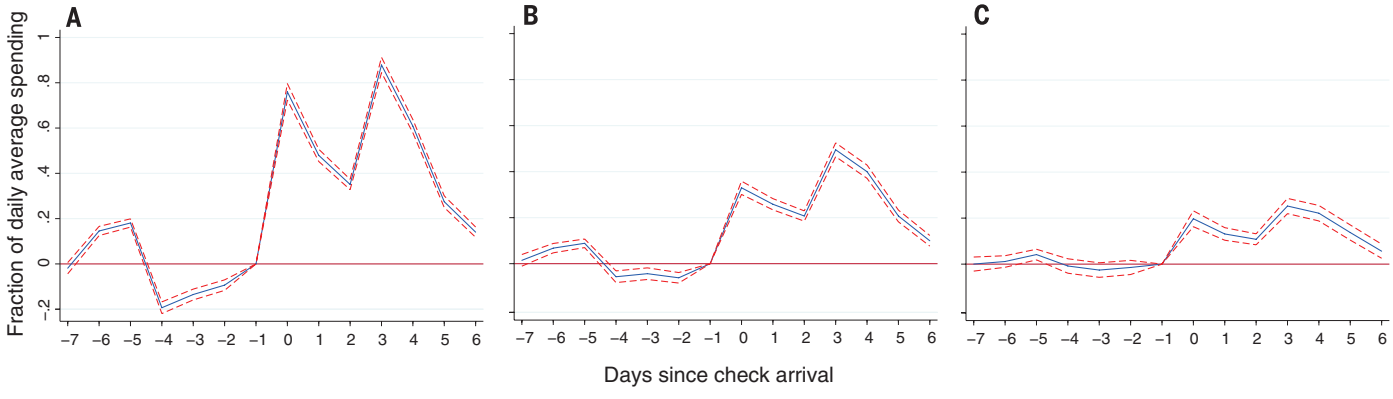

Fig. 3. Response of nonrecurring spending to income: Liquidity ratio. (**A**) Low liquidity. (**B**) Medium liquidity. (**C**) High liquidity. The solid line represents regression coefficients from Eq. 1. The dashed lines are 95% confidence intervals. Estimates are based on 1,784,460, 1,809,839, and 1,769,968 total observations from 7956, 7956, and 7955 users for panels (A), (B), and (C), respectively. The liquidity ratio is defined as the average daily balance of checking and savings accounts normalized by daily average spending.

and avoiding the bad consequences of temporary illiquidity. Given that we defined recurring spending conservatively (i.e., required that it be the same amount to the cent), this estimate is probably a lower bound on how much accounting for it reduces excess sensitivity.

Figure 2C provides still more evidence that the benchmark theory is a better description of behavior than the total spending estimates would suggest. For this imminently divisible and easily smoothed discretionary spending, we observe very modest excess sensitivity to the arrival of predictable income.

We find evidence of individual heterogeneity of excess sensitivity that is consistent with the theory that predicts such behavior among those with insufficient liquidity or available credit, perhaps due to imperfections in credit markets. Figure 3 plots estimates of β_{kc} for nonrecurring spending by terciles of liquidity. We define liquidity for each user as the average daily balance of checking and savings accounts over the entire sample period, normalized by the user's average daily spending. The average user in the lowest tercile has 5 days of spending in cash on hand; the average user in the highest tercile has 159 days. The estimates show that excess sensitivity is significantly more pronounced among those in the lowest tercile of the liquidity distribution.

Figure S2 plots estimates of excess sensitivity by terciles of the available credit utilization distribution. Excess sensitivity is concentrated among users near the limit of their ability to borrow with credit cards. Those who have little liquidity or take their debt levels very close to their limits may be poor at planning or optimizing. The evidence indicates that differences in liquidity and constraints drive heterogeneity of excess sensitivity among Check users.

Many prior studies of spending responses to income have used the CEX quarterly retrospective survey, which records self-reports of income but does not measure its timing precisely. Souleles, for example, uses it to estimate the spending response to the arrival of income tax refunds and overcomes the lack of timing information by calculating from aggregate statistics the likelihood of receiving a refund at various dates (*1*). Parker takes a similar approach and exploits anticipated changes in take-home pay when workers hit the annual cap on the Social Security payroll tax (*2*). Johnson *et al.* and Parker *et al.* measure the timing of some income more precisely by adding special questions to the CEX about tax rebates (*3*, *4*).

Some studies use higher-frequency data to estimate spending responses to income. The CEX diary survey records spending daily for 2 weeks but does not collect high-frequency income data. Stephens overcomes this limitation by studying the spending response to the receipt of Social Security benefits, which used to arrive on the same day of each month (*5*). The UK's Family Expenditure Survey collects the most recent paystub of respondents and asks them to track spending for 2 weeks. Stephens uses the paystub to infer the amount and timing of paychecks and estimates the spending response to them (*6*).

These prior studies use a variety of methods, but share an interest in estimating either an elasticity, defined as $\frac{\partial \log(\text{spending})}{\partial \log(\text{income})}$, or a marginal propensity to consume (MPC), defined as $\frac{\partial(\text{spending})}{\partial(\text{income})}$. Table S3 summarizes the key features of these prior estimates and compares them to analogous aspects of our study.

The studies differ in the time frame over which they measure spending changes in response to a change in income. This makes the levels of their estimated elasticities or MPCs difficult to compare. For our study, we present the point estimate of effects on the first day after the income arrives; that is β_{1c} from Eq. 1 for the elasticity of spending in category c. For the MPC we present the γ_{1c} from the equation

$$x_{ict} = \alpha_{ic} + \sum_{j=\text{Mon.}}^{\text{Sun.}} \delta_{jc} + \sum_{k=-7}^{6} \gamma_{kc} \text{Payment}_{ic,t-k} + \varepsilon_{ict} \quad (2)$$

where x_{ict} is the ratio of spending of individual i to i's average daily spending in category c, at date t; δ_{jc} is a day-of-week fixed effect; α_{ic} is a user fixed effect; and $\text{Payment}_{ic,t-k}$ is the ratio of the amount of the payment received by individual i divided by i's average daily spending in category c, at date $t-k$. Analogously, table S3 presents only the shortest-run effects reported in all the other studies. Although our and other studies estimate larger impacts at longer horizons, the central conclusion of table S3 about the relative precision of the estimates is not affected by the choice of horizon.

The prior estimates are important and influential but, as table S3 shows, they often lack precision. Among studies of the quarterly CEX data, Hsieh is unusual in its precision (*7*). The last four rows of table S3 include the confidence intervals for our estimates of both the elasticity and the MPC. These intervals are small, both economically and relative to other studies. Only Broda and Parker provides estimates that are as precise as those from the Check data (*8*). That paper uses Homescan data and estimates precisely an MPC out of tax rebates near 0. These estimates rely on surveys to determine receipt of the rebate, however, and would be attenuated if those reports are subject to error. The Homescan spending data are also limited in scope, largely capturing only goods with Universal Product Codes. Moreover, the Check data allow estimates of the response to routine payments such as paychecks and Social Security payments, not just particular payments such as tax rebates.

Related studies of administrative data also provide accurate measures of spending but do not cover it comprehensively. For example, Agarwal *et al.* use data from a single credit card company to study the spending response to tax rebates; they can thus track the effects of the rebate on a single account but not on overall spending (*9*). Kuchler makes use of more comprehensive administrative data collected from a debt management Web site, but the number of users (556) is relatively small (*10*). The financial application Mint (https://www.mint.com/) has a complementary data infrastructure that it is using to construct monthly time series of spending by types of goods (*11*). It has not been used for research along the lines of the estimates in this paper.

In policy discussions before the 2008 tax rebates, the Congressional Budget Office and others cited the point estimates of the effect of the 2001 rebate from Parker, Johnson, and Souleles, but not the substantial uncertainty about that estimate documented in that paper and in table S3 (*3*, *12*). More generally, estimates of spending rates from different changes in income play a key role in the evaluation of the American Recovery and Reinvestment Act (*13*), making the stakes in getting credible and precise estimates of these parameters very high. This paper shows how economic theory and policy can benefit from analysis made possible with naturally occurring data such as those provided by Check.

REFERENCES AND NOTES

1. N. S. Souleles, *Am. Econ. Rev.* **89**, 947–958 (1999).
2. J. A. Parker, *Am. Econ. Rev.* **89**, 959–973 (1999).
3. D. S. Johnson, J. A. Parker, N. S. Souleles, *Am. Econ. Rev.* **96**, 1589–1610 (2006).
4. J. A. Parker, N. S. Souleles, D. S. Johnson, R. McClelland, *Am. Econ. Rev.* **103**, 2530–2553 (2013).
5. M. Stephens Jr., *Am. Econ. Rev.* **93**, 406–422 (2003).
6. M. Stephens Jr., *Econ. J.* **116**, 680–701 (2006).
7. C.-T. Hsieh, *Am. Econ. Rev.* **93**, 397–405 (2003).
8. C. Broda, J. A. Parker, "The economic stimulus payments of 2008 and the aggregate demand for consumption" (manuscript, Sloan School of Management, Cambridge, MA, 2014).
9. S. Agarwal, C. Liu, N. S. Souleles, *J. Polit. Econ.* **115**, 986–1019 (2007).
10. T. Kuchler, "Sticking to your plan: Hyperbolic discounting and credit card debt paydown" (manuscript, Stern School of Business, New York, 2013).
11. Intuit, Intuit consumer spending index (Intuit, Mountain View, CA, 2013).
12. Congressional Budget Office, *Options for Responding to Short-Term Economic Weakness* (U.S. Congressional Budget Office, Washington, DC, 2008).
13. Congressional Budget Office, *Estimated Impact of the American Recovery and Reinvestment Act on Employment and Economic Output from July 2010 Through September 2010* (U.S. Congressional Budget Office, Washington, DC, 2010).

ACKNOWLEDGMENTS

This research was supported by a grant from the Alfred P. Sloan Foundation. M.D.S. acknowledges additional support through the Michigan node of the NSF-Census Research Network (NSF grant SES 1131500). This paper has benefited from suggestions by the participants of the NBER Summer Institute, the Conference on Economic Decisionmaking (Aspen, Colorado), and several seminars. A data set for replicating the results of this paper is available through the University of California Berkeley Econometrics Lab (EML) at https://eml.berkeley.edu/cgi-bin/HarnessingDataScience2014.cgi. To access the data, users must register with EML and agree to terms of use. The data set contains no personal or account identifiers. The data are aggregated and transformed so that they reveal no personally identifying information.

SUPPLEMENTARY MATERIALS

www.sciencemag.org/content/345/6193/212/suppl/DC1
Materials and Methods
Figs. S1 and S2
Tables S1 to S3
References

28 October 2013; accepted 13 June 2014
10.1126/science.1247727

CANCER THERAPY

Ex vivo culture of circulating breast tumor cells for individualized testing of drug susceptibility

Min Yu,[1,2]* Aditya Bardia,[1,3] Nicola Aceto,[1] Francesca Bersani,[1] Marissa W. Madden,[1] Maria C. Donaldson,[1] Rushil Desai,[1] Huili Zhu,[1] Valentine Comaills,[1] Zongli Zheng,[1,4,5] Ben S. Wittner,[1] Petar Stojanov,[6] Elena Brachtel,[4] Dennis Sgroi,[1,4] Ravi Kapur,[7] Toshihiro Shioda,[1,3] David T. Ting,[1,3] Sridhar Ramaswamy,[1,3] Gad Getz,[1,4,6] A. John Iafrate,[1,4] Cyril Benes,[1,3] Mehmet Toner,[7,8] Shyamala Maheswaran,[1,8]† Daniel A. Haber[1,2,3]†

Circulating tumor cells (CTCs) are present at low concentrations in the peripheral blood of patients with solid tumors. It has been proposed that the isolation, ex vivo culture, and characterization of CTCs may provide an opportunity to noninvasively monitor the changing patterns of drug susceptibility in individual patients as their tumors acquire new mutations. In a proof-of-concept study, we established CTC cultures from six patients with estrogen receptor–positive breast cancer. Three of five CTC lines tested were tumorigenic in mice. Genome sequencing of the CTC lines revealed preexisting mutations in the *PIK3CA* gene and newly acquired mutations in the estrogen receptor gene (*ESR1*), *PIK3CA* gene, and fibroblast growth factor receptor gene (*FGFR2*), among others. Drug sensitivity testing of CTC lines with multiple mutations revealed potential new therapeutic targets. With optimization of CTC culture conditions, this strategy may help identify the best therapies for individual cancer patients over the course of their disease.

Circulating tumor cells (CTCs) are present in the blood of many patients with solid tumors. Most of these cells, which are thought to be involved in metastasis, die in the circulation, presumably due to the loss of matrix-derived survival signals or circulatory shear stress. Nonetheless, if CTCs can be isolated from cancer patients as viable cells that can be genotyped and functionally characterized over the course of therapy, they have the potential to identify treatments that most effectively target the evolving mutational profile of the primary tumor (*1*). The isolation of viable CTCs is technically challenging: Most methods yield low numbers of partially purified CTCs that are fixed before isolation, damaged during the cell purification process, or irreversibly immobilized on an adherent matrix [see review (*2*)]. We recently reported a microfluidic technology, the CTC-iChip, which efficiently depletes normal blood cells, leaving behind unmanipulated CTCs (*3*). The cytological appearance, staining properties, and intact RNA evident within a subset of CTCs isolated by means of this tumor antigen-agnostic CTC isolation platform suggested that the cells may be viable.

To investigate whether the CTCs were in fact viable, we applied the CTC-iChip to blood samples from patients with metastatic estrogen receptor (ER)–positive breast cancer. After testing a range of culture conditions (*4*–*7*) (see supplementary methods), we found that CTCs proliferated best as tumor spheres when cultured in serum-free media supplemented with epidermal growth factor (EGF) and basic fibroblast growth factor (FGF) (*8*) under hypoxic conditions (4% O_2) (Fig. 1A). Nonadherent culture conditions were critical, because CTCs senesced after a few cell divisions in adherent monolayer culture (fig. S1). We established long-term oligoclonal CTC

[1]Massachusetts General Hospital Cancer Center, Harvard Medical School, Charlestown, MA 02129, USA. [2]Howard Hughes Medical Institute, Chevy Chase, MD 20815, USA. [3]Department of Medicine, Harvard Medical School, Charlestown, MA 02129, USA. [4]Department of Pathology, Harvard Medical School, Charlestown, MA 02129, USA. [5]Department of Medical Epidemiology and Biostatistics, Karolinska Insitutet, Stockholm, Sweden. [6]Broad Institute of Harvard and MIT, Cambridge, MA 02142, USA. [7]Center for Bioengineering in Medicine, Harvard Medical School, Charlestown, MA 02129, USA. [8]Department of Surgery, Harvard Medical School, Charlestown, MA 02129, USA. *Present address: Department of Stem Cell Biology and Regenerative Medicine, University of Southern California, Los Angeles, CA 90033, USA. †Corresponding author. E-mail: maheswaran@helix.mgh.harvard.edu (S.M.); haber@helix.mgh.harvard.edu (D.A.H.)

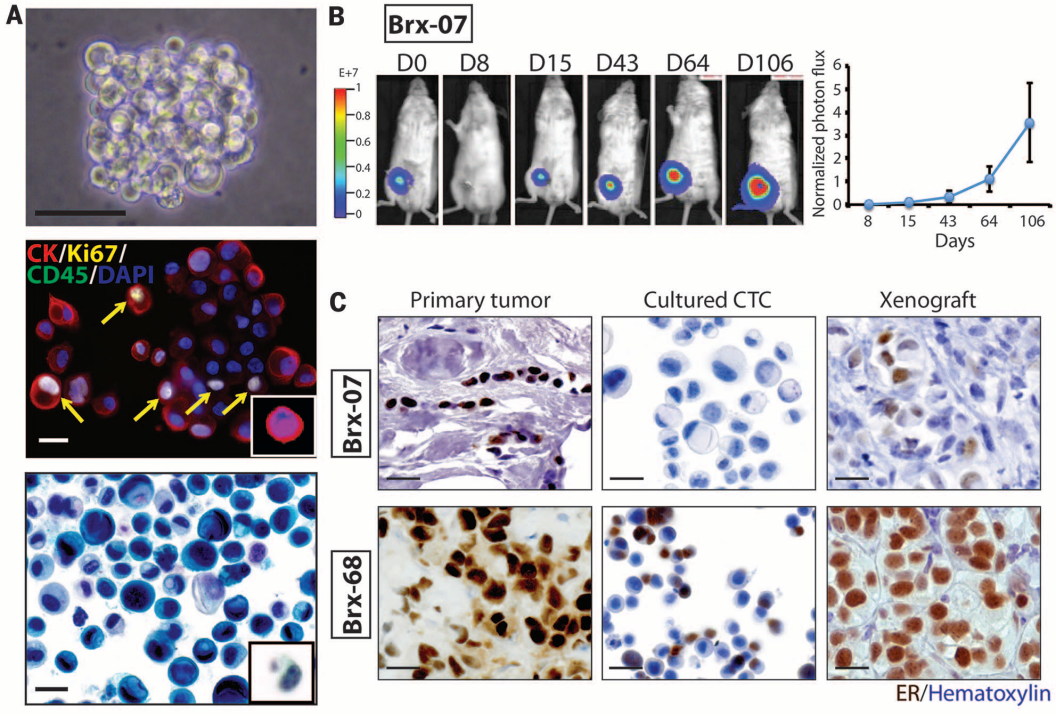

Fig. 1. Ex vivo expansion of breast cancer CTCs. (**A**) Representative images of nonadherent CTC culture (BRx-07). Top: Phase contrast. Scale bar, 100 μm. Middle: immunofluorescent staining for cytokeratin (CK, red), Ki67 (yellow), CD45 (green), nuclei [4′,6-diamidino-2-phenylindole (DAPI), blue]. Scale bar, 20 μm. Bottom: Light microscopic imaging with Papanicolaou staining. Comparable images for uncultured primary CTCs are shown in the insets. Scale bar, 20 μm. (**B**) (Left) Bioluminescent images showing growth of NSG mouse xenografts, after implantation of 20,000 cultured CTCs (BRx-07) into the mammary fat pad. (Right) Quantification of bioluminescent signals for BRx-07–derived mouse xenografts (mean ± SD, $n = 6$). (**C**) Histology of matched primary breast tumors, cultured CTCs, and CTC-derived mouse xenografts for two CTC lines. All panels show cellular staining with hematoxylin (blue) and immunohistochemical staining for ER expression (brown). Scale bar, 20 μm.

cultures (sustained in vitro for >6 months) from CTCs isolated from six patients with metastatic luminal subtype breast cancers (table S1). One or more CTC cell lines were successfully generated from 6 of 36 patients who were either off therapy or progressing on treatment. We were unable to generate CTC cell lines from nine patients who were responding to treatment at the time of attempted CTC culture. For three patients, four additional CTC cell lines were established from blood samples drawn at multiple different time points during therapy (table S1). In these cases, CTCs were successfully cultured only when patients were progressing on treatment (fig. S1).

Cultured CTCs shared cytological features with the matched primary CTCs captured on the CTC-iChip (Fig. 1A), and consistent with standard CTC definitions, they stained positive for epithelial cytokeratin (>95% of cells) and negative for the leukocyte marker CD45 (Fig. 1A) (fig. S2). The proliferative index of CTC cultures was ~30%, as defined by Ki67 staining (mean 28.1%, range 24 to 32%), and the initial doubling time of CTC cultures varied from 3 days to 3 weeks (table S1). All six primary tumors were positive for ER expression. Five CTC lines retained ER positivity in culture (>10% of cells), whereas one line (BRx-07) lost ER expression in vitro (Fig. 1C and fig. S2).

We undertook RNA sequencing analysis of each cell line and compared the results with those of 29 uncultured single CTCs from a total of 10 patients, as well as a panel of 13 commonly used established breast cancer cell lines, all using low-template single-cell resolution analysis (fig. S3). CTC cultures clustered with each other, and separately from established breast cancer cell lines or uncultured single CTCs. As expected, both CTC cultures and established breast cancer cell lines had increased proliferative signature, compared with primary uncultured single CTCs (fig. S3). We did not observe increased expression in CTC cultures of defined signaling pathways, including stem cell–related signatures, compared with established breast cancer cell lines.

To test the tumorigenicity of CTC lines, we used lentiviral transduction to label them with both green fluorescent protein (GFP) and luciferase and inoculated 20,000 cells into the mammary fat pad of immunosuppressed non-obese diabetic *scid* gamma (NSG) female mice implanted with subcutaneous estrogen pellets. Of five CTC lines tested, three (BRx-07, BRx-68, and BRx-61) generated tumors within 3 months at this low inoculum (Fig. 1B and figs. S4 and S5). CTC-derived tumors shared histological and immunohistochemical features with the matched primary patient tumor, including BRx-07, which regained ER expression (Fig. 1C).

All six patients with metastatic breast cancer had received sequential courses of hormonal and other therapies before CTC collection (fig. S6). As part of standard clinical care at Massachusetts General Hospital, a mutational panel [SNaPShot (*9*)] covering ~140 mutations in 25 genes had been performed on primary tumor specimens (BRx-68 and BRx-42) or on pretreatment biopsies of metastatic lesions (BRx-33, BRx-07, BRx-50 and BRx-61). Point mutations in *PIK3CA* (H1047R and G1049R), hot-spot mutations in breast cancer, were identified in two cases (BRx-68 and BRx-42), whereas no mutations were found in the four other cases (table S1). The availability of CTC cultures made it possible to undertake more comprehensive mutational analysis from a more abundant and purified tumor cell population. CTC lines were screened for mutations in a panel of 1000 annotated cancer genes, with a hybrid-capture–based next-generation sequencing (NGS) platform. The *PIK3CA* mutations identified by SNaPShot testing of primary tumors were confirmed by NGS in both CTC cultures (BRx-68 and BRx-42), and multiple additional mutations in other cancer-related genes were identified (Table 1). For all mutations identified in the 1000 cancer gene panel, candidate driver mutations were defined by their absence from matched germline DNA and by their annotation in pan-cancer (*10*) and COSMIC (Catalogue of somatic mutations in cancer) databases (Table 1), whereas additional mutations in known cancer genes were of uncertain relevance (table S2). To ensure that the candidate driver mutations were not acquired during the in vitro establishment of CTC cell lines, we tested for selected mutations in four additional CTC lines, which had been independently isolated at different time points from each of three patients (BRx-68, BRx-42, and BRx-61). The acquired

Table 1. Mutations detected in cultured CTC lines.

Case	Gene	DNA	Protein	Allele frequency†	In pretreatment tumor‡	In multiple CTC lines	Known mutation§
BRx33||	ESR1	A1613G	D538G	0.24	–	–	Br,# En
	NUMA1	C5501T	S1834L	0.39	–	–	Br
BRx07||	TP53	G853A	E285K	0.99	No	–	Bl, Br, Co, HN, Lu
	PIK3CA	A3140T	H1047L	1	No	–	Br, Co, GBM, HN, K_i, Lu, Me, Mel, Ov, En
	FGFR2	T1647A	N549K	0.46	No	–	Br, En
	CDH1	C790T	Q264*	1	Yes	–	Br
	APC	G7225A	G2409R	0.47	Yes	–	Mel
	DGKQ	G2530A	D844N	0.55	–	–	Lu
	MAML2	A2569G	M857V	0.52	–	–	Lu
BRx68	TP53	C1009T	R337C	0.99	No	Yes	Br, Co, HN, Hem, Ov
	ESR1	A1610C	Y537S	0.47	No	Yes	Br#, En
	PIK3CA	A3140G	H1047R	0.7	Yes	Yes	Br, Co, GBM, HN, K_i, Lu, Me, Mel, Ov, En
	MSN	G1153A	E385K	0.25	–	–	En
BRx50||	ESR1	T1607C	L536P	0.06††	–	–	Br#
	IKZF1	G1444T	G482C	0.09	–	–	Hem
	BRCA2¶	T6262del	L2039fs	–	–	–	Br (germ line)
BRx42	PIK3CA	G3145C	G1049R	0.60	Yes	Yes	Br, En, K_i
	PIK3CA	C1097G	P366R	0.54	–	–	Br
	KRAS	G35T	G12V	0.99	No	Yes	Br, Co, Hem, Es, GBM, Lu, Ov, En
	IGF1R	G3613A	A1205T	0.06	–	–	Hem
BRx61	TP53	G610T	E204*	0.98	No	Yes	Bl, Br, K_i, Lu, Ov

†Mutant allele frequency within oligoclonal cultured CTC populations was calculated as the ratio of mutant sequence reads to total reads for each gene. ‡Where sufficient material was available for analysis, matched archival pretreatment tumor specimens were subjected to Sanger sequencing to confirm selected mutations identified in CTC cultures. Insufficient tumor material is marked (–). §List of tumor types reported to harbor the same mutation in pan-cancer (*10*) or COSMIC databases. Abbreviations: breast (Br), endometrial (En), central nervous system (CNS), bladder (Bl), colorectal (Co), pancreas (Pa), stomach (St), head and neck (HN), lung (Lu), thyroid (Th), glioblastoma (GBM), kidney (Ki), prostate (Pr), medulloblastoma (Me), melanoma (Mel), ovarian (Ov), cervix (Ce), esophageal (Es), hematopoietic and lymphoid tissue (Hem), sarcoma (Sar), cholangiocarcinoma (Ch). ||Cases for which DNA from matched normal tissue was not available. ¶Germline BRCA2 mutation was detected as part of genetic counseling for familial breast cancer. #Mutations reported in recent publications (*12*–*15*). ††ESR1 T1607C mutant allele frequency increased to 0.49 after prolonged in vitro culture under low-estrogen conditions (>6 months). *Chain termination codon. fs: frameshift mutation. Abbreviations for amino acid residues: A, Ala; C, Cys; D, Asp; E, Glu; F, Phe; G, Gly; H, His; I, Ile; K, Lys; L, Leu; M, Met; N, Asn; P, Pro; Q, Gln; R, Arg; S, Ser; T, Thr; V, Val; W, Trp; and Y, Tyr.

mutations in *ESR1* (BRx-68), *TP53* (BRx-68, BRx-61), and *KRAS* (BRx-42) were universally present in all independent CTC cell lines (Table 1), confirming that they are tumor-derived mutations. In addition, the *ESR1* mutation (Y537S) present in multiple BRx-68 CTC lines was also detectable by direct RNA sequencing of uncultured CTCs isolated from this patient (fig. S7).

Activating mutations in the estrogen receptor (*ESR1*) were first identified in 1997 and are rare in primary breast cancer (*11*). While this manuscript was in preparation, multiple research groups reported *ESR1* mutations in 18 to 54% of patients treated with aromatase inhibitors (AIs), drugs that suppress estrogen synthesis and thus may favor the emergence of these ligand-independent ER mutants (*12*–*15*). We also detected *ESR1* mutations in three of six CTC lines (BRx-33, BRx-68, and BRx-50). Each of these patients had received extensive treatment with AIs, and reanalysis of the primary tumor or the pre-AI treatment biopsy of a metastatic lesion showed no evidence of *ESR1* mutations (Table 1). Other mutations identified included newly arising mutations in *PIK3CA*, *TP53*, *KRAS*, and fibroblast growth factor receptor–2 (*FGFR2*) (Table 1). Consistent with its lobular histological subtype, an E-cadherin (*CDH1*) mutation was detected in one CTC line (BRx-07). Although most mutant allele frequencies indicated heterozygous or homozygous truncal mutations shared by all CTCs, rare mutated alleles consistent with emerging tumor subpopulations were also evident. An *ESR1* mutation initially present at 6% allele frequency in BRx-50 increased to 49% allele frequency upon prolonged culture in low-estrogen–containing medium (Table 1), suggesting a proliferative advantage under these conditions. Notably, *TP53* mutations, which are thought to be rare in primary luminal breast cancers (*16*), emerged during tumor progression in three of six cases.

The availability of comprehensive tumor cell genotyping brings with it the challenge of identifying the subset of mutations whose therapeutic targeting is likely to be beneficial to an individual patient. To begin to explore this opportunity, we tested CTC lines for sensitivity to panels of single drug and drug combinations, including standard clinical regimens, as well as experimental agents targeting specific mutations. Conditions were optimized for highly reproducible testing of viability in small numbers of cells (200 cells per well) cultured as aggregates in solution. For each drug, we tested five concentrations (table S3), centered around median inhibitory concentration (IC_{50}) levels established in large-scale cancer cell line screens (*17*), with relative sensitivity or resistance defined by comparison among the CTC cell lines (Fig. 2 and figs. S8 to S10). Although CTC drug sensitivity testing was blinded to clinical history, and patient treatment selections were not informed by CTC testing, some CTC drug sensitivity measurements were concordant with clinical histories, including sensitivity to paclitaxel (BRx-07)

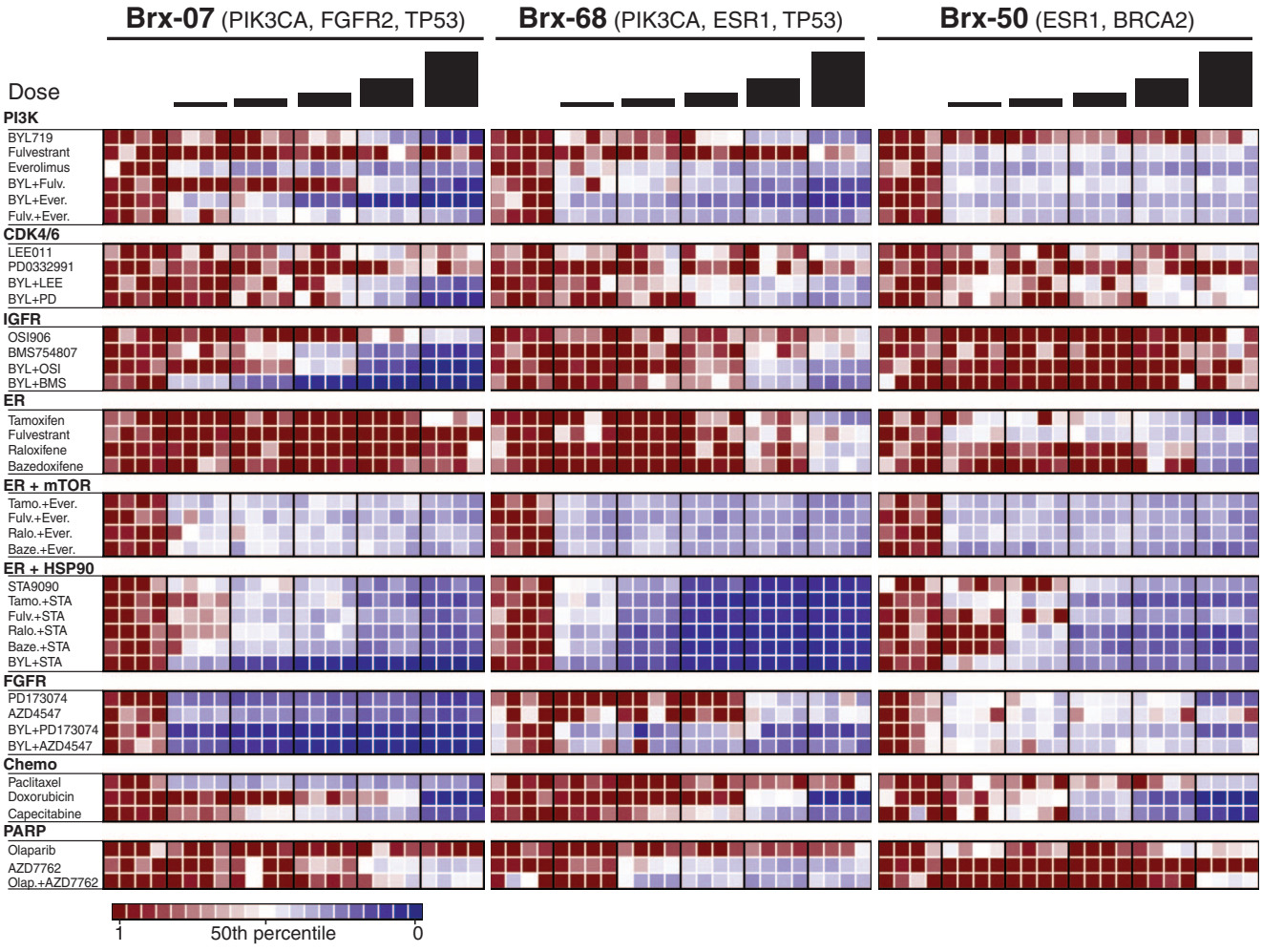

Fig. 2. Drug sensitivity of cultured CTCs. Heatmaps representing cell viability after treatment of BRx-07, BRx-68, and BRx-50 CTC lines with selected anticancer drugs, either alone or in combination. The presumed driving mutation for each CTC line is noted, and drugs are grouped according to therapeutic class and targeted pathway. For each drug, the range of concentrations tested is centered around the IC_{50} derived from large-scale breast cancer cell line screens (*17*), and each concentration represents a twofold increase from the previous dose, with each concentration tested in quadruplicate. Drug concentrations are listed in table S3. Signal from viable cells remaining after drug treatment is normalized to corresponding vehicle [dimethyl sulfoxide (DMSO)]–treated controls, with ratios plotted ranging from red (more viable) to blue (less viable). Drug abbreviations: BYL, BYL719; Fulv, fulvestrant; Ever, everolimus; LEE, LEE011; PD, PD0332991; OSI, OSI906; BMS, BMS754807; Tamo, tamoxifen; Ralo, raloxifene; Baze, bazedoxifene; STA, STA9090; Olap, Olaparib.

and capecitabine (BRx-68 and BRx-50), and resistance to fulvestrant (BRx-07 and BRx-68), doxorubicin (BRx-07), and olaparib (BRx-50) (fig. S11).

We selected two mutated drug targets identified in CTCs but not in the primary tumor for more detailed analysis; namely, *ESR1* and *PIK3CA* mutations (additional drug responses in cultured CTCs are shown in fig. S12). To facilitate interpretation of the effect of drug combinations, responses to selected drugs are represented in a 2 × 2 matrix highlighting cooperative drug effects versus independent cytotoxicity (Fig. 3; see quantitation in fig. S13). The three de novo acquired *ESR1* mutations affected distinct but adjacent residues within the ER ligand-binding domain and were present at different allele frequencies within the oligoclonal CTC cell lines. The most commonly reported *ESR1* mutation, Y537S (*12*–*14*), was observed in BRx-68 (47% allele frequency, consistent with a heterozygous mutation in all cells), with two other mutations, D538G and L536P, in BRx-33 and BRx-50 (24 and 6% allele frequencies, respectively). Each mutation arose within the context of distinct additional mutations (Table 1 and table S2). Of note, all *ESR1* mutation-positive CTC lines maintained ER expression in culture.

The optimal therapy for breast cancer patients whose ER$^+$ tumor has acquired an *ESR1* mutation is unknown; consistent with previous models (*12*–*14*, *18*), we found that the selective estrogen receptor modulators (SERMs) tamoxifen and raloxifene, and the selective ER degrader (SERD) fulvestrant, were ineffective in BRx-68 cells, either alone or in the clinically approved combination with inhibitors of the phosphatidylinositol 3-kinase–mammalian target of rapamycin (PI3K-mTOR) pathway (everolimus) (*19*) (Fig. 2). However, the HSP90 inhibitor STA9090 demonstrated cytotoxicity alone and in combination with both raloxifene and fulvestrant (Fig. 3A). ER is a client protein for HSP90, and mutated receptors are highly dependent on this chaperone for their stability (*20*). Indeed, treatment with a low dose of STA9090 (32 nM) suppressed ER levels in BRx-68 cells but had no effect in MCF7 breast cancer cells with wild-type ER, or in BRx-50 cells, where the low allele frequency of mutant *ESR1* is not associated with sensitivity to HSP90 inhibitors (Fig. 3B and figs. S12 to S14). Clinical studies of HSP90 inhibitors, along with novel ER inhibitors, will be required to define the optimal treatment for breast cancer patients whose tumor has acquired an *ESR1* mutation.

The BRx-07 cell line is noteworthy because it harbors activating mutations in both *PIK3CA* and *FGFR2*, both of which were acquired de novo during the course of therapy. Based on their respective allele frequencies, *PIK3CA* was homozygously mutated in all cells, whereas the *FGFR2* mutation was heterozygous (Table 1). Cultured CTCs were highly sensitive to the PIK3CA inhibitor BYL719 (*21*) and the FGFR2 inhibitor AZD4547 (*22*), and moderately responsive to the FGFR1 inhibitor PD173074 (*23*) (Fig. 2). Combined inhibition of both PIK3CA and FGFR2 showed cooperative effects (Fig. 3C and fig. S13), suggesting that both of these mutations may function as acquired oncogenic drivers in this tumor. Because combinations of PIK3CA and FGFR inhibitors have not been tested in clinical settings, we further quantified responses in a panel of established

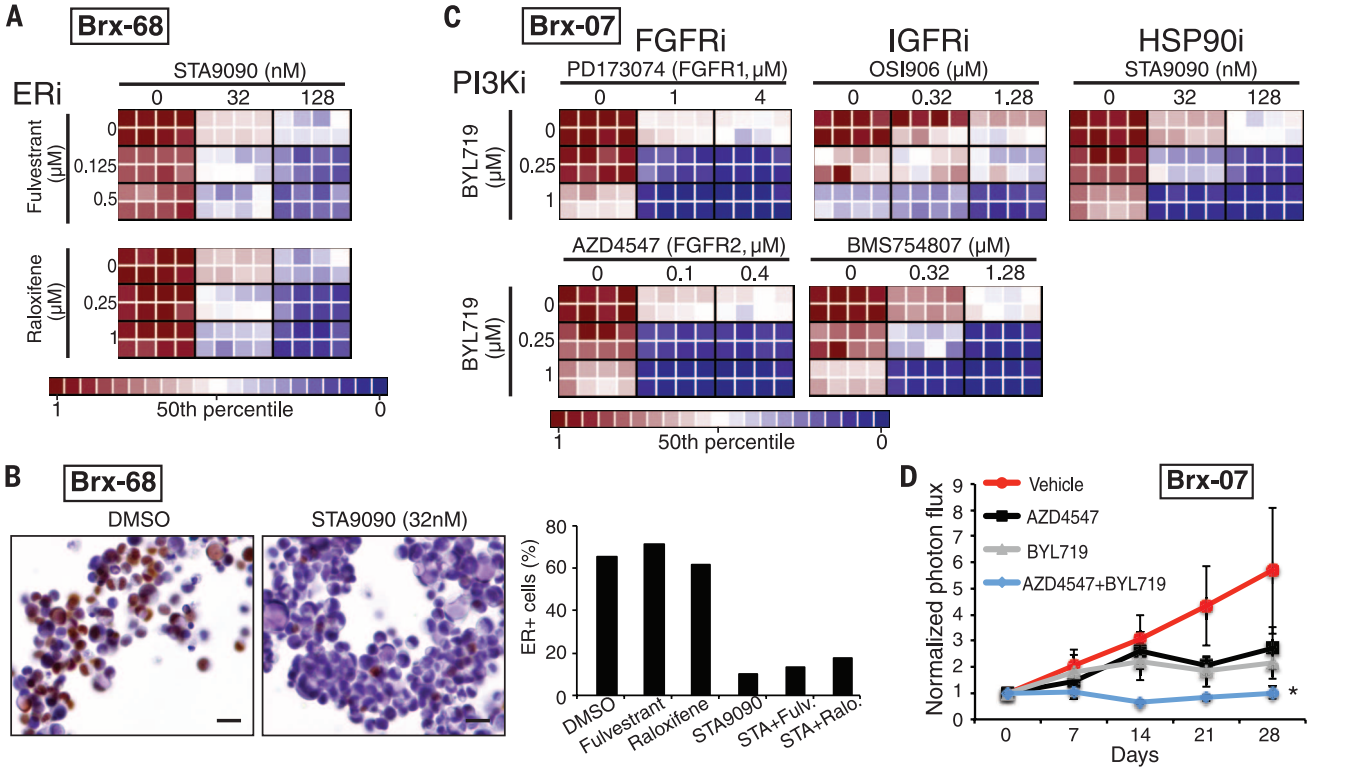

Fig. 3. Combinatorial drug targeting of mutant *ESR1* and *PIK3CA* in CTC lines. (**A**) Heatmaps representing cell viability in the BRx-68 CTC line, carrying an *ESR1* mutation (allele frequency 47%), treated with HSP90 inhibitor (STA9090) together with the selective estrogen receptor modulator (SERM) tamoxifen or degrader (SERD) fulvestrant. For these drug-combination studies, the concentrations of each drug was varied independently, and results are shown in eight replicates. Cooperative drug interactions are represented by a diagonal gradient, showing increasing cell killing as both drug concentrations increase independently. (**B**) Down-regulation of ER protein expression measured by immunohistochemical staining (brown) of BRx-68 CTC cultures treated for 24 hours with an HSP90 inhibitor (STA9090) versus vehicle (DMSO). Nuclei are stained with hematoxylin. Scale bar, 20 μm. Bar graph shows quantification of percent ER-positive cells. More than 200 cells were quantified in each condition. (**C**) Heatmaps representing cell viability in the BRx-07 line harboring mutations in *PIK3CA* (99% allele frequency) and *FGFR2* (46% allele frequency). Drugs targeting the products of these mutated oncogenic drivers were tested, along with compounds inhibiting nonmutated targets (IGFR and HSP90). Drug combinations shown are PI3Ki + FGFRi; PIK3Ki + IGFRi; PIK3Ki + HSP90i. (**D**) Response of BRx-07 CTC-derived mouse xenografts to the PI3K inhibitor BYL719 (n = 4), the FGFR2 inhibitor AZD4547 (n = 3), the combination of the two inhibitors (BYL719+AZD4547) (n = 4), or diluent control (n = 4). Mean ± SD. In vivo drug administration was initiated after mammary fat pad inoculation with genotyped CTC cultures and establishment of an expanding tumor xenograft, and tumor-derived bioluminescent measurements were normalized to pretreatment levels.

breast cancer cell lines. Of seven *PIK3CA*-mutant breast cancer lines, six were responsive to BYL719 (fig. S15). In addition to their characteristic *PIK3CA* mutation, two lines harbored mutations of unknown importance in *FGFR4* (Y367C; MDA-MB-453 cells) and in *FGFR2* (K570E; EFM-19 cells). The former showed cooperative cytotoxicity by BYL719 and AZD4547, whereas the latter was insensitive to FGFR inhibition (fig. S15). One of five *PIK3CA*-mutant breast cancer lines without an *FGFR* gene mutation showed modest sensitivity to AZD4547 (CAL51), whereas the other four were resistant. Thus, the combination of genotyping and functional testing for drug susceptibility is essential to defining therapeutically relevant driver mutations in both breast cancer cell lines and CTC cultures.

In vitro screening of additional drugs for cooperation with PIK3CA-targeted agents identified inhibitors of the insulin-like growth factor receptor 1 (*IGF1R*, inhibitors OSI906 and BMS754807) and HSP90 (inhibitor STA9090, Ganetespib) (Fig. 3C). Although neither of these is mutated in BRx-07 cells, IGF1R has been implicated in modulating signaling loops that mitigate sensitivity to PI3K inhibitors (*24*), and HSP90 is involved in stabilization of mutant kinases (*20*). To extend drug sensitivity studies to mouse xenografts, we generated BRx-07–derived mammary tumors and treated these with BYL719, AZD4547, the two agents in combination, or diluent control. In vivo tumor suppression was observed after treatment with either drug individually, whereas the combination completely abrogated tumor growth (Fig. 3D).

In this proof-of-concept study, we have shown that the culture of tumor cells circulating in the blood of patients with breast cancer provides an opportunity to study patterns of drug susceptibility, linked to the genetic context that is unique to an individual tumor. In patients with hormone-responsive breast cancer, most of whom have bone metastases that are not readily biopsied, the ability to noninvasively and repeatedly analyze live tumor cells shed into the blood from multiple metastatic lesions may enable monitoring of emerging subclones with altered mutational and drug sensitivity profiles. The successful culture of CTCs stems partly from the application of a microfluidic device capable of effectively depleting leukocytes from a blood specimen while preserving viable tumor cells for ex vivo expansion (*3*). The proliferation of cultured CTCs as nonadherent spheres differs from that of characteristic epithelial cancer cell cultures and may reflect intrinsic properties of tumor cells that remain viable in the bloodstream after loss of attachment to basement membrane. A recent report documented direct inoculation of the mouse femur with blood-derived cancer cells from a patient who had very high numbers of CTCs, but in vitro culture was not successful (*25*). Our results differ from the adherent in vitro CTC cultures described by Zhang *et al.* (*26*), but these lines appear to share the identical *TP53*, *BRAF*, and *KRAS* genotype of the highly tumorigenic MDA-MB-231 cell line.

Optimization of CTC culture conditions will be needed before this strategy can be incorporated into clinical practice. In addition, further characterization of the nonadherent CTC-derived cell lines described here will be required to define how they differ from cells cultured from primary tumor biopsies or directly implanted into mouse models (*4*, *14*). In the future, strategies such as that described here may be an essential component of "precision medicine" in oncology, where treatment decisions are based on evolving tumor mutational profiles and drug sensitivity patterns in individual patients.

REFERENCES AND NOTES

1. D. A. Haber, N. S. Gray, J. Baselga, *Cell* **145**, 19–24 (2011).
2. M. Yu, S. Stott, M. Toner, S. Maheswaran, D. A. Haber, *J. Cell Biol.* **192**, 373–382 (2011).
3. E. Ozkumur *et al.*, *Sci. Transl. Med.* **5**, 179ra47 (2013).
4. X. Liu *et al.*, *Am. J. Pathol.* **180**, 599–607 (2012).
5. T. Sato, H. Clevers, *Methods Mol. Biol.* **945**, 319–328 (2013).
6. T. A. Ince *et al.*, *Cancer Cell* **12**, 160–170 (2007).
7. J. Debnath, S. K. Muthuswamy, J. S. Brugge, *Methods* **30**, 256–268 (2003).
8. G. Dontu *et al.*, *Genes Dev.* **17**, 1253–1270 (2003).
9. D. Dias-Santagata *et al.*, *EMBO Mol. Med.* **2**, 146–158 (2010).
10. M. S. Lawrence *et al.*, *Nature* **505**, 495–501 (2014).
11. Q. X. Zhang, A. Borg, D. M. Wolf, S. Oesterreich, S. A. Fuqua, *Cancer Res.* **57**, 1244–1249 (1997).
12. D. R. Robinson *et al.*, *Nat. Genet.* **45**, 1446–1451 (2013).
13. W. Toy *et al.*, *Nat. Genet.* **45**, 1439–1445 (2013).
14. S. Li *et al.*, *Cell Reports* **4**, 1116–1130 (2013).
15. K. Merenbakh-Lamin *et al.*, *Cancer Res.* **73**, 6856–6864 (2013).
16. The Cancer Genome Atlas Network, *Nature* **490**, 61 (2012).
17. M. J. Garnett *et al.*, *Nature* **483**, 570–575 (2012).
18. K. E. Weis, K. Ekena, J. A. Thomas, G. Lazennec, B. S. Katzenellenbogen, *Mol. Endocrinol.* **10**, 1388–1398 (1996).
19. J. Baselga *et al.*, *N. Engl. J. Med.* **366**, 520–529 (2012).
20. Y. Wang, J. B. Trepel, L. M. Neckers, G. Giaccone, *Curr. Opin. Investig. Drugs* **11**, 1466–1476 (2010).
21. P. Furet *et al.*, *Bioorg. Med. Chem. Lett.* **23**, 3741–3748 (2013).
22. P. R. Gavine *et al.*, *Cancer Res.* **72**, 2045–2056 (2012).
23. M. Mohammadi *et al.*, *EMBO J.* **17**, 5896–5904 (1998).
24. M. Pollak, *Nat. Rev. Cancer* **12**, 159–169 (2012).
25. I. Baccelli *et al.*, *Nat. Biotechnol.* **31**, 539–544 (2013).
26. L. Zhang *et al.*, *Sci. Transl. Med.* **5**, 180ra48 (2013).

ACKNOWLEDGMENTS

We are grateful to all the patients who participated in this study. We thank Dr. Lecia Sequist for coordinating the clinical studies, A. McGovern, C. Hart, and the Massachusetts General Hospital (MGH) clinical research coordinators P. Spuhler, A. Shah, J. Ciciliano, and V. Pai for bioengineering technical support; R. Milano, K. Lynch, H. Robinson, and M. Liebers for technical support; L. Collins (Beth Israel Deaconess Medical Center) for providing pathological specimens; and L. Libby for mouse studies. N. Aceto is a fellow of the Human Frontiers Science Program, the Swiss National Science Foundation, and the Swiss Foundation for Grants in Biology and Medicine. This work was supported by grants from the Breast Cancer Research Foundation (D.A.H), Stand Up to Cancer (D.A.H., M.T., S.M.), the Wellcome Trust (D.A.H., C.B.), National Foundation for Cancer Research (D.A.H.), NIH CA129933 (D.A.H.), NIBIB EB008047 (M.T., D.A.H.), Susan G. Komen for the Cure KG09042 (S.M.), National Cancer Institute–MGH Proton Federal Share Program (S.M.), the MGH-Johnson and Johnson Center for Excellence in CTCs (M.T., S.M.), and the Howard Hughes Medical Institute (M.Y., D.A.H.). A.J.I. holds equity in, and is a paid consultant for, Enzymatics, Inc. M.T., D.A.H., and the Massachusetts General Hospital have filed for patent protection for the CTC-iChip technology. RNA-Seq reads have been deposited into Gene Expression Omnibus: uncultured CTCs (accession no. GSE51827); the six cultured CTC lines (accession no. GSE55807).

SUPPLEMENTARY MATERIALS

www.sciencemag.org/content/345/6193/216/suppl/DC1
Materials and Methods
Figs. S1 to S15
Tables S1 to S3
References (*27*–*30*)

13 January 2014; accepted 10 June 2014
10.1126/science.1253533

BACTERIAL CELL WALL

MurJ is the flippase of lipid-linked precursors for peptidoglycan biogenesis

Lok-To Sham,[1] Emily K. Butler,[2] Matthew D. Lebar,[3] Daniel Kahne,[3,4] Thomas G. Bernhardt,[1]* Natividad Ruiz[2]*

Peptidoglycan (PG) is a polysaccharide matrix that protects bacteria from osmotic lysis. Inhibition of its biogenesis is a proven strategy for killing bacteria with antibiotics. The assembly of PG requires disaccharide-pentapeptide building blocks attached to a polyisoprene lipid carrier called lipid II. Although the stages of lipid II synthesis are known, the identity of the essential flippase that translocates it across the cytoplasmic membrane for PG polymerization is unclear. We developed an assay for lipid II flippase activity and used a chemical genetic strategy to rapidly and specifically block flippase function. We combined these approaches to demonstrate that MurJ is the lipid II flippase in *Escherichia coli*.

Bacteria use polyisoprenoid-linked oligosaccharides to assemble the essential peptidoglycan (PG) matrix that surrounds their cytoplasmic membrane and fortifies their cell envelope against high internal osmotic pressure (*1*). The building block of PG is a disaccharide-pentapeptide that is synthesized at the cytoplasmic leaflet of the inner membrane (IM) as a precursor known as lipid II (Fig. 1A) (*1*, *2*). This precursor must be flipped across the membrane for cell wall synthesis. The identity of the lipid II flippase has been controversial, with the debate centered on two candidates: MurJ-like and FtsW/RodA-like proteins

[1]Department of Microbiology and Immunobiology, Harvard Medical School, Boston, MA 02115, USA. [2]Department of Microbiology, Ohio State University, Columbus, OH 43210, USA. [3]Department of Chemistry and Chemical Biology, Harvard University, Cambridge, MA 02138, USA. [4]Department of Biological Chemistry and Molecular Pharmacology, Harvard Medical School, Boston, MA 02115, USA.
*Corresponding author. E-mail: thomas_bernhardt@hms.harvard.edu (T.G.B.); ruiz.82@osu.edu (N.R.)

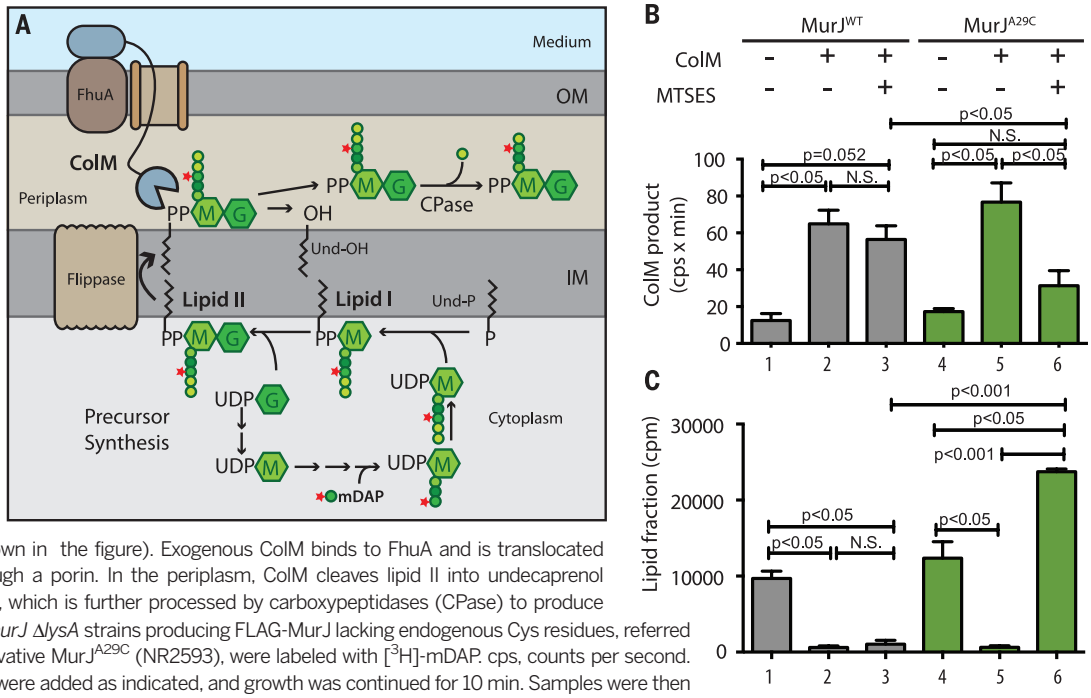

Fig. 1. In vivo assay for lipid II flippase activity. (**A**) PG precursor synthesis starts with the conversion of UDP-*N*-acetylglucosamine (UDP-G) to UDP-*N*-acetylmuramic acid (UDP-M), followed by the addition of amino acids (represented by colored spheres) to UDP-M to form the pentapeptide (pep5) stem (L-Ala-γ-D-Glu-m-DAP-D-Ala-D-Ala). The [^{3}H]-mDAP label is indicated by the red star. The UDP sugars are transferred to undecaprenol-P (Und-P) in the IM to form lipid II, which is flipped across the IM to expose the disaccharide-pep5 (M_{pep5}-G) for polymerization and cross-linking into PG (not shown in the figure). Exogenous ColM binds to FhuA and is translocated across the OM, presumably through a porin. In the periplasm, ColM cleaves lipid II into undecaprenol (Und-OH) and soluble PP-M_{pep5}-G, which is further processed by carboxypeptidases (CPase) to produce PP-M_{pep4}-G. (**B** and **C**) Cells of Δ*murJ* Δ*lysA* strains producing FLAG-MurJ lacking endogenous Cys residues, referred to as MurJ^{WT} (NR2592) or its derivative MurJ^{A29C} (NR2593), were labeled with [^{3}H]-mDAP. cps, counts per second. After 15 min, ColM and/or MTSES were added as indicated, and growth was continued for 10 min. Samples were then withdrawn and either extracted with hot water alone or sequentially with water, then butanol. Hot-water extracts were subjected to HPLC and radiodetection to quantify the labeled ColM product (B); scintillation counting was used to quantify label in the lipid (butanol) fraction (C). See figs. S1 to S4 for experimental details and peak identification. Shown are the mean ± SD from three experiments. *P* value determined with Student's *t* test. N.S., not significant.

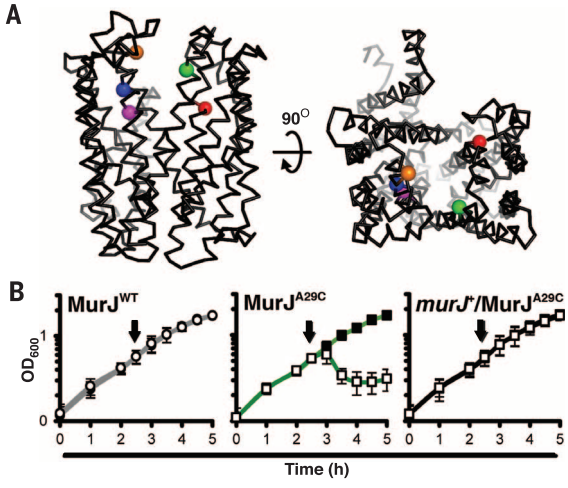

Fig. 2. MTSES specifically inhibits the function of MurJ^{A29C}. (**A**) Structural model of MurJ (*8*). Sensitivity to MTSES is limited to specific residues within the MurJ cavity: residues 29 (green) in transmembrane domain (TMD) 1; 49 (red) in TMD 2; and 263 (orange), 269 (blue), and 273 (magenta) in TMD 8. (**B**) Effect of MTSES on the growth of haploid cells producing MurJ^{WT} (left) or MurJ^{A29C} in glucose M63 medium. OD_{600}, optical density at 600 nm. Lysis of MurJ^{A29C} cells is suppressed by the presence of a wild-type *murJ* allele (right). Arrows indicate the time of MTSES addition; solid symbols, no MTSES; open symbols, MTSES-treated. Data represent mean ± SD from three experiments. See fig. S5 for the MTSES sensitivity of other variants.

(*3*–*6*). MurJ is a polytopic IM protein and a member of the MOP (multidrug/oligo-saccharidyl-lipid/polysaccharide) exporter superfamily (*7*). It is essential in *Escherichia coli*. Cells depleted of MurJ fail to complete PG biogenesis, accumulate PG precursors, and lyse (*4*, *6*). A three-dimensional structural model and corresponding transmembrane topology of MurJ are similar to those of MOP exporters of amphipathic drugs and undecaprenyl-PP–linked oligosaccharides (*8*). Furthermore, a hydrophilic central cavity in MurJ is essential for function. FtsW and its paralog RodA are polytopic IM proteins that belong to the SEDS (shape, elongation, division, and sporulation) superfamily and are required for PG synthesis during division (FtsW) or elongation (RodA) (*3*, *5*, *9*). Support for SEDS proteins functioning as flippases is based on in vitro studies in which lipid II flippase activity was detected for purified FtsW incorporated into liposomes (*10*).

The identity of the lipid II flippase has been sought after for decades (*2*). Determining which proteins flip lipid II in vivo requires a sensitive method to detect lipid II flippase activity and a method to connect this activity to a specific protein within the cell. When added to *E. coli*, the protein toxin colicin M (ColM) is translocated into the periplasm, where it cleaves lipid II (Fig. 1A) (*11*, *12*). We therefore reasoned that ColM could be used in an assay to detect freshly flipped lipid II. To evaluate this possibility, cells were metabolically labeled with [^{3}H]-mDAP, an amino acid unique to the PG peptide, and either left untreated or incubated with purified ColM. Cells were then extracted with hot water followed by butanol to separate water-soluble PG intermediates and ColM-derived products from lipid-linked PG precursors. High-performance liquid chromatography (HPLC) analysis of the water-soluble extract revealed a new peak in the ColM-treated samples (Fig. 1B and fig. S1), and its appearance correlated with the loss of radiolabel in the butanol extract (Fig. 1C). Moreover, increasing the cellular lipid II concentration by overproducing the lipid-carrier synthase UppS (*2*) enhanced the production of the ColM-specific peak (fig. S2). The ColM-specific product was identified as PP-M_{pep4}-G (figs. S3 and S4), which presumably results from the processing of the ColM product, PP-M_{pep5}-G, by a carboxypeptidase (Fig. 1A). Because carboxypeptidases function only in the periplasm (*1*), this result confirms that ColM acts on flipped lipid II.

To test whether MurJ flips lipid II, a method to rapidly and specifically inactivate it was needed. A collection of 39 functional single-Cys MurJ variants modifiable by the Cys-reacting molecule MTSES (2-sulfonatoethyl methanethiosulfonate) was previously used to determine the membrane topology of MurJ (*8*). We asked whether any of these mutant proteins were rendered nonfunctional by derivitization with MTSES. Treatment of Cys-free MurJ (MurJ^{WT}) cells with MTSES had no effect on growth, but the addition of MTSES to cells producing derivatives with Cys substitutions

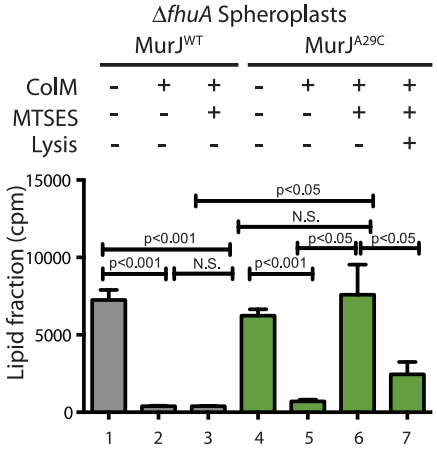

Fig. 3. MurJ activity is required for ColM-dependent cleavage of lipid II in spheroplasts. Cells lacking the ColM receptor FhuA and producing the indicated MurJ variants were grown, labeled, and treated with MTSES as for Fig. 1. Spheroplasts were then prepared. In all but one case, spheroplasts were pelleted and resuspended in ColM reaction buffer with sucrose, and MTSES (0.8 mM) was added as indicated. The lysis + sample was resuspended in buffer lacking sucrose to lyse the spheroplasts. ColM (100 μg) was added to the prepared spheroplasts as indicated, and they were incubated for 15 min at 37°C. Lipid intermediates were detected by scintillation counting after butanol extraction. Statistics are as for Fig. 1. cpm, counts per minute.

at positions 29, 49, 263, and 269 rapidly induced lysis, suggesting that MurJ function, and thus PG synthesis, was inhibited (Fig. 2 and fig. S5). In contrast, treatment of MurJ^{E273C} cells with MTSES caused cell shape defects and limited lysis indicative of an incomplete PG synthesis block due to partial MurJ inhibition. The toxicity of MTSES labeling was suppressed in all five strains by the presence of the wild-type *murJ* allele (Fig. 2 and fig. S5). Thus, MTSES specifically and rapidly inhibits these single-Cys MurJ variants. We chose MurJ^{A29C} (Fig. 2, and figs. S6 and S7) to assess the effect of MurJ inactivation on lipid II flipping.

This chemical genetic method for MurJ inactivation was compatible with the in vivo flippase assay. MTSES treatment of MurJ^{WT} cells did not affect lipid II processing by ColM (Fig. 1, B and C, and fig. S1). Additionally, in the absence of MTSES, MurJ^{A29C} cells behaved like MurJ^{WT} cells (Fig. 1, B and C, and fig. S1). However, simultaneous addition of MTSES and ColM to MurJ^{A29C} cells failed to produce significant quantities of the ColM-dependent product PP-M_{pep4}-G. In fact, radiolabel in the lipid fraction increased in these samples (Fig. 1, B and C, and fig. S1). Thus, when MurJ^{A29C} was inactivated with MTSES, lipid II was protected from ColM cleavage, and label accumulated in the lipid fraction as observed previously for MurJ-depletion strains (*4*, *6*).

The protection of lipid II from ColM cleavage upon MurJ^{A29C} inactivation suggests that either lipid II is not flipped or that inhibiting MurJ^{A29C} somehow interferes with ColM import or activity. To investigate this, we performed our assay using spheroplasting to remove the outer membrane (OM) barrier (*13*) and provide ColM with direct access to flipped lipid II. In the absence of MTSES, ColM treatment of MurJ^{WT} or MurJ^{A29C} spheroplasts reduced the amount of label in the lipid fraction (Fig. 3), indicating that lipid II was actively flipped and thus cleaved by ColM. Although MTSES did not affect ColM activity on MurJ^{WT} spheroplasts, it completely abolished lipid II processing by ColM in MurJ^{A29C} spheroplasts (Fig. 3). Moreover, lysis of MTSES-treated MurJ^{A29C} spheroplasts restored lipid II processing, indicating that the intact IM impeded the access of ColM to lipid II. Thus, MurJ appears to act as a lipid II flippase.

When MurJ^{A29C} was inactivated with MTSES, flippase activity was reduced to a level that was barely detectable and was incompatible with life. This observation indicates that the essential function of MurJ is to translocate lipid II and that other factors catalyzing lipid II flipping are unlikely to exist in *E. coli*. Nevertheless, we investigated the requirement of SEDS proteins for flippase activity by depleting FtsW in a Δ*rodA* strain. We found that lipid II flipping remained robust in this background (figs. S8 and S9). Although it is possible that residual FtsW in these cells was sufficient for the observed activity, this result suggests that SEDS proteins are not responsible for lipid II flippase activity in vivo. Alternatively, the decrease in levels of PG lipid intermediates upon FtsW depletion (fig. S9) suggests that either synthesis of PG precursors or recycling of undecaprenyl-P might be affected by the loss of SEDS activity. From these data and the fact that MurJ contains a central solvent-exposed cavity that is essential for function (*8*), we conclude that MurJ is the lipid II flippase in *E. coli*.

REFERENCES AND NOTES

1. A. Typas, M. Banzhaf, C. A. Gross, W. Vollmer, *Nat. Rev. Microbiol.* **10**, 123–136 (2012).
2. A. Bouhss, A. E. Trunkfield, T. D. Bugg, D. Mengin-Lecreulx, *FEMS Microbiol. Rev.* **32**, 208–233 (2008).
3. M. A. de Pedro, W. D. Donachie, J. V. Höltje, H. Schwarz, *J. Bacteriol.* **183**, 4115–4126 (2001).
4. A. Inoue *et al.*, *J. Bacteriol.* **190**, 7298–7301 (2008).
5. M. M. Khattar, K. J. Begg, W. D. Donachie, *J. Bacteriol.* **176**, 7140–7147 (1994).
6. N. Ruiz, *Proc. Natl. Acad. Sci. U.S.A.* **105**, 15553–15557 (2008).
7. R. N. Hvorup *et al.*, *Eur. J. Biochem.* **270**, 799–813 (2003).
8. E. K. Butler, R. M. Davis, V. Bari, P. A. Nicholson, N. Ruiz, *J. Bacteriol.* **195**, 4639–4649 (2013).
9. A. O. Henriques, P. Glaser, P. J. Piggot, C. P. Moran Jr., *Mol. Microbiol.* **28**, 235–247 (1998).
10. T. Mohammadi *et al.*, *EMBO J.* **30**, 1425–1432 (2011).
11. M. El Ghachi *et al.*, *J. Biol. Chem.* **281**, 22761–22772 (2006).
12. T. Touzé *et al.*, *Biochem. Soc. Trans.* **40**, 1522–1527 (2012).
13. L. A. Heppel, *Science* **156**, 1451–1455 (1967).

ACKNOWLEDGMENTS

We thank D. Mengin-Lecreulx for the generous gift of plasmids for ColM production and H. Joseph and R. M. Davis for their technical assistance. Research was supported by funds from the American Heart Association (L.S.) and the National Institutes of Health (NIH) under award numbers F32GM103056 (M.D.L.), R01GM100951 (N.R.), R01AI099144 (T.G.B.), and R01GM76710 (D.K.). The content is solely the responsibility of the authors and does not necessarily represent the official views of NIH. For additional data, see the supplementary materials.

SUPPLEMENTARY MATERIALS

www.sciencemag.org/content/345/6193/220/suppl/DC1
Materials and Methods
Figs. S1 to S9
Tables S1 and S2
References (*14*–*29*)

8 April 2014; accepted 28 May 2014
10.1126/science.1254522

GENETIC OSCILLATIONS

A Doppler effect in embryonic pattern formation

Daniele Soroldoni,[1,2,3]* David J. Jörg,[4]* Luis G. Morelli,[1,5] David L. Richmond,[1] Johannes Schindelin,[1,6] Frank Jülicher,[4] Andrew C. Oates[1,2,3]†

During embryonic development, temporal and spatial cues are coordinated to generate a segmented body axis. In sequentially segmenting animals, the rhythm of segmentation is reported to be controlled by the time scale of genetic oscillations that periodically trigger new segment formation. However, we present real-time measurements of genetic oscillations in zebrafish embryos showing that their time scale is not sufficient to explain the temporal period of segmentation. A second time scale, the rate of tissue shortening, contributes to the period of segmentation through a Doppler effect. This contribution is modulated by a gradual change in the oscillation profile across the tissue. We conclude that the rhythm of segmentation is an emergent property controlled by the time scale of genetic oscillations, the change of oscillation profile, and tissue shortening.

Segmental patterns are common throughout nature. In animals from diverse phyla, segmentation of the body axis occurs during embryogenesis, and in most cases, segments are added sequentially, with a distinct period as the body axis elongates. Recent findings indicate that a common mechanism involving genetic oscillations underlies this morphological segmentation in vertebrates and arthropods (*1*). We investigated how the time scale of

genetic oscillations determines the timing of segmentation.

In sequentially segmenting animals, the unsegmented tissue exhibits patterns of oscillating gene expression reminiscent of waves that travel from the posterior to the anterior, where they arrest. These waves are kinematic and emerge at the tissue level from the coordinated output of cellular genetic oscillators (*2*–*5*). This situation is similar to news ticker displays in which a moving pattern is caused by on-and-off switching of individual stationary lamps (*6*). The sequential arrest of the kinematic waves is thought to prefigure the position and set the period of segment formation (*7*). During vertebrate segmentation, the onset and arrest of these waves are controlled by a complex genetic network that acts in the unsegmented presomitic mesoderm (PSM). The PSM gives rise to the somites, which are the precursors of adult segments (vertebrae, ribs, and associated skeletal muscles). Since its discovery, it has been generally assumed that this network, termed the "segmentation clock," resembles a genetic clock with a single, well-defined period (*3*). In this simplified picture, both the onset and arrest of the kinematic waves happen with the same period, which is identical to that of segment formation (*6*–*9*). However, these fundamental assumptions have not been tested systematically because it has proven difficult to visualize oscillating gene expression in real time and simultaneously quantify the timing of morphological segmentation over a substantial time scale (*2*, *4*, *10*).

To this end, we used a transgenesis approach to generate a reliable reporter for the oscillating gene *her1*, named *Looping* (fig. S1), and developed a multidimensional time-lapse setup designed to systematically compare the periods of morphological segmentation and genetic oscillations in multiple zebrafish embryos (Fig. 1A). Our imaging setup was sensitive enough to detect reporter oscillations in real time and fast enough to simultaneously record segment formation in a population of 20 embryos (Fig. 1B and movie S1). Embryonic growth was not affected by our mounting technique, which ensured that wild-type and transgenic siblings developed normally (fig. S2). With this approach, we observed that multiple kinematic waves (Fig. 1C, color arrowheads, and movie S1) travel from the posterior to anterior PSM at each point in time. As expected, we found that the arrest of reporter oscillations in the anterior PSM coincided with the formation of every new segment (Fig. 1B, arrowhead, and movie S2) (*2*, *7*, *11*). As the waves travel along the tissue, their wavelength shortens (Fig. 1C, arrows); thus, the wave pattern can be characterized by the number of waves and by their wavelengths.

To quantify the timing of onset and arrest of kinematic waves, we locally measured the reporter expression in the anterior and the posterior PSM (Fig. 1D, circles). From previous studies, it was unclear whether the posterior PSM oscillates (*2*, *12*). We found that both regions oscillate, although with different reporter amplitudes (Fig. 1D, bottom diagram). We

[1]Max Planck Institute of Molecular Cell Biology and Genetics, Pfotenhauerstr 108, 01307 Dresden, Germany. [2]Medical Research Council (MRC)–National Institute for Medical Research, The Ridgeway, Mill Hill, London, NW7 1AA, UK. [3]Department of Cell and Developmental Biology, University College London, Gower Street, London, WC1E 6BT, UK. [4]Max Planck Institute for the Physics of Complex Systems, Nöthnitzer Strasse 38, 01187 Dresden, Germany. [5]Departamento de Física, Facultad de Ciencias Exactas y Naturales, Universidad de Buenos Aires and Instituto de Física de Buenos Aires, Consejo Nacional de Investigaciones Científicas y Técnicas, Pabellón 1, Ciudad Universitaria, 1428 Buenos Aires, Argentina. [6]Laboratory for Optical and Computational Instrumentation, University of Wisconsin at Madison, 271 Animal Sciences, 1675 Observatory Drive, Madison, WI 53706, USA.
*These authors contributed equally to this work. †Corresponding author. E-mail: aoates@nimr.mrc.ac.uk

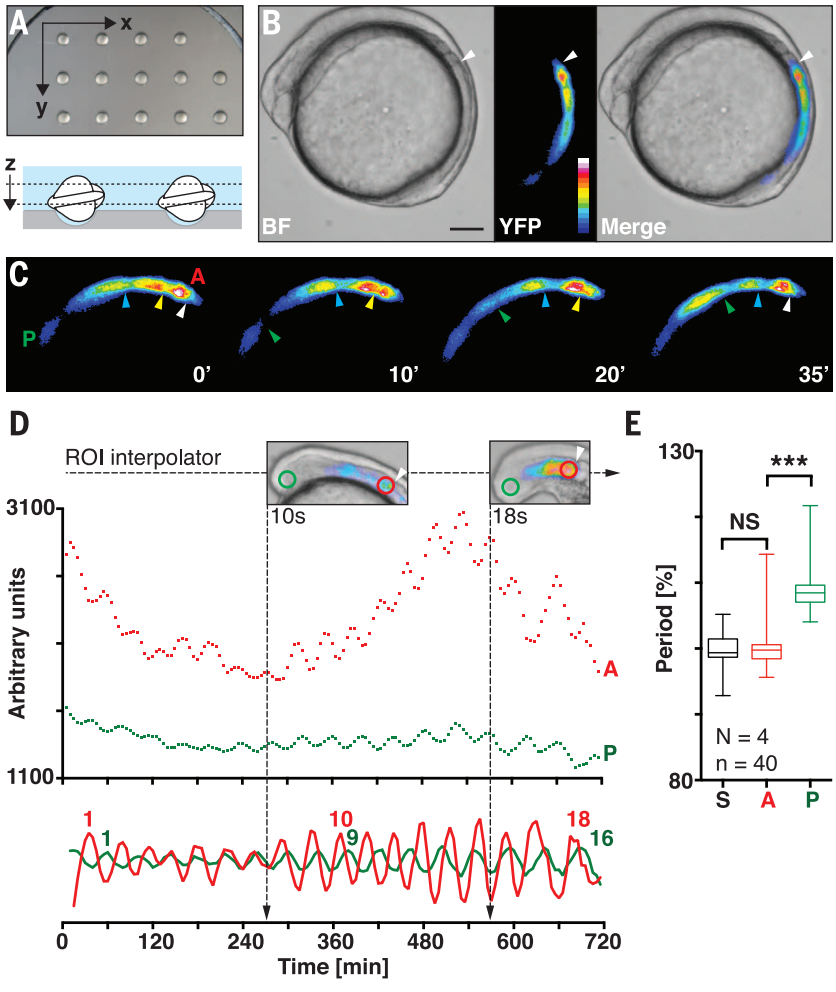

Fig. 1. Oscillations in the anterior and posterior presomitic mesoderm (PSM) have different periods. (**A**) Mounting of zebrafish embryos for multidimensional imaging. Each time-lapse experiment consists of 20 *xy* positions with a *z* stack (6 slices at 20 μm intervals) to keep the PSM in focus. (**B**) Snapshots from *Looping*, a transgenic reporter of the oscillating gene *her1*, reveal that Her1::YFP (yellow fluorescent protein) fusion protein is confined to the PSM. The white arrowhead marks the most recently formed somite/segment boundary. Scale bar, 100 μm; LUT, high (white) to low (blue) reporter intensity; BF, brightfield. (**C**) Multiple kinematic waves (different colored arrowheads) emerge from the posterior PSM ("P") and travel anteriorly ("A") till they arrest (white arrowhead). (**D**) A region of interest (ROI) interpolator is used to measure the average reporter intensity in the posterior (inset, green circle) and anterior (inset, red circle) PSM. Both regions oscillate but experience a different number of oscillations (annotated with peak number). (**E**) Periods of morphological segmentation ("S") and anterior ("A") oscillations are identical, whereas posterior ("P") oscillations occur significantly slower (~9%). Four independent experiments (*N*), forty individual embryos (*n*), Whiskers min/max (*t* test, Welch correction, ***$P < 0.0001$).

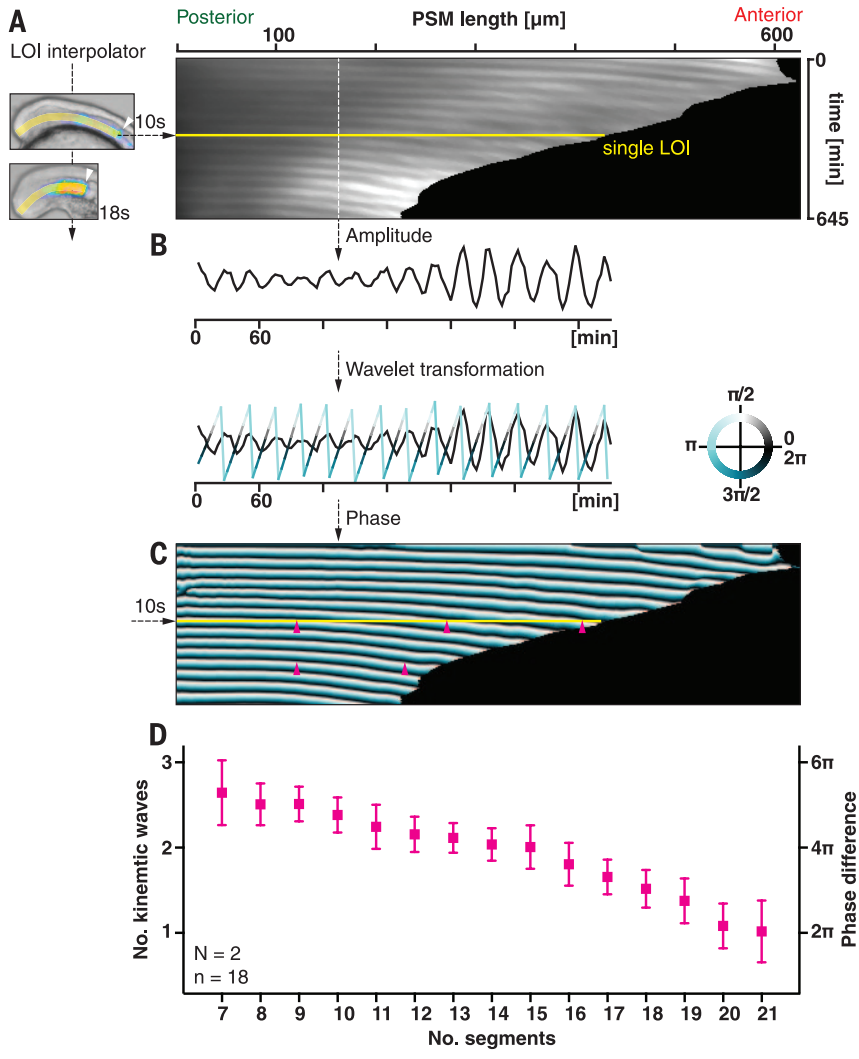

Fig. 2. The wave pattern in the PSM changes continuously as the tissue length decreases. (**A**) A LOI interpolator is used to measure the reporter intensity along the entire PSM and construct a kymograph that captures the trajectories of slowing, kinematic waves (tilted white ridges) and demonstrates the substantial decrease in PSM length. (**B**) Wavelet transformation. Each vertical line of the kymograph (white dotted line) is used to translate amplitude into phase information and construct (**C**) a phase map that is independent of local amplitude fluctuations. (A) and (C) show a single representative embryo. Yellow horizontal lines in a phase map yields the number of kinematic waves at a given time point, which (**D**) decreases with increasing segment number. The local wavelength (distance between purple ticks) also decreases over time. Data are from two independent replicates (*N*), 18 embryos (*n*).

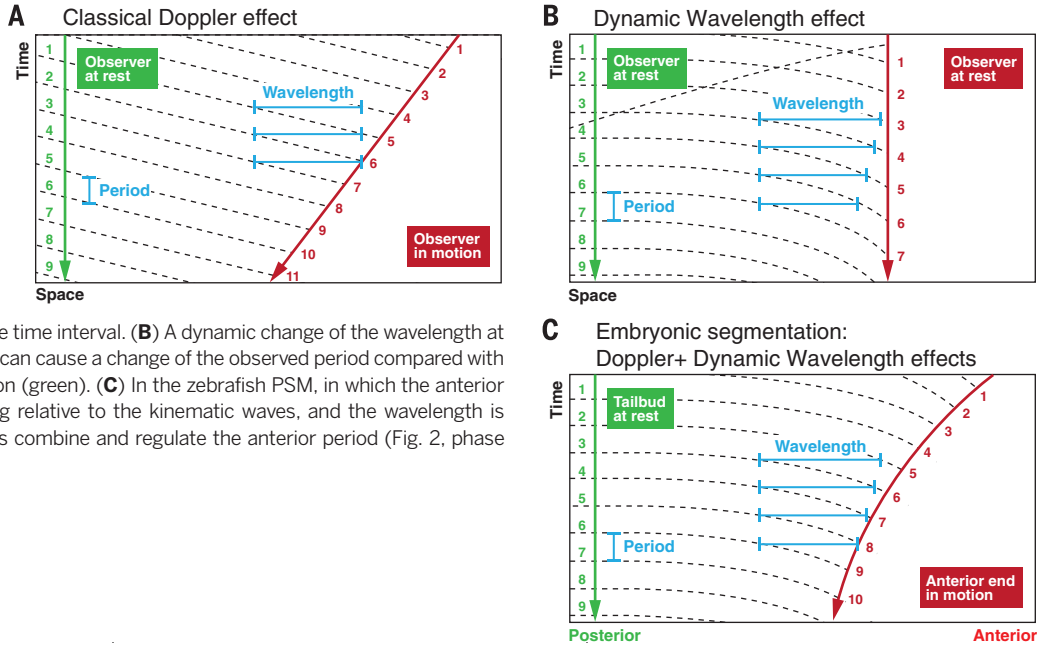

Fig. 3. Doppler and Dynamic Wavelength effects modulate the period of segmentation. (**A**) In the classical Doppler effect, an observer moving toward a sound source perceives an increased sound frequency as compared with what an observer at rest perceives. This is indicated by the larger number of wave peaks (crossing dashed lines) that an observer in motion (red) experiences compared with an observer at rest (green) during the same time interval. (**B**) A dynamic change of the wavelength at the position of an observer at rest (red) can cause a change of the observed period compared with an observer at rest at a different position (green). (**C**) In the zebrafish PSM, in which the anterior end acts as an observer that is moving relative to the kinematic waves, and the wavelength is dynamically changing, these two effects combine and regulate the anterior period (Fig. 2, phase map, in comparison).

observed that within the same time interval, the number of oscillations in the posterior was smaller than in the anterior: during nine posterior oscillations, 10 oscillations occur in the anterior (Fig. 1D). Consequently, oscillations in the posterior are slower, with an average offset of about 9% (8.8 ± 0.52%, $P < 0.0001$) (Fig. 1E). This finding is not consistent with a single, well-defined period for the segmentation clock. Next, we directly compared the periods of genetic oscillations and segment formation, focusing on the trunk segmentation where the segmentation period is known to be constant (*13*). We found that the period of anterior oscillations is the same as segmentation (Fig. 1E). Thus, the period of segmentation matches the period with which kinematic waves arrest in the anterior but is significantly faster than the period of genetic oscillations in the posterior (Fig. 1E): During nine posterior oscillations, 10 segments are formed.

To understand this paradoxical period offset, we aimed to obtain a comprehensive picture of reporter expression throughout the PSM. To this end, we generated kymographs that display the average reporter intensity along lines of interest (LOIs) throughout the entire PSM (Fig. 2A). Each horizontal line of pixels in this kymograph represents a LOI at a specific time point, and its length corresponds to the PSM length. Obvious features of all kymographs are the trajectories of kinematic waves and the substantial shortening of the PSM over time (average total shortening is 60% after 13 segments). This implies the relative motion of the anterior end of the PSM, where the waves arrest, toward the posterior end. As a consequence, the anterior end moves into the approaching kinematic waves, shortening the time interval between their onset and arrest. This is reminiscent of the Doppler effect, in which an observer moving toward a sound source perceives an increased sound frequency as compared with what an observer at rest perceives.

In the presence of a Doppler effect, the number of kinematic waves decreases as the tissue shortens (supplementary text). To test this expectation, we analyzed the spatio temporal properties of kinematic waves for a population of embryos by generating phase maps from the intensity kymographs (Fig. 2, B and C; fig. S3; and supplementary text). These phase maps capture the spatial and temporal dynamics of oscillations while being independent of local amplitude variations (Fig. 2B). A horizontal line of pixels in the phase map captures the profile of phases at a specific time point (Fig. 2C, yellow line); a phase increment of 2π along a horizontal line corresponds to one kinematic wave, and the distance covered by this increment is the local wavelength (Fig. 2C, pink ticks, and movie S3). Therefore, the number of kinematic waves can be determined by the antero-posterior phase difference divided by 2π. These phase maps can be used to determine whether the number of kinematic waves changes over time with a subinteger resolution exceeding that of simple peak counting in a kymograph. We found that the average number of kinematic waves decreases with the number of formed segments (Fig. 2D and movies S4 and S5). Consistent with this analysis, a decrease in the number of kinematic waves can also be observed from snapshots of endogenous oscillating genes in wild-type siblings at successive developmental times (fig. S4). These findings confirm the presence of a Doppler effect.

Such a Doppler effect would not occur if the wave pattern scaled (supplementary text). Scaling means that the wave pattern shrinks proportionally with the length of the tissue. Such a scaling of the wave pattern has been recently reported in in vitro–cultured mouse PSM explants (*5*) and requires that the number of kinematic waves visible along the PSM remains constant in time. The change in number of waves observed here supports the presence of a Doppler effect and rules out scaling of the wave pattern in zebrafish.

Can we conclude that a Doppler effect alone accounts for the observed decrease in kinematic wave number and the measured period offset? In a classical Doppler effect with only the observer in motion, the wavelength of the sound waves remains constant in time (Fig. 3A). In our analogy, this would imply that the anterior end of the PSM (observer) is in motion while the local wavelength remains constant, resulting in a shortened anterior period. However, from our phase maps we determined that the local wavelength is not constant but decreases over time (Figs. 2C and 3B, figs. S5 and S6, and supplementary text). This dynamic change of the wavelength tends to prolong the anterior period (Fig. 3B, fig. S7, and supplementary text) and thus opposes the Doppler effect. Hence, the period of segmentation is modulated through the combination of these two opposing effects, the Doppler effect and the dynamic wavelength (Fig. 3C and fig. S7). Although the relative contribution of these effects varies during development, the experimentally observed offset between anterior and posterior period is due to the larger average magnitude of the Doppler compared with the Dynamic Wavelength effect (fig. S7 and supplementary text). The Dynamic Wavelength effect discovered here is a general principle, and there is no reason to assume that it is restricted to the zebrafish PSM. An analogous effect would arise in a wave-carrying medium from a space- and time-dependent change of refraction.

Traditionally, genetic oscillations in the posterior PSM have been viewed as the pacemaker for the segmentation process, which is emphasized in the term "segmentation clock." Our findings show that the clock metaphor is insufficient to understand the timing of segment formation. In addition to the time scale set by the genetic network controlling the oscillations, the change in length of the PSM and the change of the kinematic wavelength must be included to understand the period of segmentation observed in vivo. The biological mechanisms by which the tissue length and kinematic wavelength change remain open questions. Our work highlights the need to go beyond descriptions of embryonic segmentation that are based on steady-state or scaling conditions and reveals the consequences of the spatial features of the wave pattern for the timing of segmentation.

REFERENCES AND NOTES

1. A. F. Sarrazin, A. D. Peel, M. Averof, *Science* **336**, 338–341 (2012).
2. E. A. Delaune, P. François, N. P. Shih, S. L. Amacher, *Dev. Cell* **23**, 995–1005 (2012).
3. I. Palmeirim, D. Henrique, D. Ish-Horowicz, O. Pourquié, *Cell* **91**, 639–648 (1997).
4. Y. Masamizu *et al*., *Proc. Natl. Acad. Sci. U.S.A.* **103**, 1313–1318 (2006).
5. V. M. Lauschke, C. D. Tsiairis, P. François, A. Aulehla, *Nature* **493**, 101–105 (2013).
6. A. C. Oates, L. G. Morelli, S. Ares, *Development* **139**, 625–639 (2012).
7. B. Bénazéraf, O. Pourquié, *Annu. Rev. Cell Dev. Biol.* **29**, 1–26 (2013).
8. F. Giudicelli, E. M. Ozbudak, G. J. Wright, J. Lewis, *PLOS Biol.* **5**, e150 (2007).
9. L. G. Morelli *et al*., *HFSP J* **3**, 55–66 (2009).
10. D. Soroldoni, A. C. Oates, *Curr. Opin. Genet. Dev.* **21**, 600–605 (2011).
11. A. Aulehla *et al*., *Nat. Cell Biol.* **10**, 186–193 (2008).
12. A. Mara, J. Schroeder, C. Chalouni, S. A. Holley, *Nat. Cell Biol.* **9**, 523–530 (2007).
13. C. Schröter *et al*., *Dev. Dyn.* **237**, 545–553 (2008).

ACKNOWLEDGMENTS

We thank L. Wetzel, L. Rohde, C. Poulet, C. Eugster, M. Gonzales-Gaitan, and J. Firmino, for comments on the manuscript; D. Hasselhoff for mental support; and the fish and light microscopy facilities of the Max Planck Institute of Molecular Cell Biology and Genetics. This work was supported by the Max Planck Society and the Medical Research Council (MC_UP_1202/3); D.S., L.G.M., and A.C.O. by the European Research Council (ERC) under the European Communities 7th Framework Programme (FP7/2007–2013)/(ERC grant 207634); D.L.R. by a European Molecular Biology Organization fellowship [ALTF1402-2011]; and A.C.O. and D.S. by the Wellcome Trust (WT098025MA). The original time-lapse recordings in this study are available for anonymous download via the Web site www.nimr.mrc.ac.uk/supplementary/oaties. The ROI and LOI are available as plugins via the Fiji website www.fiji.sc/Fiji. D.S., D.J.J., L.G.M., and A.C.O. designed experiments; D.S. performed experiments; J.S. developed analysis tools; D.S., D.J.J., L.G.M., F.J., and A.C.O. analyzed data; D.S., D.J.J., D.L.R., L.G.M., F.J., and A.C.O. developed the concepts and wrote the paper.

SUPPLEMENTARY MATERIALS

www.sciencemag.org/content/345/6193/222/suppl/DC1
Materials and Methods
Supplementary Text
Figs. S1 to S8
Tables S1 and S2
References (*14*–*26*)
Movies S1 to S5

7 March 2014; accepted 10 June 2014
10.1126/science.1253089

Aptamer Kits for Cell Isolation

AptoPrep cell isolation kit products combine the advantage of aptamers' specificity for target cells with the convenience of isolating/eluting a particular cell type from complex cell samples. AptoPrep cell isolation kits deliver positive isolation in as little as 30 minutes. The mild and unique cell releasing technology allows users to isolate bead- and aptamer-free cells in as little as one hour. By incorporating bifunctional aptamers labeled with FITC and biotin, the kits allow researchers to perform cell isolation and flow cytometry analyses simultaneously, further improving their productivity. Supplied as a complete kit (biotinylated aptamer, streptavidin magnetic bead, and buffers), AptoPrep cell isolation products deliver unmatched convenience, increased consistency, and reliability. AMSBIO has also introduced a new range of dye-conjugated monoclonal aptamers specifically designed to monitor protein expression by flow cytometry with high specificity by minimizing the background caused by nonspecific binding.
AMS Biotechnology
For info: +44-(0)-1235-828200
www.amsbio.com/aptamers.aspx

Flow Cytometer

The NovoCyte flow cytometer system addresses a full range of multi-parameter cellular analysis research needs with high performance at a low investment cost, making it more attainable for researchers to have benchtop flow cytometers in their labs. The system enables detection of up to fifteen parameters with enhanced sensitivity and resolution and is customizable to meet researchers' current and future needs with options to add-on at a later date. The NovoCyte flow cytometer is available with one to three laser options, exchangeable filters, multiple sampling options, and flexible analysis formats. Operation is intuitive with automated instrument maintenance functions and advanced data analysis capabilities for greater usability. Other important features enhance usability such as a fixed optical alignment, 24-bit detection dynamic range with no need for PMT voltage adjustment, accurate volumetric-based cell counting, pressure sensors to monitor fluidic status in real-time, and automatic cleaning and de-contamination processes.
Acea Biosciences
For info: 858-724-0928
www.aceabio.com

Traceable Tissue Storage Solution

A new externally threaded 3 mL tube provides a fully traceable storage solution for tissue samples. With a unique 2-D Data Matrix code laser encrypted on the tube bottom, and large human readable code on the tube sidewall, Micronic 3 mL tissue tubes provide easy and unambiguous identification and storage of your donor and transplant samples. The unique 2-D code identifies the sample, its coordinates within a 24-tube storage rack, the particular rack and the location of the rack in your freezer. For highly accurate and reliable results, the tissue tubes are produced from medical-grade polypropylene. The tubes have a wide shallow opening enabling easy loading/removal of tissue samples using tweezers. Produced using a double injection molding process, each Micronic 3 mL tissue tube has a black code surface that cannot be separated from the tube and a transparent sidewall enabling easy visual checking of the enclosed tissue sample.
Micronic
For info: +31-320-277070
www.micronic.com

EarlyTox Cell Integrity Kit

The EarlyTox Cell Integrity Kit is a fast, simple, and reliable fluorescence-based assay for detecting changes in cell viability based on permeability of outer cell membranes (cell integrity). This kit provides an integrated assay solution when combined with hardware and software for the rapid quantification of cell viability. The EarlyTox Cell Integrity Kit is based on two nuclear dyes: EarlyTox Live Red Dye is cell permeable and marks both live and dead cells, while EarlyTox Dead Green Dye is cell impermeable and stains only cells with damaged outer membranes. EarlyTox Live Red Dye is detected by using Cy5 channel (Ex622/Em645 wavelength); EarlyTox Dead Green Dye is detected by using FITC channel (Ex503/Em526nm) wavelength. The kit also contains a proprietary masking reagent to increase assay performance in a homogeneous format. Each kit enables a simple mix-and-read procedure whereby cells are incubated with reagents for 30 minutes and then transferred directly to the imaging instruments for evaluation.
Molecular Devices
For info: 800-635-5577
www.moleculardevices.com/cell-viability

High Performance Centrifuges

Combining high performance and application versatility, Avanti JXN-26 centrifuges offer laboratories an intuitive interface and advanced data management features. The instruments can be run from an Apple iOS or Android device using MobileFuge, the only mobile application available to run and manage laboratory centrifuges. Researchers and facilities managers can leverage the instrument's data management, user tracking, networking, and remote capabilities for ease-of-use and efficiency in biological sample preparation, and to meet quality control standards. Safety, logistics, and quality challenges in multiuser labs and Good Manufacturing Practice environments are met with software designed to improve daily operations across applications. Network functions enable monitoring, diagnostic e-mail, run-log archiving to network locations, and printing to network printers. Fast, efficient service and online help is available, and users can choose from nine operating languages. Scientists can create secure individual profiles and login to MobileFuge to track and manage centrifuge runs remotely.
Beckman Coulter Life Sciences
For info: 800-526-3821
www.beckmancoultercentrifugation.com

Electronically submit your new product description or product literature information! Go to www.sciencemag.org/products/newproducts.dtl for more information.

Newly offered instrumentation, apparatus, and laboratory materials of interest to researchers in all disciplines in academic, industrial, and governmental organizations are featured in this space. Emphasis is given to purpose, chief characteristics, and availability of products and materials. Endorsement by *Science* or AAAS of any products or materials mentioned is not implied. Additional information may be obtained from the manufacturer or supplier.

Downloaded from www.sciencemag.org on July 11, 2014

By **Elisabeth Pain,** *in Barcelona, Spain*

In praise of early independence

Many factors influence success in a science career. Hard work, ambition, flair, and luck played a role in the success of Tim Hunt, who won a share of the 2001 Nobel Prize in physiology or medicine (along with Leland Hartwell and Paul Nurse) for his discovery of cyclins, key regulators of the cell cycle. We caught up with Hunt—now a group leader emeritus at the Clare Hall Laboratories of Cancer Research UK's London Research Institute—during Postdoc Day at the Institute for Research in Biomedicine. Hunt's career demonstrates the importance of two additional success factors: playfulness and early independence. This interview was edited for brevity and clarity.

Q: After a Ph.D. at the University of Cambridge, you did a postdoc at the Albert Einstein College of Medicine. How did it go from there?

A: After a year, the boss went to MIT [Massachusetts Institute of Technology] to set up a new medical school, so it was just me and a technician—Grace Vanderhoff—and we made things up as we went. I usually had two projects going, one with Grace during the day and my own projects, which I did at night. Gradually, the night projects started to go better than the day projects. They allowed me to discover two very important things, which both came through collaborations.

After that, I returned to Cambridge to work in the Department of Biochemistry. And this is another thing that I think was very lucky: I had an independent fellowship from Clare College. I took a fivefold cut in pay, but I found myself among friends, namely Richard Jackson and Tony Hunter. It was a loose federation of graduate students and postdocs, and we could just do whatever we liked. This was terribly satisfactory, and we had a really lovely time.

We were a bit anarchic and bumbling in a way, and I sometimes regretted that I never had any proper, formal biochemical education. We had to work everything out for ourselves. I find myself reacting badly to this idea that there are skill sets you need to have, and you must pass exams to get them. I would rather emphasize the importance of playfulness and of making your own mistakes.

Q: You stood by your results when they were controversial. This takes a lot of self-confidence.

A: You have to be very sure of yourself, it's true, but you're sure of yourself because you know the experiments are robust. I always tell people, "Be your own harshest critic because then nobody can hurt you."

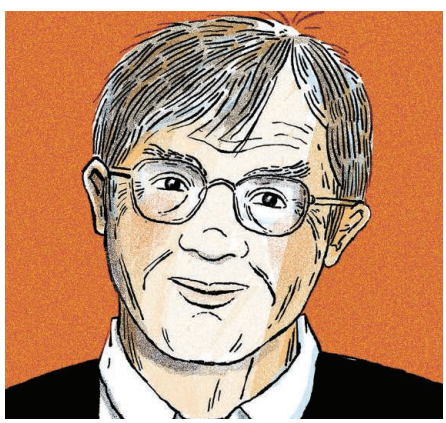

"You must somehow get independent when you are really young, and take responsibility."

Q: Can young scientists nowadays work as independent postdocs?

A: I think so. There are still lots of fellowships around, so it depends on the environment you find yourself in. You must somehow get independent when you are really young, and take responsibility. In general, however, a conventional principal investigator position takes people out of the lab just when they get really good at doing and designing experiments, and that's a shame.

Q: What was the key to your success?

A: Identifying a good problem to work on. That's the most difficult thing. I also think that, in my case, behind it all was a fairly steely ambition. It's perfectly healthy to want to win a Nobel Prize. I didn't have this ambition exactly, but I thought, "Why wouldn't you want to find out the most important thing you possibly could?" In Cambridge, we were surrounded by Nobel laureates. We never felt that we were in the same league as these Sangers, Cricks, and Brenners, but you realized that even if they were Nobel laureates, you knew stuff they didn't, and you also realized what an amazingly heterogeneous bunch they are.

When people ask me, "What is the secret to success?" I always say, "Keep your eyes on the horizon but your feet on the ground, and preferably your nose to the grindstone." In other words, you have to work. ■

Elisabeth Pain is Science *Careers' contributing editor for Europe. For more on life and career issues, visit http://www.sciencecareers.org.*

ILLUSTRATION: ROBERT NEUBECKER

Published by AAAS

cell sciences®
cytokine center

www.cellsciences.com

Buy one, get one free

Stock up now on select cytokines, growth factors and chemokines.

Order any two vials from this list for just $235
Enter promo code CYT241 when you place your order on-line or mention the promo code to get your discount when calling our toll-free number 888-769-1246.

These recombinant proteins are low endotoxin, carrier-free, highly pure, biologically active and suitable for cell culture and animal studies. Get two of the same item or pick any two different items from the list.* See our web site for complete product specifications.

Browse our web site of recombinant proteins, including hundreds more cytokines, growth factors, chemokines and neurotrophins. Bulk quantities of these proteins are available at competitive pricing. Call or visit our web site for details. Cell Sciences also carries corresponding antibodies and ELISA kits.

Catalog No:	Item:	Size:
CRB100B	Recombinant Human BMP-2	10 µg
CRC400B	Recombinant Human CNTF	20 µg
CRF000B	Recombinant Human FGF-acidic/FGF1	50 µg
CRF001B	Recombinant Human FGF-basic/FGF2	50 µg
CRK300B	Recombinant Human FGF-7/KGF	10 µg
CRG300B	Recombinant Human G-CSF/CSF3	10 µg
CRG100B	Recombinant Human GM-CSF/CSF2	20 µg
CRG101B	Recombinant Mouse GM-CSF/CSF2	20 µg
CRG500B	Recombinant Human GRO-alpha/CXCL1	25 µg
CRG502B	Recombinant Rat GRO-alpha/KC/CXCL1	25 µg
CRI004B	Recombinant Human IFN-alpha 2b	100 µg
CRI000B	Recombinant Human IFN-gamma	100 µg
CRI001B	Recombinant Mouse IFN-gamma	100 µg
CRI002B	Recombinant Rat IFN-gamma	100 µg
CRI500B	Recombinant Human IGF-1	100 µg
CRI100B	Recombinant Human IL-2	50 µg
CRI153B	Recombinant Human IL-10	10 µg
CRI137B	Recombinant Human IL-15	10 µg
CRI162B	Recombinant Human IL-17	25 µg
CRI172B	Recombinant Human IL-21	10 µg
CRI225B	Recombinant Human IL-33	10 µg
CRM151B	Recombinant Human M-CSF/CSF1	10 µg
CRR000B	Recombinant Human RANTES/CCL5	20 µg
CRS000B	Recombinant Human SDF-1 alpha	10 µg
CRS002B	Recombinant Human SDF-1 beta	10 µg
CRT100B	Recombinant Human TNF-alpha	50 µg
CRT192B	Recombinant Mouse TNF-alpha	20 µg
CRV000B	Recombinant Human VEGF 165	10 µg
CRV014B	Recombinant Mouse VEGF 165	10 µg

* Good on orders in US and Canada only. This offer may not be combined with other offers or discounts. All products for research use only.

CELL SCIENCES INC • 480 NEPONSET STREET, BUILDING 12A, CANTON, MA 02021 • INFO@CELLSCIENCES.COM
TOLL FREE: (888) 769-1246 • TEL: (781) 828-0610 • FAX: (781) 828-0542 • WEB WWW.CELLSCIENCES.COM

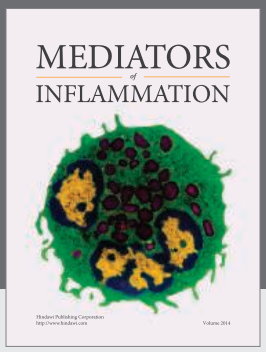

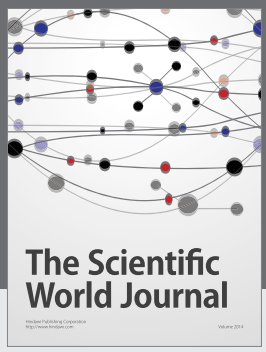

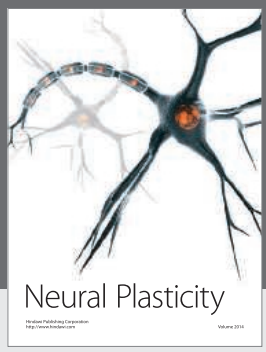

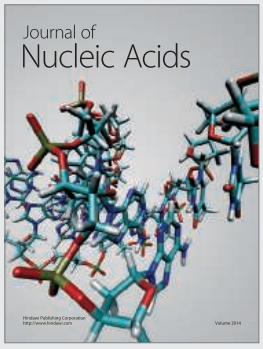

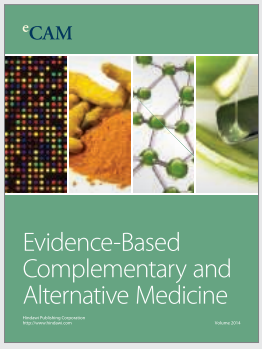

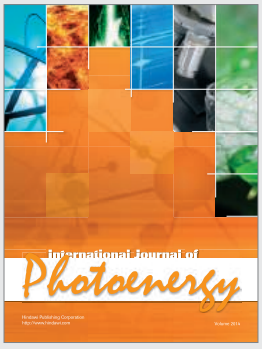

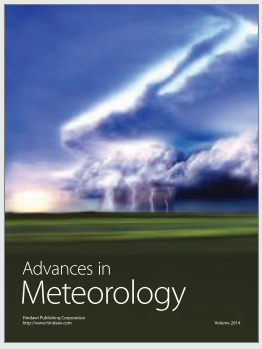

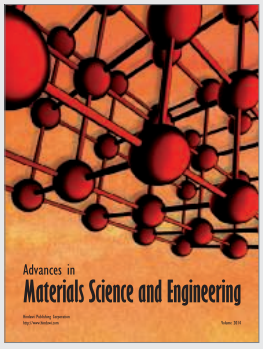

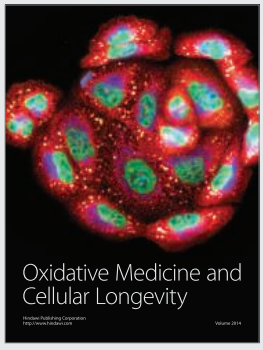

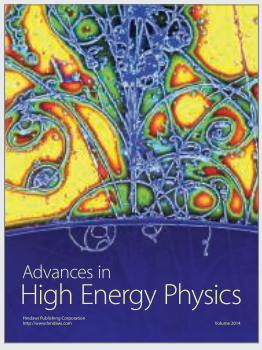

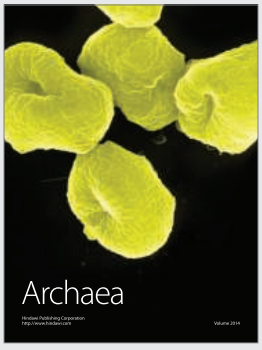

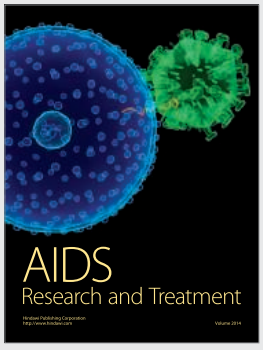

Hindawi

Submit your manuscripts at
http://www.hindawi.com

AAAS | 2015 ANNUAL MEETING

12–16 FEBRUARY • SAN JOSE, CA

INNOVATIONS, INFORMATION, AND IMAGING

The meeting will highlight the information transformation happening in science and technology brought about by recent advances in organizing, visualizing, and analyzing data.

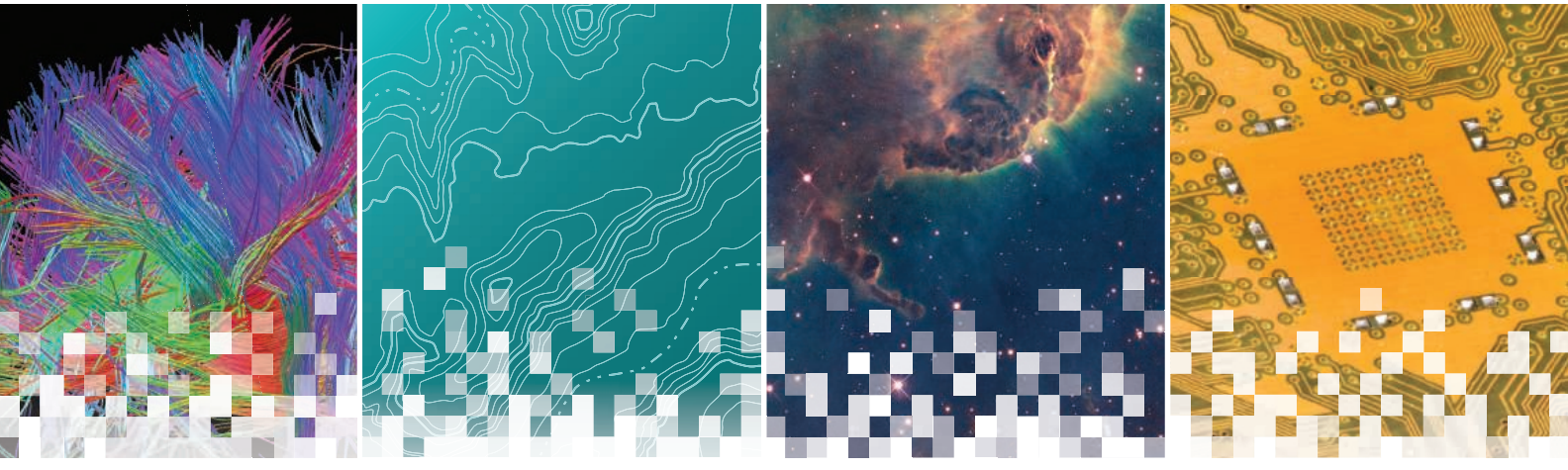

Advance Registration Opens in August

Be part of the interdisciplinary and international discussion on recent developments in science and technology.

What will you learn? Who will you meet?

Join us in San Jose. Advance registration and meeting hotel reservations open in August.

www.aaas.org/meetings

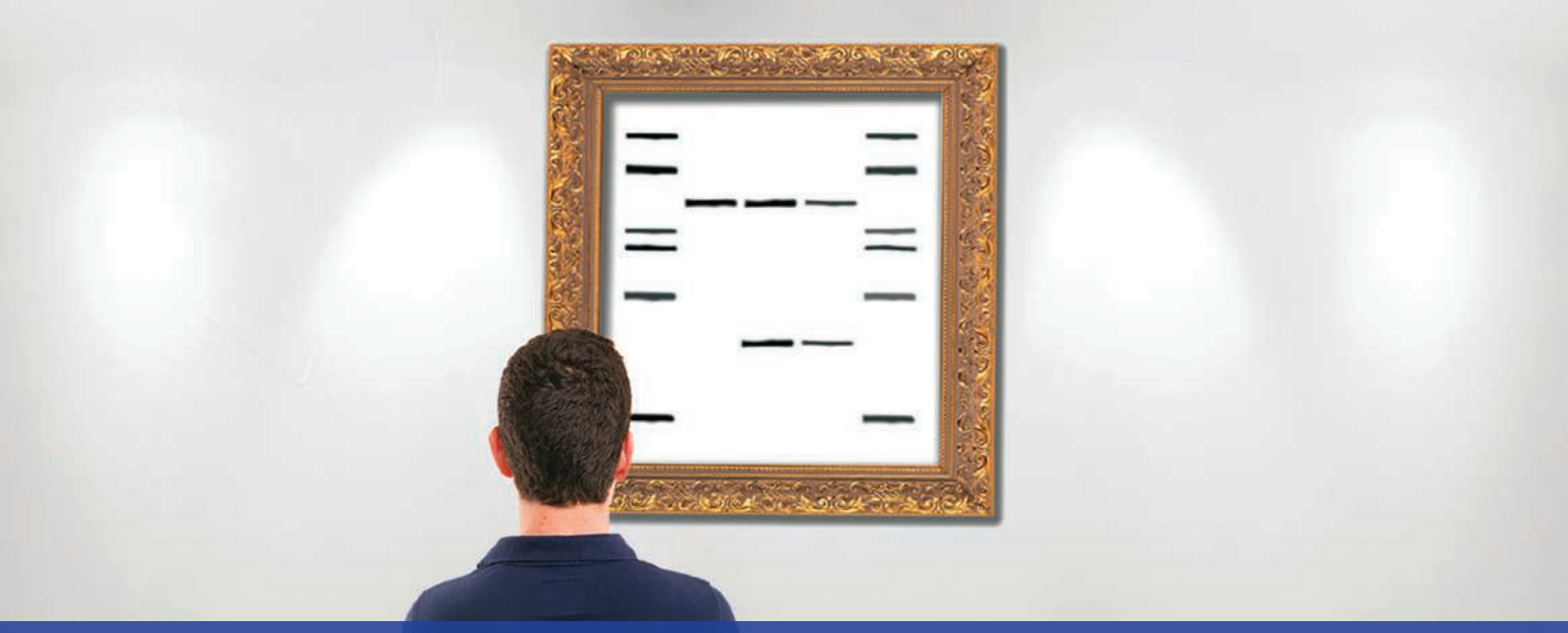

Western Blot Tips and Tricks:
Filling the Gap Between Art and Science

Wednesday, July 30, 2014
12 noon Eastern, 9 a.m. Pacific,
5 p.m. UK, 6 p.m. Central Europe

During the webinar, viewers will:

- Learn about some of the basic requirements for producing clean, reproducible Western blot data
- Gain insight into challenges and solutions for sample preparation, particularly when using dilute and precious samples
- Hear advice from experts on how you can improve your efficiency and streamline your immunoblotting workflows
- Have the chance to pose questions to the panel, live!

REGISTER NOW!
webinar.sciencemag.org

Western blotting has been a standard protein analytical technique for over 30 years and is used in practically every life sciences lab by thousands of scientists worldwide. Western blotting data appears in thousands of published papers annually but, despite its popularity, the method remains as much of a skilled art as a science, and it is often a significant challenge to produce reproducible and reliable results. In this webinar we invite three experts to give us their hints and tips of how to get the best possible Western blot data using current techniques as well as take a glimpse into the future of how technological advances could bring the needed standardization to Western blotting.

Speakers

Pier Giorgio Righetti, Ph.D.
Polytechnic University of Milan
Milan, Italy

Biji T. Kurien, Ph.D.
University of Oklahoma Health Sciences Center
Oklahoma City, OK

Nick Thomas, Ph.D.
GE Healthcare
Cardiff, Wales

Webinar sponsored by

Brought to you by the *Science*/AAAS Custom Publishing Office

@SciMagWebinars

eppendorf

Impress Yourself

The new Eppendorf Cell Culture Consumables

The all new product line of Eppendorf Cell Culture Consumables will truly delight your cells. Its outstanding design, reliability and purity is based on more than 50 years of experience.
Products created by experts, developed for perfectionists. Impress yourself!

> Unsurpassed quality, clarity, purity and sterility, providing reliable cell culture conditions
> Significantly improved design for more safety and consistency
> Maximum safety and confidence during storage and transportation

www.eppendorf.com/ccc

Eppendorf® and the Eppendorf logo are registered trademarks of Eppendorf AG, Hamburg, Germany.
All rights reserved, including graphics and images. Copyright © 2014 by Eppendorf AG.

HANDS DOWN!

Reichert surface plasmon resonance systems are the intelligent purchase with your grant dollars.

Reichert's SR7500DC surface plasmon resonance (SPR) system is the smart choice when selecting a system for label-free protein interaction analysis.

- SPR technology at a fraction of the price of the leading competitor
- Unparalleled performance, unmatched sensitivity, no better value
- Lower maintenance with off the shelf fluidics
- Affordable sensor chips for low operating costs

AMETEK®
ULTRA PRECISION TECHNOLOGIES

Reichert® TECHNOLOGIES
Life Sciences

Take advantage of our team of expert application scientists who:

- Solve problems and answer questions in a timely manner
- Support your assays with Reichert's in-depth SPR knowledge
- Arrange for a demonstration
- Install your new system

For a comparison of the Reichert SPR system and the competition go to:

ReichertSPR.com/advantage

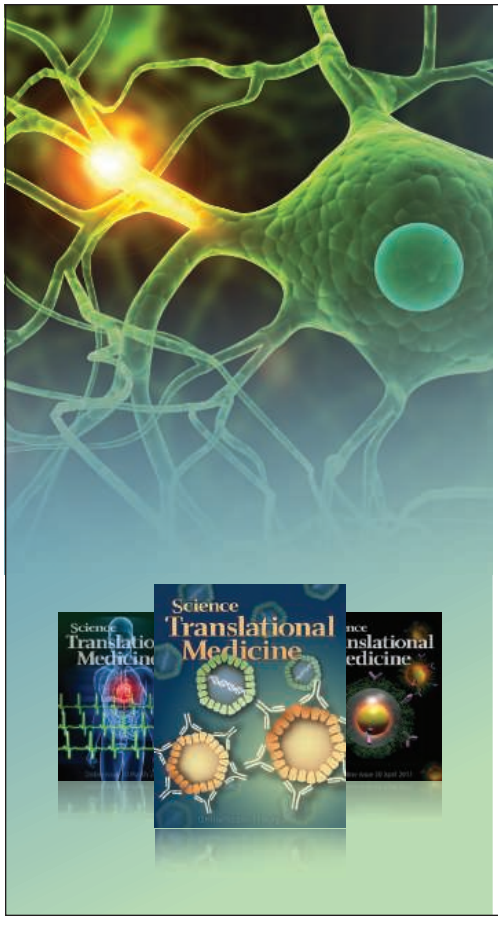

Science Translational Medicine

Integrating Science, Engineering, and Medicine

Publishing results that harness the basic sciences to advance human health in all areas of medicine

Submit your research
ScienceTranslationalMedicine.org

Recommend to your library
ScienceOnline.org/recommend

Science Translational Medicine
AAAS

scitranslmededitors@aaas.org

SAMPLE INTEGRITY

From the worldwide leader in cell stabilization

Cyto-Chex® BCT

Time and temperature can present obstacles to sample integrity. Often, sample collection in distant or resource-limited areas further complicates the concerns of sample preservation when analysis cannot be performed immediately.

Ensure the integrity of your samples with Cyto-Chex BCT from Streck.

Cyto-Chex BCT is a direct-draw blood collection tube which preserves peripheral blood sample qualitative and quantitative leukocyte subset characteristics. Cyto-Chex BCT is FDA 510(k) cleared for consistent recovery of HIV-associated lymphocyte subsets for up to 14 days.

Immunophenotypic Analysis of HIV+ Patient Samples

	EDTA tube	Cyto-Chex BCT	
Samples	Initial Test $CD4^+$ cells / µL	Day 7 $CD4^+$ cells / µL	Day 14 $CD4^+$ cells / µL
1	709	760	756
2	511	561	565
3	285	299	300
4	327	340	373
5	83	73	89

Peripheral blood samples stored in Cyto-Chex BCT provide the same results as tests performed on fresh specimens.

Minimize the adverse effects of time, storage and transportation for all your patient sample collections.

- Maintain sample integrity from collection site to analysis location and minimize patient redraws and the loss of critical data
- Samples are stable at room temperature, simplifying storage and shipping requirements and reducing associated logistical expenses
- Batch samples to optimize laboratory workflow and improve overall laboratory efficiency

Available in 5ml and 2ml tube sizes, and multiple pack configurations.

Take your study anywhere in the world – with Cyto-Chex BCT.

Streck | 866.544.0015
streck.com

TOGETHER, WE HELP EACH OTHER DO MORE.

Nationwide® is proud to partner with the AAAS.

You wouldn't be involved with the AAAS if you weren't passionate about science, but that's not the only reason you're proud of being a member of the AAAS. The AAAS also believes in the importance of philanthropy and in playing an active role in your community. Nationwide shares these values, too, and that's why our partnership works.

To learn more about what our partnership can do for you, call 1-866-238-1426 or visit nationwide.com/AAAS.

Nationwide® Insurance + AAAS ADVANCING SCIENCE, SERVING SOCIETY

Nationwide may make a financial contribution to this organization in return for the opportunity to market products and services to its members or customers. Products Underwritten by Nationwide Mutual Insurance Company and Affiliated Companies. Home Office: Columbus, OH 43215. Subject to underwriting guidelines, review, and approval. Nationwide, Nationwide Insurance, and the Nationwide framemark are service marks of Nationwide Mutual Insurance Company. © 2014 Nationwide Mutual Insurance Company. AFO-0576AO (04/14)

coming soon

bio-techne.com/launch

Copyright © 2014 Bio-Techne Inc. All rights reserved.

Science Careers Advertising

For full advertising details, go to ScienceCareers.org and click For Employers, or call one of our representatives.

Tracy Holmes
Worldwide Associate Director
Science Careers
Phone: +44 (0) 1223 326525

THE AMERICAS

E-mail: advertise@sciencecareers.org
Fax: 202-289-6742

Tina Burks
Phone: 202-326-6577

Nancy Toema
Phone: 202-326-6578

Marci Gallun
Sales Administrator
Phone: 202-326-6582

Online Job Posting Questions
Phone: 202-312-6375

EUROPE / JAPAN / INDIA / AUSTRALIA / NEW ZEALAND / REST OF WORLD

E-mail: ads@science-int.co.uk
Fax: +44 (0) 1223 326532

Axel Gesatzki
Phone: +44 (0)1223 326529

Sarah Lelarge
Phone: +44 (0) 1223 326527

Kelly Grace
Phone: +44 (0) 1223 326528

CHINA / KOREA / SINGAPORE / TAIWAN / THAILAND

Ruolei Wu
Phone: +86-1367-1015-294
E-mail: rwu@aaas.org

All ads submitted for publication must comply with applicable U.S. and non-U.S. laws. *Science* reserves the right to refuse any advertisement at its sole discretion for any reason, including without limitation for offensive language or inappropriate content, and all advertising is subject to publisher approval. *Science* encourages our readers to alert us to any ads that they feel may be discriminatory or offensive.

Science Careers
From the journal *Science* AAAS

ScienceCareers.org

TEXAS STATE UNIVERSITY
The rising STAR of Texas

Texas State University-San Marcos
is a member of the Texas State University System.

Assistant Professor Microbiology

The Department of Biology at Texas State University (www.bio.txstate.edu) invites applications for a tenure-track Assistant Professor in Microbiology. The successful candidate will be expected to teach both graduate and undergraduate courses in the Department of Biology and develop an externally funded research program that complements the existing strengths of our 34-member faculty. Required qualifications are a Ph.D. in Microbiology or related life sciences, postdoctoral experience, and a publication record in microbiology. Preferred qualifications are a record of extramural funding to support research, a record of interdisciplinary collaboration, and experience in research complementing the research strengths of the Department. The successful candidate is expected to teach one course per semester in virology or immunology. Salary and start-up package are negotiable.

Review of applications will begin **August 15, 2014** and continue until the position is filled. A letter of application with statements on research plans and teaching philosophy, CV, pdfs of five representative publications, and the names and contact information of five people willing to serve as references should be sent, as a single PDF, to **microbiology@txstate.edu**. Questions about this position should be addressed to **Dr. Robert McLean, rm12@txstate.edu, Texas State University, 601 University Drive, San Marcos, TX 78666**.

Texas State University is an Affirmative Action/Equal Opportunity Employer.

Editor-in-Chief

Integrative and Comparative Biology (ICB)

(Oxford University Press)

The Society for Integrative and Comparative Biology (SICB) seeks an Editor for the Society's journal. A five-year term begins January 1, 2016 and includes a transition period with the current Editor. *ICB* (Impact Factor 3.023) is ranked in the top 10 journals in Zoology, with a primary focus on syntheses within broad and interdisciplinary areas of Biology, from peer-reviewed symposia presented at meetings of the Society. Additional reviews and papers are also published, representing an area of innovative diversification available to the new Editor. We seek applicants who have editorial experience and skill, objectivity, evidence of leadership, creativity, and innovation within the enterprise of scientific research, with fiscal and administrative skills. Active involvement in SICB is desirable; attending the SICB annual meeting each January is required.

Contact Richard Satterlie, Chair of the Editor Search Committee (**satterlier@uncw.edu**), with nominations or applications, by **15 August 2014**.

UNIVERSITY OF CONNECTICUT 1881

FACULTY POSITIONS MOLECULAR AND CELL BIOLOGY University of Connecticut - Storrs

The Department of Molecular and Cell Biology at the University of Connecticut seeks applicants for three positions, one in each of the following areas: cell and developmental biology, genetics and microbiology. Each is a full-time, nine-month, non-tenure track faculty position at the level of **ASSISTANT PROFESSOR IN RESIDENCE** at the Storrs campus starting **August 23, 2014**.

For details on these positions, qualifications, and application instructions please visit **www.jobs.uconn.edu**.

The University of Connecticut is an EEO/AA Employer.

مؤسسة قطر
Qatar Foundation

CAREER OPPORTUNITY FOR CORE FACILITY MANAGERS

Qatar Foundation for Education, Science and Community Development is a private, chartered, non-profit organization, founded in 1995 by His Highness the Father Amir Sheikh Hamad Bin Khalifa Al Thani. Guided by the principle that a nation's greatest resource is the potential of its people, Qatar Foundation aims to develop people's abilities through a network of centers devoted to progressive education, research, and community welfare.

Qatar Biomedical Research Institute (QBRI), a member of Qatar Foundation, is a national center of excellence in biomedical research that aims to transform healthcare through harnessing and converting the latest advances in science, medicine and technology into novel discoveries that will lead to more effective treatments and preventive strategies for human diseases such as: diabetes, cancer as well as neurological disorders. QBRI's approach is holistic and multidisciplinary in nature as it focuses on prevention, diagnosis, treatments and personalized healthcare.

QBRI has plans to hire more than 100 scientists over the next two years and is slated to occupy state-of-the-art life sciences laboratories in a newly established research campus that is due to open soon.

Core Facility Managers Job Position:
To fulfill its mission, QBRI invites applications for scientific managers to develop and enable the following core facility/technology platforms:
- Advanced Microscopy.
- Flow Cytometry.
- Genomics and Genomics Technologies.
- Induced Pluripotent Stem Cells.
- Molecular Biology and Viral Production.
- Protein Biophysics and X-ray Crystallography.
- Proteomics and Mass Spectrometry.

Key Responsibilities:
- Managing the day-to-day operations of the core facility/technology platform.
- Providing technical expertise to QBRI scientists and collaborators.
- Adopting and developing novel techniques and experimental approaches to advance the research programs at QBRI.
- Ensuring that the facility maintains state-of-the-art instrumentations and is working at the frontiers of the relevant field.
- General duties also include: Managing state-of-the-art technologies; overseeing budget and spending; analyzing the cost of research projects; overseeing and maintaining essential equipment; purchasing materials and supplies; delegating responsibilities among laboratory staff and general lab maintenance.

Minimum Requirements:
- A PhD in the relevant field and at least 10 to 15 years of experience in the management of core facilities.
- Excellent and effective communication, management and organizational skills.
- Teaching/training capability.
- Demonstrated ability to work in a team/matrix environment.

If you are interested and fulfill the criteria mentioned above, kindly send to **qfjobs@qf.org.qa** the following: A copy of your résumé, a two-page summary of your research interest (Times New Roman 10 font), a list of your bibliography/publications, and three reprints of your most relevant publication, as well as the names and contacts of a minimum of three references. Kindly include the name of the position in the subject field of your email. The closing date to receive applications is: **Aug 31st , 2014.**

For more information please visit: www.qf.org.qa and www.qbri.org.qa

Institut Pasteur

Call for Candidates to Head a Research Unit in Bacterial Resistance to Antibiotics at Institut Pasteur in Paris, France

The Institut Pasteur launches an international call for outstanding candidates who wish to develop a ground-breaking research programme on « Bacterial Resistance to Antibiotics ». This call is broad in scope, including the major fields of the discipline from medical to fundamental bacteriology. It focuses on bacterial pathogens with relevance to humans, and resistance mechanisms of clinical importance. Key issues that can be addressed are: molecular basis of resistance to antimicrobials; understanding of the selection of resistant microbes and their subsequent spread; antibiotic effects on the host and its microbiota, identification of specific signatures associated with the ability to acquire and express resistance to antimicrobials; development of novel tools to monitor rapidly changing patterns in drug resistance; search for novel antimicrobials and new targets for therapeutics and diagnostics.
Multidisciplinary projects using cutting-edge technologies [such as single cell analysis, microfluidic-based approaches, cell biology techniques including fluorescence microscopy, genomic tools and high-throughput techniques] will be favoured.

This call is open to young, mid-career, and senior scientists wishing to establish an outstanding research laboratory on the campus of Institut Pasteur in Paris, France. Packages will include a position for the PI and fully equipped facilities. Personnel and recurrent budget will be adapted to the degree of seniority.

The Institut Pasteur is a non-profit private foundation dedicated to fundamental research in human biology and the prevention and treatment of diseases, with a large focus on infectious diseases, through basic science, education, and public health activities. The Paris campus houses 146 research units belonging to 10 research departments, employing about 2,600 people. It is recognized worldwide as a leader in infectious disease research and is ranked as a top level institution for publication impact in the field of microbiology. The Institut Pasteur has developed a world-class technological center, its "Technopole" composed of 10 state-of-the-art technological platforms, which closely collaborate with the researchers and cover their needs for studying modern biology from genomic to post-genomic activities, including bioinformatics, genotyping, DNA and protein sequencing, transcriptomics, proteomics, protein and antibody production, crystallography and X ray diffraction, macromolecular interactions, collections, animal facilities and an exceptional imaging centre (Imagopole).

The application should comprise the following (in order) in a single pdf file:
1. A brief motivation letter.
2. A Curriculum Vitae and a full publication list.
3. A description of past and present research activities (4-5 pages with 1.5 spacing). 4. The proposed research project (8-10 pages with 1.5 spacing).

Additional information can be obtained by contacting Dr Nathalie de Parseval, General Scientific Secretary (**dir-sci@pasteur.fr**)

Applications should be sent to **Isabelle Porteret** (**isabelle.porteret@pasteur.fr**) before **September 15, 2014**.

SciLifeLab

Discover the Future

8 Leading Positions at SciLifeLab

To further strengthen our unique research environment SciLifeLab is looking to recruit eight outstanding young group leaders:

Karolinska Institutet

- Two positions as Assistant Professor in Biomedical Sciences

KTH Vetenskap och Konst

- Assistant Professor in Systems Biology
- Assistant Professor in Computational Biophysics

Stockholms universitet

- Assistant Professor in Structural Biochemistry
- Assistant Professor in Molecular Bioscience

Uppsala Universitet

- Assistant Professor in Molecular Medicine
- Assistant Professor in Biodiversity Informatics

For more information, please visit: **www.scilifelab.se/fellows**

SciLifeLab is a Swedish national center for molecular biosciences with focus on health and environmental research. The center combines frontline technical expertise with advanced knowledge of translational medicine and molecular bioscience. SciLifeLab is a joint effort between Karolinska Institutet, KTH Royal Institute of Technology, Stockholm University and Uppsala University. SciLifeLab was established in 2010 and appointed a national center in 2013. Today, approximately 1,500 people work at the center's two sites in Stockholm and Uppsala.

Science & SciLifeLab PRIZE FOR YOUNG SCIENTISTS

SciLifeLab also supports a global prize for young scientists.
For more information, please visit: www.sciencemag.org/scilifelabprize

Science Careers online @sciencecareers.org

AAAS is here –

helping scientists achieve career success.

Every month, over 400,000 students and scientists visit ScienceCcareers.org in search of the information, advice, and opportunities they need to take the next step in their careers.

A complete career resource, free to the public, *Science* Careers offers a suite of tools and services developed specifically for scientists. With hundreds of career development articles, webinars and downloadable booklets filled with practical advice, a community forum providing answers to career questions, and thousands of job listings in academia, government, and industry, *Science* Careers has helped countless individuals prepare themselves for successful careers.

As a AAAS member, your dues help AAAS make this service freely available to the scientific community. If you're not a member, join us. Together we can make a difference.

To learn more, visit
aaas.org/plusyou/sciencecareers

AAAS + U = Δ

The David Starr Jordan Prize For Innovative Contributions to the Study of Evolution, Ecology, Population and Organismal Biology

In 1986, Cornell, Indiana and Stanford Universities established a joint endowment to fund a prize in honor of David Starr Jordan, a scientist, educator and institution builder, who had enormous influence on higher education in the United States and important ties to each of these universities. The prize is international in scope and presented approximately every three years to a young scientist (not over the age of 40 at the deadline for nomination, or if over 40, less than 10 years since receiving the Ph.D.).

The intent of this prize is to recognize young scientists who are making novel innovative contributions in one or more areas of Jordan's interest: evolution, ecology, population and organismal biology, and who are likely to redirect the principal foci of their fields. In addition to a $20,000 cash award, the recipient will receive a commemorative medal, will attend an awards ceremony, visit each of the sponsoring institutions and give scholarly presentations of his/her work. The selection of the prize winner will be made by a committee composed of representatives from each of the three institutions. This year the award ceremony will be held at Indiana University.

Nominations forms are posted on the David Starr Jordan Prize Website (www.davidstarrjordan.org). Nomination forms with supporting materials should be submitted electronically. Questions should be directed to:

Dee Verostko
Indiana University
Department of Biology
1001 E. Third Street, JH 127
Bloomington, IN 47405
(812-855-6283 - FAX 812-855-6705 - email dverostk@indiana.edu)

All nomination materials must be received prior to September 15, 2014.

For more information including a list of previous prize winners and their accomplishments, visit: **www.davidstarrjordan.org**

Tufts UNIVERSITY

Tufts University, Department of Biomedical Engineering – seeks candidates for a tenure-track faculty position at the Assistant or Associate Professor level, with rank determined by experience and accomplishments. Truly exceptional senior candidates may also be considered for appointment at the rank of Full Professor. Preference will be given to candidates whose research interests involve regenerative medicine, medical imaging, and biomedical optics, but all areas of biomedical engineering will be considered. The successful candidate will join an active department that offers B.S., M.E., M.S. and Ph.D. programs, and thus must demonstrate the potential to develop an outstanding, internationally recognized research program, excel in teaching, and develop strong interschool collaborations. Teaching responsibilities include graduate and undergraduate courses. A doctorate is required and postdoctoral experience is desirable. Additional information about the department can be found at **engineering.tufts.edu/bme/**.

Interested applicants should send their Curriculum Vitae, cover letter, research plan, and names of three references to:

Faculty Search Committee
Department of Biomedical Engineering
Tufts University
4 Colby Street
Medford, MA 02155

Evaluation of candidates will begin at the end of October 2014 and continue until the position is filled.

Tufts University is an Affirmative Action/Equal Opportunity Employer. We are committed to increasing the diversity of our faculty. Applications from women and members of underrepresented groups are strongly encouraged.

UNIVERSITY OF MICHIGAN

BIOLOGICAL SCIENCES SCHOLARS PROGRAM
For Junior, Tenure-Track Faculty

The University of Michigan announces recruitment for the Biological Sciences Scholars Program (BSSP) to enhance its investigational strengths in the life sciences research programs. Now entering its 15th year, this Program has led to the recruitment of outstanding scientists in the areas of genetics, microbiology, immunology, virology, structural biology, biochemistry, molecular pharmacology, stem cell biology, cancer biology, physiology, cell and developmental biology, bioinformatics, and the neurosciences. The Program seeks individuals with PhD, MD, or MD/PhD degrees, at least two years of postdoctoral research experience and seeking their first appointment as an assistant professor. Candidates will show evidence of superlative scientific accomplishment and scholarly promise. Successful candidates will be expected to establish a vigorous, externally-funded research program, and to become leaders in departmental and program activities, including teaching at the medical, graduate, and/or undergraduate levels. Primary college and department affiliation will be determined by the applicant's qualifications and by relevance of the applicant's research program to departmental initiatives and focus. All faculty recruited via the BSSP will be appointed at the Assistant Professor level.

APPLICATION INSTRUCTIONS: Please apply to the Scholars Program through the BSSP website at: **http://bssp.med.umich.edu**. A curriculum vitae (including bibliography), a three page research plan, an NIH biosketch, and three original letters of support should all be submitted through the BSSP website. More information about the Scholars Program, instructions for applicants and those submitting letters of recommendation, and how to contact us is located on the BSSP web site: **http://bssp.med.umich.edu**. The deadline for applications is **Friday, October 17, 2014**.

The University of Michigan is an Affirmative Action/Equal Opportunity Employer.

College of Engineering
UNIVERSITY OF WISCONSIN-MADISON

Professor and Director of the Grainger Institute for Engineering

The UW Madison, College of Engineering (CoE), is currently recruiting for a Professor and Director of the new Grainger Institute for Engineering.

The Grainger Institute for Engineering (http://graingerinstitute.engr.wisc.edu) is designed to serve as a new research incubator within the College of Engineering. The Institute will foster a trans-disciplinary research and educational environment and provide the infrastructure to address grand technological challenges. New research directions will be launched and nurtured within the Institute, with initial targeted efforts in the areas of advanced manufacturing and materials engineering.

The Grainger Institute Director will be responsible for developing and managing the Grainger Institute for Engineering. Through leadership excellence, the Director will sustain and enhance the trans-disciplinary research environment of the Institute. Specific responsibilities include faculty and staff hiring, budget management, creation and support of new research initiatives and centers, coordination with undergraduate and graduate educational programs, and public outreach. As a faculty member at the full-professor rank, the Director will have a tenure home in one of the College of Engineering academic departments.

For a complete position description and instructions on how to apply, please go to: **http://go.wisc.edu/2q0c21**.

UW-Madison is an Equal Opportunity/Affirmative Action Employer.

ETH zürich

Professor of Physical Activity and Health

→ The Department of Health Sciences and Technology (www.hest.ethz.ch) at the ETH Zurich invites applications for the above-mentioned professorship. The research of this professorship should focus on measuring how physical activity impacts on human physiology in order to restore or maintain health. This can include a variety of methods such as system's physiology, molecular approaches, (epi)genetics, medical imaging, and performance measurements. One essential aspect is that the research addresses questions relevant for humans – be it healthy individuals, patients or athletes, ranging from young to old age. The successful candidate possesses high visibility in his/her research field and has an excellent track record in attracting research funds at the national or international level. The new professor is expected to bridge the gap between fundamental research and applications in humans, which can include clinical trials. There should be a tangible link to one of the strategic research areas of the Department. The successful candidate is expected to have a strong background in exercise physiology, sport medicine, or related disciplines. He or she should be an enthusiastic colleague with a clear research vision and the ability to lead a research group. Interdisciplinary collaborations with clinical and basic science groups are expected. Additional prerequisites are a strong motivation and commitment to student education and teaching.

→ The new professor will be part of the Institute of Human Movement Sciences and Sport and is expected to develop the associated major programme that is part of the Health Sciences and Technology master and/or the physical education teacher training. The professorship will be embedded in the Department's programme in Health Sciences and Technology and will be expected to teach both undergraduate (mainly German) and graduate level courses (in English).

→ **Please apply online at www.facultyaffairs.ethz.ch**

Applications should include a curriculum vitae, a list of publications, and a statement of future research and teaching interests. The letter of application should be addressed **to the President of ETH Zurich, Prof. Dr. Ralph Eichler. The closing date for applications is 30 September 2014.** ETH Zurich is an equal opportunity and family friendly employer and is further responsive to the needs of dual career couples. We specifically encourage women to apply.

Download your free copy today.

ScienceCareers.org/booklets

From technology specialists to patent attorneys to policy advisers, learn more about the types of careers that scientists can pursue and the skills needed in order to succeed in nonresearch careers.

Science Careers
From the journal *Science* AAAS

POSITIONS OPEN

ASSISTANT PROFESSOR OF ECOLOGY
Department of Integrative Biology UT Austin

The University of Texas at Austin invites applications for a tenure-track appointment in its Department of Integrative Biology. We seek an innovative scientist working in any area of ecology ranging from organismal (any taxa) to ecosystems. We are particularly interested in candidates who will contribute to core teaching in ecology, who complement current research strengths within our Department, and who employ novel approaches possibly spanning levels of biological organization or transcending traditional disciplinary boundaries. We are interested in candidates who will contribute to diversity and equal opportunity in higher education through their teaching, research, and service. The appointment will be made at the Assistant Professor level. A Ph.D. is required at the time of appointment. Applicants should send a single PDF file containing the following items in order: cover letter, curriculum vitae, research statement, teaching statement, and up to five reprints/preprints. The PDF application file should be named with the candidate's lastname_firstname and electronically sent to **e-mail: ibjobsearch@austin.utexas.edu.** In addition, three letters of recommendation should be sent directly to **e-mail: ibjobsearch@austin.utexas.edu.** Review of applications will begin on August 25, 2014. For more detailed information about the department, see **website: http://www.biosci.utexas.edu/ib/.** *University of Texas, Austin is an Equal Employment Opportunity/Affirmative Action Employer.*

CAREER OPPORTUNITY

Doctor of Optometry (O.D.) degree in 27 months for Ph.D.s in science and M.D.s. Excellent career opportunities for O.D./Ph.D.s and O.D./M.D.s in research, education, industry, and clinical practice. This unique program starts in March of each year, features small classes, and 12 months devoted to clinical care.

Contact the Admissions Office, **telephone: 800-824-5526** at the **New England College of Optometry, 424 Beacon Street, Boston, MA 02115.** Additional information at website: **http://www.neco.edu** or at **e-mail: admissions@neco.edu.**

Find your future here.

Science Careers
From the journal *Science* AAAS

www.ScienceCareers.org

MARKETPLACE

PREMIUM REFURBISHED
GC/MS and LC/MS Systems
Save up to 50%
agilent.com/chem/refurbished
Agilent Technologies

南京理工大学
NANJING UNIVERSITY OF SCIENCE & TECHNOLOGY

Recruitments of talents abroad by Nanjing University of Science and Technology

http://rczp.njust.edu.cn/urp-portal/portal/group/Recruit

Nanjing University of Science and Technology (NUST) is one of the first national "211 Project" universities affiliated with the Ministry of Industry and Information Technology. It has become a multi-disciplinary and coordinated developing engineering-based university along with science, liberal arts, economics, management, law, education, etc. It is an ideal place for research work for its strong scientific research ability, prominent advantages, perfect construction of infrastructural facilities and it's also a pleasant place to live in since the beautiful scenery of Dr. Sun Yat-sen's Mausoleum which is only less than one mile away.

Please refer to the following application guidelines and we welcome your applications.

Majors for recruitment:

Related disciplines of Ordnance Science and Technology, Mechanical Engineering, Instrumentation Science and Technology, Chemical Engineering and Technology, Chemical, Electronic Science and Technology, Information and Communication Engineering, Optics, Optical Engineering, Computer Science and Technology, Control Science and Technology, Electrical Engineering, Transportation Engineering, Aerospace Science and Technology, Power Engineering and Thermal Physics, New Energy, Mechanics, Mathematics, Physics, Civil Engineering, Materials Science and Engineering, Environmental Science and Engineering, Biomedical Engineering, Law, Intellectual Property, Public Administration, Sociology, Economics, Management Science, (Applied) Linguistics and Literature, Art and Design.

Position and requirements:

Recruiting position: "Zijin scholars" distinguished professor, "Young Talents Professors", Professor, Associate Professor, Assistant Professor.

Basic qualities: Overseas talents with a doctorate degree, passion for education, high academic achievement and strong research capability and, good professionalism, academic character and team spirit as well. Among them, the candidates for "Young Talent Professor" staff position should be under 35 years old.

Related treatment:

The full-time employed teachers will be directly categorized into national institution, enjoying free medical care, pensions and other state welfare, and the family issues such as children's nursery and schooling will be addressed. We provide the high-level personnel and young talents with transitional housing, financial relief, research funding and other supports with generous salaries, comfortable working and living conditions. For high-level talents, we help settle down in terms of team building, work, housing, etc. Specific treatment will be determined by personal discussion.

1. For the full-time "Thousands of Plans" and other leading talents, NUST will provide 600 thousand to 1 million RMB annual salary and no less than 8 million RMB research start-up funds.
2. For the "Thousands Youth Talents" and other related talents, we provide no less than 300 thousand RMB annual salary, 1 million RMB financial relief and 2-4 million RMB research start-up funds.
3. For the "Zijin scholars" distinguished professor, we provide 500 thousand to 2 million RMB financial relief, 1 to 5 million RMB research funds and stipulated wages and other benefits along with certain amount of professor allowances per year.
4. For the "Young Talented Professors", we provide 300 thousand RMB annual salary, with certain financial relief and start-up funds.
5. For the professor, associate professor, assistant professor, we will provide salary and financial relief which is competitive in the same region, as well as starter home, and provide appropriate amount of research funds.

Way for recruitment:

The recruitments of talents abroad by NUST is under way regularly, please log in NUST Recruitment Network http://rczp.njust.edu.cn/urp-portal/portal/group/Recruit to have a registration, or contact us directly.

Contact us:

JI Wenchao Meng Yang
Tel: 86-25-84316943
Mail: rcb@njust.edu.cn
NUST website: www.njust.edu.cn

Job Vacancies in China's Universities

赛尔互联 CERNET

Science Careers
From the journal Science AAAS

赛尔互联：《科学》在中国大陆高校人才引进服务独家合作伙伴

CER is Science's exclusive agent for recruitment advertisement service in mainland China universities and colleges

China's Rapid Development
—— More Opportunities

- **Zhejiang University** (Zhejiang, China)
  Zhejiang University (ZJU) is seeking faculty candidates for its newly launched, highly competitive and well funded "Hundred Talents Program".
- **Nanchang University** (Jiangxi, China)
  The Institute of Life Science (ILS) of Nanchang University invites professcrs to lead an independent in neural development, synaptic plasticity, and brain disorders.
- **Zhejiang University of Technology** (Zhejiang, China)
  Zhejiang University of Technology provides positions for global experts on multiple disciplines.
- **Hunan University** (Hunan, China)
  Faculty positions in the areas of Mathematics, Physics,Biology, Environmental Science, Material Science and Chemistry...

For more details, visit http://www.eol.cn/

广告联系：赵佳 zhaojia@cernet.com +86 10 62603373

eol 中国教育在线 www.eol.cn 是赛尔互联旗下品牌

南京工业大学
NANJING TECH UNIVERSITY

海外领军人才招聘

Overseas Talents Recruitment

Nanjing Tech University, with a history of more than one hundred years, is a multidisciplinary university with a particular strength in engineering.

Aiming at excellence and innovation, Nanjing Tech University is set to become a first-class research university with a global vision. We are now seeking outstanding academic and research leaders in the following and related fields: Basic disciplines from within the Physical Sciences; Cutting edge disciplines from within the Life Sciences; Applied disciplines from within the Information Sciences; Humanities represented by Management Science.

Applicants should have a Ph.D. with at least 3-years research experience from leading universities or institutes. Candidates should demonstrate an internationally recognized research record and outstanding achievements. Successful candidates are expected to develop vigorous research programs and lead an independent research team. Successful candidates will be provided with a competitive relocation fee and salary package, generous start-up funds and spacious laboratories.

Interested candidates should visit **http://rczyb.njtech.edu.cn** for application details.

Phone: **Ms. Wang +86-25-58139148.**

E-mail: **job@njtech.edu.cn**